

**INVESTIGATION OF THE MAGNETIC PROPERTIES OF
AMORPHOUS Fe-RICH $Fe_{100-x}Zr_x$ AND $Fe_{90-y}Co_yZr_{10}$ ALLOYS
USING FERROMAGNETIC RESONANCE AND MOSSBAUER
TECHNIQUES**

**A THESIS SUBMITTED IN PARTIAL FULFILMENT OF
THE REQUIREMENTS FOR THE DEGREE OF
DOCTOR OF PHILOSOPHY**

**BY
VASUDEVA SIRUGURI**



**SCHOOL OF PHYSICS
UNIVERSITY OF HYDERABAD
HYDERABAD — 500 134**

INDIA

MAY 1993

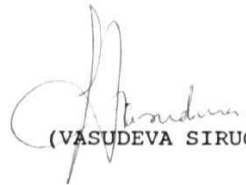
For Mom and Dad

STATEMENT

I hereby declare that the matter embodied in this Thesis is the result of investigations carried out by me in the School of Physics, University of Hyderabad, Hyderabad, under the supervision of Prof. S.N. Kaul.

Place : Hyderabad

Date : 28-5-1993.




(VASUDEVA SIRUGURI)

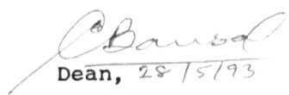
CERTIFICATE


Certified that the work contained in this thesis entitled, "**Investigation of the magnetic properties of amorphous Fe-rich $\text{Fe}_{100-x}\text{Zr}_x$ and $\text{Fe}_{90-y}\text{Co}_y\text{Zr}_{10}$ alloys using ferromagnetic resonance and Mossbauer techniques**", has been carried out by Mr. Vasudeva Siruguri under my supervision and the same has not been submitted for the award of research degree of any University.

Place : Hyderabad

Date : 28-5-1993.


(Thesis Supervisor)


Dean, 28/5/93
School of Physics.
DEAN,
SCHOOL OF PHYSICS,
UNIVERSITY OF HYDERABAD

INDIA
HYDERABAD-500 134
UNIVERSITY OF HYDERABAD
SCHOOL OF PHYSICS
PROF. S.N. KAUL


ACKNOWLEDGEMENTS

Being the first doctoral student, it is with great pride and high regard that I express my profound gratitude to Prof. S.N. **Kaul**, a person of deep physical insight and extraordinary perception, for suggesting this exciting research problem and for evincing keen interest and inspiring guidance at every stage of my work.

I **thank** the Dean, School of Physics, for providing all the necessary facilities.

I am extremely grateful to Dr. G. **Rajaram** for helping to overcome my teething problems with **Mössbauer spectroscopy**.

I thank Prof. Girish Chandra and Dr. A.K. **Nigam** at the Tata Institute of Fundamental Research, Bombay, and Dr. M.D.Sastry at the Radiochemistry Division, Bhabha Atomic Research Center, Bombay, for allowing me to use their experimental facilities.

I am grateful to the Principal Scientific Officer, Central Instrumentation Laboratory, and all the staff for their cooperation and help.

I must express my deep gratitude to my parents, to whom I dedicate this work, and other members of my family who have been a constant source of encouragement and provided me with that extra bit of cushion when the going got rough.

I must also thank :

- the University authorities for providing all the necessary facilities for my research work;
- Mr. P.D. Babu, for assisting with some of the calculations and programming;
- Mr. M. **Sambasiva** Rao and Mr. Ch.V. Mohan for their help and cooperation;
- Dr. **J.T.Thampi**, Mr. Y.S.Raosaheb and others for useful discussions and assistance;
- Mr.K. Srinivas for assisting with the wordprocessor;
- all friends and colleagues who have shared with me the good times as well as the bad.

*L'ordre est le plaisir de la raison; mais le desordre est
le délice de l'imagination.*

Paul Claudel
Le Soulier de Satin

CONTENTS

CHAPTER - I

1.1.	Introduction	1
1.2.	Classification , Preparation and Characteri- zation of Amorphous alloys	2
1.3.	Atomic Structure	4
1.3.1.	<i>Structural models</i>	4
1.3.2.	<i>Short range order</i>	6
1.3.3.	<i>Types of disorder</i>	8
1.4.	Influence of disorder on magnetic properties	10
1.4.1	<i>Density of states</i>	10
1.4.2.	<i>Magnetic moment</i>	11
1.4.3.	<i>Exchange interactions and Curie temperature</i>	12
1.4.4.	<i>Magnetic anisotropy</i>	13
1.4.5.	<i>Temperature dependence of magnetization</i>	13
1.5.	Concentration regimes	16
1.5.1.	<i>Dilute systems</i>	16
1.5.2.	<i>Intermediate concentration regime</i>	17
1.5.3.	<i>Concentrated systems</i>	19
1.6.	Theoretical models for different kinds of magnetic order	20
1.7.	Aim and scope of the thesis	27
	REFERENCES	34

CHAPTER - II

2.1.	Ferromagnetic resonance - Introduction	40
2.2.	Theoretical background and lineshape calcu- lations	41
2.3.	FMR experimental set-up	49
2.4.	Sample preparation, characterization and the measuring procedure	50
2.5.	Experimental accuracy and sources of error	54

2.6.	Mossbauer effect - Introduction	56
2.7.	The Fe decay scheme	57
2.8.	Hyperfine interactions	58
2.8.1.	Isomer shift	58
2.8.2.	Magnetic hyperfine interaction	59
2.8.3.	Electrical quadrupole interaction	61
2.8.4.	Combined magnetic and electric hyperfine coupling	62
2.8.5.	Intensity ratios	62
2.9.	Experimental procedure	63
	REFERENCES	66
 <u>CHAPTER - III</u>		
3.1.	Analysis of FMR spectra of metallic glasses	67
3.2.	Power Absorption Derivative curves	70
3.3.	Resonance fields	72
3.3.1.	Temperature dependence	72
3.3.2.	Concentration dependence	73
3.3.3.	Angular dependence	74
3.4.	Linewidths	75
3.4.1.	Temperature dependence	75
3.4.2.	Concentration dependence	11
3.5.	In-plane uniaxial magnetic anisotropy	77
3.6.	Magnetization	78
3.7.	Analysis of ME spectra of amorphous alloys	80
3.8.	Window method	82
3.9.	Two-pattern analysis	85
3.10.	Experimental results	86
	REFERENCES	89

CHAPTER - IV

SECTION A - FERROMAGNETIC RESONANCE

4.1.	Resonance fields	91
4.1.1.	<i>Temperatures around and above Curie point</i>	91
4.1.2.	Temperatures in the low and intermediate ranges	101
4.2.	Linewidths	109
4.2.1.	<i>Critical behaviour and LLG damping</i>	109
4.2.2.	<i>Intermediate temperature range</i>	111
4.2.3.	<i>Low temperature behaviour</i>	115

SECTION B - MOSSBAUER EFFECT

4.3.	Hyperfine field distributions	122
4.4.	Hyperfine fields	128
4.5.	Isomer shift	138
4.6.	Linewidth	139
4.7.	Intensity ratio and magnetic moment alignment	140
	REFERENCES	143

SUMMARY AND CONCLUSIONS	149
LIST OF PUBLICATIONS	155

CHAPTER - I

1.1. Introduction

Magnetic properties of amorphous alloys have been, in the recent years, a subject of intense experimental and theoretical interest. In the initial stages, scientific interest in such non-crystalline systems was mainly aroused by the attractive technological prospects that these alloys were supposed to offer. A complete success in the realization of the envisaged technological applications has, in turn, triggered off intensive research activity regarding the fundamental properties of amorphous alloys. When viewed in retrospect, a study of the magnetic properties of amorphous materials was, initially, not given serious consideration due to the belief that magnetic ordering and structural disorder are incompatible with each other. The possible existence of amorphous ferromagnetism was first explored theoretically by Gubanov [1], who predicted that amorphous solids would be ferromagnetic on the grounds that the electronic band structure of crystalline solids does not change in any fundamental way upon transition to the liquid or amorphous state (implying thereby that the band structure is basically controlled by the short-range order). Ferromagnetism, which is sustained by the direct exchange interactions between the nearest-neighbour spins, should, therefore, not be destroyed in the corresponding amorphous solid. The predictions of Gubanov were experimentally verified only after the first amorphous alloy, stable at room temperature, was prepared by Duwez and coworkers [2] by rapid-quenching of the melt. Of particular significance was the work of Duwez and Lin [3] on liquid-quenched

amorphous Fe-P-C alloy, which exhibited properties like high saturation magnetization, low coercive field, high Curie temperature and good stability at room temperature against crystallization. Since then, a huge amount of data on the fundamental as well as applied properties of amorphous alloys has accumulated and their physical implications have formed the subject of several books and review articles [4-10]. A complete bibliography about amorphous magnetism and magnetic materials has been compiled by Ferchmin and Kobe [11,12].

1.2. Classification, Preparation and Characterization of Amorphous alloys

Amorphous alloys or metallic glasses, as they are more commonly known, have been grouped according to the nature of their constituent atoms. For instance, the transition metal-metalloid **(TM-M)** glasses consisting of 3d transition metals (Fe, Co, Ni) and metalloids (B, C, P, Si) form the first group. Other groups combine an early transition metal (Fe, Co, Ni) with a late transition metal (Zr, Hf, Ti). Yet another group of alloys is formed out of the simple metals themselves or rare-earths with transition metals. These alloys cannot be formed in the amorphous state over the entire concentration range but within the concentration regimes which are narrow and generally centered around the deep eutectic points in the alloy phase diagrams. The width of the concentration range over which a particular alloy series can be formed in the amorphous state also depends on the type of preparation technique used.

There exist a number of techniques for the preparation of amorphous alloys. Most of them fall into two **main** categories: melt-quenching and deposition techniques. Melt-quenching methods include, (i) splat-cooling, (ii) roller-quenching, (iii) spark-erosion and (iv) laser glazing [13-18]. Fabrication of amorphous alloys in a concentration range away from the eutectic point is facilitated by the deposition techniques which include vacuum thermal evaporation [19] and sputter deposition **methods** [20]. Other less popular, but occasionally used techniques, are electro-deposition [21], ion-implantation [22] and solid-state reaction [23].

Metallic glasses are characterized through a study of their structural, physical, chemical or other properties. The simplest way of determining whether the atomic structure conforms to the amorphous state or not is to take an X-ray diffraction pattern. The diffraction pattern of an amorphous solid typically consists of diffuse rings or a broad peak at low 2θ values in a diffraction scan. But it is impossible to detect crystallites of size less than 15-20Å by diffraction methods. Consequently, it is not possible at once to distinguish between a microcrystalline structure and a homogeneous random distribution of atoms on the basis of diffraction patterns alone. A more refined X-ray technique, called Extended X-ray Absorption Fine Structure (**EXAFS**), has been developed to probe the local atomic structure of glassy alloys [24]. EXAFS is the oscillatory modulation of the absorption coefficient on the high energy side of X-ray absorption edge of a con-

stituent atom in a **system**. Another extremely powerful technique for probing short-range order of amorphous alloys is neutron scattering. Since neutron scattering length of an individual nucleus varies with different isotopes and their spin states, coherent and incoherent scattering takes place according to the existence and absence of interference occurring between neutron waves scattered by different nuclei. The coherent neutron scattering provides the information of collective structure and atomic pair correlation function, while incoherent neutron scattering probes the localized vibration and atomic diffusion. Local structural information can also be inferred from resonance of atomic nuclei in amorphous solids measured by NMR or **Mössbauer** spectroscopy. These techniques are more sensitive to variations in the local environment than methods which yield only partial distribution functions.

The chemical composition of metallic glass can be analyzed by using different techniques. Atomic absorption spectroscopy, X-ray **fluorescence**, electron **microprobe** analysis, Auger spectroscopy and secondary-ion mass spectroscopy are some of the techniques used for this purpose.

1.3. Atomic Structure

1.3.1. *Structural models*

A number of theoretical models have been proposed to describe the atomic arrangement in amorphous alloys,

Bernal [25] introduced the idea of dense random packing of

hard spheres (DRPHS) to **simulate** the structure of mono-atomic liquid metals. There is a random distribution of atoms such that only weak correlations exist between spheres separated by five or more sphere diameters. This work was followed up by Scott [26] and Finney [27], who concluded that the maximum density of a hard sphere non-crystalline packing was 0.6366 ± 0.0004 . With **this** model it was possible to calculate an accurate radial distribution function (defined in the subsection 1.3.2.) which reproduced **the** split second peak. But this model was not entirely successful as no real amorphous alloy can be thought of as an experimental realization of the hard-sphere model or consisting of only one species of atoms.

Subsequent models improvised on the DRPHS model by considering realistic softer potentials and by observing the structural changes when two (or more) components and their chemistry are considered. One such model is due to Gaskell [28] who first built **the** required chemical ordering and then allowed relaxation processes to bring in the dense packing constraints. He used trigonal prismatic units as basic building blocks as compared to the tetrahedral structures of Bernal. This type of chemical ordering is at the expense of packing constraints like large cavities. These constraints are then manipulated by computer-relaxing the whole assembly. Gaskell successfully applied this model to $\alpha\text{-Pd}_{80}\text{Si}_{20}$ and related **TM-M** alloys.

Besides these models, several other models [29,30,31] **have** been put forward which involve computer simulation and allow **for**

the interplay between local chemical ordering and overall packing constraints of high density structures.

1.3.2. Short range order

Instead of assigning a negative description to the **amorphous** character as that lacking in atomic periodicity, a localized picture in terms of short-range correlations and distributions is more appropriate. The microscopic structural quantity that can be directly determined from the scattering experiments is the atomic pair distribution function. But many properties cannot be described by the pair distribution function alone as they are either dependent on more collective correlations or on the local environments of each atom. This necessitates definition of a chemical short range order in terms of the pair distribution function. In most glassy alloys, on a local scale, the chemical composition is different from the macroscopic average and this deviation is called Chemical or Compositional short-range order (CSRO). This type of order is specific to the first nearest-neighbours only and hence can be described in terms of a deviation in the nearest-neighbour composition **from** the average. For a binary **system** (A-B), the **Warren-Cowley** short-range order parameter, α_p , is defined as

$$\alpha_p = 1 - \frac{z_{AB}}{\langle z \rangle C_B} = 1 - \frac{z_{BA}}{\langle z \rangle C_A} \quad (1.1)$$

where z_{AB} (z_{BA}) denotes the number of B (A) atoms in the nearest-neighbour coordination of an A (B) atom, C_A (C_B) is the concentra-

tion of A (B) atoms, and $\langle z \rangle$ is the average coordination number. α can be determined from the pair distribution function, which describes the probability that two dissimilar atoms A and B are separated by a distance \vec{r} and is given by [32]

$$\rho_{AB}(\vec{r}) = \frac{1}{4\pi^2 N} \sum_{ij} \delta(\vec{r} - \vec{r}_{ij}) (c_i^A c_j^B / C_A C_B) \quad (1.2)$$

where C , c denote the atomic concentration, N is the total number of atoms, r is the separation between the atoms occupying the sites i and j and $c_i = 1$ ($c_j = 1$) if the atom at the site i (j) is A (B) and 0 otherwise. For an isotropic amorphous solid with identical atoms, this function can be described in terms of a radial distribution function (RDF), which describes the number of atoms in a spherical shell of radius r and thickness dr around some chosen atom as origin averaged by taking each atom in turn as origin, i.e.,

$$\text{RDF}(r) = 4\pi r^2 \rho(r) \quad (1.3)$$

This is an oscillatory function with a parabolic baseline. Hence, this function can be more conveniently described in terms of a *reduced radial distribution function*,

$$G(r) = 4\pi r^2 [\rho(r) - \rho_0] \quad (1.4)$$

where ρ_0 is the average atomic density. $G(r)$ has a sharp but intense peak at the average nearest-neighbour atomic spacing besides

the second peak, which is usually split into two sub-peaks, and the higher order peaks that fade away with distance (Fig. 1.1). Area under the first peak gives the average coordination number.

There is another kind of short-range order (SRO) which depends on the degree of randomness of the structure. This is more applicable to single elementary glasses which are free from the effects of CSRO. This SRO is called *topological short range order* (TSRO). Geometrical distortions that are independent of topology are also possible. Therefore, the SRO that characterizes the local structure of an elementary glass may be called *Geometrical short range order* (GSRO), which includes both TSRO and *distortional short range order* (DSRO).

The local topology of the structure may be described in terms of the Voronoi polyhedra [33]. The Voronoi polyhedron is the equivalent of the Wigner-Seitz cell in crystalline solids. It is defined by planes which bisect the lines drawn between the center atom and its neighbours.

2.3.3. *Types of Disorder*

Amorphous structure is generally regarded as that lacking in long-range periodic order, i.e., the correlations between the atoms are lost completely beyond a few atomic spacings. The various types of disorder that result have a direct bearing on the **magnetic** properties of these alloys. Some of these types of disorder

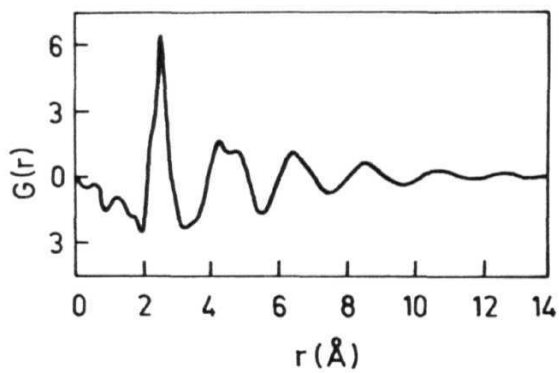


Fig. 1.1. Reduced radial distribution function $G(r)$ for a typical amorphous alloy.

der are described below.

(a) Bond disorder:

Fig. 1.2(a) shows a perfect two-dimensional **monoatomic** crystal. If the bond lengths and bond angles are distorted, then an aperiodic structure would result. This kind of disorder is called *bond disorder* (Fig. 1.2(b)). The network, however, still **remains** topologically equivalent to a crystal.

(b) Topological disorder;

Fig. 1.2(c) shows a much stronger disruption of periodicity called *topological disorder*. Rings with different numbers of atoms randomly distributed among **six-membered** rings are seen in the figure. One can also arrive at this situation by making the number of bonds at each atom in Fig. 1.2(b) deviate **from** three. Hence topological disorder includes bond disorder but such a disordered network cannot be distorted back into a crystal.

(c) Chemical disorder:

The complexity of the structure can be increased by considering a binary AB alloy (Fig. 1.2(d)). *Chemical disorder* can be induced by altering and swapping the positions of **atoms** A and B, without affecting the bond lengths or their number (Fig. 1.2(e)). The crystalline nature of the alloys is not affected by doing this. The bond lengths of the chemically ordered (Fig. 1.2(d)) and disordered (Fig. 1.2(e)) lattices can be altered to result in **bond** disordered lattices (Figs. 1.2(f) & (g)). To further increase **the**

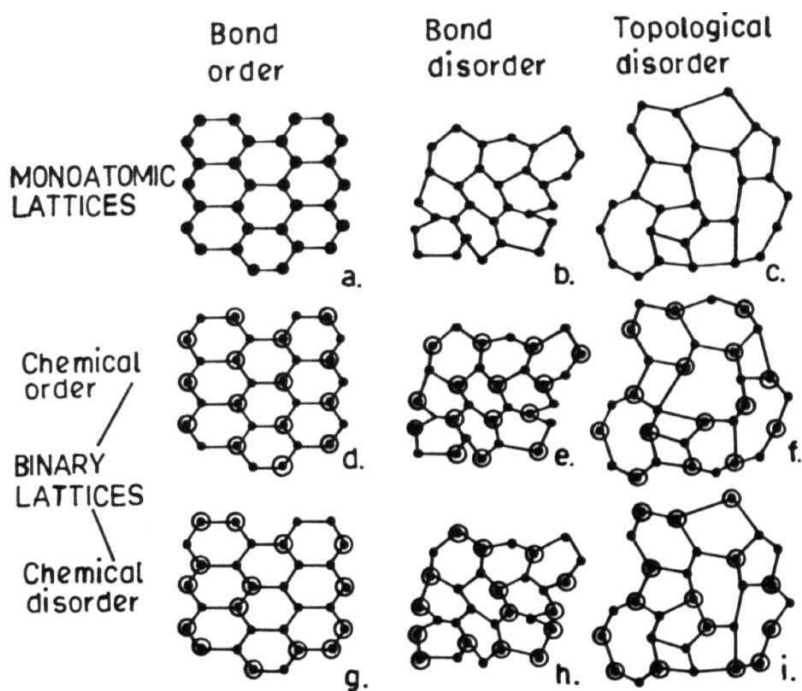


Fig. 1.2. Types of disorder on two-dimensional **monoatomic** and binary lattices.

disorder, conditions of topological disorder can be **imposed** on each of these two bond disordered lattices to result in Figs. 1.2(h) & (i), respectively.

Chemical disorder with topological disorder in the binary alloy system A_B can give rise to interesting magnetic phases depending on the type of atoms A and B and their concentration. If A is a magnetic atom and $x \rightarrow 0$ while atom B is of a non-magnetic species, A_B alloy then consists of a dilute magnetic impurity in an otherwise non-magnetic host. When x is increased beyond a certain specific limit, called the **percolation threshold**, the dilute alloy can be transformed into a magnetically concentrated one, which can support long-range **ferromagnetic** order.

1.4. Influence of disorder on magnetic properties

1.4.1. *Density of states*

A major influence of structural and chemical disorder is on the symmetry and density of electronic states at the Fermi energy, E_F . The dominant contribution of the density of states at E comes from regions of Fermi surface in which the wave functions have strong d-character. For pure amorphous transition metals, it has been theoretically proved [34] that structural disorder does not drastically affect the electronic structure with respect to their crystalline counterparts. In view of the fact that most amorphous materials are alloys of transition metals with **glass-forming** metalloids or with other metals, one might wonder as to how much

of the d-character of density of states at E_F is still preserved. It has been observed experimentally that the main contribution to the density of states at E_F still arises from d electrons in transition-metal base amorphous alloys. Therefore, one can safely assume that the main contribution to the magnetism in these alloys comes from the electrons of the d-band.

1.4.2. Magnetic moment

The variation of magnetic moment, μ , and Curie temperature, T_C , for amorphous alloys as a function of transition metal content was first reported by Mizoguchi *et al* [35], who plotted μ and T_C as functions of the number of valence electrons for amorphous $T_{80}B_{10}P_{10}$ ($T=Fe, Co, Ni$) thin films. It was observed that both μ and T lie consistently lower than those of crystalline transition metal alloys of the same composition. The variations in μ were explained on the basis of the *rigid band model* [36], which is based on the assumption that the d-bands do not alter on alloying and a transfer of charge from metalloid atoms to the d band takes place. However, the rigid band model represents an **oversimplification** as ample experimental evidence exists to show that the addition of metalloids changes the structure of the d-band and does not merely transfer charge. Alben *et al* [37] came out with an alternative explanation and suggested that the moment suppression is a result of a loss of d character by the magnetic states because of their participation in local chemical bonding with the **metalloid** species termed as p-d hybridization.

1.4.3. Exchange interactions and Curie temperature

The **dominant** magnetic interactions in transition metals are the direct exchange interactions resulting from the overlap of **wavefunctions** of nearest-neighbour atoms. This is **phenomenologically** represented by the isotropic Heisenberg interaction for a pair of localized spins as

$$\vec{H}_{ij} = - 2J_{ij} \vec{S}_i \cdot \vec{S}_j \quad (1.5)$$

where J_{ij} is the exchange integral between spins at sites i and j . The sign of J_{ij} is positive for **ferromagnetic** coupling and negative for **antiferromagnetic** coupling. Apart from direct exchange, there are other exchange mechanisms like superexchange via ligands and indirect exchange via conduction electrons, also called the **Ruderman-Kittel-Kasuya-Yoshida** (RKKY) interaction. The RKKY interaction is the main exchange coupling in dilute 3d alloys where direct exchange cannot operate and it is an oscillatory function of r , the interatomic distance. All these interactions depend sensitively on the distance between the interacting spins. Fig (1.3) shows a schematic variation of exchange coupling J as a function of distance between spins in the 3d-shell for 3d transition metals. A direct inference from Fig. 1.3 is that a distribution in interatomic distances in an amorphous alloy can lead to a distribution of exchange interactions. In spite of the distribution of exchange interactions in amorphous **ferromagnetic** alloys, they usually exhibit a well-defined Curie temperature, T_C . For amorphous alloys, T_C is a smooth function of the alloy composition in

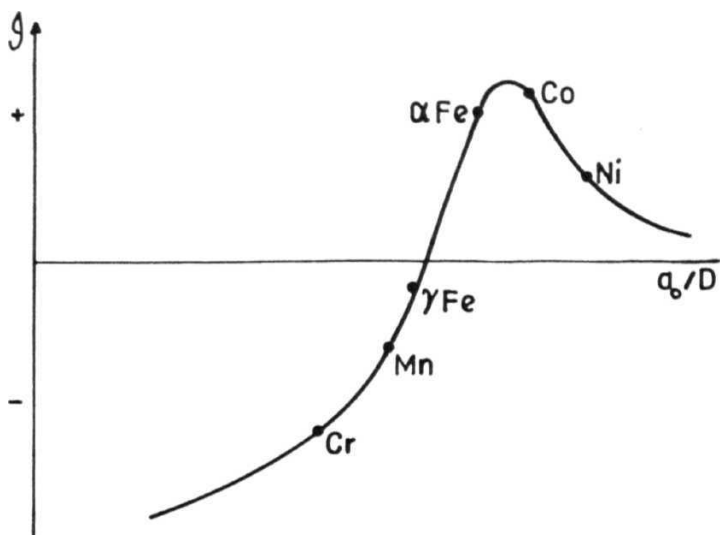


Fig. 1.3. Schematic variation of exchange coupling as a function of distance between the spins in the 3d shells in 3d transition metals.

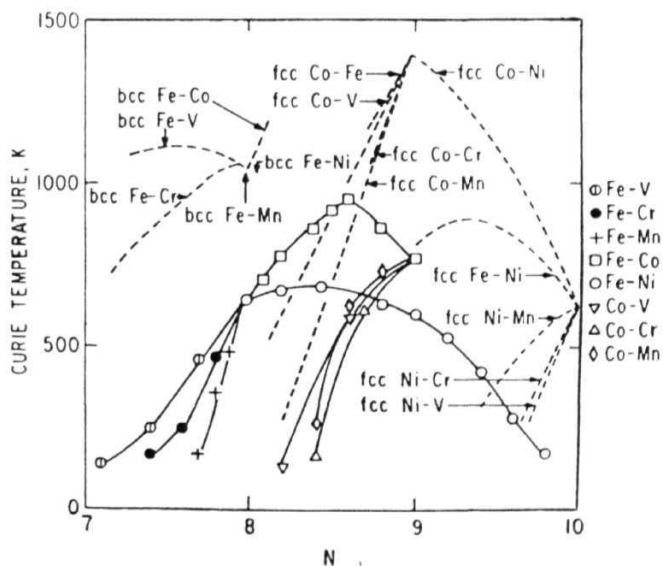


Fig. 1.4. Curie temperature as a function of the valence electron concentration N of the metallic atom for some typical amorphous alloys of 3d transition metals [35].

the entire range, as shown in Fig. (1.4). It is observed that Curie temperatures of amorphous alloys are slightly lower than those of the corresponding crystalline alloys. This is an indication of the strong influence of short-range order on the exchange interaction.

1.4.4. Magnetic anisotropy

Another important magnetic property that is influenced by disorder is the magnetic anisotropy. Amorphous alloys do not possess long-range order and hence are normally considered to be isotropic on a macroscopic scale. As a result, the magnetization vector is supposed to point in all directions with equal probability. However, most amorphous alloys exhibit magnetic anisotropy. Several mechanisms [38] have been proposed for this anisotropic behaviour and magnetic anisotropy reflects the existence of short-range order in these alloys.

1.4.5. Temperature dependence of magnetization

The coexistence curves, i.e., the plot of reduced magnetization $M(T)/M(0)$ versus reduced temperature T/T_c of amorphous ferromagnets generally fall below those of their crystalline counterparts. Handrich [39] assumed a distribution of exchange integrals (resulting from the structural **fluctuations**) in amorphous alloys and arrived at the following **equation** for reduced magnetization

$$m(T) = M_S(T)/M_S(0) = \frac{1}{2} \left\{ B_S[(1+\Delta)x] + B_S[(1-\Delta)x] \right\} \quad (1.6)$$

where B_S is the Brillouin function, $x = [3S_m / (S+1)] (T_C/T)$ and Δ is a measure of degree of disorder.

$$\Delta^2 = \frac{\langle \sum_j \Delta J_{ij} \sum_k \Delta J_{ik} \rangle}{\langle J_{ij} \rangle^2} \quad (1.7)$$

$$J_{ij} = \langle J_{ij} \rangle + \Delta J_{ij} \quad (1.8)$$

J_{ij} is the exchange integral between spins at the sites i and j with radius vectors r_i and r_j , ΔJ_{ij} is the deviation of J_{ij} from the average value $\langle J_{ij} \rangle$ and $\langle \rangle$ denotes the structural average. It is obvious that Δ is the root mean square of deviation from an average exchange integral between two nearest-neighbour spins. Though much of the reduced magnetization data for amorphous alloys have been interpreted in terms of this model [40], Alben et al [41] point out that since similar flattening effects are observed in disordered crystalline alloys [42], local chemical disorder is responsible for the flattening of $m(T)$ rather than local structural disorder.

The existence of well-defined spin-wave excitations obeying a normal **ferromagnetic** dispersion relation, $E = A + Dq^2 + E_0q^4 \dots$, has been confirmed by inelastic neutron scattering measurements [43] on amorphous alloys. Correspondingly, magnetization at low temperatures varies with temperature as

$$M_S(T)/M_S(0) = 1 - BT^{3/2} - CT^{5/2} - \quad (1.9)$$

The coefficient of the $T^{3/2}$ term, B , was found to be five to ten times larger than in comparable crystalline alloys. This is understood to be a consequence of the chemical disorder. Kaneyoshi [44] contends that while exchange fluctuations alone can describe **the** magnetization behaviour of rare-earth-based amorphous alloys, 3d transition-metal-based alloys behave quite differently with temperature, in that they exhibit faster thermal demagnetization than that predicted by Handrich's model. This is due to the fact that in the 3d transition metal alloys, where the moment is more easily perturbed by its environment, both the variations in moment magnitude as well as the exchange fluctuations play a decisive part in determining $m(T)$.

In many amorphous systems, particularly in those exhibiting Invar behaviour, the spin-wave stiffness constant D determined from neutron scattering measurements, D , is found to be larger than that (D_m) calculated from magnetization data [45]. This discrepancy between the values of D_n and D_m , has been attributed to **the** total neglect of the contribution to thermal demagnetization due to Stoner single-particle excitations [46] while analyzing the magnetization data. For weak itinerant **ferromagnets**, both the single-particle and spin wave excitations contribute to the decrease of magnetization with increasing temperature but the contribution due to the former type of excitations dominates over that arising from the latter type. For weak itinerant **ferromagnets**, **the**

single-particle contribution varies with **temperature** as

$$M(T)/M(0) = 1 - AT^2 - \dots \quad (1.10)$$

1.5. Concentration regimes

The various **magnetic** phases that come into existence as the magnetic impurity concentration in a **diamagnetic** host is progressively increased are briefly described in the following text.

1.5.1. *Dilute systems*

The subject of dilute transition metal alloys has been a well-studied one. The non-interacting 3d magnetic impurities dissolved in a non-magnetic host are classified under the general heading of Kondo (effect) alloys. In these systems, the appearance of magnetic moment on the 3d impurity is the result of a balance between two processes: intra-atomic interactions concerning mainly d electrons, and interaction of the impurity states with the conduction (itinerant) electrons of the host. The interactions between the magnetic impurities can induce, within the dilute limit, a random magnetic state termed as a spin glass. A spin glass can be more clearly defined as a random, mixed-interacting magnetic system characterized by a random, yet cooperative, freezing of spins at a well-defined temperature T_f below which a highly irreversible, **metastable** frozen state occurs without the usual long range spatial order. The magnetic impurities interact with each other through RKKY interaction which has a $1/r^3$ dependence, where

r is the distance between impurities. **RKKY** interaction is oscillatory in nature and hence the alignment of the two impurity spins may be parallel or anti-parallel depending on r . This gives rise to competing ferromagnetic and **antiferromagnetic** interactions. The combination of spatial randomness induced by dilution plus competing interactions give rise to frustration, which is the basic ingredient for a spin-glass type of ordering. The main experimental characteristics of spin glasses include: (i) a cusp in the ac susceptibility versus temperature curve at the freezing temperature T_f ; the shape of the cusp as well as T_f are sensitive to measuring frequency and dc applied field, (ii) **thermomagnetic** history effects occurring at temperatures close to, but below, T_f , e.g., displaced hysteresis loops, decay with time of the remanence, and (iii) for certain low concentration range of impurities, all the relevant physical parameters characterizing the spin glass state scale with concentration.

1.5.2. Intermediate concentration regime

When the magnetic impurity concentration is continuously increased, a magnetic alloy undergoes a series of transitions from one complex magnetic ordering regime to the other. First, there is an increased statistical probability of the magnetic impurity being the first or second nearest-neighbour to another impurity. Since the 3d electron wave-function has a finite spatial extent, the interatomic wavefunctions overlap and a direct exchange results. A short-range exchange interaction, depending on its

sign, can couple neighbouring impurity spins parallel or anti-parallel. Thus, magnetic clusters are formed as a result of concentration fluctuations in a random alloy. These magnetic clusters then freeze in random orientations below a certain temperature to form a cluster spin glass. When the impurity concentration is increased further, two or more magnetic clusters coalesce to form a bigger cluster and hence the clusters grow in size. This concentration regime is termed as **mictomagnetic** [47]. As the impurity concentration is increased beyond the mictomagnetic limit, a situation is reached where each magnetic site has at least one magnetic nearest-neighbour and a macroscopic connection or uninterrupted chain from one end of sample to the other is established. The critical impurity concentration at which a long-range ferromagnetic order first sets in is called the **percolation threshold**. Alternatively, the percolation threshold is the concentration at which the probability that a given occupied site belongs to an unbounded cluster becomes finite. The alloys with composition just above the percolation threshold (or critical concentration) have attracted considerable attention both from theoretical and experimental points of view during the past couple of decades because they exhibit very unusual magnetic properties at low temperatures. These phenomena have come to be known better as the 'reentrant' ferromagnetism or reentrant spin-glass. These alloys undergo a phase transition from paramagnetic (PM) to ferromagnetic (FM) state as the temperature is reduced and against further lowering of temperature the FM state becomes unstable and paves way to a **magnetically** disordered state, the spin glass (SG) state. The SG

state is characterized by an abrupt drop in ac **susceptibility** at a certain temperature called the reentrant temperature, T_{RSG} , and other magnetic effects such as the onset of magnetic viscosity and history dependent effects at T_{RSG} . Many amorphous alloys have been identified which exhibit reentrant behaviour and their magnetic phase diagrams determined. Such a phase diagram for a typical **re-**entrant alloy is shown in Fig. (1.5). The critical lines between the PM-FM, FM-SG and PM-SG intersecting at a **multi-critical** point (MCP) are determined by the scaling analysis of dc magnetization data taken at finite fields. The nature of transitions between these different magnetic phases has been investigated by **different** experimental techniques and the results of these investigations have given rise to a lot of controversy about their exact nature.

1.5.3. *Concentrated systems*

As the concentration of transition metal is increased well above the percolation threshold, a conventional **ferromagnetic** ordering results. This is due to the dominance of direct exchange interactions over indirect and competing exchange interactions. However, the onset of long range order in amorphous alloys is inhomogeneous in character, presumably due to the fluctuations in the coordination number and interatomic spacings. All the phenomena exhibited by dilute and '**slightly concentrated**' (intermediate-concentration) alloys like Kondo effect, spin glass, reentrant ferromagnetism **etc.**, completely disappear in this concentration regime.

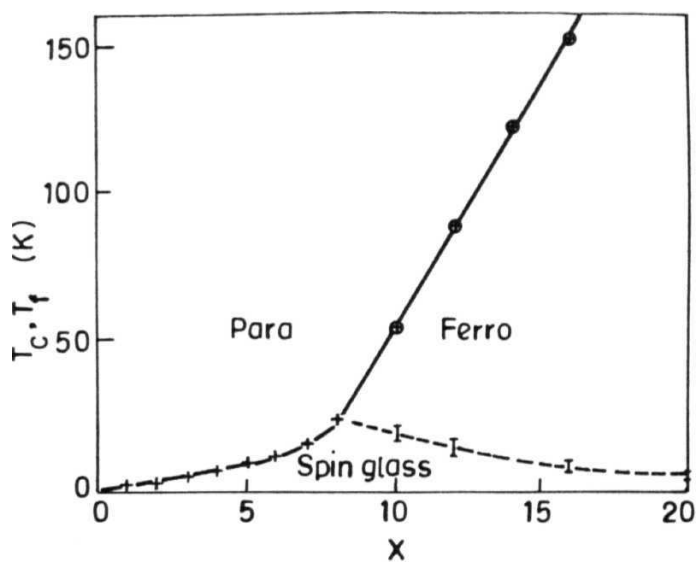


Fig. 1.5. Magnetic phase diagram of the reentrant alloy series a-
 $(\text{Fe}_x\text{Ni}_{1-x})_{79}\text{P}_{13}\text{B}_8$ [44].

1.6. Theoretical models for different **kinds of** magnetic order

A number of theoretical models have been proposed to describe the nature of spin-glass order. These models try to describe the phenomena that set-in at the characteristic spin freezing temperature, T_f . Edwards and Anderson (EA) [48] were the first to propose a model to describe the transition at T_f . They postulated the existence of a ground state where each spin freezes in a preferred direction that is randomly oriented and different at every site. In order to describe transition to the above ground state at T_f , it is necessary to define some order parameter. In all ordinary phase transitions, there not only exists a *long-range order* which does not depend on time (i.e., ergodic behaviour), but also an ordinary spatial order parameter, which is absent in spin glasses. Hence, as spin glasses do not possess long-range order in space, EA introduced a long-range order in time, i.e., a local autocorrelation function in time, defined as

$$q = \lim_{t' \rightarrow \infty} [\langle S_i(t=0) S_i(t=t') \rangle] \quad (1.11)$$

where the inner angular brackets represent thermal average while the outer brackets represent average over all the spin configurations. It is assumed that q is finite for $T < T_f$ and is zero for $T > T_f$ when the system is in the paramagnetic state. Thus, the non-vanishing value of the local autocorrelation function in time differentiates a spin glass phase from the paramagnetic state and the thermodynamics of the spin glass phase crucially depends on the

temperature variation of q . EA considered the Hamiltonian

$$\mathcal{H} = - \sum_{ij} J_{ij} \vec{S}_i \cdot \vec{S}_j - \sum_i \vec{H}_i \cdot \vec{S}_i \quad (1.12)$$

which is relevant to classical spins on sites i and j **interacting** via the exchange interaction J_{ij} and H_i is a local field. J_{ij} occur with **probabilities**

$$P(J_{ij}) = \frac{1}{\sqrt{2\pi} \Delta} \exp(-J_{ij}^2/2\Delta^2) \quad (1.13)$$

The free energy of the spin **system** is calculated by evaluating the partition function Z , or more precisely the free energy $(-kT \ln Z)$. That is, $\ln Z$ has to be averaged over a random distribution of J_{ij} 's, or more simply, average Z^n , where n is an integer. To do this, EA resorted to the famous '**replica trick**' in which n identical systems $S_i^{(1)}, S_i^{(2)}, \dots, S_i^{(n)}$, specified by S_i are introduced. The formal structure which is obtained involves a coupling between the different "replicas" α and in particular, coupling between two replicas α and β can be interpreted as representing the system at two different times so that the replica-replica correlation function behaves in a manner identical to the long-time autocorrelation function $[\langle S_i(0) S_i(\infty) \rangle]$. EA obtained the following expression for the susceptibility, χ ,

$$\chi = \chi_p (1 - q) \quad (1.14)$$

where $\chi = C/T$ is the paramagnetic susceptibility. Since $q=0$ for $T > T_f$ but is finite for $T \lesssim T_f$, χ obeys the Curie law for $T > T_f$ and

deviates from it for $T < T_f$ giving rise to a kink in the susceptibility at $T = T_f$.

Sherrington and Kirkpatrick (SK) [49] proposed a variant of the EA model in which the mean-field theory should be exact and which accounts for the reentrant behaviour at low temperatures. The mean field theory of **ferromagnetism** becomes exact in the limit of infinite range interactions where every spin couples equally with every other spin. SK considered **Ising** spins interacting via an exchange interaction of infinite range and a Gaussian distribution for J_{ij} of width Δ which is centred about a finite value J_0 , i.e.,

$$P(J_{ij}) = (N/2\pi)^{1/2} (1/\Delta) \exp\left[-N\{J_{ij} - (J_0/N)\}^2/2\Delta^2\right] \quad (1.15)$$

SK used the replica method and calculated the free energy exactly for all identical systems n and then, taking the thermodynamic limit $N \rightarrow \infty$, extrapolated to $n \rightarrow 0$. The results achieved were almost identical to those of the EA model. Fig. (1.6) shows the phase diagram for the SK solution. For $1 \leq J_0/\Delta \leq 1.2J$, the system undergoes a phase change from a paramagnetic to a ferromagnetic to a **'reentrant'** spin glass phase as the temperature is reduced. But the SK model gives unphysical results for $T \rightarrow \infty$: the entropy becomes negative, the free energy has a maximum and ground state energy is too low. Also, an exact solution does not have a reentrant spin glass phase.

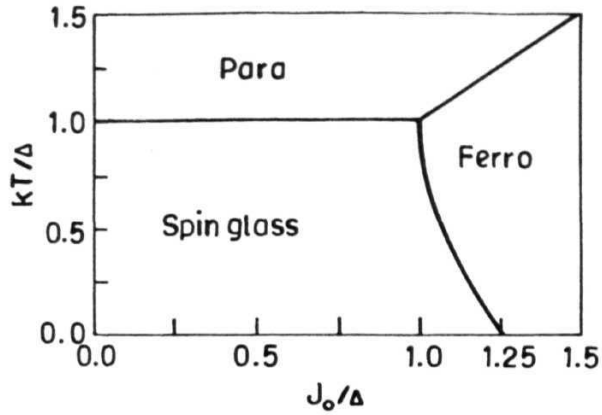


Fig. 1.6. Magnetic phase diagram predicted by the Sherrington-Kirkpatrick (SK) model [49].

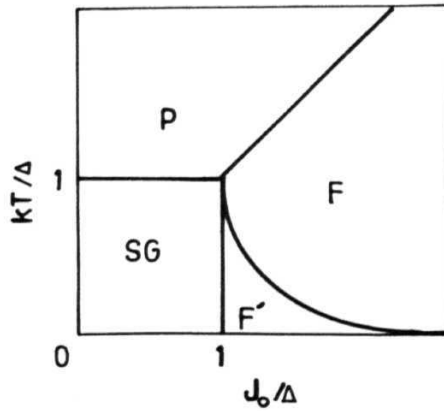


Fig. 1.7. The presumed exact phase diagram of the SK model with $H=0$. F' is a ferromagnetic phase with replica symmetry breaking (irreversibility) and is separated from F (where the SK solution is exact) by the de Almeida and Thouless line [49].

An alternative **method** for the solution of the SK model was suggested by Thouless, Anderson and Palmer (TAP) [50] who avoided the replica trick. In the replica method, disorder is averaged right away to obtain an effective Hamiltonian. TAP first determined the local mean-field equations for the site magnetizations for a given set of bonds and then performed the thermal average followed by averaging over disorder. This model removes all the apparent shortcomings of the SK model, but permits a large number of solutions which possess a range of free energies, those with lowest energies being stable and others, **metastable**.

A thorough analysis of the SK solution by de Almeida and Thouless (AT) [51] resulted in the problem being traced to the choice of a solution that is symmetric in replica labelling, i.e., treating replicas as indistinguishable. This study resulted in a modified phase diagram of the SK model, Fig. (1.7). The AT line is the boundary between the **FM** phase and the modified **ferromagnetic (FM')** phase. Above the AT line, the SK solution is stable and exact, but below this line, the solution is unstable. The solution below the AT line is due to Parisi [52] who postulated that there is a breakdown of the permutation symmetry of the replicas. A further interesting development came in the form of the infinite-range vector spin glass model of Gabay and Toulouse (GT) [53]. In the (T, \mathbf{J}) phase diagram two mixed phases are introduced [Fig. (1.8)]. The mixed phase \mathbf{M}_1 is characterized by the coexistence of a ferromagnetic order in the **z-direction** (longitudinal direction) and a spin-glass ordering, corresponding to frozen transverse (xy-

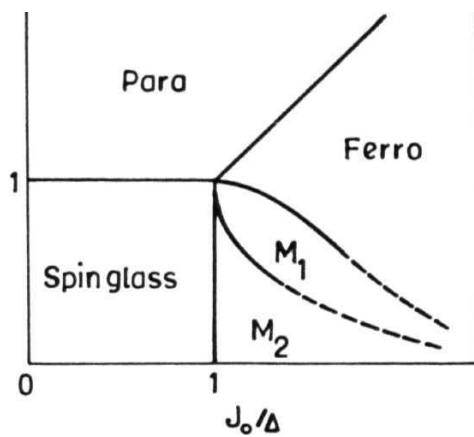


Fig. 1.8. Magnetic phase diagram predicted by the **Gabay-Toulouse** model [53].

) components of the spins. The transition line between the FM and **M** phases is the **Gabay-Toulouse** (GT) line. The mixed phase **M** has the same coexisting phases as in **M** and in addition, involves the spontaneous breaking of replica symmetry.

All the above models are based on the assumption that magnetic order is created by random exchange only. Hence, they neglect the effects of random anisotropy. Another totally independent basic approach is to assume that magnetic order is created by random axial anisotropy in the presence of **ferromagnetic** exchange. The **Hamiltonian** for this model, due to Harris et al [54], has the form

$$\mathcal{H} = - \sum_{i>j} J_{ij} \vec{S}_i \cdot \vec{S}_j - \sum_i D_i (\vec{n}_i \cdot \vec{S}_i)^2 - \sum_i g\mu_B S_{iz} H \quad (1.14)$$

where \vec{n}_i is a randomly-oriented easy direction at site i , D , the anisotropic **crystal-field** parameter and H , the external magnetic field. If the magnitude of the random anisotropy is large compared to the exchange, the local anisotropy fields orient the spins along their anisotropy axes, whose random orientation gives rise to a magnetically disordered state termed as the **speromagnetic** state. In the presence of external magnetic field, the above Hamiltonian gives an ordered state, with a net magnetization in the z -direction, but with individual spins canted away from this direction by amounts determined by the local anisotropy axes. Such an ordered state is termed as the **asperomagnetic** [55] state. In the strong anisotropy limit, random fields and anisotropies destroy long-range ferromagnetic order even though the exchange favo-

urs such an order. In the absence of external magnetic field, the local **magnetization smoothly** and **stochastically** rotates over the volume. This state is called the correlated spin-glass (CSG) [56] state. In the presence of magnetic field, this state transforms into a ferromagnetic state which still has some amount of disorder. Such a state has been given the name "**Wandering-axis ferromagnet**" [57]. The CSG state has zero net magnetization and at small distances, the spins are ferromagnetically correlated, but at large distances the correlation between the directions of spins decays exponentially with distance between the spins. In the Wandering-axis ferromagnetic state, the system is not completely ordered, since the random anisotropy causes the local direction of magnetization to wander slightly over a few atomic spacings.

Apart from these random exchange and random anisotropy models, there are several phenomenological models based on cluster percolation. A cluster is formed when, for a given group of spins, the short range exchange energies are much larger than the disordering effect of the temperature, $k_B T$. In order to present a physical interpretation of the essential phenomena of some archtypal spin glasses, Mydosh [58] proposed that as the temperature is lowered from $T > T_f$, the spin freezing temperature, many of the randomly positioned and freely rotating spins get locally correlated and group themselves into clusters. The spins within these clusters may be ferromagnetically coupled so as to result in a **superparamagnetic** moment. The remaining spins, the ones that do not belong to any cluster, are independent of each other, but

serve to transmit interactions between the clusters. As $T \rightarrow T_f$, the various spin components begin to interact with each other over a longer range and there is an increase in the size and density of cluster. The system would seek a lower energy state in which the clusters lock themselves along a favourable set of randomly aligned axes. Strongly interacting clusters give rise to a broadening in the distribution of relaxation times. The formation of the lower energy state causes a sudden shift in the height of energy barriers for various clusters. The height of energy barriers is proportional to the cluster moment. As a consequence, the larger clusters freeze earlier and finally at $T = T_f$ even the the smallest finite clusters and the individual spins freeze in random in orientations. The finite clusters retain their identity but no longer respond to an external field since they are embedded in the matrix of randomly frozen individual spins. Palmer et al [59] and Sarkisian [60] show that the Kohlrausch anomalous relaxation law describes the dynamics of the clusters for temperatures above and below T_f . In this model, Kohlrausch relaxation, which is of a stretched exponential form, is the result of hierarchical dynamic constraints over many energy barriers associated with the cluster size **distribution**, i.e., the smaller fast clusters constrain the large slow clusters over many time scales. Hence, clusters of different sizes freeze at different temperatures.

Coles et al [61] postulate, in a model for alloys with composition just above the percolation limit, that finite magnetic clusters coexist with an infinite cluster and contain a larger

proportion of the iron **moments**. These finite clusters respond relatively freely to external fields at temperatures immediately below the Curie temperature T_c of the infinite cluster, but freeze like a spin glass at a lower temperature T_g .

Kaul [62] considered the spin system for $T \leq T_c$ to be composed of an infinite three-dimensional ferromagnetic (FM) network or matrix and finite spin clusters that are embedded in this matrix (Fig. 1.9). In this model, a magnetic cluster denotes a set of strongly (**ferromagnetically**) coupled spins and has a vanishingly small interaction with the FM network due to frustration (caused by the topological disorder and by the combined action of sizable quenched-in local stresses and large volume magnetostriction) of exchange bonds around the boundary of the clusters. Only those spins that constitute the FM matrix participate in the transition at T_c whereas the finite spin clusters are responsible for the **superparamagnetic-like** behavior at $T \gg T_c$. As the temperature is decreased well below T_c , there is another temperature, T_{RE} , below which the finite spin clusters are frozen in random orientations and coexist with the FM matrix. The spin freezing process is not abrupt but proceeds slowly extending over a wide temperature range from temperatures well above T_{RE} to T_{RE} . Hence, below T_{RE} , there is a mixed state, in which long-range ferromagnetic order coexists with the spin glass order.

1.7. Aim and scope of the thesis

A number of amorphous alloys have been shown to **exhibit** re-



$$T < T_C$$

Fig. 1.9. The **infinite** ferromagnetic matrix plus finite ferromagnetic clusters model [62,87].

entrant spin glass behavior. But most of the existing *theoretical* models [48-57] do not *adequately* reproduce the experimentally observed phenomena. The basic mechanism of reentrant behavior is still unclear and the diverse findings based on various investigations have complicated the situation further.

For instance, despite the fact that the amorphous Fe-rich Fe-Zr alloy system has been the subject of intense experimental investigation during the recent years, the magnetic properties of this alloy system form a subject of much debate and **controversy**. The magnetic phase diagram [63-67] for amorphous $\text{Fe}_{90\pm} \text{Zr}_{10\pm}$ alloys shows a **multicritical** point at 93 at.% Fe (Fig. 1.10). It is noticed from the figure that there is a transition from **the** paramagnetic (PM) state to the **"ferromagnetic-like" (FM)** state at the Curie temperature, T_c , followed, at a lower temperature, T_{NF} , by another transition from the FM to the mixed phases M_1 and M [53] for concentrations in the range $0 \leq x \leq 3$. It is the exact nature of these phases that is a matter of debate as different experimental groups have reported conflicting results. First, the FM phase has found two main but contradictory descriptions based on different experimental findings. On the one hand, the following observations have been made: (i) a low value of saturation Fe atomic moment; (ii) a broad hyperfine field distribution with finite probability even at zero fields [66-71] for $T < T_c$; (iii) magnetic broadening in the Mossbauer spectra for temperatures well above T_c [66-67]; (iv) values of critical exponents considerably larger than those theoretically predicted for an ordered three-dimensional nearest-neighbour isotropic Heisenberg **ferromagnet**,

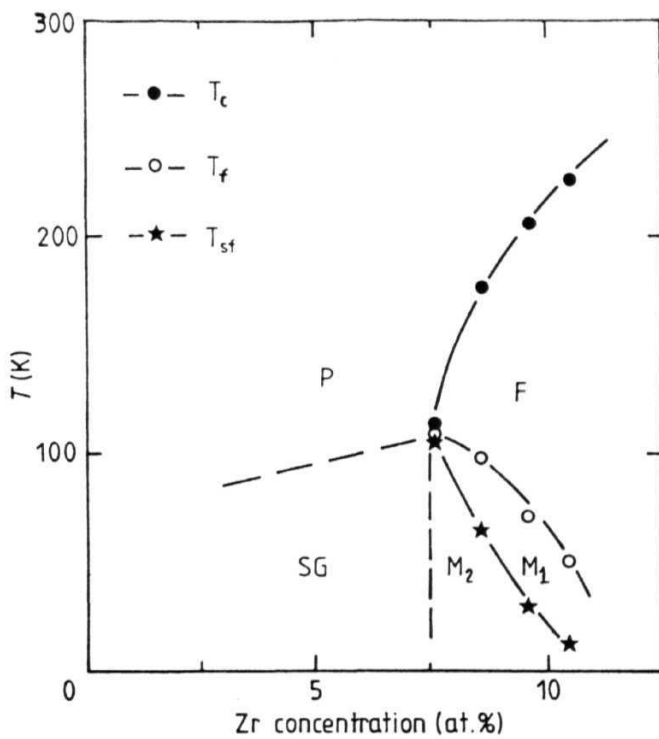


Fig. 1.10. Magnetic phase diagram proposed for the α -Fe Zr alloys [65].

which either satisfy [72] or do not satisfy [73] the Widom scaling relation; and (v) the *finite* (≈ 27 Å) spin-spin correlation length ξ at $T=T_C$ indicated by small-angle neutron scattering data [74] on $\alpha\text{-Fe}_{91}\text{Zr}_9$. The observations (i)-(v) have been taken to imply that the alloys in question behave either as "Wandering-axis ferromagnets", in which the spin structure is *locally ferromagnetic* [66,67] with small variations in spin directions on neighbouring sites **but** the local **ferromagnet** axis changes direction over distances of order ξ , or as a strongly **exchange-frustrated** system [74] in which the *ferromagnetic correlations are short-ranged* (≈ 27 Å), or else these alloys enter the spin glass state directly [76] at $T=T$ (i.e., *in no case does a long-range ferromagnetic order develops at any temperature* and the transition at T is not a true phase transition in the **thermodynamic** sense). On the other hand, AC susceptibility (χ_{ac}), measurements in the absence and presence of a superposed static magnetic field [76-78] as well as the recent bulk magnetization, M , data [78,79] taken in a narrow temperature range around T_C demonstrate that the transition at T , marked by the divergence [65,76-78] in 'zero-field' susceptibility at T_C , is a second-order magnetic phase transition characterized by 3D **Heisenberg-like** critical exponents and the ferromagnetic order for temperatures below T_C has a long-range character as inferred from the demagnetization-limited behaviour of both χ_{ac} and $M(T)$ in external dc fields < 10 Oe for $T < T_C$.

The nature of the transition at $T=T$ and the reentrant phase below T_{RE} is also not clearly understood. The changes in

various physical parameters, which characterize the behaviour of the spin system, as a function of temperature consequent upon a transition to the reentrant state have been basically understood from *three divergent* points of view. The first approach [66,80-83] considers the reentrant phase as a mixed phase in which the (long-range) ferromagnetic order along the z-direction coexists with the spin glass order in the xy-direction, following the transverse spin freezing (TSF) model of Gabay and Toulouse (Section 1.6). In this picture the appearance of 2 and 5 lines in the '**finite-field**' **Mössbauer** spectrum corresponding to the $\Delta m_I = 0$ nuclear transitions below a certain temperature $T = T_{\text{DF}}$ when the sample is cooled through T_{xy} is an external magnetic field intense enough to *nearly* saturate the sample (so that the $\Delta m_I = 0$ transitions are completely suppressed for $T > T_{\text{xy}}$) at temperatures above T_{xy} and applied **parallel** to the **γ -ray** direction (z-direction) is taken to imply that the transverse (xy) components of *local* magnetization at different sites freeze in random orientations in the **xy-plane** at $T = T_{\text{xy}}$ while the longitudinal (z) components point in the field direction **and** their resultant remains unaltered. The second school of thought [63,65,84] regards the reentrant state as consisting of the *spin clusters of anti ferromagnetic* (AFM) Fe spins and the ferromagnetic Fe-Zr *matrix* in which these clusters are frozen in random orientations. The onset of irreversibility [85] in the low-field magnetization as well as the evidence of a peak [84] in the imaginary part of the ACS at $T \approx T_R$ and the rapid decline in the '**zero-field-cooled**' magnetization for $T < T_{\text{--}}$ [85,86] can be satisfactorily accounted for in this model by properly correcting for

self-demagnetizing effects in the presence of **exponentially** increasing coercivity (caused by pinning of domain walls by the frozen AFM spin clusters in the ferromagnetic matrix) and the associated magnetic hardness (magnetic anisotropy energy) on cooling through T_{RE} . The third model [62,77,78,87-88] postulates that the spin systems for $T \leq T_{RE}$ comprises an *infinite* 3D **ferromagnetic** (FM) network or matrix and finite spin clusters (composed of a set of ferromagnetically coupled spins) which are frozen in random directions and embedded in the FM matrix. Though all the three models agree in that the reentrant state is a mixed state (a state in which long-range ferromagnetic order coexists with spin glass order), the underlying mechanism varies from model to model. For instance, in the TSF model, the longitudinal and transverse spin components coexist at every site and hence the spin system is perfectly *homogeneous* even on the microscopic scale. Such a picture would-be in sharp contrast with the spatial segregation of finite spin clusters and FM matrix in the other two models. The origin of this spatial segregation is the *concentration fluctuations* in case of the AFM clusters plus FM matrix model. Concentrations fluctuations imply that the glassy alloys in question consist of Fe-rich regions in which a given Fe atom has only Fe neighbors in an **fcc-like** nearest neighbour (NN) coordination (AFM Fe clusters), and the remaining Fe-poor bulk (FM matrix), in which a given Fe atom has at least one Zr neighbour. In the third model, the spatial segregation originates from the *density fluctuations*, which mean that in these alloys, which are homogeneous as far as the chemical composition is concerned, there exist microscopic regions of low-

density in an otherwise high-density bulk such that the average NN distance between Fe atoms in these "low-density pockets" is appreciably *greater* than that in the **remaining** bulk, and as a consequence the ferromagnetic coupling between spins within the finite clusters (low-density regions) is much stronger than that between the spins in the FM matrix (high-density bulk).

A systematic study of the magnetic properties of amorphous **Fe_{90+x}Zr_{10-x}** and **Fe_{90-y}Co_yZr₁₀** alloy series was undertaken with a view to find out the exact nature of magnetic order in **the** former alloys and to bring out the effect of partial substitution of Fe with Co on the FM and reentrant states in the parent alloy **a-Fe₉₀Zr₁₀**. The other extreme composition in the latter alloy series, i.e., the **a-Co₉₀Zr₁₀** alloy, serves as a reference in that it is known [64] to behave as a conventional **ferromagnet** for temperatures down to 4.2 K.

In this thesis, the results of a detailed study of the magnetic properties of **a-Fe_{100-x}Zr_x** ($x=9,10$) and **a-Fe_{90-y}Co_yZr₁₀** ($y=0,1,2,4,6,8,10$ and 18), using ferromagnetic resonance and Mossbauer spectroscopic techniques, are presented. These results include:

- i) The temperature dependence of linewidth, resonance field and **magnetization**.
- ii) Angular dependence of **the** resonance field for temperatures below and above T_C .
- iii) Determination of the critical exponents and critical **ampli-**

tudes characterizing the **FM-PM** phase transition.

- iv) **Temperature** dependence of average hyperfine fields and other **Mössbauer parameters**.

REFERENCES

- [1] A.I. Gubanov, Sov. Phys. Solid State, 2, 468 (1960).
- [2] W. Klement, R.H. Willens and P. Duwez, Nature **187**, 869 (1960).
- [3] P. Duwez and S.C.H. Lin, J. Appl. Phys., 38, 4096 (1967).
- [4] F.E. Luborsky, in *Ferromagnetic Materials*, edited by E.P. Wohlfarth (North-Holland, Amsterdam, 1980) Vol. 1, p. 451.
- [5] T. Mizoguchi, A.I.P. Conf. Proc. 34, 286 (1976).
- [6] *Amorphous Magnetic Alloys*, edited by F.E. Luborsky (Butterworths, London, 1983).
- [7] T. Egami, Rep. Prog. Phys. 47, 1601 (1984).
- [8] K. Handrich and S. Kobe, *Amorphous Ferro- and Ferrimagnetics* (Akademie Verlag, Berlin, 1980).
- [9] *Glassy Metals: Magnetic, Chemical and Structural Properties*, edited by R. Hasegawa (CRC, Boca Raton, Florida, 1983).
- [10] K. Moorjani and J.M.D. Coey, *Magnetic Glasses* (Elsevier, Amsterdam, 1984).
- [11] A.R. Ferchmin and S. Kobe, *Amorphous Magnetism and Metallic Magnetic Materials - Digest, Selected Topics in Solid State Physics*, Vol. 17 (North-Holland, Amsterdam, 1983).
- [12] S. Kobe, A.R. Ferchmin, H. Nose and F. Stobiecki, J. Magn. Magn. Mater. 60, 1 (1986).
- [13] P. Petrokowsky, Rev. Sci. Instrum. 34, 445 (1963).
- [14] H.S. Chen and C.E. Miller, Rev. Sci. Instrum. 41, 1237 (1970).
- [15] H.H. Liebermann and C.D. Graham, Jr., IEEE Trans. Mag. **MAG-**

12, 921 (1976).

- [16] S. Kavesh, in *Metallic Glasses*, edited by J.J. **Gilman** and H.J. **Leamy**, (ASM, Metal Park) p. 36.
- [17] T. **Yamaguchi** and K. Narita, IEEE Trans. Mag. **MAG-13**, 1621 (1977).
- [18] B.H. Kear, **J.W.** Mayer, J.M. Poate and P.R. Struti, *Metallurgical Treatises*, edited by J.K. Tien and **J.F.** Elliot, (**AIME**, Warrendale, Phoenix, 1981) p. 321.
- [19] R. **Glang**, in *Handbook of Thin Film Technology*, edited by L.I. Maissel and R. Glang (McGraw Hill, New York, 1970).
- [20] *Thin Film Processes, Part II*, edited by J.L. Vossen and W. Kern, (Academic Press, New York, 1978).
- [21] A. Brenner, D.E. Couch and E.K. Williams, J. Res. Nat. Bur. Std. 109 (1950).
- [22] A. Ali, W.A. Grant and P.J. Grundy, Phil. Mag. B37, 353 (1978).
- [23] W.L. Johnson, M. **Atzmon**, M. Van **Rossum**, B.P. Dolgin and X.L. Yeh, in *Rapidly Quenched Metals*, edited by S. Steeb and H. **Warlimont** (Elsevier, North-Holland, New York, 1985)p. 1515.
- [24] J. Wong, in *Glassy Metals*, edited by H.-J. Guntherodt and H. Beck (Springer Verlag, Berlin, 1981) Chapter 4.
- [25] J.D. Bernal, Nature, 188, 910 (1960).
- [26] G.D. Scott, Nature, 194, 956 (1962).
- [27] J.L. Finney, **Proc. Roy. Soc.** London, A319, 479 (1970).
- [28] **P.H.** Gaskell, J. Non. Cryst. Solids, 32, 207 (1979).
- [29] L.V. Woodcock, J. **Chem.** Soc. Faraday II, 72, 1667 (1976).
- [30] D.S. Boudreaux and J.M. Gregor, J. App. Phys. 48, 5057

- (1977).
- [31] L. Von **Heimendahl** and J. Hafner, Phys. Rev. Lett. 42, 386 (1979).
 - [32] A.B. Bhatia and D.E. Thornton, Phys. Rev. **B2**, 3004 (1970).
 - [33] J.L. Finney, in *Amorphous Magnetic Alloys*, edited by F.E. Luborsky (Butterworths, London, 1983).
 - [34] S.N. Khanna and F. **Cyrot-Lackmann**, J. Phys. (Paris) 41, C8-423 (1980).
 - [35] T. **Mizoguchi**, K. **Yamauchi** and H. **Miyajima**, in *Amorphous Magnetism*, edited by H.O. Hooper and A.M. **deGraaf**, (Plenum Press, New York, 1973) p. 325.
 - [36] K. Yamauchi and T. Mizoguchi J. Phys. **Soc.** Japan, 39, 541 (1975).
 - [37] R.A. **Alben**, J.I. Budnick and G.S. Cargill III, in *Metallic Glasses*, edited by J.J. **Gilman** and H.J. **Leamy**, p. 3 04, (ASM, Metals Park, Ohio, 1978).
 - [38] **R.C.** O'Handley, in *Amorphous Metallic Alloys*, edited by F.E. Luborsky (Butterworths, London, 1983) p. 272.
 - [39] K. Handrich, Phys. Stat. Solidi, 32, K55 (1969).
 - [40] **C.C.** Tsuei and H. Lillienthal, Phys. Rev. B13, 4899 (1976).
 - [41] R.A. Alben, G.S. Cargill III and J. Wenzel, Phys. Rev. B13, 835 (1976).
 - [42] J. Crangle and **G.C. Hallam**, **Proc.** Roy. Soc, A272, 119 (1963).
 - [43] H.A. Mook, N. Wakabayashi and D. Pan, Phys. Rev. Lett., **34**, 1029 (1975).
 - [44] T. Kaneyoshi, in *Metallic Glasses: **Magnetic**, Chemical and*

Structural Properties, edited by R. Hasegawa (CRC, Boca Raton, Florida , 1983) p. 37.

- [45] R. Hasegawa and R. Ray, Phys. Rev. B20, 211 (1979).
- [46] **E.P. Wohlfarth**, J. Magn. Magn. Mater., 45, 1 (1984); S.N. **Kaul**, Sol. State Commun. 52, 1015 (1984).
- [47] **P.A. Beck**, Met. Trans. 2, 215 (1971).
- [48] S.F. Edwards and P.W. Anderson, J. Phys. F5, 965 (1975).
- [49] D. Sherrington and S. Kirkpatrick, Phys. Rev. Lett. 35, 1792 (1975).
- [50] D.J. Thouless, P.W. Anderson and R.G. **Palmer**, Phil. Mag., 35, 593 (1977).
- [51] J.R.L. de Almeida and D.J. Thouless, J. Phys. All, 983 (1978).
- [52] G. Parisi, Phys. Rep. 67, 25 (1980).
- [53] M. Gabay and G. Toulouse, Phys. Rev. Lett., 47, 201 (1981).
- [54] R. Harris, M. **Plischke** and M.J. **Zuckermann**, Phys. Rev. Lett., 31, 160 (1973).
- [55] J.M.D. Coey, J. Appl. Phys. **49**, 1646 (1978).
- [56] E.M. Chudnovsky and R.A. Serota, Phys. Rev. B26, 2697 (1982).
- [57] E.M. Chudnosky, W.M. Saslow and R.A. Serota, Phys. Rev. B33, 251 (1986).
- [58] J.A. Mydosh, in *Amorphous Magnetism II*, edited by R.A. Levy and R. Hasegawa (Plenum, New York, 1977) p. 73.
- [59] R.G. Palmer, D.L. Stein, E. Abrahams and P.W. Anderson, Phys. Rev. Lett. **53**, 958 (1984).
- [60] B.V.B. Sarkissian, J. Phys.:Condens. Matter. 2, 7873 (1990).

- [61] B.R. Coles, B.V.B. Sarkissian and R.H. Taylor, **Philos. Mag.** B37, 489 (1978).
- [62] S.N. Kaul, Solid State **Commun.** 36, 279, (1980); IEEE Trans. Magn. **MAG-20**, 1290 (1984); J. Mag. Magn. Mater. 53, 5 (1985).
- [63] H.Hiroyoshi and K.Fukamichi, J. **Appl. Phys.** 53, 2226 (1982).
- [64] S.N. Kaul, Phys. Rev. **B27**, 6923 (1983).
- [65] N. Saito, H. Hiroyoshi, K. **Fukamichi** and Y. **Nakagawa**, J. Phys. F : Met. Phys. 16, 911 (1986).
- [66] **D.H.** Ryan, **J.M.D.** Coey, E. Batalla, Z. Altounian and J.O. **Ström-Olsen**, Phys. Rev. B35, 8630 (1987).
- [67] J.M.D. Coey, D.H. Ryan and R. Buder, Phys. Rev. Lett. 58, 385 (1987).
- [68] R. **Oshima**, M. **Tanimoto**, E.F. Fujita, M. Nose and T. Masu-
moto, *Proc. of Fourth Int. Conf. on Rapidly Quenched Metals*,
edited by T. **Masumoto** and K. Suzuki (**Instt.** of Metals, **Sen-**
dai, 1981) vol. II, p. 117.
- [69] H. **Yamamoto**, H. Onodera, K. **Hosoyama**, T. Masumoto and H.
Yamauchi, J. Magn. Magn. Mater. 31-34, 1579 (1983).
- [70] H. Tange, K. **Inoue** and K. **Shirakawa**, J. Magn. Magn. Mater.
54-57, 303 (1986).
- [71] J.A. Heller, E.F. Wassermann, M.F. Braun and R.A. Brand, J.
Magn. Magn. Mater. **54-57**, 307 (1986).
- [72] K. Winschuh and M. Rosenberg, J. Appl. Phys. 61, 4401,
(1987).
- [73] H. Yamauchi, H. Onodera and H. Yamamoto, J. Phys. **Soc.**
Japan, 53, 747 (1984).

- [74] J.J. Rhyne and G.E. **Fish**, J. Appl. Phys. 57, 3407 (1985).
- [75] G.E. Fish and J.J. Rhyne, J. Appl. Phys. **61**, 454 (1987).
- [76] S.N. **Kaul**, A. **Hofmann** and H. **Kronmüller**, J. Phys. F : Met. Phys. 16, 365 (1986).
- [77] S.N. Kaul, J. Appl. Phys. **61**, 451 (1987).
- [78] S.N. Kaul, J. Phys. F : Met. **Phys.** 18, 2089 (1988).
- [79] R. Reisser, M. **Fähnle** and H. **Krönmüller**, J. Magn. Magn. Mater. 75, 45 (1988).
- [80] D.H. Ryan, in *Magnetic Properties of Amorphous Metals*, edited by A. Hernando, V. Madurga, M. C. Sanchez-Trujillo and M. Vazquez (Elsevier, Amsterdam, 1987) **p.244**.
- [81] D.H. Ryan, J.O. **Ström-Olsen**, R. Provencher and M. Townsend, J. Appl. **Phys.** 64, 5787 (1988).
- [82] M. Ghafari, W. Keune, R.A. Brand, R.K. Day and J.B. Dunlop, Mat. Sci. Engg. 99, 65 (1988); M. Ghafari, N. **Chmielek**, W. Keune and C.P. **Foley**, Physica B **161**, 222 (1989) .
- [83] D.H. Ryan and H. Ren, J. Appl. Phys. 69, 5057 (1991).
- [84] D.A. Read, G.C. **Hallam** and M. **Chirwa**, J. Magn. Magn. Mater. 82, 83 (1989).
- [85] W. Beck and H. **Kronmüller**, Phys. Stat. Sol. (b) **132**, 449 (1985).
- [86] D.A. Read, T. Moyo and G.C. **Hallam**, J. Magn. Magn. **Mater.****54-57**, 309 (1986).
- [87] S.N. Kaul, J. Phys. :Condens. Matter 3, 4027 (1991).
- [88] S.N. Kaul, C. Bansal, T. **Kumaran** and M. Havalgi, Phys. Rev. **B38**, 9248 (1988).

CHAPTER - II

2.1. Ferromagnetic resonance

Introduction

Ferromagnetic resonance is the resonant absorption of external microwave radiation in **ferromagnetic** materials. When a spin (electron), which acts like a magnetic dipole, is placed in an external magnetic field of uniform strength H , it precesses around the direction of the magnetic field. The frequency of the precession (the **Larmor** precession frequency) is related to H by

$$\omega_L = \gamma H \quad (2.1)$$

where $\gamma = g\mu_B/\hbar$ is the **gyromagnetic** ratio of the electron. Resonant absorption of energy can occur when this magnetic dipole is exposed to an external electromagnetic radiation of frequency $\omega = \omega_L$, applied perpendicular to H , and the resonance condition can be written as

$$\hbar\omega = g\mu_B H \quad (2.2)$$

This phenomenon is the well-known electron spin resonance (ESR) which occurs in substances with unpaired electron spins and in which the moments are non-interacting. In the case of ferromagnetic substances the situation is quite different from that of non-interacting spins as in **paramagnetics**. The phenomenon of ferromagnetic resonance (**FMR**), first discovered by Griffiths [1], is the resonant microwave absorption in a system of strongly interacting spins. This strong exchange interaction leads to a parallel alignment of spins which, in turn, gives rise to a large resultant magnetization or a large internal field. The resonance condition, Eq.(2.2), is no longer valid in the sense that in the case under consideration the external field H has to be replaced by an effective

tive field \mathbf{H}_{eff} which, besides \mathbf{H} , takes into account the anisotropy fields present in ferromagnetic materials.

2.2. Theoretical background and lineshape calculations

The first phenomenological equation of motion for magnetization in a **ferromagnet** in the presence of an external magnetic field \mathbf{H} of the form,

$$\frac{d\vec{M}}{dt} = -\gamma (\vec{M} \times \vec{H}) - \frac{\lambda}{M_S^2} (\vec{M} \times \vec{M} \times \vec{H}) \quad (2.3)$$

where the parameter λ characterizes the relaxation rate, is due to Landau and Lifshitz [2]. As this equation is not entirely correct at low frequencies, Gilbert [3] suggested a modified equation of motion, i.e.,

$$\frac{d\vec{M}}{dt} = -\gamma (\vec{M} \times \vec{H}) + \frac{\lambda}{\gamma M_S^2} (\vec{M} \times \frac{d\vec{M}}{dt}) \quad (2.4)$$

The third equation of motion for magnetization is due to Bloembergen [4], who used the Bloch's relaxation equation

$$\frac{d\vec{M}}{dt} = -\gamma (\vec{M} \times \vec{H}) - \frac{M_x}{T_2} \hat{i} - \frac{M_y}{T_2} \hat{j} - \frac{M_z - M_0}{T_1} \hat{k}$$

where T and T are the longitudinal and transverse relaxation times, respectively. Bloembergen assumed that

$$\frac{1}{T_2} = \frac{1}{2T_1} + \frac{1}{T_2^*} \quad (2.6)$$

where T is the spin-lattice relaxation time and T_2 is the spin-spin relaxation time. The **Bloch-Bloembergen** form, unlike the

Landau-Lifshitz and Gilbert forms of damping, does not conserve the magnitude of magnetization, $|\vec{M}|$. The thin-film switching experiments on ferromagnetic materials have demonstrated that $|\vec{M}|$ is conserved during switching. Hence, the **Bloch-Bloembergen** form of damping does not form a correct description of damping in **ferromagnets**. In the small damping limit, the **Landau-Lifshitz** and Gilbert forms are equivalent and the usage of a particular form is a matter of convenience or familiarity. With the choice of the relaxation term of Gilbert form and neglecting the exchange conductivity contribution to $d\vec{M}/dt$ for reasons stated later (Section 3.1), the appropriate resonance conditions and the line-shape are derived as follows.

Consider an ellipsoidal isotropic ferromagnetic sample which is subjected to a homogeneous external static magnetic field \vec{H} directed along the z-axis and to a weak alternating magnetic field, $\vec{H}(t) = \vec{H} e^{i\omega t}$ ($|\vec{H}(t)| \ll |\vec{H}|$) acting in the xy plane. As a result of the combined action of these fields, the magnetization comprises a steady and an alternating component, i.e., $\vec{M} = \vec{M}_0 + \vec{m}(t)$ with $\vec{m}(t) = \vec{m} e^{i\omega t}$ and $|\vec{m}(t)| \ll |\vec{M}_0|$. Assuming that the steady field is intense enough to saturate the ferromagnetic sample so that \vec{M}_0 and \vec{H} point in the same direction, the Gilbert form of equation of motion for magnetization (hereafter referred to as the LLG equation) is

$$\frac{d\vec{M}}{dt} = -\gamma (\vec{M} \times \vec{H}_{\text{eff}}) + \frac{\lambda}{\gamma M^2} (\vec{M} \times \frac{d\vec{M}}{dt}) \quad (2.7)$$

where the first term is the torque experienced by the magnetization vector and the second term is the damping term and $\vec{H}_{\text{eff}} = \vec{H} +$

$\vec{H}(t) = \vec{H}_{\text{dem}} + \vec{H}_k$, $\vec{H}_{\text{dem}} = \vec{D} \cdot \vec{M}$ is the demagnetizing field and $\vec{H}_k = -\vec{D}_k \cdot \vec{M}$ is the uniaxial anisotropy field with easy axis along it; \vec{D} and \vec{D}_k are diagonal tensors, $\gamma = g|e|/2mc$ is the gyromagnetic ratio, M_s is the saturation magnetization and X is the Gilbert damping parameter.

Substitution for \vec{M} and \vec{H}_{eff} in Eq. (2.7) yields

$$\begin{aligned} \frac{d\vec{m}(t)}{dt} = & -\gamma [\vec{M}_s \times \vec{H}(t) + \vec{m}(t) \times \vec{H} - \vec{M} \times (\vec{D} \cdot \vec{M}) - \vec{M} \times (\vec{D}_k \cdot \vec{M}) \\ & + \frac{\lambda}{\gamma M^2} ([\vec{M}_s + \vec{m}(t)] \times \frac{d}{dt} [\vec{M}_s + \vec{m}(t)]) \end{aligned} \quad (2.8)$$

where use has been made of the relation $d\vec{M}/dt = 0 = -\gamma (\vec{M} \times \vec{H})$ and the term $-\gamma [\vec{m}(t) \times \vec{H}(t)]$ has been dropped because of its small magnitude. Using the above-mentioned exponential form for $\vec{m}(t)$ and neglecting the second order terms, the Cartesian components of Eq. (2.8) can finally be written in the form

$$(i\omega/\gamma)m_x + [H + (D_y + D_{ky} - D_z - D_{kz})M_s + i\Gamma]m_y = M_s h_y \quad (2.9)$$

$$- [H + (D_x + D_{kx} - D_z - D_{kz})M_s + i\Gamma]m_x + (i\omega/\gamma)m_y = -M_s h_x \quad (2.10)$$

and

$$m_z = 0 \quad (2.11)$$

where $\Gamma = \lambda\omega/\gamma^2 M_s$. Elimination of m_y from Eqs. (2.9) and (2.10) gives

$$m_x = \chi_{xx} h_x + \chi_{xy} h_y \quad (2.12)$$

with

$$\chi_{xx} = [H + (D_y + D_{ky} - D_z - D_{kz})M_s + i\Gamma]M_s^{-1} \quad (2.13)$$

$$\chi_{xy} = (i\omega/\gamma) M_S \eta^{-1} \quad (2.14)$$

and

$$\begin{aligned} \eta = & [H + (D_x + D_{kx} - D_z - D_{kz}) M_S][H + (D_y + D_{ky} - D_z - D_{kz}) M_S] - \Gamma^2 - (\omega/\gamma)^2 \\ & + i\Gamma[2H + (D_x + D_y + D_{kx} + D_{ky} - 2D_z - 2D_{kz}) M_S] \quad (2.15) \end{aligned}$$

Elimination of m_x instead of m_y from Eqs. (2.9) and (2.10) would have resulted in

$$m_y = \chi_{yx} h_x + \chi_{yy} h_y \quad (2.16)$$

where $\chi_{xx} = \chi_{yy} = \chi$ is the dynamic susceptibility and $\chi_{xy} = -\chi_{yx} = iG$, \vec{G} is the gyration vector. Recalling that both the dynamic susceptibility and dynamic permeability μ are complex, i.e., $\chi = \chi' - i\chi''$ and $\mu = \mu' - i\mu''$, and using the relation $\mu = 1 + 4\pi\chi$, the real and imaginary parts of the (complex) dynamic permeability are given by

$$\begin{aligned} \mu' = & \left[\alpha \left\{ [H + (D_y + D_{ky} - D_z - D_{kz}) M_S][B + (D_x + D_{kx} - D_z - D_{kz}) M_S] - \Gamma^2 - (\omega/\gamma)^2 \right\} \right. \\ & \left. + \beta \Gamma [(B+H) + (D_x + D_y + D_{kx} + D_{ky} - 2D_z - 2D_{kz}) M_S] \right] / (\alpha^2 + \beta^2) \quad (2.17) \end{aligned}$$

$$\begin{aligned} \mu'' = & \left\{ -\alpha\Gamma[(B+H_K) - (H+H_K)] + \beta[(B+H_K) - (H+H_K)] \right. \\ & \left. \times [H + (D_y + D_{ky} - D_z - D_{kz}) M_S] \right\} / (\alpha^2 + \beta^2) \quad (2.18) \end{aligned}$$

with

$$\alpha = [H + (D_x + D_{kx} - D_z - D_{kz}) M_S][H + (D_y + D_{ky} - D_z - D_{kz}) M_S] - \Gamma^2 - (\omega/\gamma)^2 \quad (2.19)$$

$$\beta = \Gamma[2H + (D_x + D_y + D_{kx} + D_{ky} - 2D_z - 2D_{kz})M_s] \quad (2.20)$$

and

$$B = H + 4\pi M_s \quad (2.21)$$

For a flat rectangular plate (the sample shape used in the present experiments), with H applied along the symmetry axis (z axis) so far as the uniaxial anisotropy is concerned and lying in the sample plane (parallel geometry or configuration), $D_x = D_z = 0$, $D_y = 4\pi$ (x -axis is taken to coincide with the polar axis), $D_{kx}M_s = D_{ky}M_s = H_k$ and $D_{kz} = 0$. Substituting these values of components of \vec{D} and \vec{D}_k , Eqs. (2.17)-(2.20) are simplified to yield

$$\mu' = \frac{[(H+H_k)(B+H_k) - \Gamma^2 - (\omega/\gamma)^2][(B+H_k)^2 - \Gamma^2 - (\omega/\gamma)^2] + 2\Gamma^2 (B+H_k)(B+H+2H_k)}{[(H+H_k)(B+H_k) - \Gamma^2 - (\omega/\gamma)^2]^2 + \Gamma^2 (B+H+2H_k)^2} \quad (2.22)$$

and

$$\mu'' = \frac{-2\Gamma[(B+H_k)[(H+H_k)(B+H_k) - \Gamma^2 - (\omega/\gamma)^2] + \Gamma(B+H+2H_k)[(B+H_k)^2 - \Gamma^2 - (\omega/\gamma)^2]}{[(H+H_k)(B+H_k) - \Gamma^2 - (\omega/\gamma)^2]^2 + \Gamma^2 (B+H+2H_k)^2} \quad (2.23)$$

The power absorbed by the sample, which is proportional to the surface impedance, in the parallel geometry is given by

$$P_{\parallel} \propto [(\mu'^2 + \mu''^2)^{1/2} + \mu'']^{1/2} \quad (2.24)$$

The theoretical variation of dP_{\parallel}/dH with H can, therefore, be computed by combining equations (2.22)-(2.24) and taking the field derivative of the resulting expression. From Eqs. (2.8) and (2.9), the resonance frequency $\omega = \omega_{\text{res}}$ is calculated by the condition

that \mathbf{m}_x and \mathbf{m}_y have non-trivial solutions only when $h_x = h_y = 0$. In other words, this implies that

$$\begin{vmatrix} i\omega_{\text{res}}/\gamma & -[H_{\text{res}} + (D_y + D_{ky} - D_z - D_{kz})M_s + i\Gamma] \\ -[H_{\text{res}} + (D_x + D_{kx} - D_z - D_{kz})M_s + i\Gamma] & i\omega_{\text{res}}/\gamma \end{vmatrix} = 0$$

where H is the steady field corresponding to ω . After a few simplifying steps, the following relation is arrived at

$$[(\omega/\gamma)^2 + \Gamma^2] = [H_{\text{res}} + (D_y + D_{ky} - D_z - D_{kz})M_s][H_{\text{res}} + (D_x + D_{kx} - D_z - D_{kz})M_s] \quad (2.25)$$

The subscript for ω is dropped because in experiments the **microwave-field** frequency, ω , is kept constant while the steady field, H , is swept through the resonance.

In the horizontal-parallel (\parallel^h) **configuration**, H is directed along the z -axis (the sample length and also the symmetry axis) in the sample (thin ribbon) plane, which also contains the x -axis. Hence, $D_x = D_z = 0$, $D_y = 4\pi$, $D_{kx}M_s = D_{ky}M_s = H_k$ and $D_{kz} = 0$, and Eq.(2.25) reduces to

$$[(\omega/\gamma)^2 + \Gamma_{\parallel}^2] = (H_{\text{res}}^{\parallel h} + 4\pi M_s + H_k)(H_{\text{res}}^{\parallel h} + H_k) \quad (2.26)$$

In the vertical-parallel (\parallel^v) **configuration**, both H and the symmetry axis lie in the ribbon plane and point in the z -direction (perpendicular to the ribbon axis) and x direction, respectively. Hence, $D_x = D_z = 0$, $D_y = 4\pi$, $D_{ky}M_s = D_{kz}M_s = H_k$ and $D_{kx} = 0$. These values when substituted in Eq. (2.25) yield

$$[(\omega/\gamma)^2 + \Gamma_{\parallel v}^2] = (H_{\text{res}}^{\parallel v} + 4\pi M_s)(H_{\text{res}}^{\parallel v} - H_k) \quad (2.27)$$

In the horizontal-perpendicular (1) geometry, H points in the z direction and is normal to the sample plane, which contains both x and y (symmetry) axes. In this case, $D = D = 0$, $D = 4\pi$, $D_{kz}M_s = D_{kx}M_s = H_k$ and $D_k = 0$ so that Eq.(2.25) assumes the form

$$[(\omega/\gamma)^2 + \Gamma_{\perp h}^2] = (H_{\text{res}}^{\perp h} - 4\pi M_s - H_k)(H_{\text{res}}^{\perp h} - 4\pi M_s) \quad (2.28)$$

In order that Eq.(2.27) has a form similar to that of Eq.(2.26) the assumption that $H \ll 4\pi M$ is made and Eq. (2.27) is rewritten as

$$[(\omega/\gamma)^2 + \Gamma_{\parallel v}^2] \approx (H_{\text{res}}^{\parallel v} + 4\pi M_s - H_k)(H_{\text{res}}^{\parallel v} - H_k) \quad (2.29)$$

Since the linewidth parameter r is independent of H and ω is kept **fixed**, the left-hand side of Eqs.(2.26) and (2.29) has the same value regardless of the magnitude of H_k . Setting $H = 0$ in these equations, therefore, yields

$$(H_{\text{res}}^{\parallel} + 4\pi M_s)H_{\text{res}}^{\parallel} = (H_{\text{res}}^{\perp h} + 4\pi M_s + H_k)(H_{\text{res}}^{\perp h} + H_k) \quad (2.30)$$

and

$$(H_{\text{res}}^{\parallel} + 4\pi M_s)H_{\text{res}}^{\parallel} \approx (H_{\text{res}}^{\parallel v} + 4\pi M_s - H_k)(H_{\text{res}}^{\parallel v} - H_k) \quad (2.31)$$

It can be immediately observed that these equations are identically satisfied only when

$$H_{\text{res}}^{\parallel} = H_{\text{res}}^{\perp h} + H_k \quad \text{or} \quad H_{\text{res}}^{\perp h} = H_{\text{res}}^{\parallel} - H_k \quad (2.32)$$

and

$$H_{\text{res}}^{\parallel} = H_{\text{res}}^{\parallel \text{v}} + H_{\text{k}} \quad \text{or} \quad H_{\text{res}}^{\parallel \text{v}} = H_{\text{res}}^{\parallel} + H_{\text{k}} \quad (2.33)$$

From Eqs. (2.32) and (2.33), it follows that

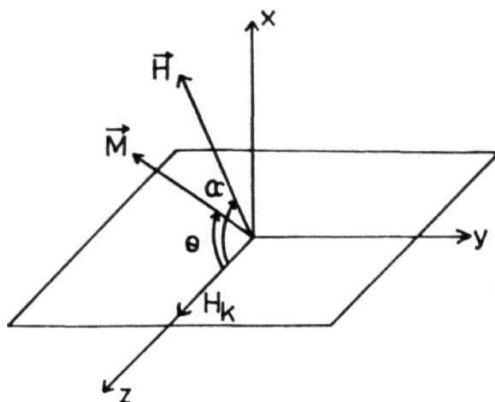
$$H_{\text{k}} = (H_{\text{res}}^{\parallel \text{v}} - H_{\text{res}}^{\parallel \text{h}}) / 2 \quad (2.34)$$

The Eqs.(2.26) (2.27) and (2.28) constitute the resonance conditions for the three sample geometries used.

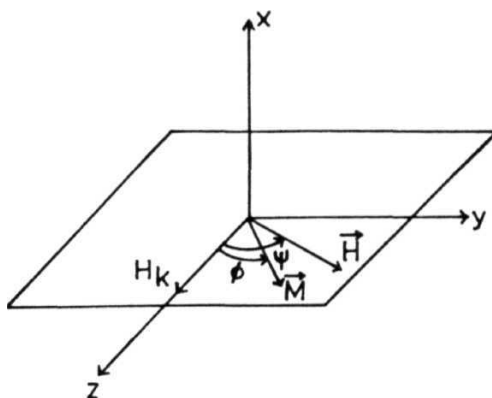
For any general direction of the external magnetic field with respect to the sample **plane**, the resonance conditions may be derived as follows. Two sample **geometries**, i.e., in-plane (**IP**), in which the external field, H , always lies in the sample plane, and **out-of-plane** (**OP**), where H could be oriented at any angle in the range 0° to 360° with respect to the sample plane, are considered.

For a thin film with an in-plane uniaxial anisotropy field $H_{\text{k}} = 2K_{\text{u}}/M_{\text{s}}$, the coordinate systems for **out-of-plane** (**OP**) and in-plane (**IP**) cases shown in Figs. 2.1(a) and 2.1(b) are adopted. For the **OP** case it is assumed that the external field H and magnetization vector \vec{M} lie in the **xz-plane** and make angles α and ϑ , respectively, with the z -axis (**Fig. 2.1(a)**) which represents the easy anisotropy axis (i.e., H_{k} lies along this direction). Since the frequency is held constant and H is varied in the present experiments, H and M are not parallel to each other so that the change in H is not the same as the change in the effective field. Also, as the field H changes, the direction of M changes, which is quite substantial when H is directed out of the sample plane.

For an arbitrary orientation of H with respect to the sample



a. Out-of-plane case



b. In-plane case

Fig. 2.1. Coordinate system showing various angles used in the computation of angular variation of resonance field for (a) OP and (b) IP cases.

plane in the OP **case**, the resonance and the equilibrium conditions are given by

$$(\omega/\gamma)^2 = [H_{\text{res}} \cos(\alpha-\vartheta) + 4\pi M_s \cos 2\vartheta + 2H_k \cos^2 \vartheta] \times [H_{\text{res}} \cos(\alpha-\vartheta) + 4\pi M_s \cos 2\vartheta + H_k \cos 2\vartheta] \quad (2.35)$$

and

$$\frac{\sin \alpha}{\sin \vartheta} - \frac{\cos \alpha}{\cos \vartheta} - \frac{(4\pi M_s + H_k)}{H_{\text{res}}} = 0 \quad (2.36)$$

For the IP case the applied field lies in the sample plane and ψ and ϕ are the angles that the external magnetic field and magnetization subtend with z-axis (Fig. 2.1(b)). The resonance condition for an arbitrary orientation of H within the **sample** plane takes the form

$$(\omega/\gamma)^2 = [H_{\text{res}} \cos \phi + H_k \cos 2(\phi-\psi)] \times [H_{\text{res}} \cos \phi + 4\pi M_s + H_k \cos^2(\psi-\phi)] \quad (2.37)$$

while the corresponding equilibrium condition for the direction of M is given by

$$H_{\text{res}} \sin \phi = (H_k/2) \sin 2(\psi-\phi) \quad (2.38)$$

2.3. FMR experimental set-up

A commercial ESR spectrometer operating in the X-band has been used for the detection of **FMR** in the present samples. The block diagram of the basic instrumental set-up is depicted in **Fig.** (2.2). The sample is placed in a cavity resonator that is positioned between the pole pieces of an electromagnet. The electromagnet produces a steady uniform field which can be swept at a constant rate and is modulated at a frequency of 100 kHz. The sample is then subjected to a transverse microwave field of constant

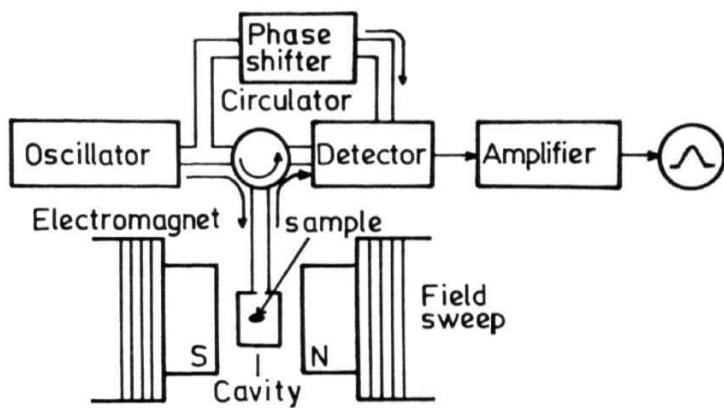


Fig. 2.2. Block diagram of the ESR spectrometer.

frequency. At resonance, sample absorbs a part of the **microwave** energy as a result of which the **Q-value** of the cavity resonator changes. The microwave energy from the oscillator is divided by **means** of a directional coupler, one line being fed into a phase shifter and the other to the cavity resonator through a circulator. The reflected wave from the cavity and the phase-adjusted reference wave are then detected in the detector and then amplified before being displayed. In the off-resonant condition the reference wave is adjusted to give a reflection equal in amplitude and opposite in phase to the reflection from the sample and cavity and thus, sending zero power to the detector. When the resonance occurs, the off-balance signal is detected.

2.4. Sample **preparation**, sample characterization and the measuring procedure

Amorphous $\text{Fe}_{100-x}\text{Zr}_x$ ($x=9,10$), $\text{Fe}_{90-y}\text{Co}_y\text{Zr}_{10}$ ($y=0, 1, 2, 4, 6, 8, 10$ and 18) and $\text{Co}_{90}\text{Zr}_{10}$ alloys were prepared under helium (inert) atmosphere by the single-roller melt-quenching technique in the form of long ribbons of $\sim 2\text{mm}$ width and $30\text{--}40\ \mu\text{m}$ thickness. The amorphous nature of the samples at room temperature was ascertained by using Mo $\text{K}\alpha$ X-ray diffraction method. A typical X-ray diffraction pattern is shown in Fig.(2.3). The presence of a single broad peak at about $2\theta = 20^\circ$ indicates amorphous nature of the sample and absence of sharp peaks at higher angles suggests that a minor **crystallographic** phase, if present, is less than 5 **volume** percent of the main amorphous phase. The 100 percent **amorphicity** of the alloys in question was confirmed by electron micro-

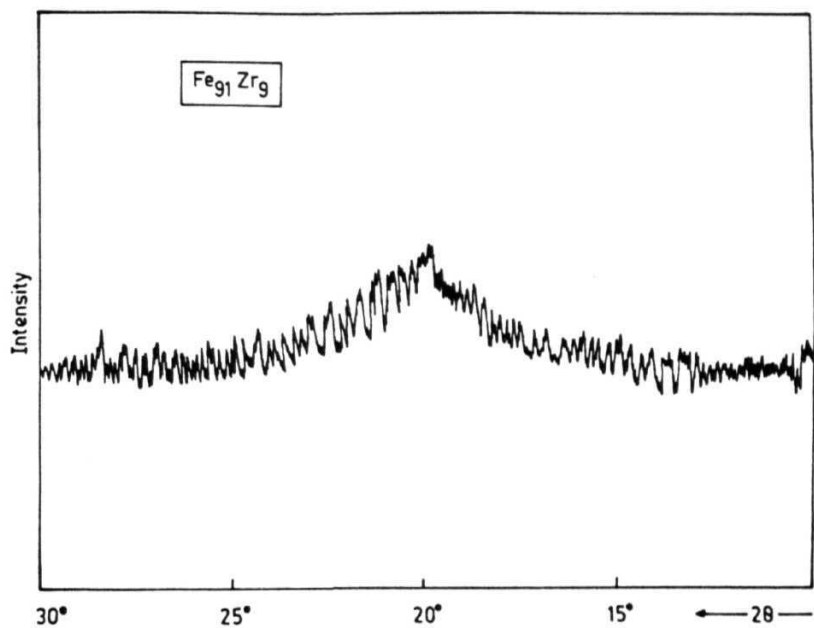


Fig. 2.3. Typical X-ray diffraction pattern (Mo $K\alpha$: reflection geometry) of the a-Fe Zr_9 alloy.

scopic examination.

JEOL FE-3X ESR spectrometer operating in the X-band with a fixed microwave frequency of ~ 9.23 GHz was used for FMR measurements. Variation in the sample temperature could be accomplished by a variable temperature accessory. Sample was cooled by cold nitrogen gas, obtained by boiling liquid nitrogen, circulated through the cavity. In this way the sample temperature, monitored by a **pre-calibrated** copper-constant thermocouple in physical contact with the sample, could be varied from 100K to 300 K. The temperature just outside the microwave cavity was measured by another pre-calibrated copper-constant thermocouple and controlled to within ± 0.5 K (± 0.1 K at the sample site) at every temperature setting by regulating the cold nitrogen gas flow. A proper gas flow regulation was achieved by controlling the power input to a heater, immersed in the liquid nitrogen container, with the aid of a **PID** temperature controller. The sample temperature was varied from 300K to 500K by heating air, blown through the cavity by a compressor. Measurements at 77K were performed by immersing the sample in liquid nitrogen, contained in a tailed dewar, which had been inserted into the microwave cavity. Low-temperature FMR measurements extending down to 10K were also performed on a few alloy compositions using the low-temperature ESR facility available at the **Radiochemistry** Division, BARC, Bombay. The spectrometer used was a **Bruker** Model ESP100 ESR spectrometer operating in the X-band with a fixed microwave frequency of ~ 9.25 GHz. A closed-cycle refrigerator was coupled to the spectrometer in order to attain **low** temperatures. The sample holder consisted of an OFHC copper

rod ($\phi=5\text{mm}$) which was **thermally** anchored to the cold head of the refrigerator. The temperature was controlled using a **PID** controller to a stability better than 100 **mK**. Measurements were taken at fixed temperatures after the sample had been cooled down to the lowest temperature (9K) in zero-external field or in an external field of 5 kOe.

As amorphous alloys are extremely sensitive to stress, it is very important that the samples do not experience any stresses during the measurement. An appropriate sample mounting technique [5], which ensures high reproducibility in the data by getting rid of specious stress-induced effects, was used for **measurements**. The sample holder consisted of a quartz rod **half-cut** at one **end**. The sample (a strip of typical dimensions $2\times4\times0.03$ mm cut from the ribbons free from crystalline regions and thoroughly cleaned using ethanol) was mounted on the flat surface and sandwiched with a small flat quartz piece on top and kept in position by two paper spacers of thickness just greater than the sample thickness. The quartz rod was then inserted into a quartz tube, which was then inserted into the cavity. The cavity is provided with a goniometer arrangement which enables to rotate and orient the sample plane at specific angles with respect to the external field during the measurement of the angular dependence of resonance field and line-width. Three different sample geometries were used for FMR **measurements** - (i) horizontal-parallel (\parallel), in which the external field H lies in the ribbon plane and is directed along the length, (ii) vertical-parallel (\parallel^V), in which H lies in the ribbon plane and is directed along the breadth, and (iii) horizontal-

perpendicular (\perp), in which H is normal to the ribbon plane. FMR **measurement** consists of recording the field derivative of the microwave power (P) ' dP/dH ' that is absorbed during the resonance process as a function of the external static magnetic field H at different fixed temperatures in one of the sample geometries just mentioned. To check the reproducibility, data were repeatedly taken on the same sample which was remounted several times and also on samples that were cut from different parts of the ribbon of a given alloy composition.

The resonance field and linewidth were studied as functions of the angle between the external static magnetic field and the sample plane using the goniometer arrangement. Such measurements were performed on each sample at two temperatures using two different **sample-configurations**. Given that the field H is always along the z-direction and the sample plane coincides with the **yz-plane** with its length directed along z-axis, the sample is rotated about the y-axis from $0^\circ - 360^\circ$. In the second **configuration**, the sample plane coincides with the **xz-plane** and the sample is again rotated about the y-axis from $0^\circ - 360^\circ$, but now H lies always within the sample plane. In each of these two **configurations**, power absorption derivatives for each sample at different angles were recorded at the temperatures, $0.6 T_C$ and $1.2 T_L$.

Since the microwave field penetrates only the surface layer of thickness $\approx 1 \mu m$, it is imperative to ascertain whether the observed resonances are characteristic of the bulk. In order to verify this, the samples were either etched in **nital** solution (10%

HNO₃ plus 90% ethanol) or mechanically polished and then power absorption derivative (PAD) curves were recorded. These experiments [6] demonstrated that the observed resonances were indeed characteristic of the bulk and did not originate from the surface layer.

The results of all the experiments described above are presented and analyzed in the next chapter.

2.5. Experimental accuracy and sources of error

The accuracy with which the PAD curves are measured is basically decided by two factors, namely resolution in the measurement of the external field and the stability limits of the sample temperature. Since the resolution of the field is ± 5 Oe (± 2.5 Oe) when the sweep-width is 2000 Oe (1000 Oe), the upper bound on the error in the measurement of the resonance field is given by the above resolution limit whereas in the measurement of the peak-to-peak linewidth the maximum error could be twice this value. Stability of the temperature becomes important especially in the temperature region where slope of H_{res} and ΔH versus T curves becomes steep, i.e., in and around the critical region. The long-term (time duration greater than 1 hour) temperature stability of the present set-up was better than 50 mK while a stability of better than 25 mK was achieved for short durations of time (≈ 30 minutes).

Inappropriate and incorrect sample mounting is a major source of error in FMR measurement of amorphous ribbons. The magnetic properties of these alloys are extremely sensitive to

stress, the effects of which manifest themselves as highly distorted lineshapes, multiline FMR spectra, irreproducible values of linewidth and resonance centers when measurements are repeated after remounting the sample, etc. The most appropriate sample mounting technique which gave reproducible results free from stress-induced effects is the one described in Section 2.4. A slight misorientation of the sample from the required sample geometry can result in drastic changes in the values of linewidth, resonance field and intensity, especially in the horizontal-perpendicular geometry. Hence, in order to minimize/eliminate the error in the measurements, the sample should be mounted in a stress-free manner and in the correct orientation.

2.6. Mossbauer effect

Introduction

Since its **discovery**, the Mossbauer effect [7] has been studied extensively and recognized as a powerful microscopic probe to study local environments of certain nuclei. The theory of **Mössbauer** effect spectroscopy (MES) has been extensively dealt with in several text books and review articles [8-12] and hence, only some important aspects of the theory will be presented.

When a **γ -ray** is emitted by a nucleus in a free atom, the energy of the **γ -ray** is reduced by the recoil energy that is imparted to the nucleus in accordance with the momentum conservation laws. The same occurs in the case of absorption also. Hence, initially it was very difficult to observe γ -ray resonance. Early methods that sought to compensate this energy loss either by heating to increase the thermal broadening of emission and absorption profiles so as to cause an overlap or by mechanical motion at high velocity with the aid of an ultracentrifuge were not successful. However, if the emitting nucleus is embedded in a solid lattice or matrix, the recoil energy can be transferred to the crystal as a whole through the quantified vibrational energies, leading to a negligible recoil energy. Then, there is a finite probability for zero-phonon transitions where a fraction of γ -rays is emitted without any transfer of recoil energy to the lattice. This fraction, **f** , called the recoil-free fraction, is given, in the Debye approximation, by

$$f = \exp \left[- \frac{6E_R}{k_B \theta_D} \left\{ \frac{1}{4} + \left(\frac{T}{\theta_D} \right)^2 \int_0^{\theta_D/T} \frac{x dx}{e^x - 1} \right\} \right] \quad (2.39)$$

where E is the recoil energy and θ is the Debye temperature of the host lattice. At low temperatures, i.e., for $T \ll \theta_D$, Eq. (2.39) reduces to

$$f = \exp \left[\frac{-E_R}{k_B \theta_D} \left\{ \frac{3}{2} + \frac{\pi^2 T^2}{\theta_D^2} \right\} \right] \quad T \ll \theta_D \quad (2.40)$$

whereas in the high temperature limit, it takes the form

$$f = \exp \left[\frac{-6E_R T}{k_B \theta_D^2} \right] \quad T > \theta_D/2 \quad (2.41)$$

To date, Mossbauer effect has been observed in a number of nuclei, but the most widely used one has been that of iron, Fe.

2.7. The ^{57}Fe Decay Scheme

The decay scheme for Fe Mossbauer effect is shown in Fig. (2.4). ^{57}Co , having a half life of 270 days, in the state $I=7/2$ decays through electron capture into the $I=5/2$ state of ^{57}Fe . Eleven percent of the decays from this state result in a 136.32 keV r-ray and 85%, in a 121.9 keV γ -ray. The $I=3/2$ state then decays to the ground ($I=1/2$) state through emission of 14.41 keV r-rays. The lifetime of this energy state is about 99 ns, corresponding to a Heisenberg linewidth of 0.192 mm/s. The power of MES lies in this narrow linewidth with which finely spaced nuclear energy levels, which are a result of nuclear interactions, can be resolved and observed.

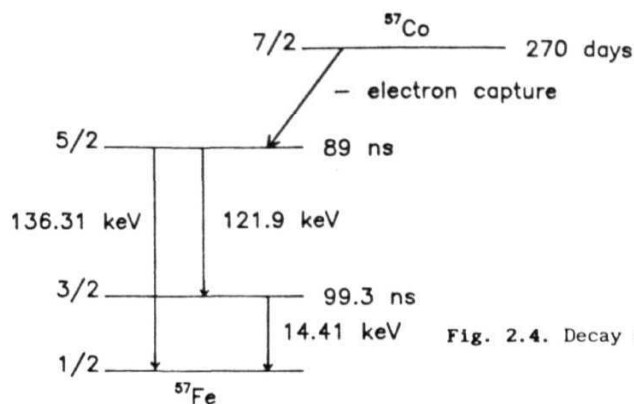


Fig. 2.4. Decay scheme for ^{57}Fe .

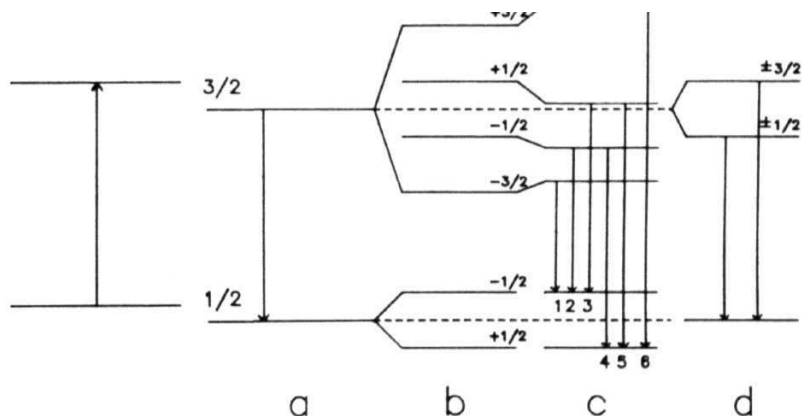


Fig. 2.5. Nuclear energy level scheme for the 14.41 keV Mössbauer transition in ^{57}Fe as modified by various hyperfine interactions: (a) Isomer shift, (b) magnetic hyperfine interactions, (c) combined magnetic hyperfine and quadrupole interactions and (d) quadrupole interactions.

2.8. Hyperfine interactions

The various interactions that play a role in the transitions between the nuclear energy levels of the absorber nucleus are a combination of one or more of the following hyperfine interactions: (i) the **isomer** shift, a result of the **Coulombic** interactions between the nucleus and the surrounding electrons, (ii) the hyperfine field, on account of a resultant magnetic field at the nucleus that causes a nuclear **Zeeman** splitting of the energy levels, and (iii) the electric quadrupole moment, due to the interaction between the nuclear electric quadrupole moment and an electric field gradient at the nuclear site.

2.8.1. *Isomer shift*

The effective nuclear size gets altered during the course of nuclear transitions. This implies that the **s-electron wavefunctions**, which have a non-zero electron charge density within the nuclear volume, will be different for the emitting (E) and absorbing (A) nuclei. The net energy difference between the two transitions can be written as

$$\delta = (2\pi/5) Ze^2 \left\{ |\psi_s^A|^2 - |\psi_s^E|^2 \right\} \left[\langle R_e^2 \rangle - \langle R_g^2 \rangle \right] \quad (2.42)$$

where Z is the nuclear charge, R_e and R_g are the nuclear radii in the excited and ground state, respectively. This shift in the energy levels is the isomer or chemical shift, which is only a minute fraction of the total Coulomb interaction and hence, observable only by comparing against a suitable reference. This inter-

action is schematically depicted as case (a) in Fig. (2.5). There is also a relativistic **temperature-dependent** contribution to the **isomer** shift which is caused by the time dilations resulting from the thermal motions of the **γ -ray** emitting and absorbing nuclei. This contribution, called the second-order Doppler (SOD) shift, is proportional to the mean square velocity of the nucleus and is given by

$$\frac{\delta E_Y}{E_Y} = -\langle v^2 \rangle / 2c^2 \quad (2.43)$$

where E is the recoilless **γ -ray** energy, δE is its shift and v is the velocity of the emitting nuclei. In the harmonic approximation, the temperature dependence of the centroid of the ME spectrum is given by (in velocity units)

$$\delta v_T = -\frac{C_L}{2Mc} (T_a - T_s) \quad (2.44)$$

where M is the atomic mass, C_L is the lattice specific heat, and T_a and T_s denote the temperature of the absorber and source, respectively. In the high temperature limit ($T_a, T_s \gg \theta_D$), $C_L \approx 3k_B$ and δv_T is a linear function of temperature with slope $-3k_B/2Mc$.

2.8.2. Magnetic **hyperfine** interaction

In the presence of a magnetic field at the nuclear site, a nuclear **Zeeman** splitting of the energy levels occurs. The **Hamiltonian** that describes the hyperfine interaction is given by

$$\mathcal{H} = -g\mu_N \vec{I} \cdot \vec{H} \quad (2.45)$$

where μ_N is the nuclear Bohr magneton, \vec{I} is the nuclear spin and H is the magnetic field. The energy eigenvalues for this **Hamiltonian** can be written as

$$E_m = -g\mu_N H m_I \quad (2.46)$$

where m is the magnetic quantum number representing the z component of \vec{I} if it is oriented along the z -axis. For $I=3/2$, $m=\pm 3/2, \pm 1/2$ and for $I=1/2$, $m=\pm 1/2$ and the transitions between various levels are governed by the selection rule $\Delta m = 0, \pm 1$ (case (b), **Fig** (2.5)). There are several possible origins for the magnetic field. In general, this field can be written as

$$H = H_O - DM + \frac{4}{3} \pi M + H_S + H_L + H_D \quad (2.47)$$

H_O is an externally applied field, $-DM$ is the demagnetizing field and $\frac{4}{3} \pi M$ is the Lorentz field for cubic symmetry. H_S , called the Fermi contact term, arises from the interaction of nuclear spin with the unpaired **s-electron** spin density at the nucleus and is

$$H_S = - \left(\frac{16\pi}{3} \right) \mu_B \left\langle \sum_i S_i^z \delta(r_i) \right\rangle \quad (2.48)$$

where the term in angular brackets is the expectation value of the local spin density, r_i is the radial coordinate of the i -th electron. This field is the dominant contribution to the hyperfine field in case of transition metals. The last two terms in Eq. (2.47),

$$H_L = -2\mu_B \langle 1/r^3 \rangle \langle \vec{L} \rangle = -2\mu_B \langle 1/r^3 \rangle (g-2) \langle \vec{S} \rangle \quad (2.49)$$

and

$$H_D = -2\mu_B \langle 3\vec{r}(\vec{S} \cdot \vec{r})/r^5 - \vec{S}/r^3 \rangle \quad (2.50)$$

arise from a non-zero orbital angular momentum and the dipolar interaction of the nucleus with the neighbouring **spins**, respectively. Both the terms are either zero or negligible for transition elements, but can be larger for rare-earths because in that case, the orbital angular momentum is not quenched.

2.8.3. Electrical **quadrupole** interaction

When any nucleus has a spin quantum number greater than $I=1/2$, the nucleus no longer has spherical symmetry and hence higher order terms in the **multipole** expansion of the electrostatic interaction between nuclear and electronic charge come into being. The deviation of the nucleus from spherical symmetry is described by the nuclear quadrupole moment, given by

$$eQ = \int \rho r^2 (3\cos^2\theta - 1) d\tau \quad (2.51)$$

where e is the charge of the proton, ρ is the charge density in a volume element $d\tau$, which is at a distance r from the center of nucleus and makes an angle θ with the nuclear spin quantization axis. The quadrupole interaction lifts the spin degeneracy of the excited states only partially (Fig. (2.5), case (d)). The interaction **Hamiltonian** of the nuclear electric quadrupole moment with the electric field gradient (efg, which is a traceless tensor with components in the principal axes directions V_{xx} , V_{yy} and V_{zz} and $V_{zz} + V_{xx} + V_{yy} = 0$) is given by

$$H_{EQ} = \frac{eQq}{4I(2I-1)} \left[3\hat{I}_z^2 - I(I+1) + \eta(\hat{I}_x^2 - \hat{I}_y^2) \right] \quad (2.52)$$

where $\eta = (V_{xx} - V_{yy})/V_{zz}$ is the **asymmetry** parameter and $|V_{zz}| > |V_{xx}| \geq |V_{yy}|$, so that $0 \leq \eta \leq 1$. The **Hamiltonian** given by Eq. (2.52) has the eigenvalues

$$E_Q = \frac{eQq}{4I(2I-1)} \left[3m_I^2 - I(I+1) \right] (1+\eta^2/3)^{1/2} \quad (2.53)$$

2.8.4. Combined magnetic and electric **hyperfine** coupling

Under the combined action of magnetic hyperfine and electric quadrupole interactions, an additional shift in the excited state energy levels (Fig. (2.5), case (c)) occurs. If the efg tensor is axially **symmetric** with its principal axis making an angle θ with the magnetic axis, the quadrupole interaction may be treated as a first order perturbation to the magnetic interaction, provided that $eQq \ll \mu H$. Then, the energy eigenvalues for $I=3/2$ are given by

$$E = -g\mu_N H m_I + (-1)^{|m_I|+1/2} \frac{eQq}{4} \left(\frac{3\cos^2\theta - 1}{2} \right) \quad (2.54)$$

When the quadrupole interaction is no longer a small perturbation on the hyperfine field, the splittings and intensities become difficult to predict or to interpret when observed and usually recourse has to be taken to analysis by computer simulation [13].

2.8.5. Intensity ratios

The intensities of the six **Zeeman** transitions ($\Delta m = 0, \pm 1$) are, in general, a function of the angle θ between the hyperfine field and the direction of the **γ -ray**. Given the energy levels of

the **Zeeman Hamiltonian** and their spin quantum numbers, the intensities can be calculated from the theory of the coupling of two angular momentum states, which gives two terms. One of them depends on θ whereas the other does not. The intensities are proportional to the product of angle-dependent and angle-independent terms, which are obtained from the appropriate Clebsch-Gordon coefficients. The angular dependence of various transitions is given by, $-3/2 \rightarrow -1/2$ ($\Delta m_I = +1$, intensity = I_1), $(9/4)(1+\cos^2\theta)$; $-1/2 \rightarrow -1/2$ ($\Delta m_I = 0$, I_2), $3\sin^2\theta$; $+1/2 \rightarrow -1/2$ ($\Delta m_I = -1$, I_3), $(3/4)(1+\cos^2\theta)$; $-1/2 \rightarrow +1/2$ ($\Delta m_I = +1$, I_4) $\rightarrow (3/4)(1+\cos^2\theta)$; $+1/2 \rightarrow +1/2$ ($\Delta m_I = 0$, I_5), $3\sin^2\theta$ and $+3/2 \rightarrow +1/2$ ($\Delta m_I = -1$, I_6), $(9/4)(1+\cos^2\theta)$.

For a thin, **polycrystalline/amorphous** absorber, the angular term can be integrated over all orientations to give an average value. In such a case, the average value of $\cos \theta$, denoted by $\langle \cos^2\theta \rangle$, turns out to be $1/3$ and $\langle \sin^2\theta \rangle = 2/3$. The ratio of line intensities can be written as **3:b:1::1:b:3** where

$$b = I_2/I_3 - I_5/I_4 = 4\sin^2\theta/(1+\cos^2\theta) \quad (2.55)$$

According to this equation, b assumes the values 0 and 4 when all the moments are aligned parallel ($\theta=0^\circ$) and perpendicular ($\theta=90^\circ$) to the **γ -ray** direction, respectively, and for a perfectly random alignment of the local moments, $b = 2.0$.

2.9. Experimental procedure

All the Mossbauer experiments were carried out in the standard transmission geometry in a zero external field. The spectra were taken using two different spectrometers operating in the con-

ventional constant acceleration mode. Room temperature ME spectra for all the samples were taken using an Elscint **Mössbauer** spectrometer with a 25 mCi $^{57}\text{CoRh}$ source having an intrinsic linewidth (FWHM) of about $0.25 \pm 0.01 \text{ mm.s}^{-1}$. The source transducer was driven by a triangular waveform and a proportional counter was used for detection. Spectra were collected over 512 channels and then folded. Typically 10 counts were collected per channel.

Low temperature ME spectra were taken with the Mossbauer facility using 50 mCi $^{57}\text{CoRh}$ source available with the Low Temperature Physics section, **TIFR**, Bombay. Folding of the spectra was obviated by driving the velocity transducer by a linear ramp waveform, the end of which is returned to the starting point by two parabolas. These parabolas are such that the velocity and acceleration are continuous functions of time to avoid 'ringing'. A high efficiency scintillation counter with 0.2 mm thick **NaI (Tl)** scintillator stage was used for detection. The multichannel analyser was provided with a serial port through which data, collected over 512 channels, could be transferred directly to a computer. A schematic diagram of the Mossbauer spectrometer is shown in Fig. (2.6). For calibration, natural α -iron foils were used. Typical intrinsic linewidths for the innermost lines were $0.24 \pm 0.01 \text{ mm.s}^{-1}$.

The low temperature cryostat was of the continuous flow type (Lake Shore, Model 310) with which measurements were made from 5K to 300K. The samples were fixed at one end using GE 7031 varnish and sandwiched between 0.5 mm thick Beryllium plates, which were clamped to the copper tail. The temperature was measured using a

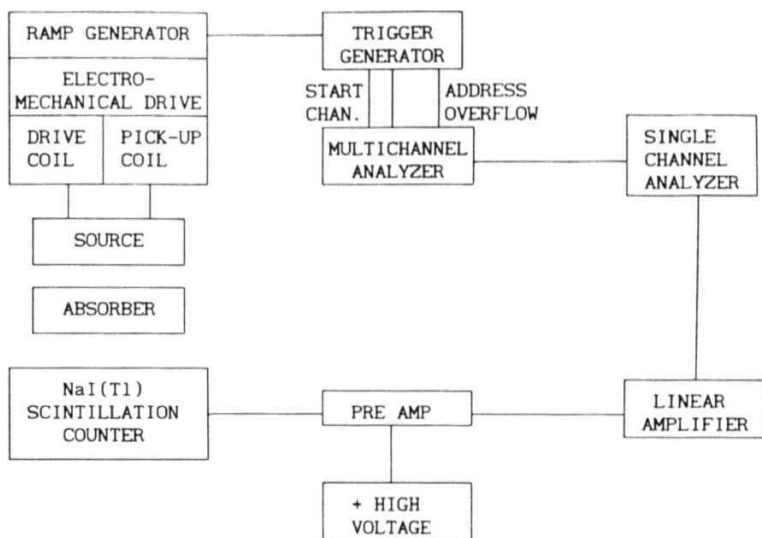


Fig. 2.6 Block diagram of the Mössbauer spectrometer

6b

Si diode and controlled by a **PID** temperature controller to a stability better than 50 **mK**. The time taken to acquire typically 10 counts per channel for each spectrum was of the order of 24-36 **hours**.

REFERENCES

- [1] J.H.E. Griffiths, *Nature* **158**, 670 (1946).
- [2] L. Landau and E. Lifshitz, *Phys. Z. Sowjetunion* 8, 153 (1935).
- [3] T.L. Gilbert, *Phys. Rev.* **100**, 1243 (1955).
- [4] N. Bloembergen, *Phys. Rev.* 78, 572 (1950).
- [5] S.N. Kaul and T.V.S.M. Mohan Babu, *J. Phys.: Condens. Matter* 1, 8509 (1989).
- [6] V. Siruguri, Ch.V. Mohan and S.N. Kaul, unpublished results.
- [7] R.L. Mossbauer, *Z. Physik* **151**, 124 (1958).
- [8] N.N. Greenwood and T.C. Gibb, *Mossbauer Spectroscopy* (Chapman and Hall, London, 1971).
- [9] H. Fraunfelder, *The Mossbauer Effect* (Benjamin, New York, 1962).
- [10] G.K. Wertheim, *Mossbauer Effect, Principles and Applications* (Academic Press, New York, 1964).
- [11] *Mossbauer Spectroscopy-I, Topics Appl. Phys.*, Vol. 5 and *Mossbauer Spectroscopy-II, Topics Current Phys.*, Vol.25, edited by U. Gonser (Springer, Berlin, 1975 and 1981).
- [12] R.J. Gruverman, *Mossbauer Effect Methodology, Vols.* 1-11 (Plenum, New York, 1965-1976).
- [13] J.R. Gabriel and S.L. Ruby, *Nuclear Instrum. Methods* 36, 23 (1965).

CHAPTER - III

3.1. Analysis of FMR spectra of metallic glasses

In ferromagnetic **materials**, apart from the damping term, there is also a contribution to the line broadening because of the exchange interaction and electrical conductivity. It is well-known that in highly conducting metallic specimens, microwave field penetrates only a thin surface layer of the sample of thickness $<10^{-5}$ cm and as a result, the dynamic magnetization becomes **inhomogeneous**. The spatial variations in magnetization exert a torque on \vec{M} which is expressed as $(2A\gamma/M_s^2)(\vec{M} \times \nabla \vec{M})$, where A is a phenomenological exchange stiffness parameter. Thus the equation of motion of the magnetization should be augmented by this term and then solved in conjunction with the Maxwell's equations to obtain a correct solution for the observed lineshape. The exchange term leads to a shift in the resonance field and also contributes to the broadening of the resonance line. This term would become unimportant if the conductivity is low or if the exchange stiffness is small. The conductivities of amorphous alloys are typically one or two orders of magnitude lower than those of their crystalline counterparts. It has also been observed [1] that the stiffness parameter values are a factor of two or three smaller. Hence, a total neglect of the exchange-conductivity term while writing the equation of motion of magnetization in the case of amorphous alloys is fully justified.

The temperature dependence of FMR linewidth is extremely sensitive to the type of magnetic order in the sample under study. This feature is effectively utilized in the analysis of linewidth behavior with temperature in reentrant amorphous alloys. To **eluci-**

date this point further, the **FMR** linewidth Γ is independent of temperature T [2] for $T < 0.8 T_C$ but increases steeply for temperatures above T in the case of a concentrated homogeneous ferromagnet whereas Γ increases exponentially [3] as temperature is lowered below $-2T_{FF}$, the spin-freezing temperature, has practically little or even no variation with temperature within the interval $2T_{FF} < T < 0.8 T_C$ and exhibits a steep rise for $T > T_C$ for a re-entrant spin-glass.

For an archtypal cluster spin glass with composition just below the percolation threshold [4], Γ varies exponentially with T for $T \lesssim 3T_{SG}$ and passes through a broad minimum around $3T_{SG}$ before displaying a linear dependence on temperature in the paramagnetic region. It has been observed through frequency-dependent FMR measurements [2,3,5] on a large number of amorphous ferromagnetic alloys that within the temperature range where Γ is nearly a constant (i.e., $\Gamma \approx \Gamma_0$), Γ comprises frequency-independent and -dependent parts given by the relation

$$\Gamma_0 = a + b \nu \quad (3.1)$$

where ν is the frequency of the microwave field.

In view of the fact that LLG equation of motion for dynamic magnetization (Eq.2.7), on which Eqs. (2.17) and (2.18) are based, is, as stated earlier, strictly valid for a single crystal ferromagnetic alloy in which magnetization is homogeneous and $\vec{H}_{eff} = \vec{H} + \vec{H}_{int}$, where \vec{H} static applied field and $\vec{H}_{int} = \vec{H}_k - \vec{H}_{dem} + \vec{H}_{an}$ includes demagnetizing field, it, , ft, and other anisotropy fields, it_{an}, with easy axis along it, the frequency-dependent term $b\nu$ in amorphous ferromagnetic systems has its origin in LLG rela-

xation and can be adequately described by Eq. (2-7) provided \vec{M} and \vec{H} are replaced by their average values, i.e., $\langle \vec{M} \rangle$ and $\langle \vec{H}_{int} \rangle$. The frequency-independent term 'a' originates from exchange fluctuations, inhomogeneous magnetization and local random anisotropy which, in turn, arise from the topological disorder (fluctuations in the nearest-neighbor distances between atoms) and can be accounted for by using the fluctuation parts of \vec{M} and \vec{H}_{int} , i.e., $\delta \vec{M}(\vec{r}, t)$ and $\delta \vec{H}_{int}(\vec{r}, t)$, instead of \vec{M} and \vec{H}_{int} in Eq. (2.7) or by invoking the two-magnon scattering mechanism [6,7] in which magnon scattering is caused by spatial inhomogeneities in the local random anisotropy fields and/or inhomogeneities in the local exchange interactions. In case of the former approach, for amorphous ferromagnets, \vec{M} and \vec{H}_{ff} in Eq.(2.7) should be replaced by $\vec{M} = \langle \vec{M} \rangle + \delta \vec{M}(\vec{r}, t)$ and $\vec{H}_{eff} = \vec{H} + \vec{H}_{int}(\vec{r}, t) = \vec{H} + [\langle \vec{H}_{int} \rangle + \delta \vec{H}_{int}(\vec{r}, t)]$ and the microwave power absorbed during the resonance process could then be calculated [2,3,8] by assuming Gaussian distribution for magnetization and internal fields centered around $\langle \vec{M} \rangle = \vec{M}$ and $\langle \vec{H}_{int} \rangle$ with standard deviation δ_M and δ_H , respectively. The inclusion of δ_M and δ_H has only a slight effect [3] on the lineshape but explains the increased magnitude of Γ . Consequently, it is possible to represent the resonance line by a A_{ff} value in Eq. (2.7) but then λ_{eff} would be a function of v . However, in the absence of a complete knowledge about the constant part Γ , the A_{ff} values so obtained cannot be relied upon as they are bound to overestimate A and hence, one can talk only about the relative differences in A from one alloy concentration to the other.

3.2. Power Absorption Derivative Curves

The observed functional dependence of dP/dH on H in the horizontal-parallel (\parallel) **configuration** is depicted in Figs. 3.1(a-c) for three ranges of temperature for **a-Fe₉₀Zr**. Each of the figures (a-c) represents the power absorption derivative (PAD) curves at a few selected values of temperature in the low ($10 \text{ K} \leq T \leq T_{RE}$), intermediate ($T_{RE} \leq T \leq T_C$) and high ($T > T_C$) temperature ranges. These PAD curves are also representative of those recorded for **a-Fe₉₀Zr** in the vertical-parallel **configuration** and for **a-Fe₉₁Zr₉** and **a-Fe₉₀-Co Zr₁₀** in both \parallel^h and \parallel^v (vertical-parallel) geometries. At this stage, it should be mentioned that an attempt was made to measure the **FMR** spectra in the horizontal-perpendicular (\perp) **configuration** but the resonance in this sample-**configuration** was observed at 9.23 GHz only for $T > T_C$ because the primary as well as secondary resonances are expected to occur well above 10 **kOe**, the highest value of the field obtainable with the available electromagnet. Moreover, in spite of utmost care exercised in sample **mounting** and its positioning in external field, the lineshape for \perp^h **configuration** and hence, the values of the resonance centers for $T > T_C$, could not be reproduced with an accuracy comparable to that achieved in the case of the parallel **configuration**, presumably due to the extreme sensitivity of $H_{res}^{\perp h}$ to the angle between the field direction and sample plane. Thus, any consistency between the observed values of H and those calculated using the numerical estimations of the parameters like g and M_S , deduced from the lineshape analysis for the parallel **configuration**, in the resonance condition for \perp **configuration**

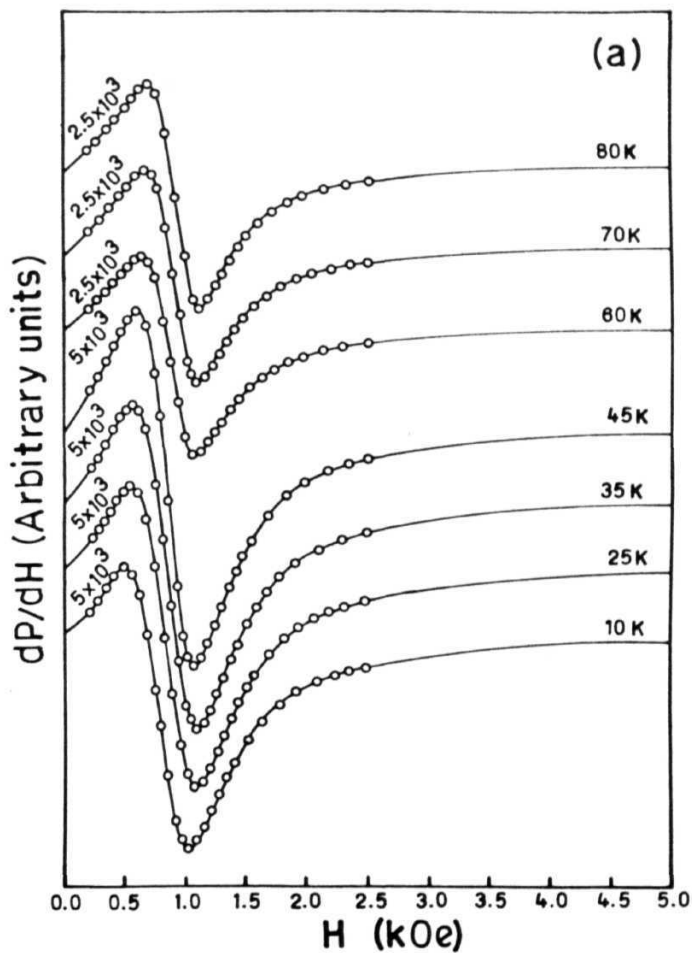


Fig. 3.1a. Field dependence of the microwave power absorption derivatives for $a\text{-Fe}_{90}\text{Zr}_{10}$ using II sample geometry in low temperature region. Full curves depict the observed variation whereas open circles denote values calculated using Eqs. (2.22)-(2.24).

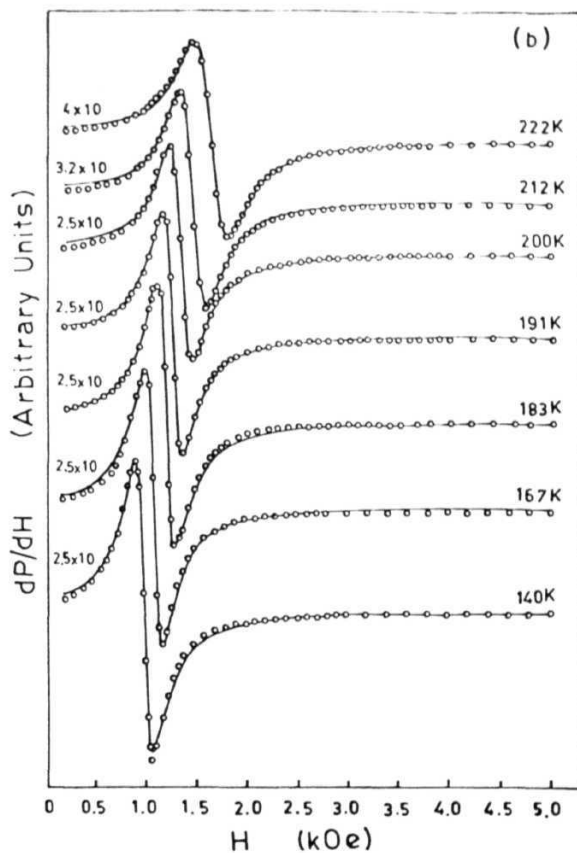


Fig. 3.1b. Field dependence of the microwave power absorption derivatives for $\alpha\text{-Fe}_{0.9}\text{Zr}_{0.1}$ using II sample geometry in the intermediate temperature region. Full curves depict the observed variation whereas open circles denote values calculated using Eqs. (2.22)-(2.24).

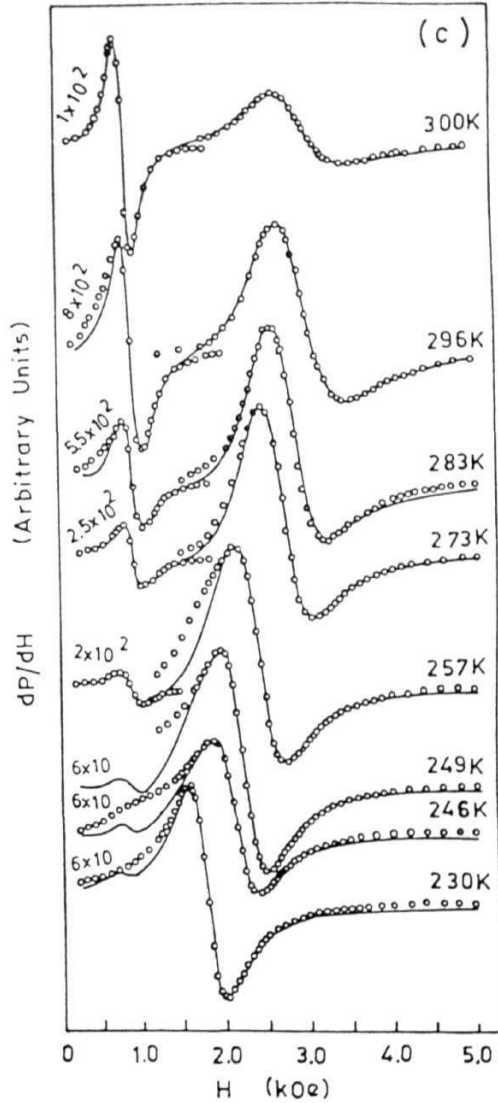


Fig. 3.1c. Field dependence of the microwave power absorption derivatives for $a\text{-Fe}_{90}\text{Zr}_{10}$ using II sample geometry in the region near and above the Curie temperature. Full curves depict the observed variation whereas open circles denote values calculated using Eqs. (2.22)–(2.24).

(Eq.(2.28)), is purely coincidental. The full curves in the figure depict the observed variation whereas the open circles denote the values calculated using **Eqs. (2.22)-(2.24)**. Figs. 3.1(a) and 3.1(b) show that the dP/dH curves for temperatures in the range $10K \leq T < T_c$ ($\approx 240K$ for a-Fe Zr₀) consist of a single resonance (henceforth referred to as the primary or main resonance) line which shifts to higher fields as temperature is increased. This resonance broadens at a rapid rate for $T > 0.8T_c$. Apart from this resonance, the signature of a secondary resonance at a lower field value (~ 800 Oe) is noticed at $T \approx T_c$ in the most sensitive setting of the spectrometer (the numbers on the left-hand side of the dP/dH curves indicate the spectrometer sensitivity at which the spectra have been recorded, Fig. 3.1(c)). This secondary resonance gets better resolved as the temperature is increased beyond $T_c + 10$ K. The physical quantities that are deduced from the dP/dH curves are the resonance field, H_{res} (defined as the field where the $dP/dH=0$ line cuts the dP/dH versus H curve or alternatively as the field where dP/dH possesses half the peak-to-peak value if the dP/dH curves is symmetrical about the baseline), and the peak-to-peak linewidth, ΔH (defined as the field difference between the points of **inflection** of the dP/dH versus H curve). It has been observed that the peak-to-peak linewidth, ΔH , forms an appreciable fraction of the resonance field, H_{res} , for the alloys under study, and hence, the observed value of H_{res} can differ significantly from the actual ("true") resonance center. For this reason, a complete lineshape calculation **for** each resonance line has been carried out separately. Such a calculation consists of fitting the theoretical expression, Eq. (2.24), with the aid of Eqs. (2.22)

and (2.23), by making use of a non-linear least-squares fit computer program which treats the **Landé** splitting factor g and saturation magnetization M_s as free fitting parameters while using the observed values of AH_{pp} ($= 1.45 \lambda \omega / \gamma^2 M_s$) and the values of H_K derived from Eqs.(2.32) and (2.34). The theoretical fits so obtained, denoted by open circles in Figs. 3.1(a-c), indicate that the LLG equation adequately describes the resonant behavior over the entire temperature range covered in the present investigation. In addition, the lineshape analysis reveals that the splitting factor g has a temperature-independent value of 2.07 ± 0.02 within this temperature range and that the correction to the observed values of H_{pp} due to finite linewidth turn out to be negligibly small even for temperatures as high as 325K where AH_{pp} attains a fairly large value for the primary resonance.

3.3. Resonance Fields

3.3.1. *Temperature dependence*

The resonance field, H_{res} , deduced from the lineshape analysis for both II and IV configurations as a function of temperature is depicted in Fig. 3.2 for the primary resonance for **a-Fe₉₀Zr₁₀** and **a-Fe₉Zr** alloys. Fig. 3.3 depicts the H_{res} (primary) versus T/T_C curves for **a-Fe₉₀CoZr₁₀** alloys for II configuration. The variation of H_{res} with T in the low temperature region ($10K \leq T \leq 80K$), for a few selected samples on which **FMR experiments** were performed in the specified temperature range, is shown in Figs. 3.4(a-d). H_{res} exhibits a slow increase up to $T \approx 0.8T_C$ and then

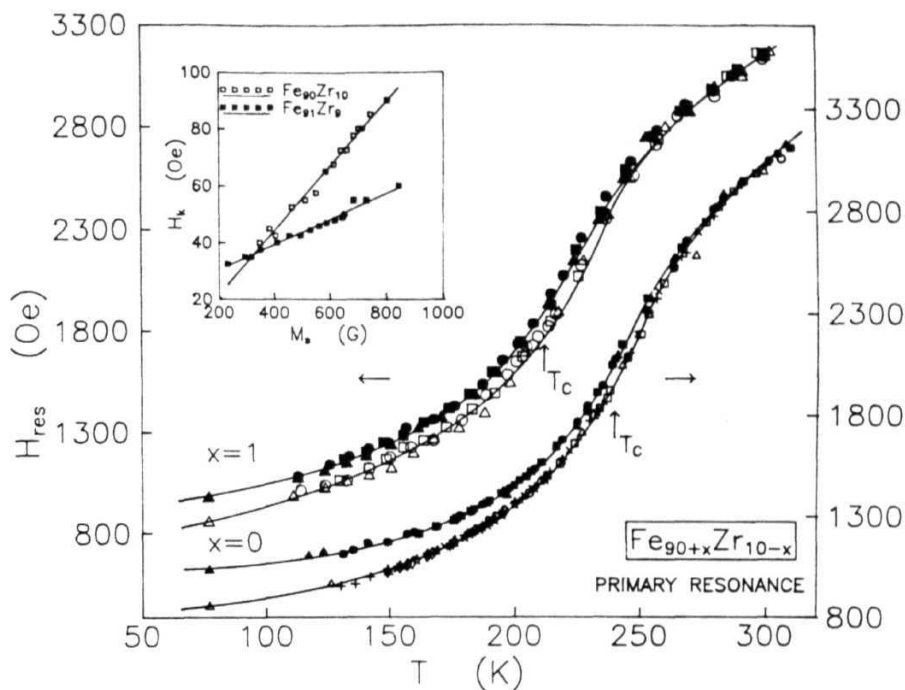


Fig. 3.2 Temperature dependence of resonance field, H_{res} , for the primary resonance in $a\text{-Fe}_{90+x}\text{Zr}_{10-x}$ alloys. Open and solid symbols denote the experimental data taken using \parallel^h and \parallel^v sample configurations, respectively, in different experimental runs. The inset shows H_k plotted against M .

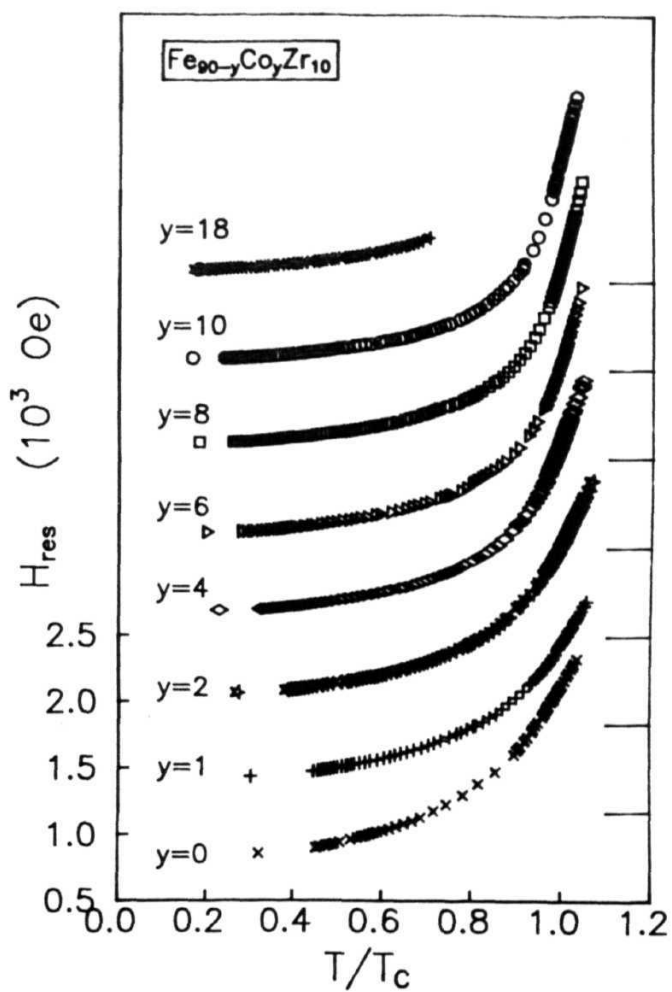


Fig. 3.3. H_{res} versus T/T_c for the primary resonance (II sample configuration) in a-Fe Co Zr alloys.

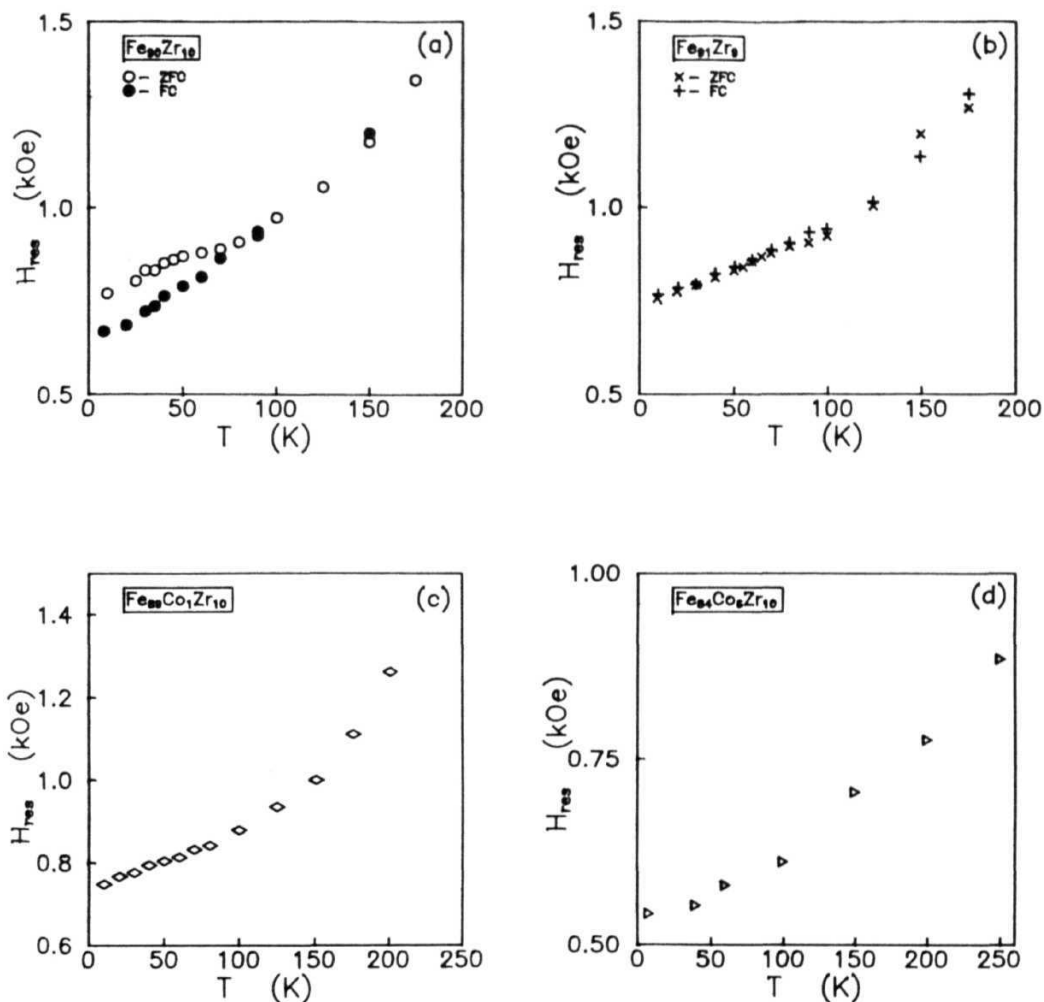


Fig. 3.4 Variation of H_{res} with T in the low temperature region for the primary resonance in (a) $a\text{-Fe}_{90}\text{Zr}_{10}$ (ZFC and FC denote the data taken after the sample is cooled in zero external field and a field of 5kOe, respectively), (b) $a\text{-Fe}_{91}\text{Zr}_9$, (c) $a\text{-Fe}_{89}\text{Co}_1\text{Zr}_{10}$ and (d) $a\text{-Fe}_{84}\text{Co}_6\text{Zr}_{10}$ alloys.

increases steeply with further increase in **temperature**. At very low T , H_{res} decreases faster with decreasing temperature than can be ascribed to an increase in magnetization for some of the samples. This behaviour has been observed earlier in reentrant glassy systems [8] and has been attributed to the anisotropy fields that develop in the reentrant state.

The variation of the secondary resonance field, H'_{res} , which is first noticed at $T \approx T_C$, with temperature is shown in Figs. 3.5(a-b) for $\text{a-Fe}_{90}\text{Zr}_{10}$ and $\text{a-Fe}_{91}\text{Zr}_9$, respectively. Fig. 3.5c shows the variation of H' with T for $\text{a-Fe}_{90-y}\text{Co}_y\text{Zr}_{10}$ alloys. It is observed that for $\text{a-Fe}_{90}\text{Zr}_{10}$ and $\text{a-Fe}_{91}\text{Zr}_9$, the secondary resonance, H' , increases with temperature and in the latter case, a steep decline in H' occurs for $T > 450$ K, which is indicative of structural relaxation effects. In $\text{a-Fe}_{90-y}\text{Co}_y\text{Zr}_{10}$ alloys, the increase in H' with T is observed for the alloys with $y=1, 2$ and 4 only. By contrast, this resonance in the alloys with $y=6, 8$ and 10, could not be studied to high enough temperatures so as to discern an increase in $H'_{\text{res}}(T)$ because the upper temperature limit of the high-temperature attachment of the spectrometer is only 500 K.

3.3.2. Concentration dependence

Fig. 3.6 shows the variation of H_{res} with Co concentration y for $\text{a-Fe}_{90-y}\text{Co}_y\text{Zr}_{10}$ alloys. Values of H_{res} for the primary resonance have been compared for the different alloy concentrations at different T/T_C values. In general, there is a decrease in H_{res} with concentration. For Co concentrations $y < 6$, H_{res} decreases at a rapid rate whereas this rate of decrease slows down for $y > 6$.

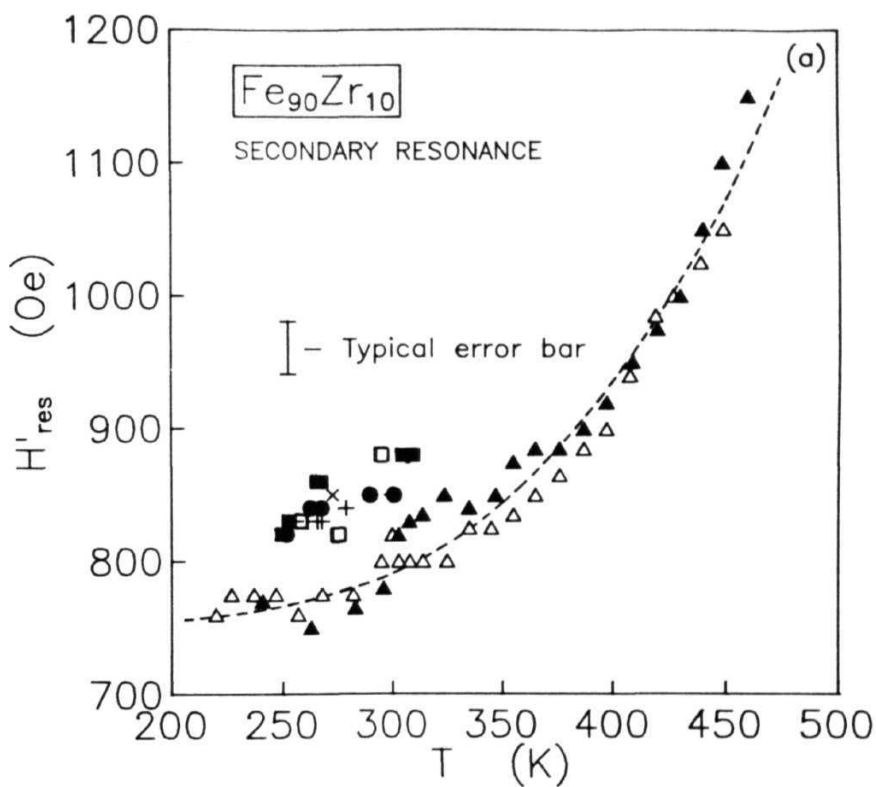


Fig. 3.5a. Variation of the resonance field, H' , for the secondary resonance with T in $a-Fe_{90}Zr_{10}$ observed in different experimental runs. The symbols have the same meaning as in Fig. 3.2 and the dashed curve through the data points is intended to serve as a guide to the eye.

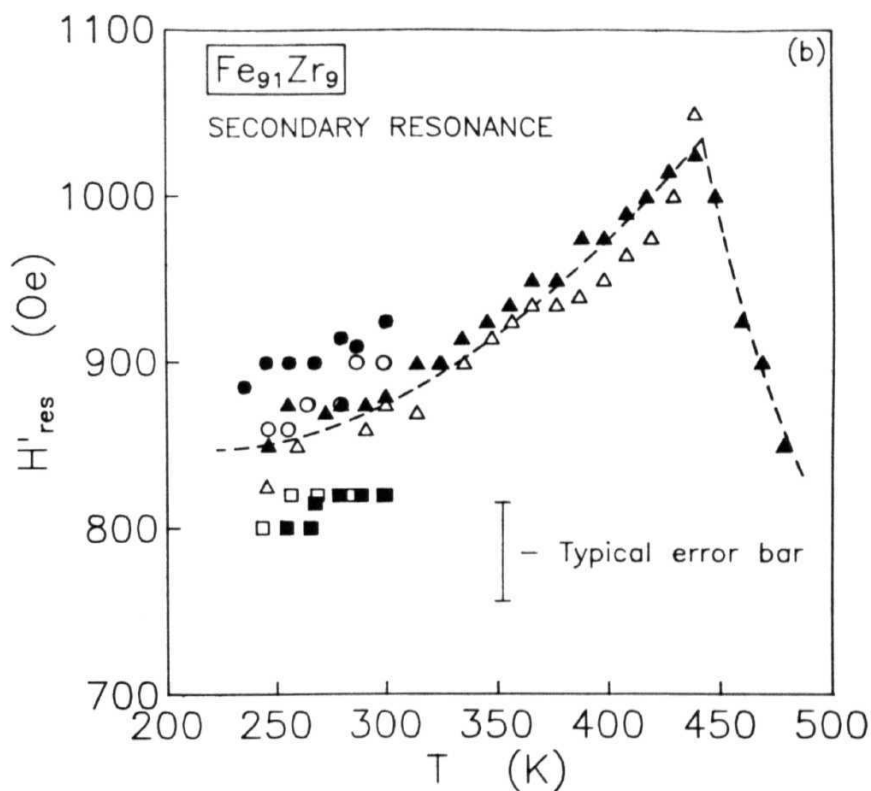


Fig. 3.5b. Variation of the resonance field, H' for the secondary resonance with T in α -Fe₉₁Zr₉ observed in different experimental runs. The symbols have the same meaning as in Fig. 3.2 and the dashed curve through the data points is intended to serve as a guide to the eye.

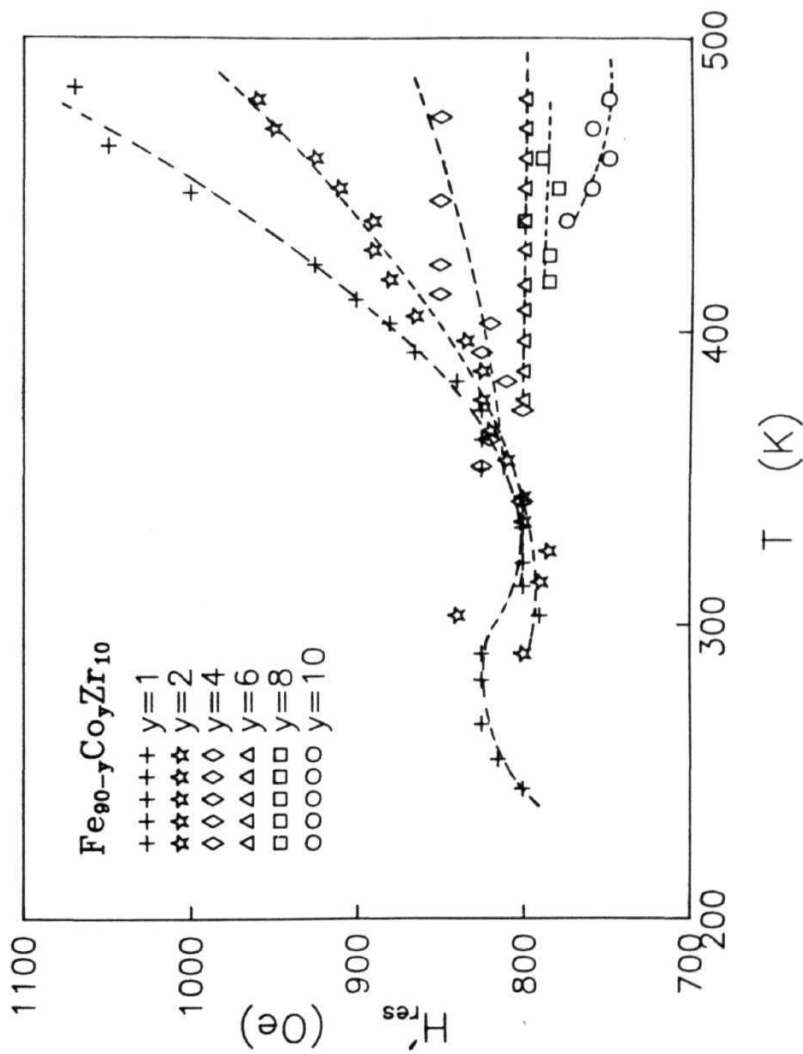


Fig. 3.5c. Variation of H'_{res} with T in a-Fe_{90-y}Co_yZr₁₀ alloys. The curve drawn through the data corresponding to a given composition is intended to highlight the observed variation.

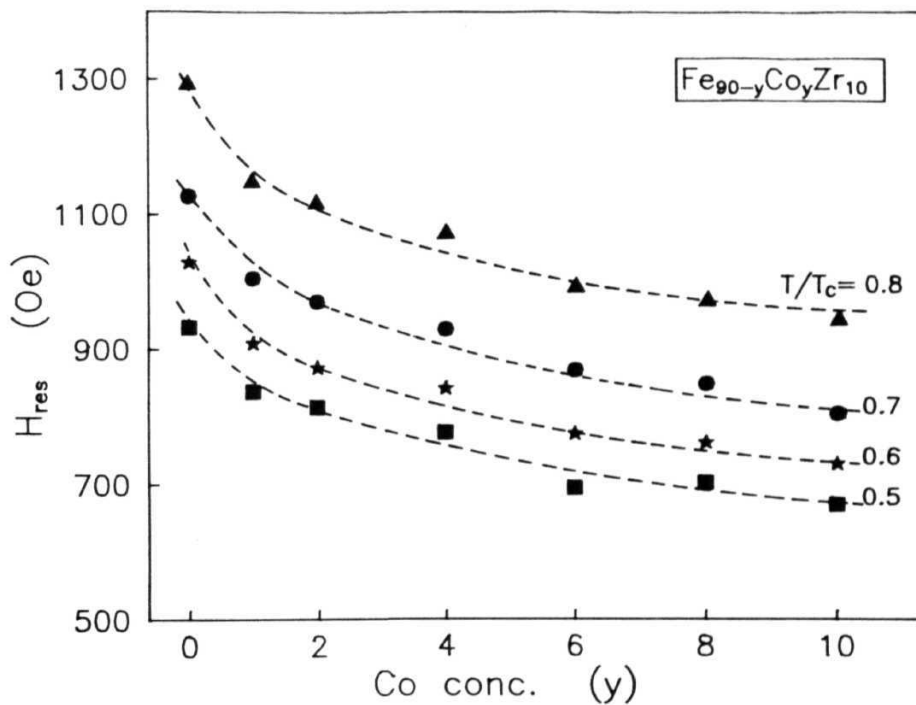


Fig. 3.6. Variation of H_{res} with Co concentration at different T/T_c values in a- $Fe_{90-y}Co_yZr_{10}$ alloys. The curve drawn through the data corresponding to a given T/T_c value is intended to highlight the observed trend.

such that H has a value of 725 Oe for $y=10$. In case of $a\text{-Fe}_{90+x}\text{Zr}_{10-x}$ alloys, H_{res} has a value of 1028 Oe (1017 Oe) for $x=0$ ($x=1$) at $0.6 T_C$.

For the secondary resonance, H'_{res} has a value of 800 Oe for all the concentrations at a temperature of $T_C + 10$ K where this resonance is fully resolved.

3.3.3. Angular dependence

As mentioned earlier, the FMR spectra for the alloys in question exhibit a single resonance for $T < T_C$ called the primary resonance and for $T > T_C$ an additional resonance, referred to as the secondary resonance, appears while the primary resonance broadens and shifts to higher fields. The secondary resonance, which gets well-resolved for $T_C + 10\text{K}$, has properties that are quite different from those of the primary resonance. Hence, in this section, the results of the angular variation of the primary resonance for $T < T_C$, i.e., $T = 0.6T_C$, and that of the secondary resonance for $T > T_C$, i.e., $T = 1.2T_C$, are described. Figs. 3.7(a) and 3.7(b) show the dP/dH curves plotted against the external field for various angles of H for the in-plane (IP) and out-of-plane (OP) sample geometries at $0.6T_C$ for the primary resonance in $a\text{-Fe}_{88}\text{Co}_2\text{Zr}_{10}$ alloy. The angular dependence of H_{res} at $0.6T_C$, for the primary resonance in $a\text{-Fe}_{90-y}\text{Co}_y\text{Zr}_{10}$ alloys is depicted in Figs. 3.8(a) and 3.8(b) for the in-plane (IP) and out-of-plane (OP) cases. The continuous curves through the data points are least-squares fits based on Eqs. (2.35) and (2.37). It is evident from the two figures that while the change in H in the IP case as the angle ψ is

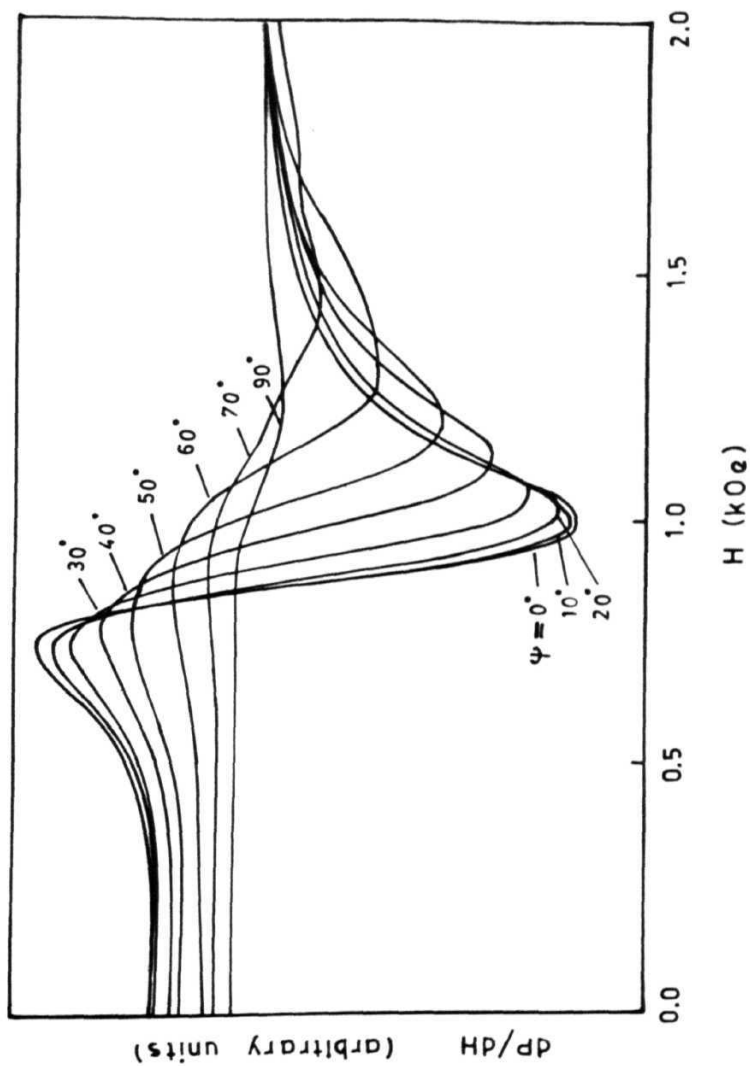


Fig. 3.7a. dP/dH vs. H curves for various angles ψ (IP case).

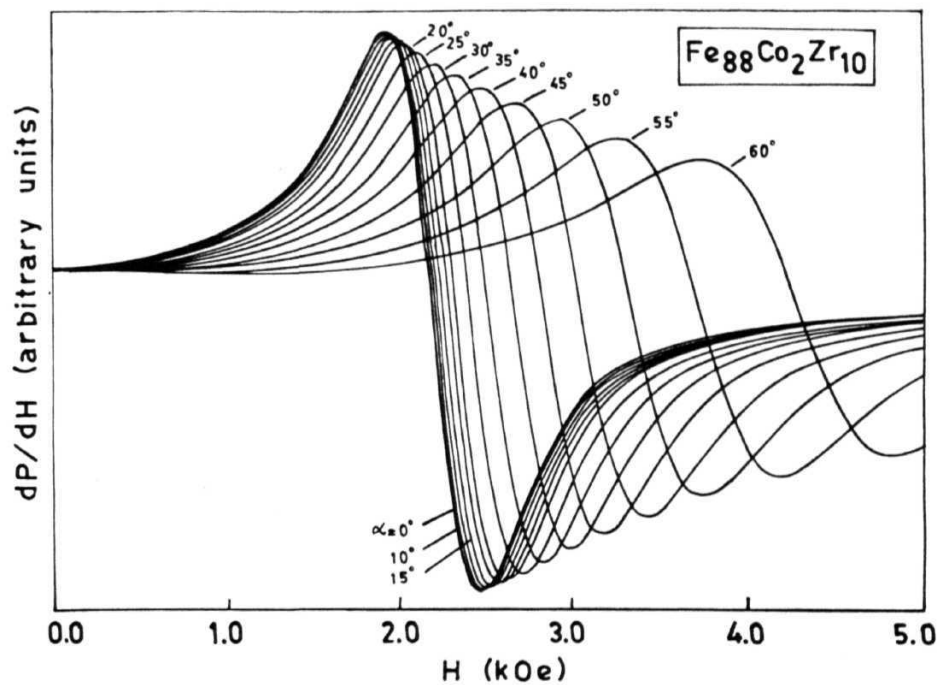


Fig. 3.7b. dP/dH vs. H curves for various angles α (OP case).

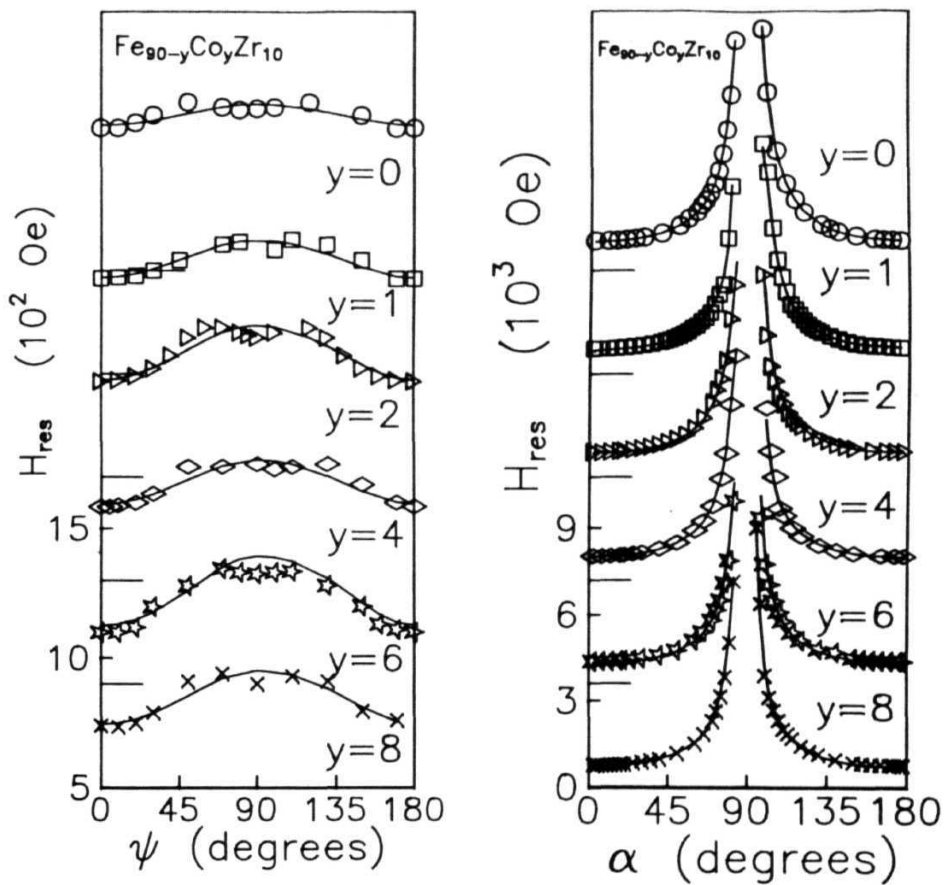


Fig. 3.8. Variation of H_{res} with (a) angle ψ for the IP case and (b) angle α for the OP case, in $a\text{-Fe}_{90-y}\text{Co}_y\text{Zr}_{10}$ alloys. The continuous curves through the data points are the LS fits based on Eqs. (2.36) and (2.38).

swept through 90° is of the order of a few hundred Oersts, H_{res} changes by more than an order of magnitude from its value at $\alpha=0$ when α goes through 90° in the OP case. The break in the curve in Fig. 3.8 (a) at $\alpha=90^\circ$ should not be interpreted as a signature of a **divergence**, instead the resonance field for α in the immediate vicinity of 90° exceeds the highest magnetic field generated by the electromagnet coupled to the spectrometer. The variation of θ , the angle between the magnetization and sample plane, with α , the angle between the external field and sample plane in the OP case for various Co concentrations is depicted in Fig. 3.9. It is noticed from this figure that M lags behind H until α reaches a value of $\approx 45^\circ$ beyond which it orients itself abruptly along the direction of H . The values for M and H_{res} have been **self-consistently** obtained from Eqs. (2.35)-(2.38) and are shown in Figs. 3.10(a) and 3.10(b).

3.4. Line widths

3.4.1. *Temperature dependence*

The variation of 'peak-to-peak' linewidth, ΔH , with temperature in the \parallel and \parallel^V configurations for $\text{a-Fe}_{1-x}\text{Zr}_x$ alloys with $x=0$ and 1 is depicted in Fig. 3.11 (a). ΔH goes through a flat minimum in the temperature range $0.5 T_C < T < 0.8 T_C$ ($0.6 T_C < T < 0.8 T_C$) for $\text{a-Fe}_{90}\text{Zr}_{10}$ ($\text{a-Fe}_{91}\text{Zr}_9$) where it assumes a constant value ≈ 210 Oe (≈ 290 Oe) for both \parallel and \parallel^V configurations. For $T > 0.8 T_C$, ΔH exhibits a steep rise. Fig. 3.11(b) displays the variation of ΔH_{pp} with reduced temperature (T/T_C) for $\text{a-Fe}_{90-y}\text{Co}_y\text{Zr}_{10}$ alloys, in the \parallel^h configuration. For $T < 0.8 T_C$,

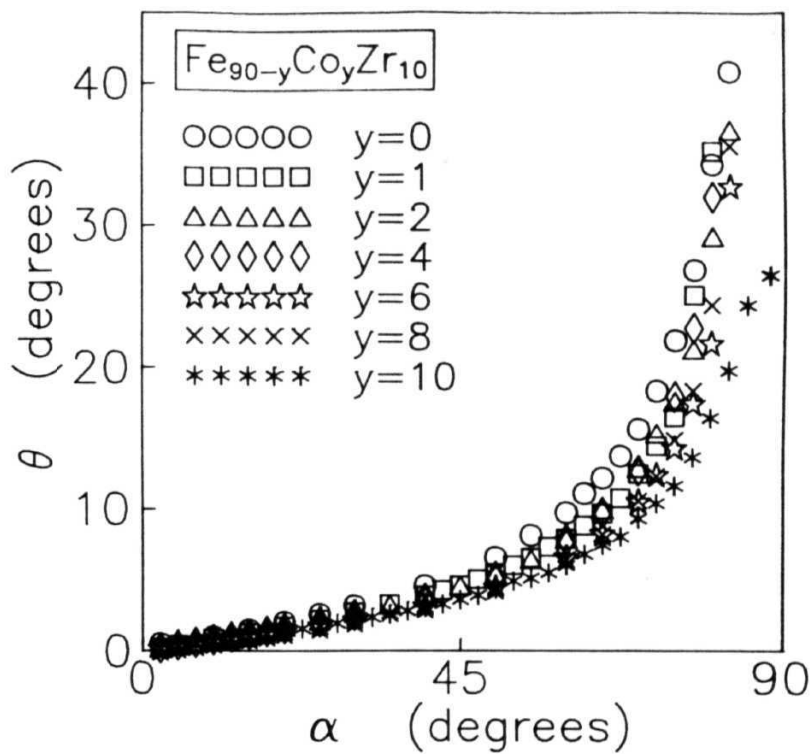


Fig. 3.9. Variation of the magnetization angle θ with α , the angle between the external field and the sample plane.

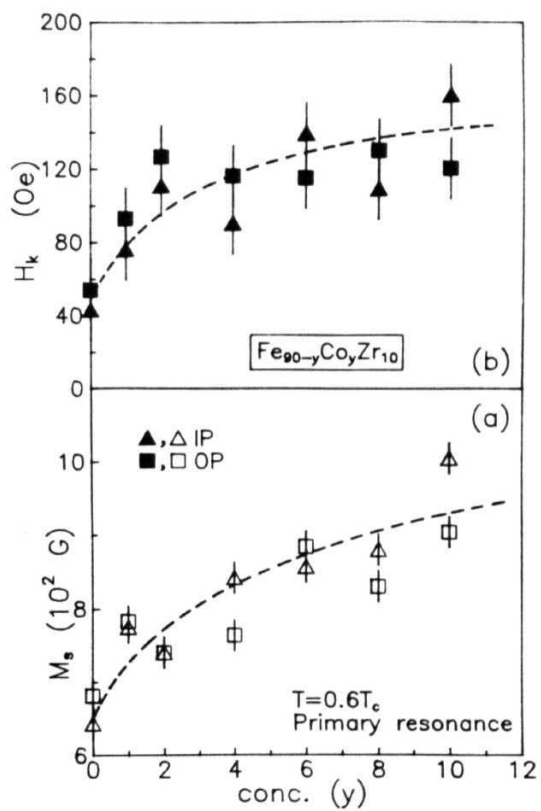


Fig. 3.10. Dependence on Co concentration, y , of (a) M and (b) H

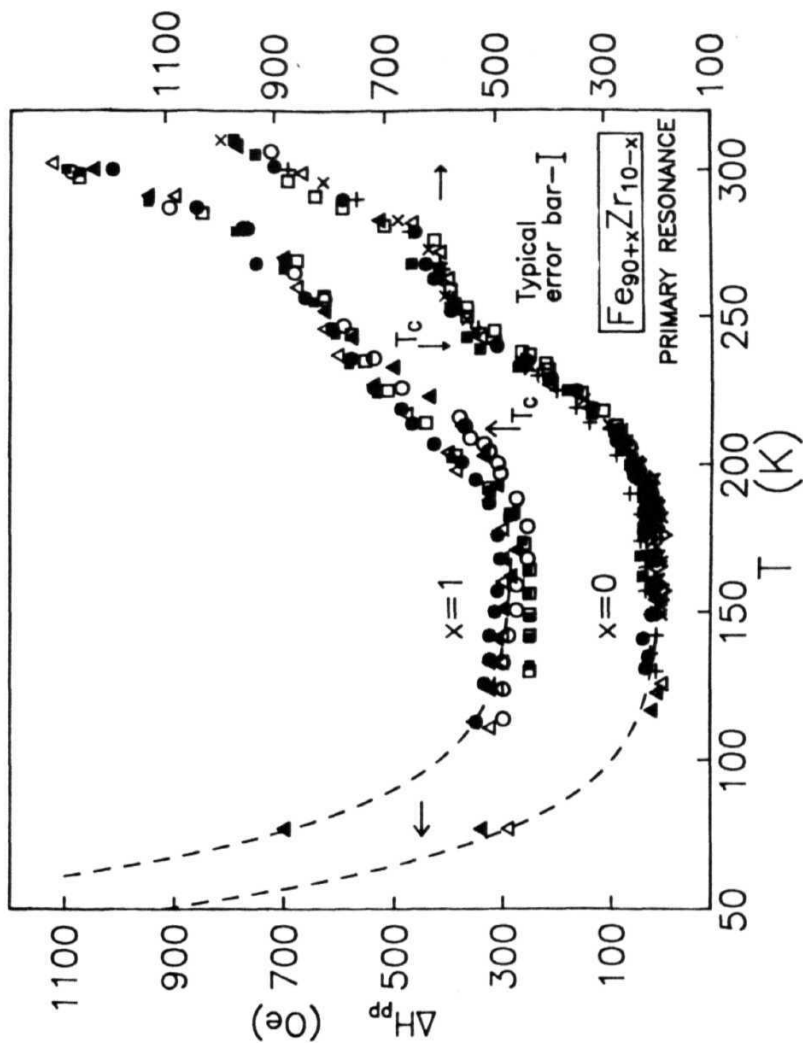


Fig. 3.11a. Variation of peak-to-peak linewidth, ΔH_{pp} , with T for the primary resonance in $a\text{-Fe}_{90+x}\text{Zr}_{10-x}$ alloys. Data symbols have the same meaning as for Fig. 3.2.

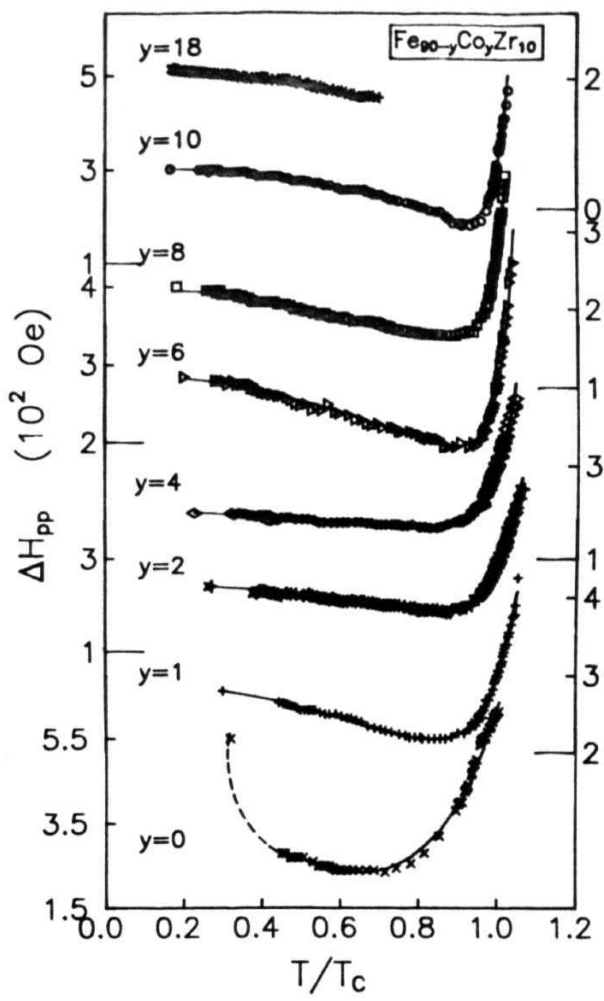


Fig. 3.11b. Variation of AH with T/T_c in the intermediate temperature range for the primary resonance in $\alpha\text{-Fe}_{90-y}\text{Co}_y\text{Zr}_{10}$ alloys. -

ΔH_{pp} for these compositions exhibits a weak increase with decreasing temperature. Fig. 3.11(c) shows ΔH plotted against temperature in the range $10 \text{ K} < T < 250 \text{ K}$ in an independent experimental run for a few selected samples which have been reported [9,10] to exhibit spin glass-like behaviour at low temperatures. The dashed curves depict the variation of ΔH with temperature obtained from the theoretical expression [3]

$$\Delta H_{pp} = \Gamma_o + \Gamma_1 (T/T_o) \exp(-T/T_o) \quad (3.2)$$

with the choice of the parameters Γ_o, Γ_1 and T_o determined from a least-squares fit to the data and given in Table 3.1.

Table 3.1

Composition	Γ_o (Oe)	Γ_1 (Oe)	Γ_o (K)
Fe₉₀Zr₁₀	334.7	257	31.10
Fe₉₁Zr₉	257.0	580	22.68
Fe₈₉Co₁Zr₁₀	236.7	321	48.20

The variation of linewidth for the secondary resonance, $\Delta H'$, with temperature in the range $T + 10 \text{ K} < T < 500 \text{ K}$ is depicted in Figs. 3.12 (a-c). Figs. 3.12(a) and 3.12(b) show the variation of $\Delta H'_{pp}$ with T for **a-Fe₉₀Zr₁₀** and **a-Fe₉₁Zr₉**, respectively. $\Delta H'$ goes through a minimum at $T_{min} \approx 410 \text{ K}$ for both the compositions. However, for **a-Fe₉₁Zr₉**, $\Delta H'$ also undergoes a steep decline for $T > 450 \text{ K}$. Fig. 3.12(c) displays the variation of $\Delta H'$ with temperature in the range $200 \text{ K} < T < 500 \text{ K}$ for **a-Fe_{90-y}Co_yZr₁₀** alloys. For all the compositions, $\Delta H'$ decreases with increasing temperature. For the alloys with $y=1$ and 2, $\Delta H'$ goes through a minimum at $\sim 420 \text{ K}$

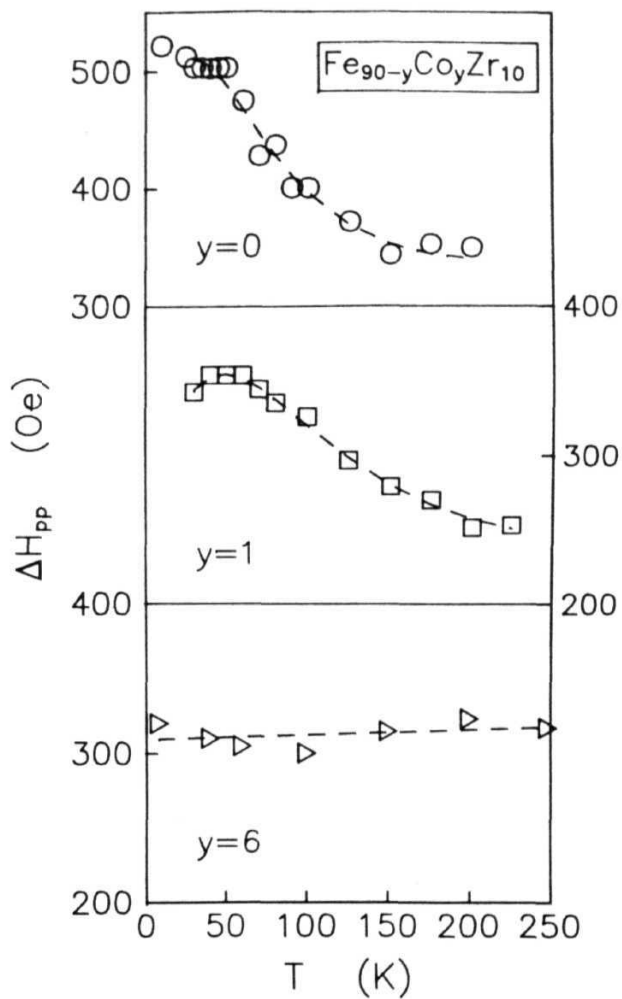


Fig. 3.11c. Low-temperature behaviour of ΔH for some typical alloy concentrations in a- $\text{Fe}_{90-y}\text{Co}_y\text{Zr}_{10}$ alloys. The dashed curves through the data points are the LS fits based on the Eq. (3.2).

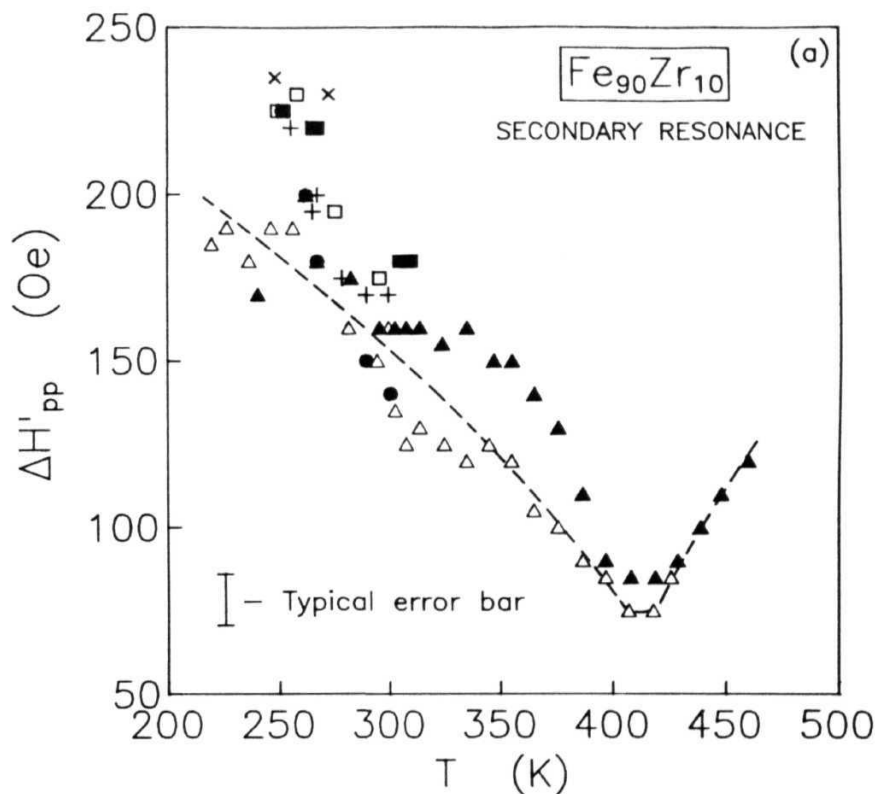


Fig. 3.12a.

Variation of linewidth, $\Delta H'_{pp}$, for the secondary resonance with T for $\alpha\text{-Fe}_{90}\text{Zr}_{10}$ observed in different experimental runs. The symbols have the same meaning as in Fig. 3.2 and the dashed curve through the data points is intended to serve as a guide to the eye.

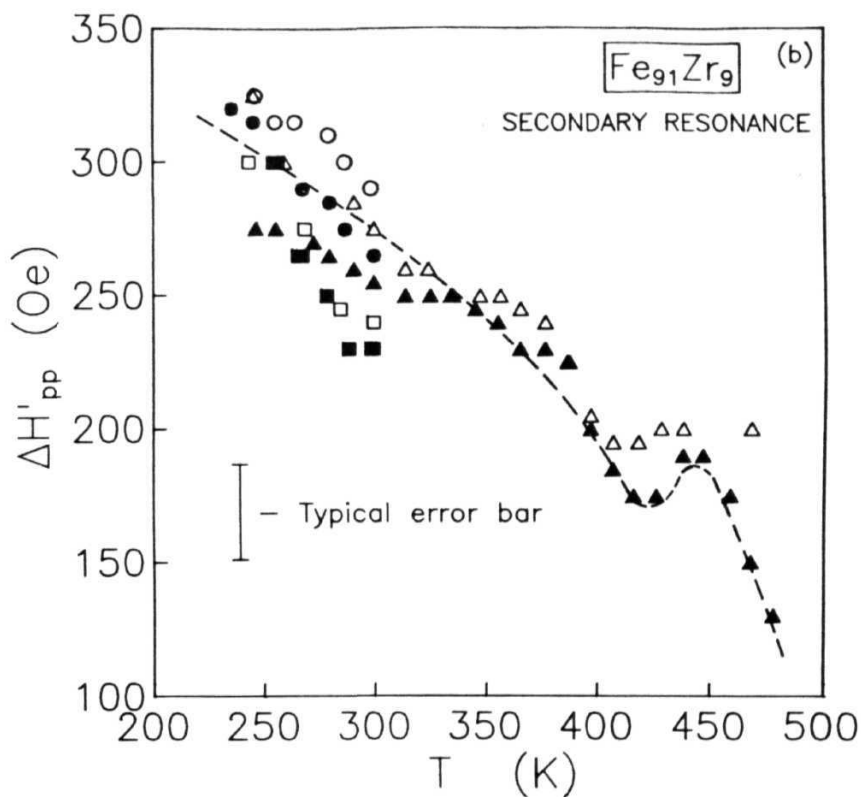


Fig. 3.12b. Variation of linewidth, $\Delta H'$, for the secondary resonance with T for $\alpha\text{-Fe}_{91}\text{Zr}_9$ observed in different experimental runs. The symbols have the same meaning as in **Fig. 3.2** and the dashed curve through the data points is intended to serve as a guide to the eye.

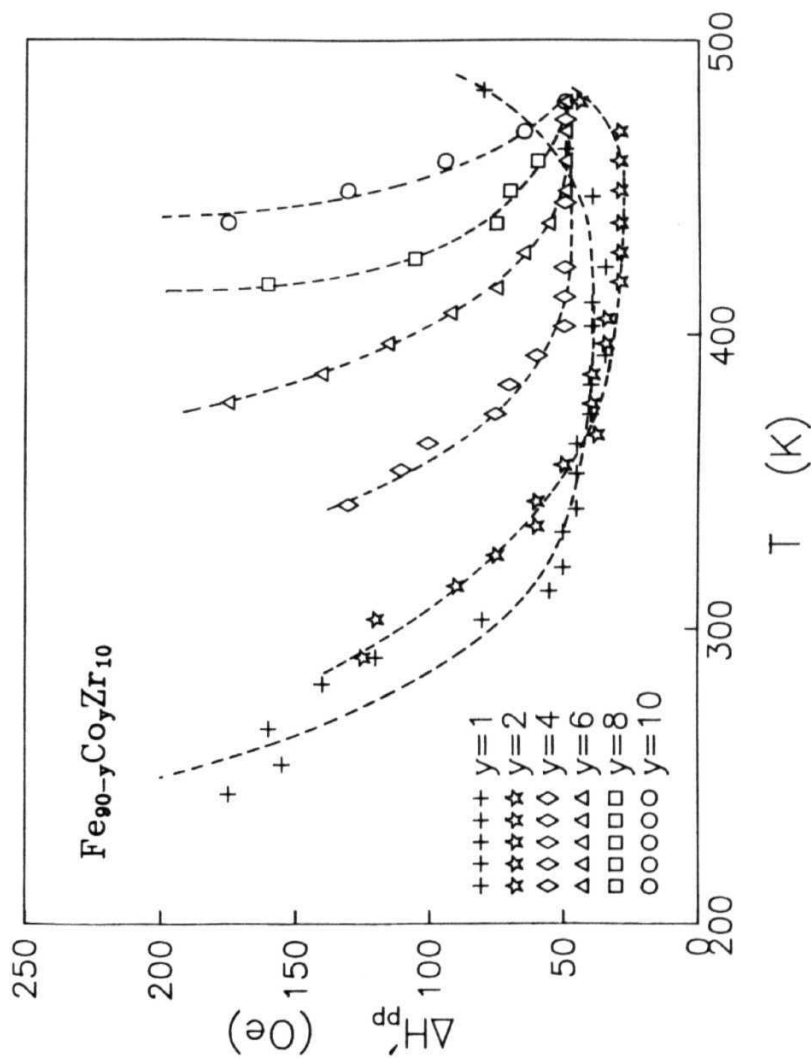


Fig. 3.12c. $\Delta H'_{pp}$ vs. T in the range $200\text{K} \lesssim T \lesssim 500\text{K}$ for $\text{a-Fe}_{90-y}\text{Co}_y\text{Zr}_{10}$ alloys. The curves drawn through the data points serve as a guide to the eye.

before displaying a slight increase.

3.4.2. Concentration dependence

It has been observed that ΔH for the **primary** resonance does not show any systematic variation with concentration and varies between 180 Oe and 250 Oe at 0.6 T . By contrast, the line-width for the secondary resonance, $\Delta H'$, attains a value of <50 Oe above 400 K for all the compositions.

3.5. 'In-plane' uniaxial magnetic anisotropy

Values for the 'in-plane' uniaxial anisotropy, H_k , have been calculated for all the alloy compositions at different **temperatures** from the values of $H_{res}^{\parallel h}$ and $H_{res}^{\parallel v}$, using Eq. (2.34). The values of H_k so obtained are plotted against saturation magnetization, M_s , deduced from the lineshape analysis and it is observed that H_k ($=2K_u/M_s$) is related to M_s through a *linear* relation of the type

$$H_k(T) = a M_s(T) \quad (3.3)$$

or, alternatively

$$K_u(T) = (\alpha/2) [M_s(T)]^2 \quad (3.4)$$

Inset of Fig. 3.2 shows H_k plotted against M_s for **a-Fe_{90+x}Zr_{10-x}** alloys. The slope a determined by a **least-squares-fit** method yields values of the uniaxial anisotropy constant K at $T=77K$ for the alloys with $x=0$ and 1 as $K_u(77K) = (2.91 \pm 0.40) \times 10^4$ **erg.cm⁻³** and $(1.6 \pm 0.2) \times 10^4$ **erg.cm⁻³**, respectively. Fig. 3.13

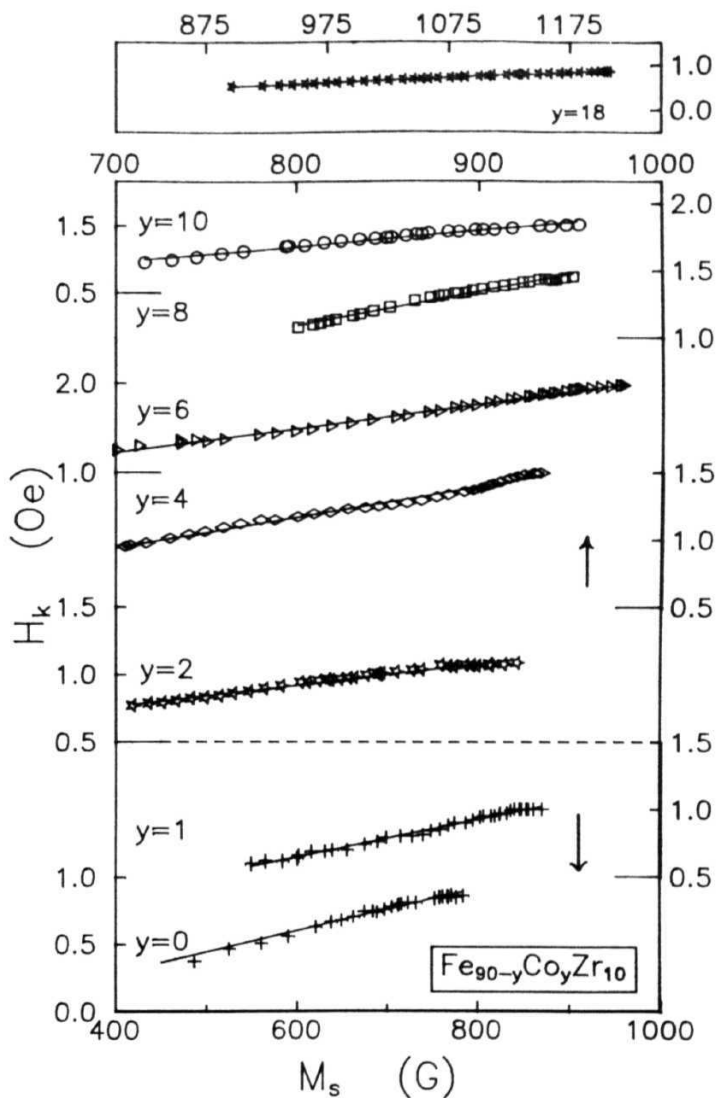


Fig. 3.13a. H_k vs. M_s for $a\text{-Fe}_{90-y}\text{Co}_y\text{Zr}_{10}$ alloys. The straight lines through the data points represent the best least-squares fits to the data based on Eq. (3.3).

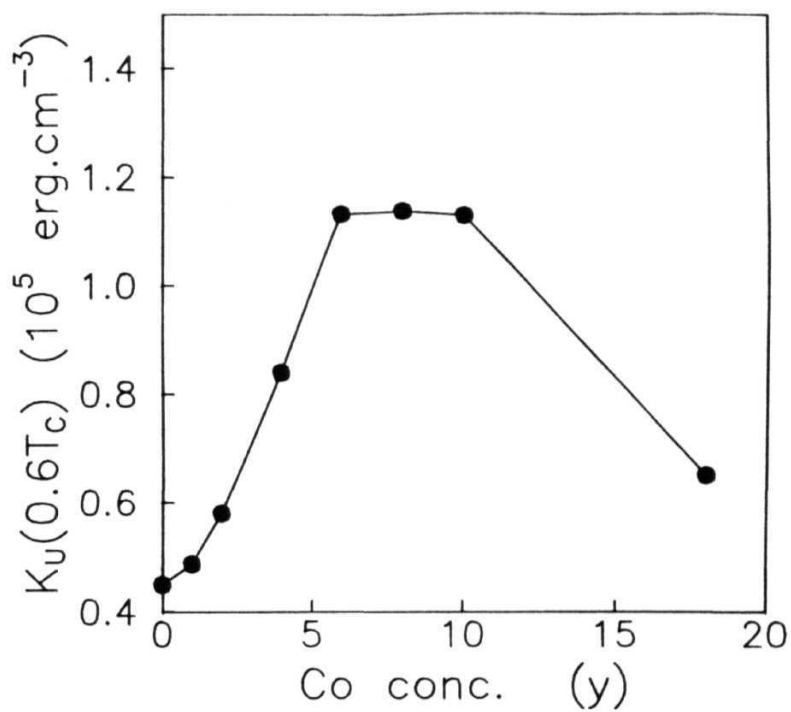


Fig. 3.13b. Variation of K_u at $T=0.6T_c$ with Co concentration.

(a) and (b) depict the variation of H_k with M_s , and K_u as a function of Co concentration at $T=0.6 T_C$ for $a\text{-Fe}_{90-y}\text{Co}_y\text{Zr}_{10}$ alloys.

3.6. Magnetization

Values of saturation magnetization, M_s , have been deduced from the lineshape analysis of the spectra taken in \parallel geometry at different temperatures for the primary resonance on $a\text{-Fe}_{90+x}\text{Zr}_{10-x}$ and $a\text{-Fe}_{90}\text{CoZr}_{10}$ alloys. It is customary to determine $M_s(T)$ either by using the resonance condition for \parallel configuration (Eq. 2.26) and the results of FMR measurements performed in the same geometry at widely spaced values of the microwave frequency or by making use of the resonance conditions for the \parallel and \perp configurations (Eqs. (2.26) and (2.28)) and the FMR results obtained for these configurations at a single microwave frequency. Neither of these approaches has been followed in the present study for the following reasons. First, the experimental set-up used for this study was limited to only one microwave frequency value of ≈ 9.23 GHz in the X-band. Second, due to considerably large values of $4\pi M_s$ for temperatures below T_C , the resonance in the \perp configuration occurs at fields much higher than 10 kOe, the upper instrumental limit. Hence, neither the primary nor the secondary resonance is observed at any temperature below T_C in the \perp configuration. The values of M_s , deduced from the lineshape analysis, have been plotted against temperature in Figs. 3.14 (a) and 3.14(b) for $a\text{-Fe}_{90+x}\text{Zr}_{10-x}$ and $a\text{-Fe}_{90-y}\text{Co}_y\text{Zr}_{10}$ alloys, respectively.

Fig. 3.15 shows the variation of M_s with composition at

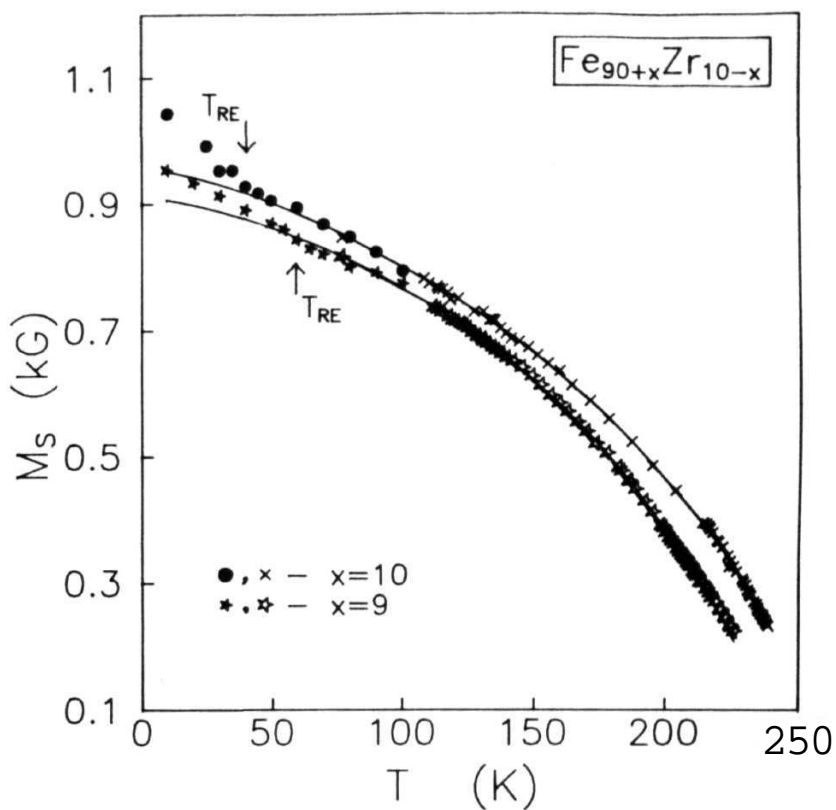


Fig. 3.14a. Variation of M_s with T for $\alpha\text{-Fe}_{90+x}\text{Zr}_{10-x}$ alloys. The continuous curves through the data points are the best least-squares fits to the data taken in the intermediate temperature range $100 \leq T \leq 250\text{K}$ based on Eq. (4.7). Filled symbols represent data taken in the low temperature region.

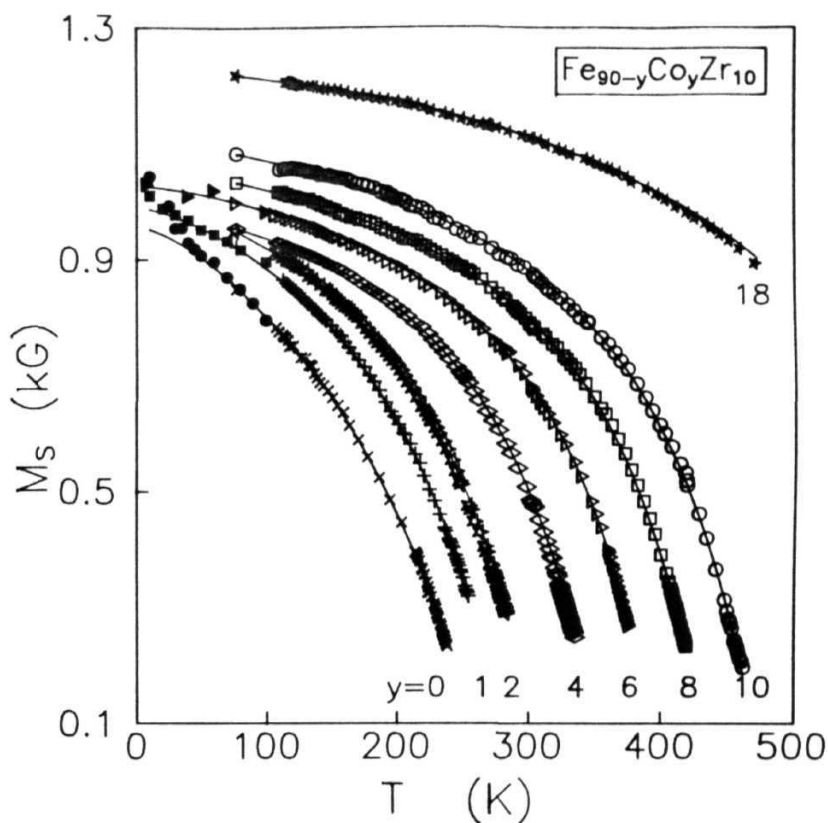


Fig. 3.14b. Temperature dependence of M for α -Fe-Co-Zr alloys. The continuous curves through the data points are the best least-squares fits to the data taken in the intermediate temperature range $100 \leq T \leq 500\text{K}$ based on Eq. (4.7). Filled symbols represent data taken in the low temperature region.

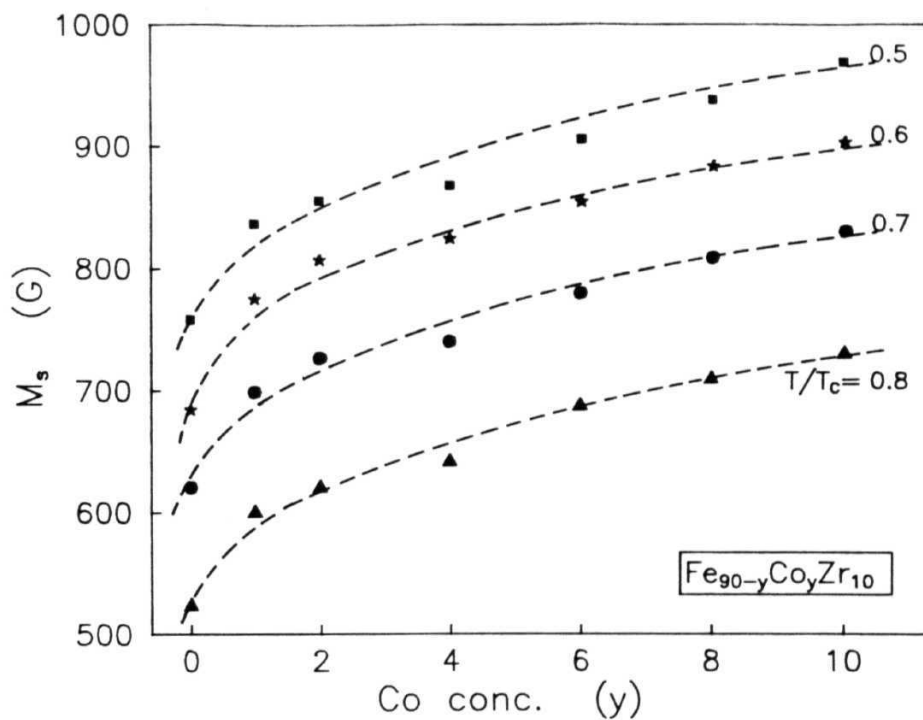


Fig. 3.15. Variation of M_s with Co concentration at different T/T_c values in $\text{a-Fe}_{90-y}\text{Co}_y\text{Zr}_{10}$ alloys. The curves through the data serve to highlight the observed variation.

different values of T/T_C for the different compositions in the **a-Fe_{90+x}Zr_{10-x}** and **a-Fe_{90-y}Co_yZr₁₀** alloy series. It is observed that for **a-Fe₉₀Zr₁₀** and **a-Fe₉₁Zr₉** alloys, M_S has a value of 684.0 Oe and 698.6 Oe, respectively, at $T=0.6 T_C$. For **a-Fe₉₀CoZr₁₀** alloys, M_S exhibits a sharp increase up to the Co concentration $y=6$ and beyond this concentration the rate of increase decreases drastically.

Apart from the measurements on a-Fe-Zr and **a-Fe-Co-Zr** alloys, a detailed comparative FMR study on **a-Co₉₀Zr₁₀** alloy, which represents the end composition at the Co-rich side of the **Fe-Co-Zr** alloy series, was undertaken in order to gain further physical insight into the nature of magnetism in the above-mentioned alloy series for $T < T_C$. **a-Co₉₀Zr** is known [10] to exhibit conventional ferromagnetism down to 4.2 K. Fig. 3.16 shows the temperature variation of H and ΔH in the \parallel and \parallel^V sample configurations in the temperature range $77 \text{ K} < T \leq 500 \text{ K}$. It is observed that in contrast with the temperature-induced variations of the above parameters for **a-Fe_{90+x}Zr_{10-x}** and **a-Fe_{90-y}Co_yZr₁₀** alloys, the quantities $\Delta H^{\parallel} = 115 \pm 5 \text{ Oe}$, $\Delta H^{\parallel} = 175 \pm 5 \text{ Oe}$ and $g=2.07 \pm 0.02$ remain unaltered (within error limits) while $H_{\text{res}}^{\parallel h}$ and $H_{\text{res}}^{\parallel v}$ (hence M_S and H_K) have a very weak dependence on temperature for **a-Co₉₀Zr** in the temperature range covered, as expected for a ferromagnet with a high Curie temperature ($T_C >$ crystallization temperature (750 K) [11] for **a-Co₉₀Zr₁₀**).

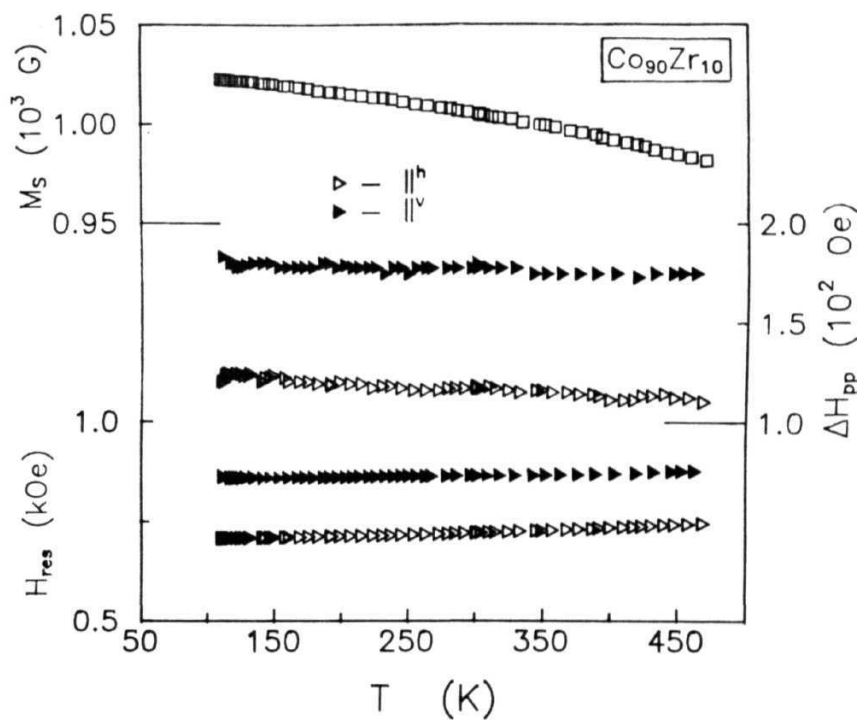


Fig. 3.16. Variation of H_{res} , ΔH_{pp} (for \parallel^h and \parallel^v sample geometries) and M with T for $a\text{-Co}_{90}\text{Zr}_{10}$.

3.7. Analysis of ME spectra of amorphous alloys

Mössbauer (ME) **spectroscopy**, being a local probe, is **extremely** sensitive to small changes in the local environments of **atoms**, i.e., when two **Mössbauer** atoms in the same sample have different local environments, their individual **Mössbauer** spectra will also be different, each having its own set of Mossbauer parameters. In amorphous alloys, there exists a wide distribution in local environments of the Mossbauer atoms due to chemical and topological disorder. As a result of this distribution, the hyperfine field, **isomer** shift and the electric field gradient (EFG) vary from one iron nuclear site to the other and this variation, in turn, gives rise to broad overlapping Mossbauer lines. Hence, the interpretation of ME spectra in these materials is often difficult and a judicious choice of the method of analysis has to be made in order to arrive at the correct values for the ME parameters.

The most important aspect of the analysis of ME spectra is the determination of the Mossbauer parameters (described in Sec. 2.8) isomer shift δ , quadrupole splitting A , intensity ratio b and evaluation of the hyperfine fields and their distributions. Given the fact that ME spectra of amorphous ferromagnetic alloys consist of structureless, broad and partly overlapping lines, often with some degree of asymmetry, certain assumptions have to be made before evaluation and analysis of ME spectra. It is generally observed that the electric quadrupolar effects are negligible for amorphous ferromagnetic alloys below the magnetic ordering **tempe-**

perature T_c [12]. The quadrupole interaction at each site in such an alloy can be approximately described by $e qQ (3\cos^2\theta-1)$, where e^2qQ is the quadrupole interaction energy and e is the angle between the z-axis of the principal EFG tensors and the hyperfine field. The z-axis is determined by site symmetry, which varies spatially throughout the **sample**, whereas the magnetic hyperfine field, which is antiparallel to the magnetization axis in a ferromagnetic sample does not vary randomly. Hence, the value of $(3\cos^2\theta-1)$ spatially averages out to zero. In order to account for the observed asymmetry in the ME lineshape, a linear correlation between the local **isomer** shift and the local hyperfine field of the form [13]

$$\delta(H_{hf}) = \delta(H_{hf}^O) - a (H_{hf} - H_{hf}^O) \quad (3.5)$$

is assumed, which implies that δ also has a distribution similar to that of H_{hf} but so narrow compared to the latter that it can be treated as a delta function. A similar correlation may be assumed for $T > T_c$ between the quadrupole moment and the hyperfine field.

Several methods exist in the literature for the evaluation of hyperfine field distributions, $P(H_{hf})$, from the measured ME spectra. These fall into two broad categories: (i) a definite shape of $P(H_{hf})$ is assumed *a priori*, e.g., a single Gaussian [14], modified **Lorentzian** [15] or a split-Gaussian [16] (the parameters of such functions are determined by a least-squares fitting procedure), (ii) no *a priori* assumption is made as regards the shape of $P(H_{hf})$, e.g., the **Window method** [17] in which $P(H_{hf})$ is expanded in a Fourier series, or the discrete field method proposed by

Hesse and Rubartsch, [18] which was later improved upon by Le Cŕer and Dubois [19], or the method due to Vincze [20], in which $P(H_{hf})$ is approximated by a binomial distribution.

In the present study, two methods, one from each of the above categories, have been used to analyze the ME spectra. These are (i) the Window method, in which no assumption is made about the shape of $P(H_{hf})$ and (ii) the a two-pattern method in which the $P(H_{hf})$ consists of two Gaussians.

3.8. Window method

$P(H_{hf})$ is described by

$$P(H_{hf}^W) = \sum_{i=1}^m a_i w_i(H) \quad (3.6)$$

where w_i are 'elementary' functions of hyperfine field distribution between $H=0$ and $H=H_{max}$. If $w_i(H)$ is defined as

$$w_i(H) = \cos[i\pi(H-H_{min})/(H_{max}-H_{min})] - (-1)^i \quad (3.7)$$

$P(H)$ can be expanded in a Fourier (cosine) series,

$$P(H_{hf}^W) = \sum_{i=1}^m a_i [\cos\{i\pi(H-H_{min})/(H_{max}-H_{min})\} - (-1)^i] \quad (3.8)$$

The distribution w_i creates a spectrum S_i ,

$$S_i(\nu) = \int_0^{H_{max}} w_i(H) \cdot L_6(H, \nu) dH \quad (3.9)$$

where v is the relative velocity between the source and the absorber and $L_c(H, v)$ is a sextuplet of Lorentzian lines.

The complete spectrum is written as

$$S(v) = \sum_{i=1}^m a_i S_i(v) \quad (3.10)$$

The unknown coefficients a_i can be calculated by a least-squares program, with the constraints,

$$P(H_{\max}) = 0 \quad ; \quad (dP/dH)_{H_{\min, \max}} = 0 \quad , \quad (3.11)$$

In addition, the area under the $P(H)$ curve is normalized, i.e.,

$$\sum_{\min}^{H_{\max}} P(H_{hf}) = 1 \quad (3.12)$$

All the spectra were first evaluated using this method. While expanding the $P(H_{hf})$ in a cosine series (Eq. (3.8)), it is assumed that (i) the spectrum can be described by a single value of the **isomer shift**, δ , (ii) the quadrupole splitting, A , is negligible for $T < T_c$, and (iii) an average value of the intensity ratio b of the component spectra, i.e., $I_6 : I_5 : I_4 : I_3 : I_2 : I_1 = 3:b:1$, can adequately describe the observed spectrum. Although none of these assumptions is strictly valid for amorphous ferromagnetic systems, it has been demonstrated [21] that this method can nonetheless be used to accurately determine $P(H_{hf})$ provided that the important Mossbauer fitting parameters, e.g., the full width at half maximum (**FWHM**) of the subspectral lines, T , intensity ratio, b , **and** the number of terms in the Fourier expansion, N , are properly chosen. For instance, too small a value of N can obscure

some genuine details of the $P(H_{hf})$ curve whereas too large a value of N gives rise to unphysical structure in $P(H_{hf})$ because a large number of terms in the Fourier series (Eq. (3.8)) tend to fit the statistical fluctuations in the measured spectrum.

The optimum choice of the parameters, b , Γ and N for each spectrum is based on the minimization of χ^2 , defined by

$$\chi^2 = (m-n_p)^{-1} \sum_{i=1}^m (Y_{exp}^i - Y_{cal}^i)^2 / Y_{exp}^i \quad (3.13)$$

(where m and n are the number of channels and free-fitting parameters, respectively, while Y_e^1 and Y_{cal}^1 are the experimental data points and the corresponding points on the fitted curve), with respect to the free-fitting parameters δ , Γ , b and the correlation between the isomer shift and hyperfine field, a^* . The line-width r of the Fe subspectra was at first fixed at the intrinsic FWHM of the source ($=0.24 \text{ mm s}^{-1}$), N was set equal to 10, the fitting parameters δ and a were left free and χ^2 was evaluated for a value of b , which was progressively increased in steps of 0.1 in the interval $0 \leq b \leq 4$. It is evident from Fig. 3.17 (a) that χ^2 as a function of b goes through a minimum at $b=2.1$ for the spectrum taken at 5 K for $a\text{-Fe}_{90}\text{Zr}_{10}$. Next, b and N were fixed at 2.1 and 10, respectively, and χ^2 was determined as a function of the line-width r . Fig. 3(b) shows that $\chi^2(\Gamma)$ exhibits a well-defined minimum at a value $r=0.33 \text{ mm.s}^{-1}$, which differs appreciably from the earlier choice of $r=0.24 \text{ mm.s}^{-1}$. A repetition of the calculation of $\chi^2(b)$ with Γ fixed at 0.33 mm.s^{-1} showed that the value of b does not differ from 2.1. The intensity ratio b and linewidth Γ were then fixed at their optimum values and χ^2 was monitored as a

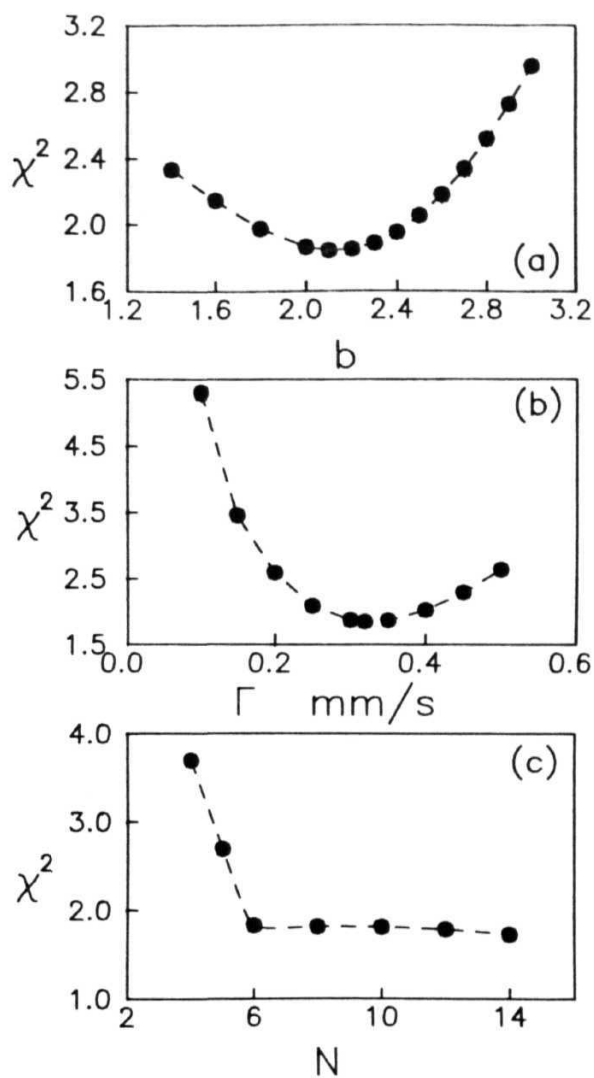


Fig. 3.17. χ^2 plotted against (a) the intensity ratio, b , for $\Gamma = 0.24 \text{ mm.s}^{-1}$ and $N=10$, (b) the FWHM linewidth, Γ , for $b = 2.1$ and $N=10$, and (c) the number of terms in the Fourier expansion (Eq. (3.8)), N , for $b = 2.1$ and $\Gamma = 0.33 \text{ mm.s}^{-1}$.

function of N in the interval $4 \leq N \leq 14$. χ^2 drops steeply as N is increased from 4 to 6 but a further increase in N brings forth only a slight improvement in χ . Thus, $N=8$ can be taken as the most appropriate value of N . The optimum values of the parameters b , Γ , δ and a as well as of \bar{H}_{hf}^W (average hyperfine field) from the $P(H_{hf})$, evaluated using Eq. (3.13), are determined for three different values of N , i.e., $N=8$, 10 and 12, for each spectrum. The CPU time taken for 30 $P(H_{hf})$ evaluations on a Microvax-II computer was typically 1000 seconds.

3.9. Two-pattern analysis

The assumptions on which this method is based are (i) $P(H_{hf})$ consists of two hyperfine field values whose individual probabilities are of Gaussian form, (ii) the distribution in the hyperfine field is primarily responsible for line broadening, (iii) the quadrupole splitting A is negligible for both subspectra, (iv) the intensity (or area) ratio of the outermost to the innermost lines in each sextet is 3, (v) the two six-line patterns are characterized by two distinctly different but average values of the intensity ratio b and of the center shift δ and (vi) a linear correlation between δ and H_{hf} exists for each subspectrum. The $P(H_{hf})$ is first generated by the superposition of two Gaussian curves at H_{hf} intervals that are 2 kOe apart, with $H_{hf}^{\max} = 400$ kOe. A linear combination of two independent subspectra, $S_i(v)$, is calculated using Eq. (3.8) for the above-mentioned $P(H_{hf})$ ($\equiv W_i(H)$ in Eq. (3.8)). An appropriate baseline is then added to $S_i(v)$ and the calculated spectrum can be written as

$$Y(v) = (\text{average baseline counts}) \left[1 - \int_0^{H_{\max}} P(H_{hf}) \cdot L_6(H, v) dH \right] \quad (3.14)$$

This is compared with the measured spectrum and optimized using Eq. (3.13) in least-squares fit method. The optimum parameters of the two Gaussian distributions and those of the two sub-spectra that reproduce the measured spectrum are determined from the fit. The typical CPU time taken for each spectrum was approximately 24 to 36 hours.

A comparison of the x values (corrected for the number of free-fitting parameters) obtained from the TP analysis and the Window method shows that the quality of TP fits is far superior to those obtained by the latter **method**, Fig. 3.18. At this juncture, it should be mentioned that the ME spectra were also fitted on the assumption that either one or three Gaussian distributions constitute $P(H_{hf})$. While the single-Gaussian fits gave unsatisfactory results in that the residual plots (the plots of the deviations of the experimental **γ -counts** from those calculated from the best fit versus doppler velocity) at all temperatures **$T < T_c$** revealed that the low-field part of the spectra, in particular, was unaccounted for in these fits, the three-Gaussian fits, even with a much larger number of free fitting parameters, did not lead to any significant improvement in the quality of fits compared to that achieved by assuming $P(H_{hf})$ to be the sum of two Gaussian distributions.

3.10. Experimental results

As mentioned earlier, the two-pattern fit **method** is clearly

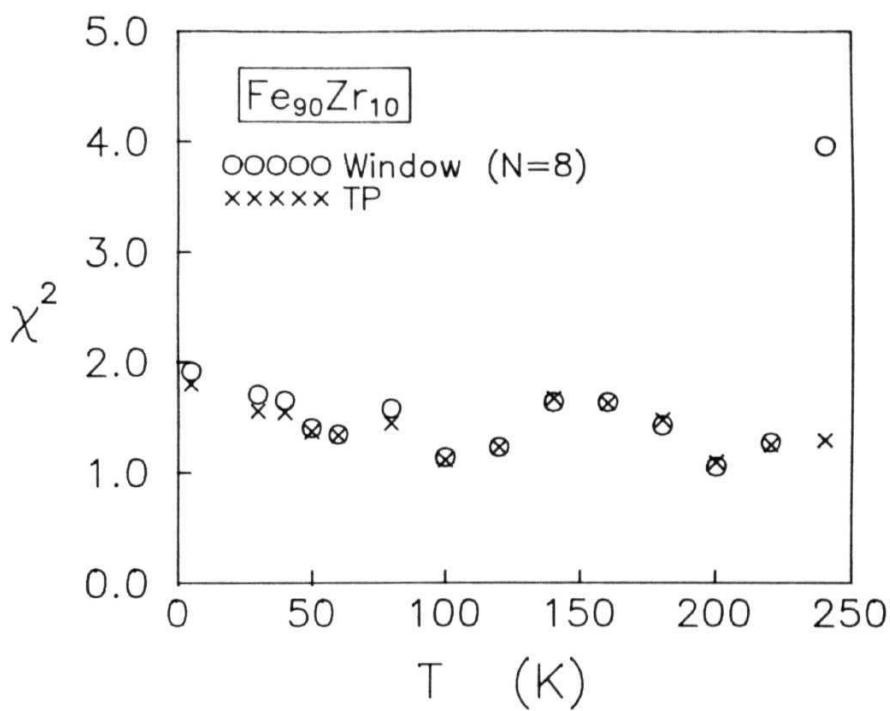


Fig. 3.18. Reduced χ as a function of **temperature** for the Window method (o) and the TP fit method (x) for **a-Fe₉₀Zr₁₀**.

superior to the Window method at all temperatures and hence zero field Fe ME spectra at a few representative temperatures in the range 5-300K together with the best two-pattern fits for $\text{a-Fe}_{90}\text{Zr}_{10}$ are shown in Fig. 3.19(a). The two subspectra sextets and their line positions are also shown for each spectrum. Fig. 3.19(b) shows the corresponding component Gaussian distributions and their resultant distribution. From the figure, it is clear that, (i) the $P(H_{\text{hf}})$ is bimodal in nature, (ii) the peak positions of both the two Gaussian distributions shift to lower field values as temperature is increased, and (iii) the intensity (area under) of the low-field component of $P(H_{\text{hf}})$ increases at the expense of that of the high-field component with temperature. Fig. 3.20 shows a similar variation with temperature of the measured spectra and their fits and distributions for a-Fe Zr_9 . These results show a behavior similar to that of $\text{a-Fe}_{90}\text{Zr}_{10}$. Figs. 3.21-3.23 show the ME spectra at a few representative temperatures alongwith their corresponding $P(H_{\text{hf}})$ for a few selected concentrations in the $\text{Fe}_{90}\text{-Co Zr}_{10}$ alloy series. The bimodal distribution in $P(H_{\text{hf}})$ persists down to 9K in the alloy with $y=1$, gets partially suppressed in the alloy with $y=2$ and is totally absent for the alloy with $y=6$. Another observation is that the average hyperfine field increases with the concentration of cobalt. ME spectra taken at room temperature for all the alloy compositions are depicted in Fig. 3.24. The Curie temperatures for the $\text{a-Fe Zr}_{10}\text{- alloys}$ with $x=0$ and 1 and $\text{a-Fe}_{90}\text{Co Zr}_{10}$ alloys with $y=1$ and 2 are below room temperature and hence, one can observe quadrupole splitting only for these alloys at room temperature. Fig. 3.25 depicts $P(H_{\text{hf}}^{\text{W}})$ yielded by the Window analysis of the Mössbauer spectra of

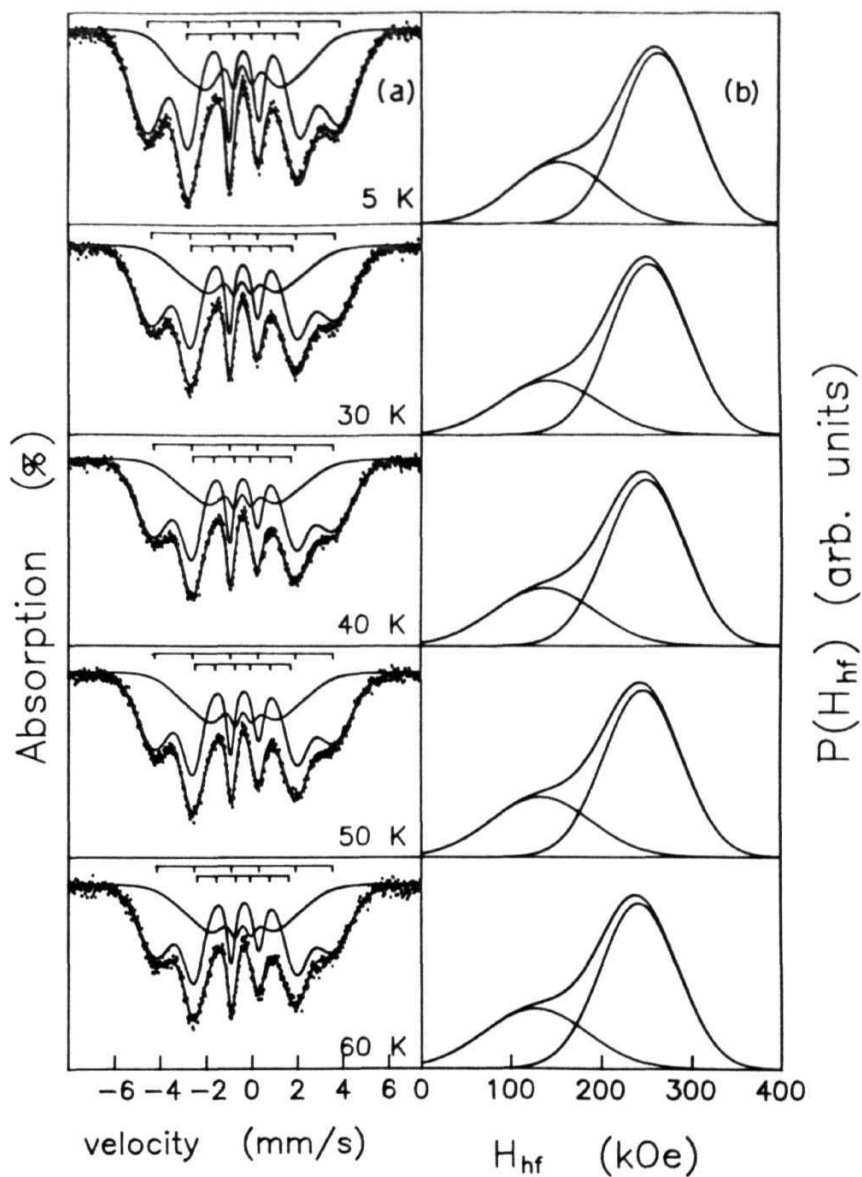


Fig. 3.19. (a) Mössbauer spectra at a few representative temperatures together with the best two-Gaussian fits and the sub-spectra sextets of Lorentzian lineshape for α -Fe-Zr. (b) The corresponding component Gaussian distributions and their resultant distribution.

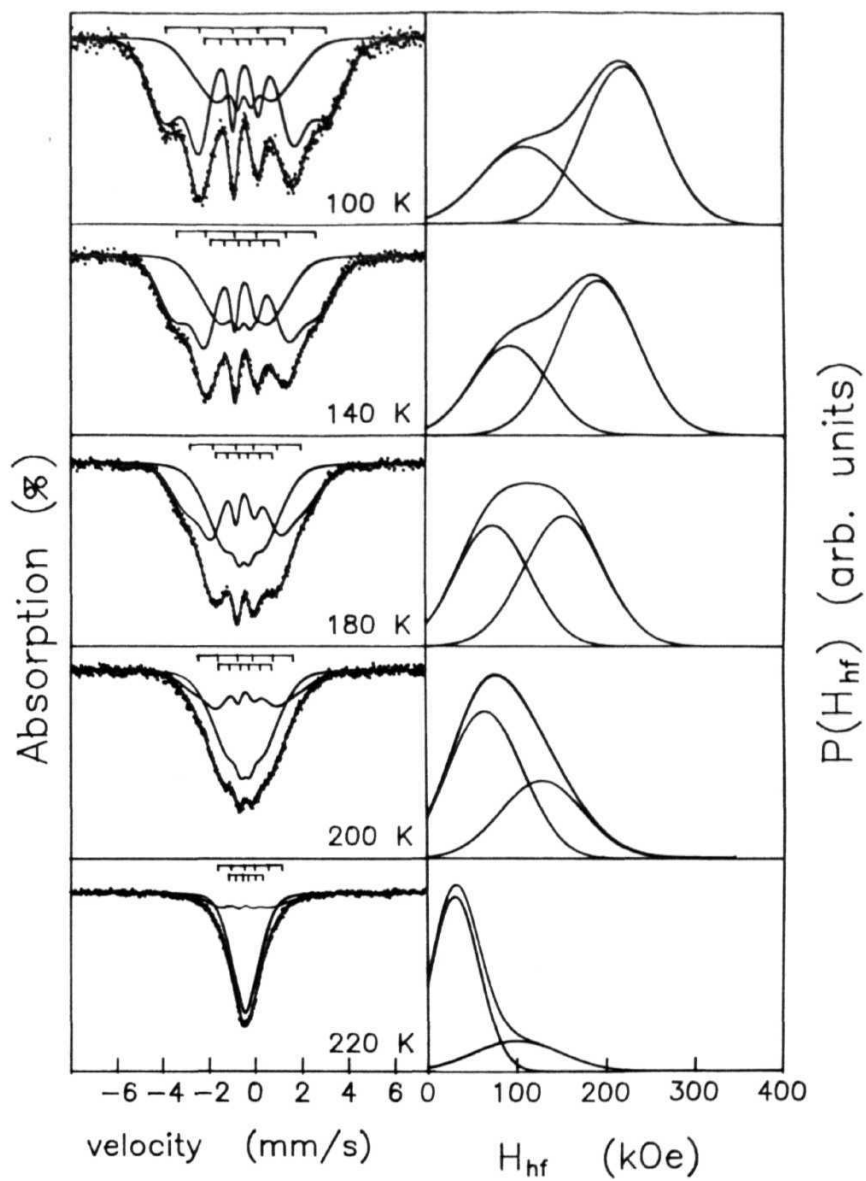


Fig. 3.19. Continued.

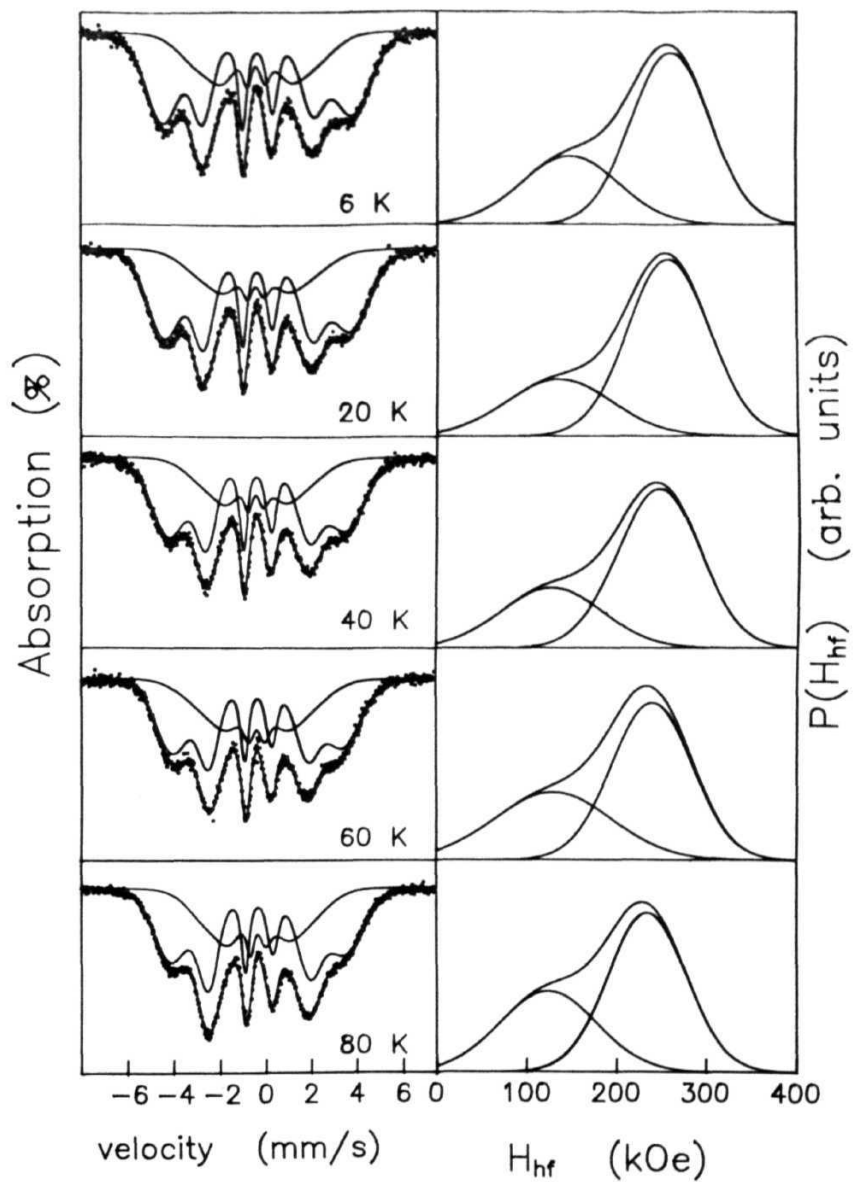


Fig. 3.20. ME spectra at a few representative temperatures along with their corresponding $P(H_{\text{hf}})$ (deduced by the TP fit method) for $\alpha\text{-Fe}_{91}\text{Zr}_9$.

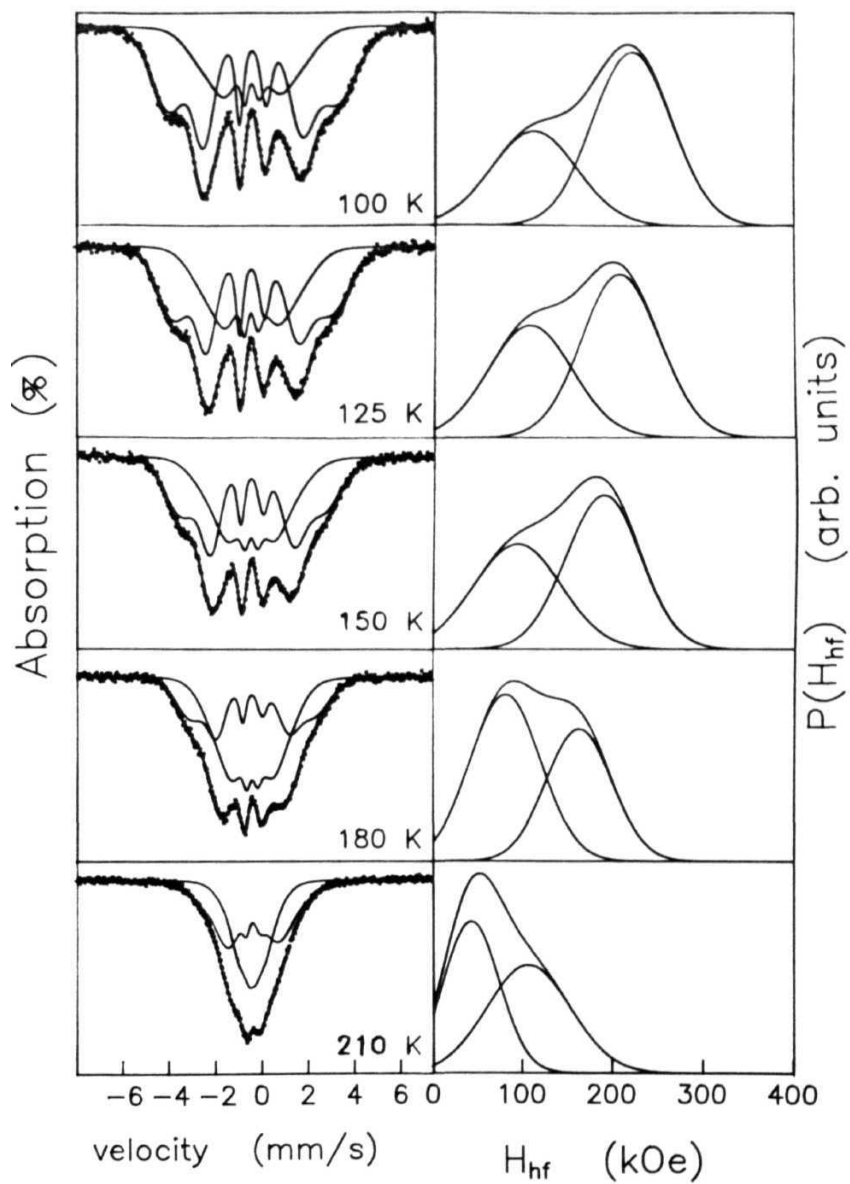


Fig. 3.20. Continued.

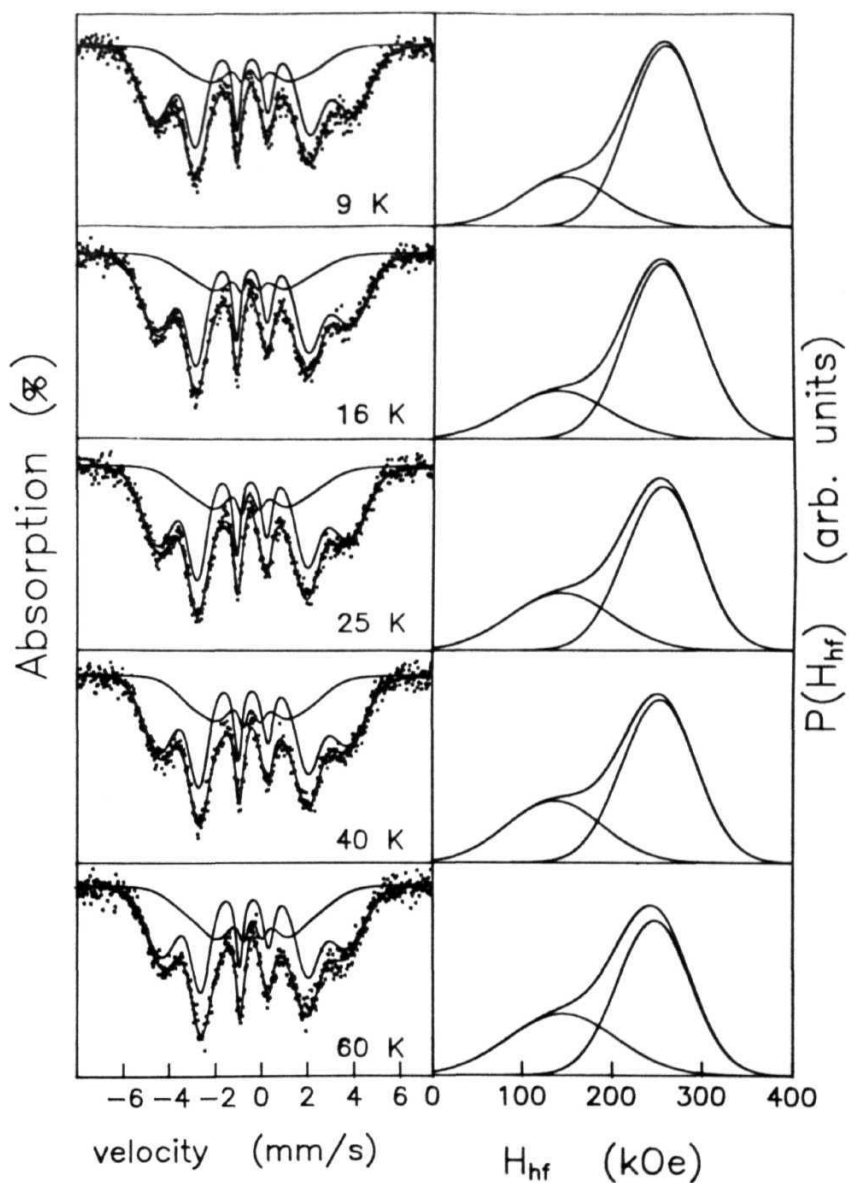


Fig. 3.21. ME spectra at a few representative temperatures along with their corresponding $P(H_{\text{hf}})$ (deduced by the TP fit method) for $\alpha\text{-Fe}_{89}\text{Co}_1\text{Zr}_{10}$.

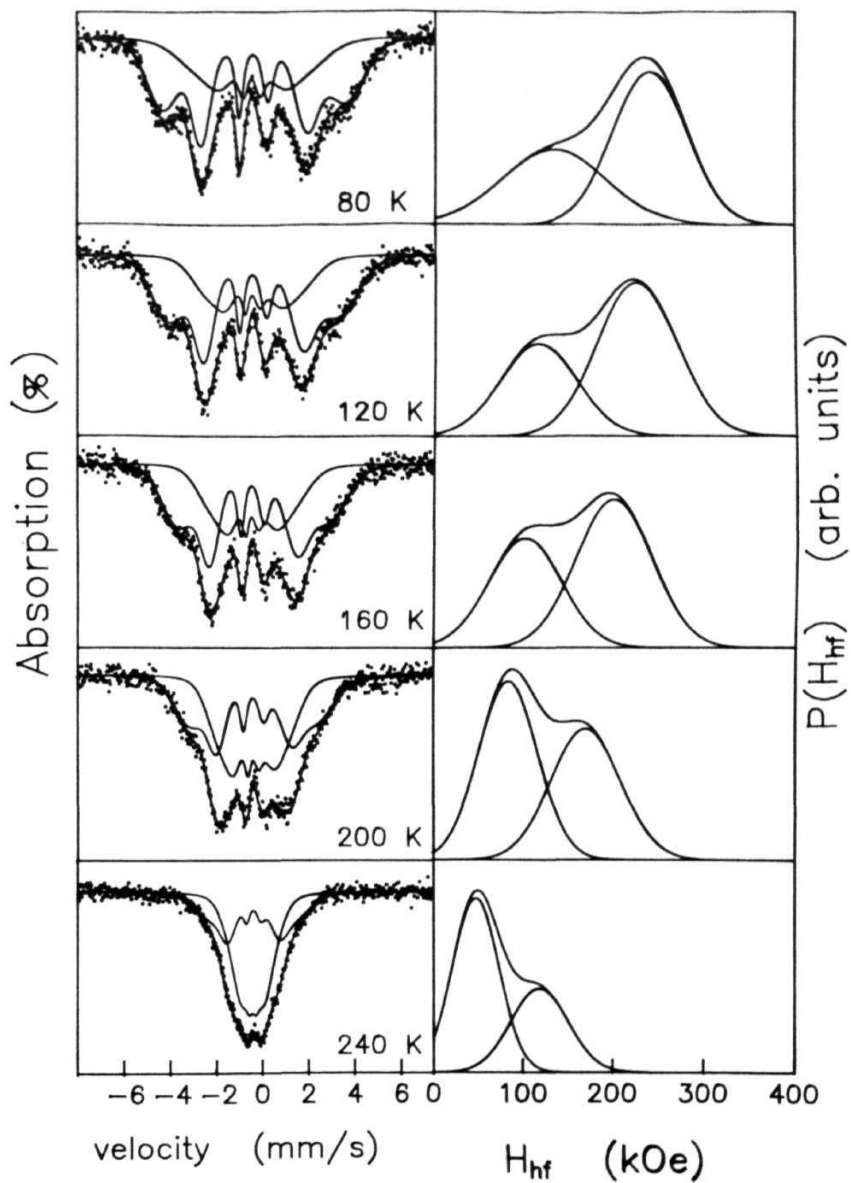


Fig. 3.21. Continued.

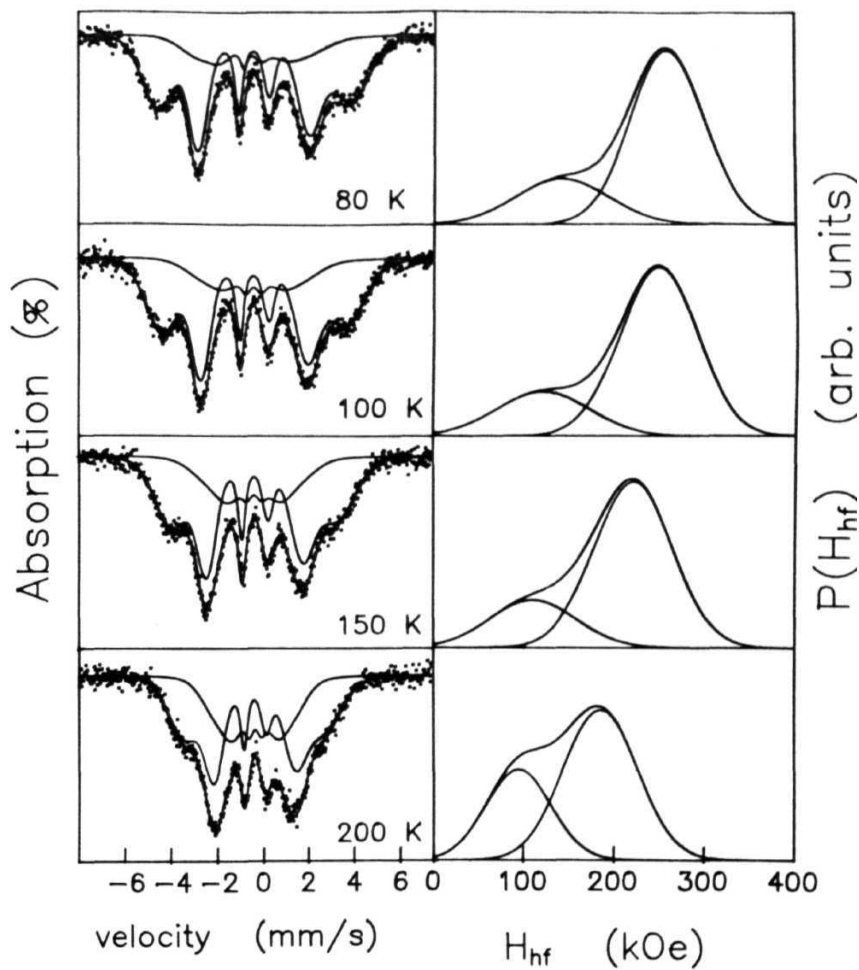


Fig. 3.22. ME spectra at a few representative temperatures along with their corresponding $P(H_{\text{hf}})$ (deduced by the TP fit method) for $a\text{-Fe}_{88}\text{Co}_2\text{Zr}_{10}$.

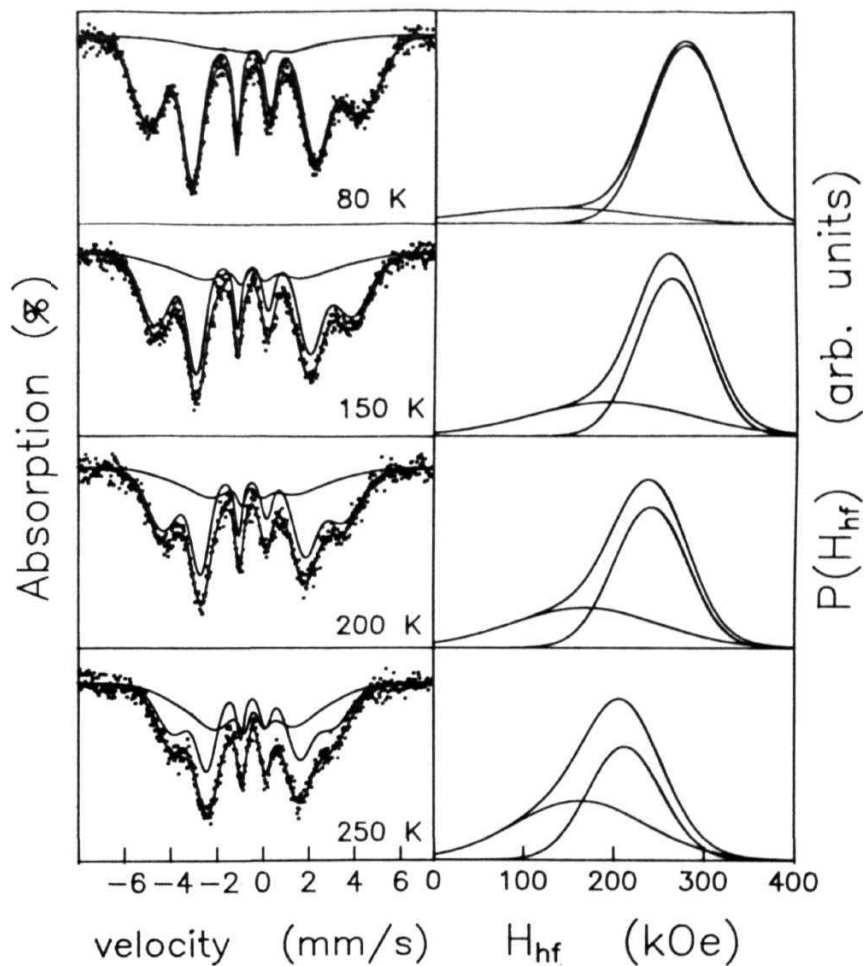


Fig. 3.23. ME spectra at a few representative temperatures along with their corresponding $P(H_{\text{hf}})$ (deduced by the TP fit method) for $\alpha\text{-Fe}_{84}\text{Co}_6\text{Zr}_{10}$.

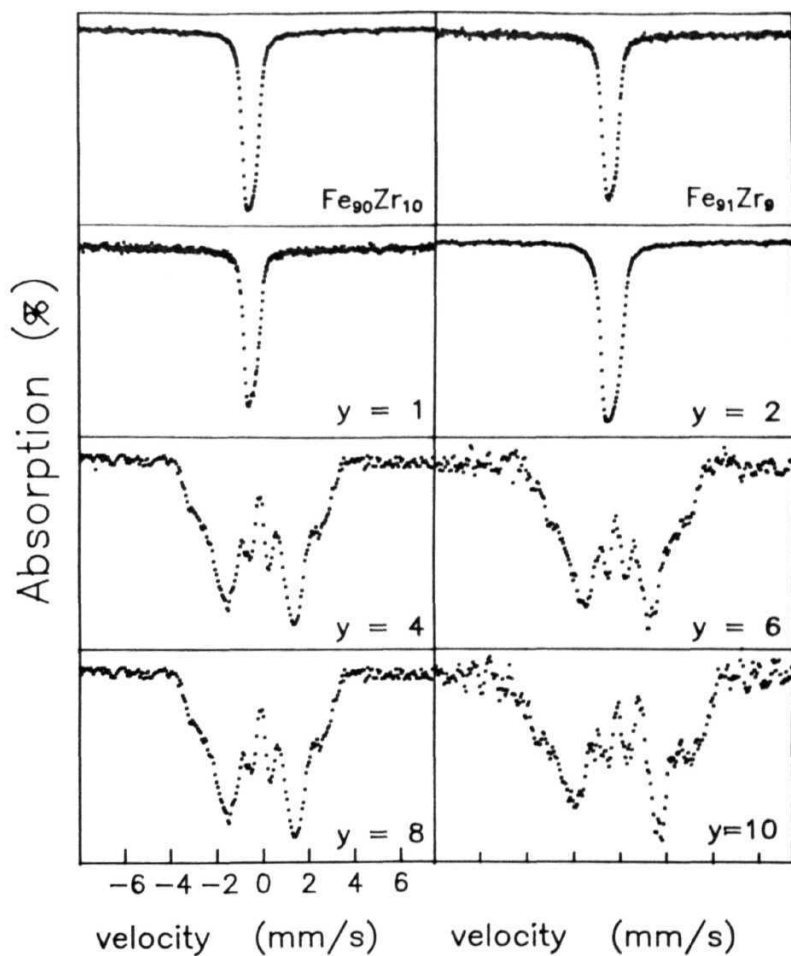


Fig. 3.24. Room temperature ME spectra for $\alpha\text{-Fe}_9\text{CoZr}_{10}$ alloys with $0 \leq y \leq 10$.

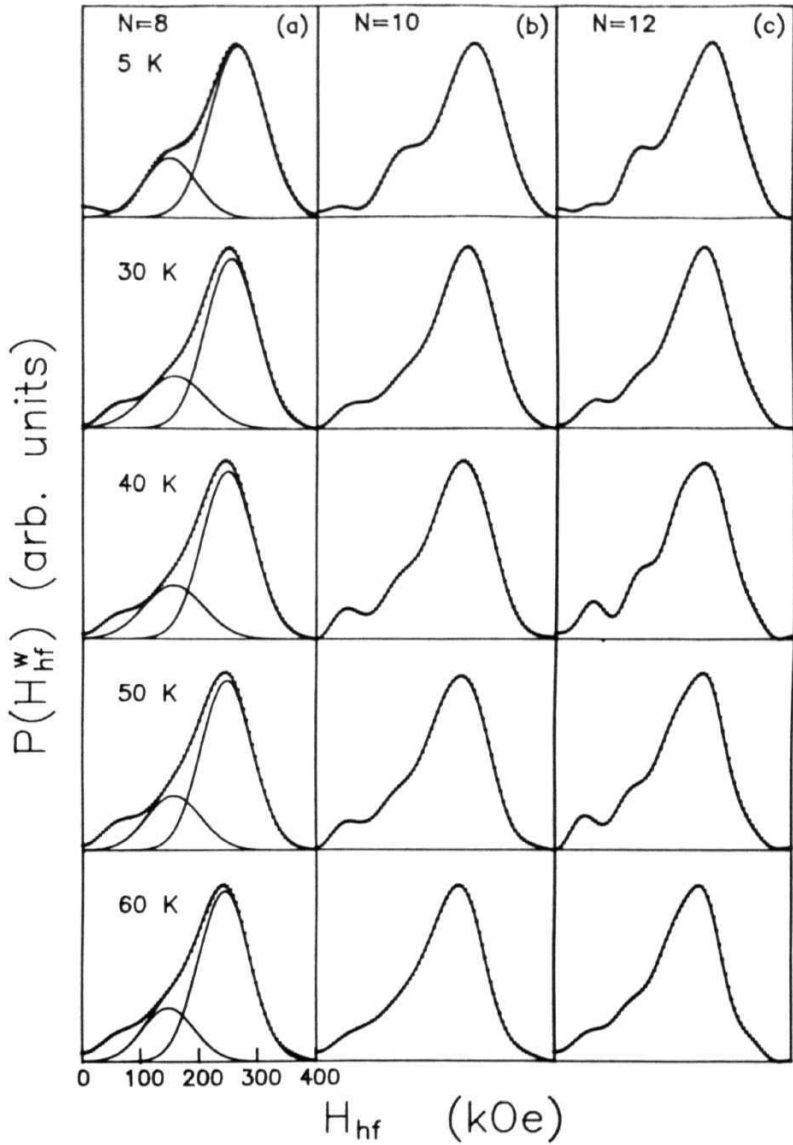


Fig. 3.25. $P(H_{hf}^w)$ versus H_{hf} curves determined by the Window method for (a) $N=8$, (b) $N=10$ and (c) $N=12$ for $\alpha\text{-Fe}_{90}\text{Zr}_{10}$. The two-Gaussian fits to the $P(H_{hf}^w)$ vs. H_{hf} curves are also shown by the continuous curves in part (a) of the figure.

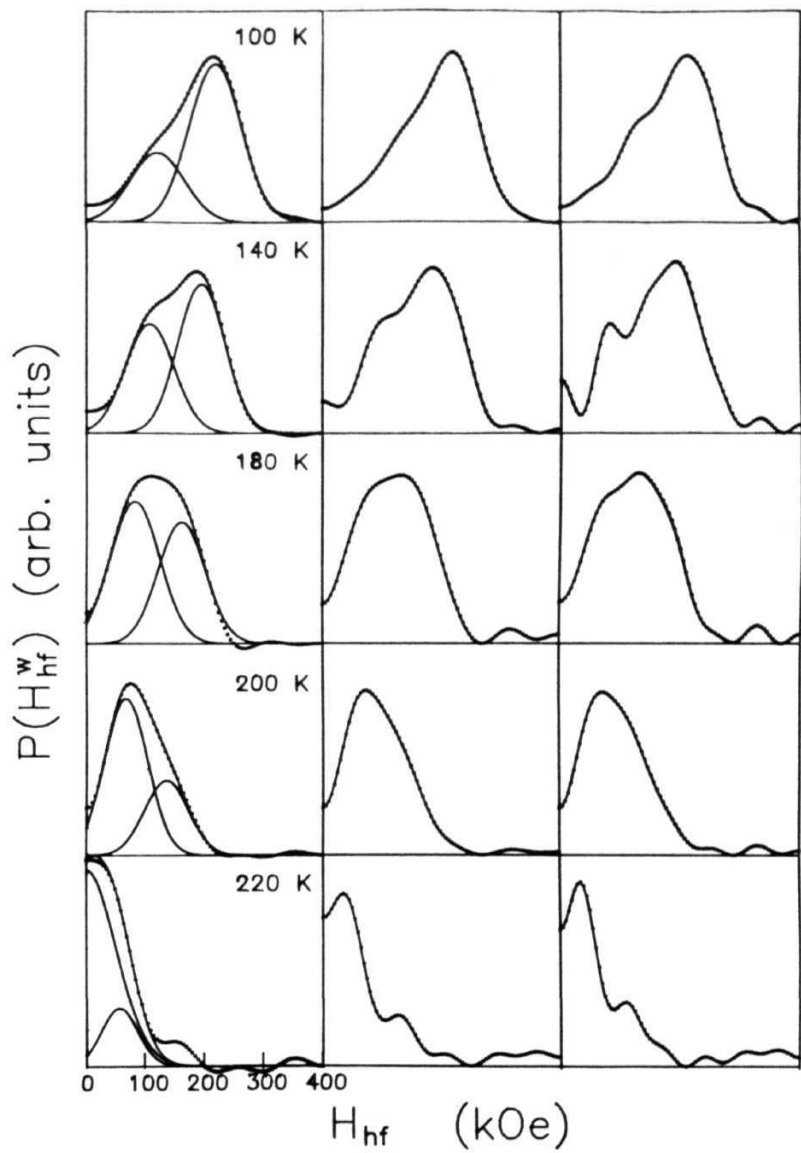


Fig. 3.25. Continued.

a-Fe₉Zr for **N=8**, 10 and 12. An attempt was made to fit the $P(H_{\text{f}}^{\text{W}})$ for **N=8** to the sum of two Gaussian distributions and the outcome of this exercise is depicted in the above figure by continuous curves.

The optimum values of the Mossbauer parameters, isomer shift, δ^{W} , FWHM linewidth, Γ^{W} , intensity ratio, b^{W} , correlation coefficient between the isomer shift and hyperfine field, a^{W} and $\bar{H}_{\text{hf}}^{\text{W}}$

the average hyperfine field, which have been deduced from the Window analysis (the superscript W denotes the Window method) are depicted in Fig. 3.26 as a function of temperature for **a-Fe₉Zr** for **N=8**, 10 and 12. The values of all the parameters so obtained were found to be insensitive to the value of N in the interval 8

W

$8 \leq N \leq 12$ but $P(H_{\text{hf}}^{\text{W}})$ undergoes pronounced changes in that a specious structure develops at low fields due to statistical scatter in the spectrum. Fig. 3.27 shows the same Mössbauer parameters, i.e., isomer shifts, δ^{CL} and δ^{FM} , FWHM linewidth, Γ^{CL} and Γ^{FM} , intensity ratios, b and b , correlation coefficients between isomer shift and hyperfine field, α^{CL} and \bar{a}^{FM} and the average $\bar{H}_{\text{hf}}^{\text{TP}}$

hyperfine field H_{f} and the most probable hyperfine fields corresponding to the two Gaussian components, H_{f}^{CL} and $H_{\text{hf}}^{\text{FM}}$ as functions of temperature for each of the two independent subspectra deduced from the TP analysis for **a-Fe₉₀Zr₁₀**. The superscripts CL and FM denote clusters and FM matrix, respectively, referred to earlier (Section 1.6) in connection with the infinite FM matrix plus finite clusters model.

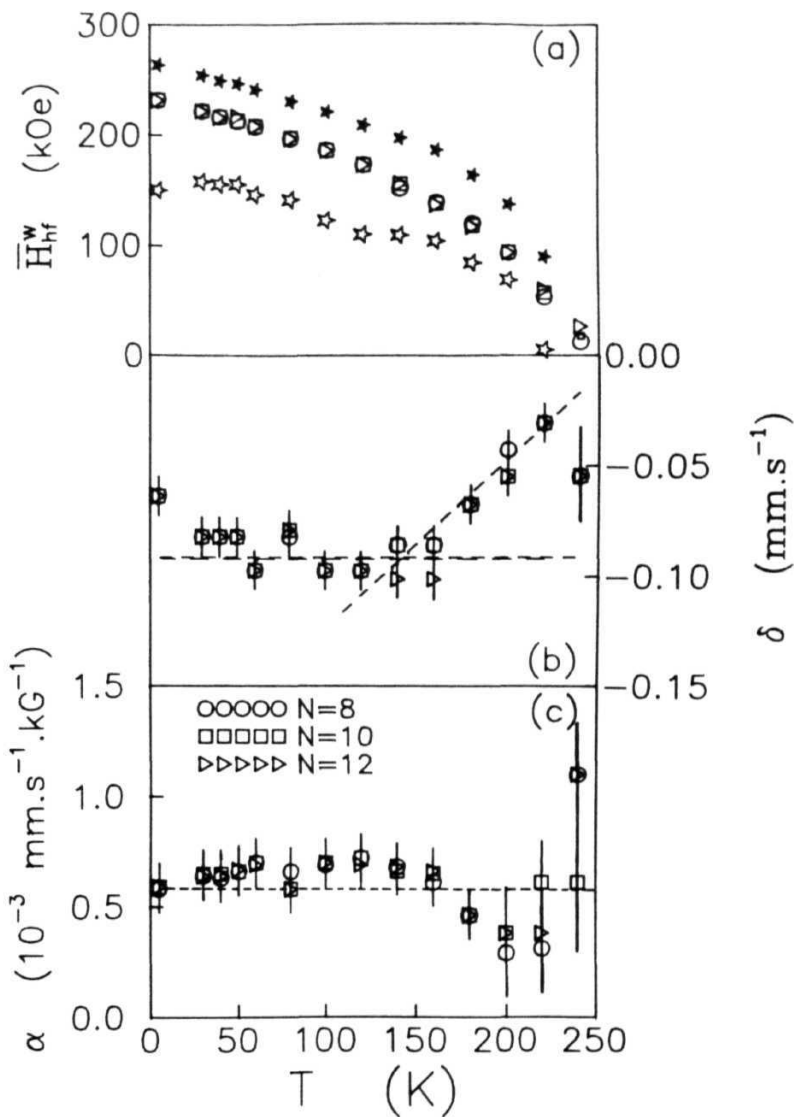


Fig. 3.26. Temperature dependence of the Mössbauer parameters deduced from the Window analysis for $N=8$, 10 and 12 for

$\alpha\text{-Fe}_{90}\text{Zr}_{10}$.

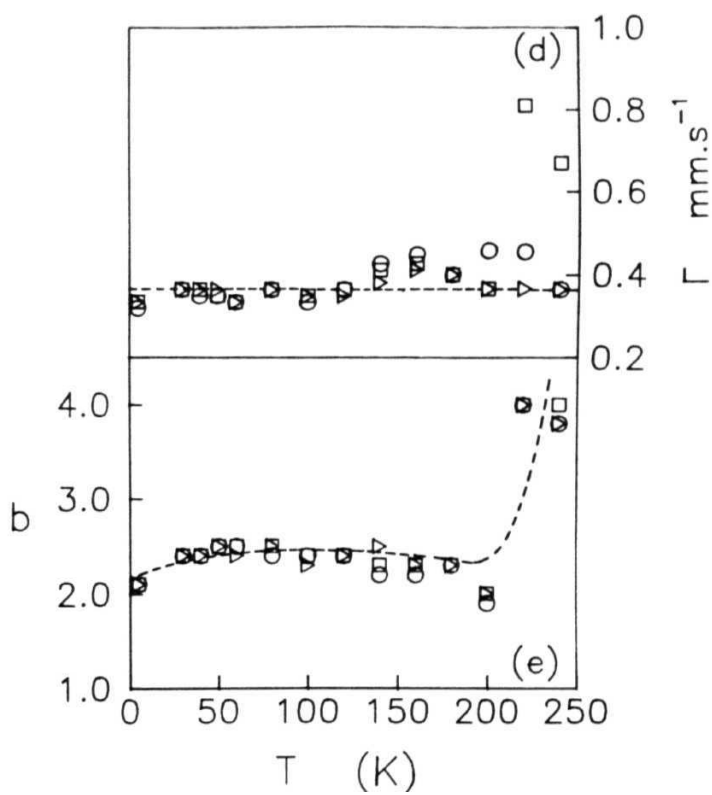


Fig. 3.26. Continued.

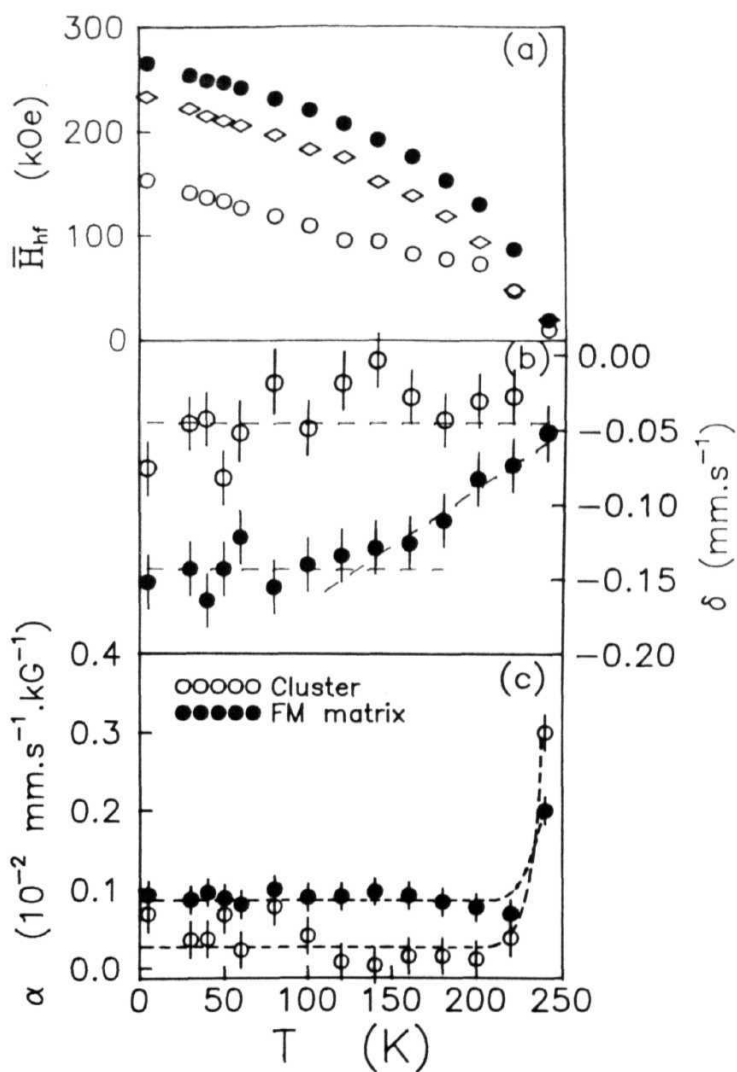


Fig. 3.27. Temperature dependence of the Mossbauer parameters deduced from the TP analysis for $a\text{-Fe}_{90}\text{Zr}_{10}$.

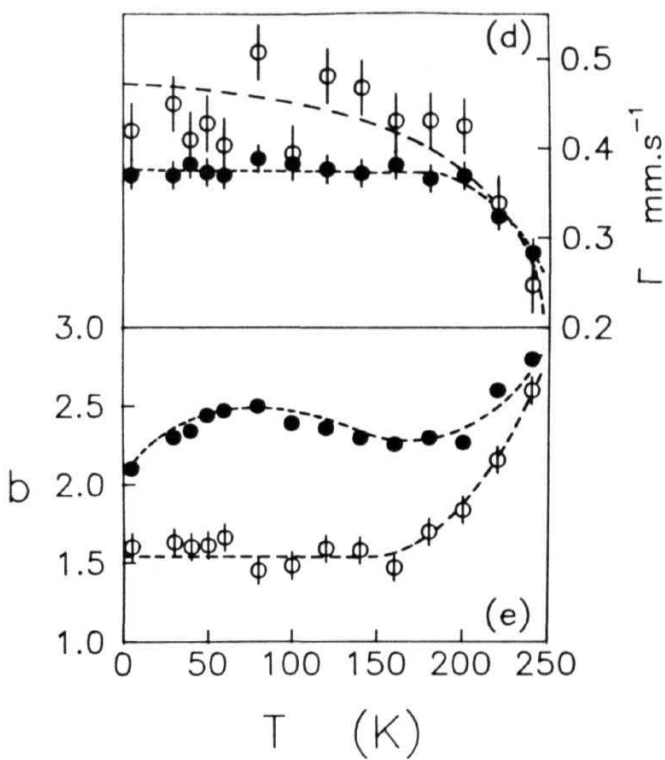


Fig. 3.27. Continued.

REFERENCES

- [1] S.M. Bhagat, S. Haraldson and O. **Beckman**, J. Phys. Chem. Solids 38, 593 (1977) .
- [2] B. Heinrich, J.M. Rudd, **K.** Urquhart, K. Myrtle, J.F. Cochran and R. Hasegawa, J. **Appl.** Phys. 55, 1814 (1984).
- [3] S.M. Bhagat, D.J. Webb and M.A. **Manheimer**, J. Magn. Magn. Mater. 53, 209 (1985).
- [4] M.J. Park, S.M. Bhagat, M.A. **Manheimer** and K. Moorjani, J. Magn. Magn. Mater. 59, 287 (1986).
- [5] L. Kraus, Z. Frait and J. Schneider, Phys. Stat. Solidi (a) 63, 669 (1981).
- [6] B. Heinrich, J.F. Cochran and R. Hasegawa, J. Appl. Phys. 57, 3690 (1985).
- [7] J.F. Cochran, R.W. Qiao and B. Heinrich, Phys. Rev. B39, 4399 (1988).
- [8] D.J. Webb and S.M. Bhagat, J. Magn. Magn. Mater. **42**, 109 (1984).
- [9] P. Deppe, K. **Fukamichi**, F.S. Li, M. Rosenberg and M. Sostarich, IEEE Trans. Magn. **MAG-20**, 1367 (1984) .
- [10] S.N. **Kaul**, Phys. Rev. B27, 6923 (1983).
- [11] H. Tange, K. **Inone** and K. Shirakawa, J. Magn. Magn. Mater. **54-57**, 303 (1986).
- [12] C.L. Chien and R. Hasegawa, Phys. Rev. **B16**, 3024 (1977).
- [13] C.L. Chien and H.S. Chen, J. Phys. (Paris) Colloq. **40**, C2-118 (1979).
- [14] T.E. Sharon and C.C. Tsuei, Solid State **Commun.** 9, 1923 (1971).

- [15] T.E. Sharon and **C.C.** Tsuei, Phys. Rev. B5, 1047 (1972).
- [16] J. Logan and E. Sun, J. Non-Cryst. Solids. 20, 285 (1976)
- [17] B. Window, J. Phys. E4. 401 (1971).
- [18] J. Hesse and A. Rubartsch, J. Phys. **E7**, 526 (1974).
- [19] G. **LeCâer** and J.M. Dubois, J. Phys. E12, 1083 (1979).
- [20] I. Vincze, Solid State Commun. 25, 689 (1978).
- [21] H. Keller, J. **Appl.** Phys. 52, 52 68 (1981).

CHAPTER - IV

SECTION - A

FERROMAGNETIC RESONANCE

4.1. Resonance fields

Before embarking on a discussion of the **FMR results**, the main observations regarding the FMR spectra are recalled. It was observed that the FMR spectra for temperatures $T < T_C$ consist of a single primary resonance which shifts to higher fields and broadens as temperature is increased. Apart from this resonance, a secondary resonance at a lower field value (≈ 800 Oe) appears at $T \approx T_C$, which gets well-resolved for temperatures $T > T_C + 10K$.

4.1.1. *Temperatures around and above Curie point*

Primary resonance

The nature of the paramagnetic (PM) to ferromagnetic (FM) phase transition in **a-Fe_{100-x}Zr_x alloys with $x \ll 10$ at. %** (Section 1.7) and **a-Fe₉₀CoZr₁₀ alloys with $0 \leq y \leq 6$** has been one of the most controversial topics in amorphous magnetism in the recent years. The values of the critical exponents for spontaneous magnetization, M , initial susceptibility, χ_0 , and critical isotherm, i.e. β , ν and δ , deduced from bulk magnetization (BM) measurements in the critical region [1,2] were roughly 1.4 times larger than the renormalization group estimates [3] for an isotropic nearest-neighbour (NN) three-dimensional (3D) Heisenberg **ferromagnet**. In addition, these exponents either satisfy [2] or do not satisfy [1] the **Widom** scaling relation, $\beta\delta = \beta + \gamma$, and their anomalously

large values were taken to reflect a large fluctuation in the exchange interaction. A subsequent analysis of BM data and also a reanalysis [4] of the published data [1,5] on $\text{a-Fe}_{100-x}\text{Zr}_x$ alloys revealed that the exponents β , γ and 6 possess values that are fairly close to 3D NN Heisenberg values. This result is in direct contradiction with the earlier finding which quotes **anomalously** large values for the critical **exponents**. Hence, a detailed study of the critical behaviour in these alloys is called for.

In the present study, the exponents β and γ , which characterize the **FM-PM** phase transition at the Curie temperature, T_C , for $\text{a-Fe}_{90+x}\text{Zr}_{10-x}$ and $\text{a-Fe}_{90-y}\text{Co}_y\text{Zr}_{10}$ alloys have been determined by using the **FMR** technique. This technique has been previously used to determine the critical exponents for some of the concentrations in the above-mentioned alloys series [6]. The additional feature in the present study is that the concentration range has been extended, an attempt has been made to approach the Curie temperature closer than in previous experiments [6] and measurements have been taken at much closer temperature intervals with a view to arrive at reliable estimates for the critical exponents and amplitudes. Values of saturation magnetization, M , have been determined to a high precision from the lineshape analysis as described in Section 2.2. The lineshape analysis reveals that the LLG equation of motion for magnetization adequately describes **the** resonant behaviour in the critical region and also that g has a **temperature-independent** and concentration-independent value of 2.07 ± 0.02 within the investigated temperature and concentration range. Similar observations, i.e., the LLG equation adequately describes the behaviour of resonance field, $H_{\text{res}}(T)$, and the line-

width, $AH(T)$, in the critical region, have also been made on crystalline **ferromagnets** [7]. Fig. 3.14 shows the variation of M_s with temperature for $a\text{-Fe}_{90+x}\text{Zr}_{10-x}$ and $a\text{-Fe}_{90-y}\text{Co}_y\text{Zr}_{10}$ alloys. Earlier studies on $a\text{-Fe}_{90-y}\text{Co}_y\text{Zr}_{10}$ alloys have demonstrated that the $M(T)$ values deduced from the lineshape analysis are in good agreement with the values of $M(T)$ deduced from **BM** measurements performed at an external magnetic field whose strength is comparable to H_{res} . Thus, $M(H_{res}, T)$ is identified with $M(H, T)$ and H_{res} with the ordering field H conjugate to M . The magnetic or scaling equation of state (SES), **defined** as

$$m = f_{\pm}(h), \quad (4.1)$$

where $m \equiv M/|c|^P$ and $h \equiv H/|c|^P$ are the scaled magnetization and scaled field, respectively, and $c \equiv (T - T_C)/T_C$ while the plus and minus signs refer to temperatures above and below T_C , is then used to arrive at the correct choice of β and γ and of the Curie temperature, T_C which makes the $M(H, T)$ data in the critical region to fall on two universal curves, f_- for $c < 0$ and f_+ for $c > 0$ in an m vs h plot. The choice of the parameters β , γ and T_C for an optimum collapse of the data onto the two universal curves, however, depends sensitively on the temperature range used for the fit and is, **therefore**, not **unique**. Hence, a **range-of-fit** SES analysis is used wherein the range of temperatures in an m vs h plot is progressively narrowed down by excluding more and **more** of the data taken at temperatures far away from T_C **from** the analysis so that the values of exponents β and r become increasingly sensitive to **the choice of T_C and even a** slight deviation of the exponent values from the correct choice results in a strong departure of

the data from the curves $f_-(h)$ and $f_+(h)$. The asymptotic values of the exponents are obtained only when they become stable against further reduction in the range of c . Fig. 4.1 shows the $\ln m$ vs $\ln h$ scaling plot for $a\text{-Fe}_{90+x}\text{Zr}_{10-x}$ alloys with the corresponding values of the exponents β and γ and of T_C .

Critical exponents alone do not fully characterize the critical behaviour near the FM-PM transition, but do so only in association with the corresponding critical amplitudes. Therefore, a complete understanding of the critical behaviour at T_C is achieved only when the values of the critical exponents together with the critical amplitudes are determined. The values of the critical amplitudes are extremely sensitive to the choice of T_C and hence, a very high accuracy in the determination of T_C is called for. When a double-logarithmic plot of the type shown in Fig. 4.1, is used to determine the values of the exponents and T_C , the values so obtained may not be accurate enough as small deviations of the data from the universal $f_-(h)$ and $f_+(h)$ curves are covered up due to the insensitive nature of the log-log scale. A more rigorous method of analysis that gets rid of these ambiguities and determines more accurately the values of the exponents and T_C , is based on the SES form

$$m^2 = +a_{\pm} + b_{\pm}(h/m) \quad (4.2)$$

where the plus and minus signs as well as h and m have the same meaning as in Eq. (4.1). In an m^2 -vs- h/m plot, slight deviations, which escape detection in a $\ln m$ vs. $\ln h$ plot, can be discerned with ease. In view of the definitions

$$M_S(e) = \lim_{H \rightarrow 0} M(H, e) = m_0 (-e)^{\beta}, \quad e < 0 \quad (4.3)$$

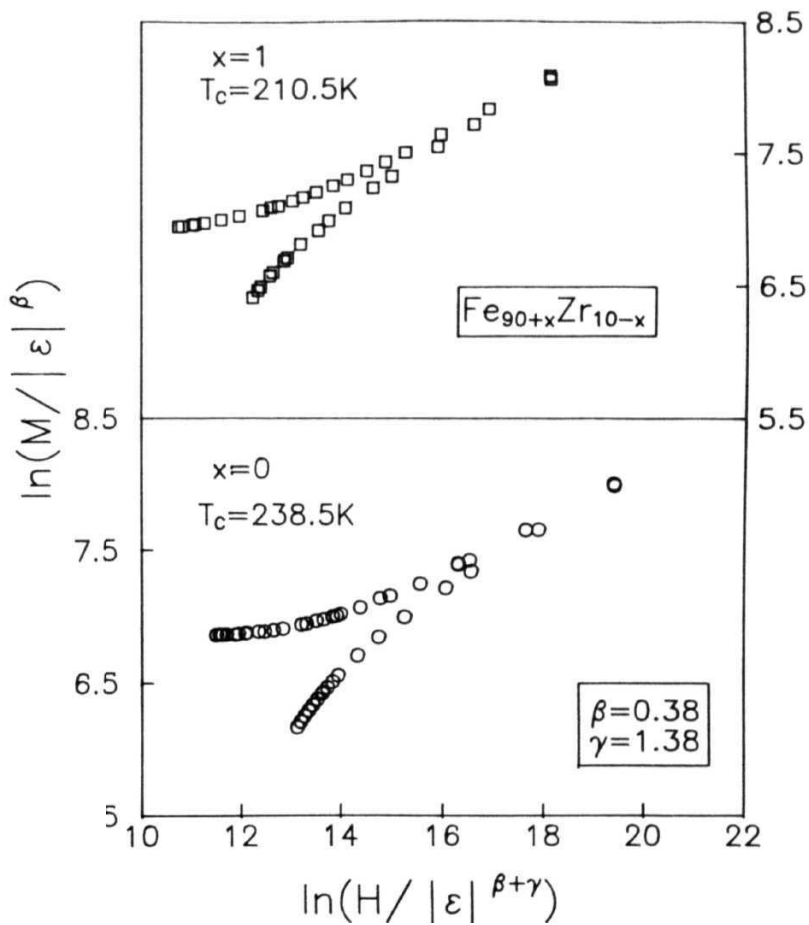


Fig. 4.1. Plot of $\ln(M/|\epsilon|^\beta)$ against $\ln(H/|\epsilon|^{\beta+\gamma})$ for $a-Fe_{90+x}Zr_{10-x}$.

and

$$\chi_0^{-1}(\epsilon) = \left[\left| \frac{\partial M(H, \epsilon)}{\partial H} \right|_{H=0} \right]^{-1} = (h_0/m_0) \epsilon^\gamma, \quad \epsilon > 0 \quad (4.4)$$

the coefficients in Eq. (4.2) can be related to the critical amplitudes m_0 and h/m as

$$a_-^{1/2} = m_0 \quad (4.5a)$$

and

$$a_+/b_+ = h_0/m_0 \quad (4.5b)$$

The intercepts of the universal curves with the m and h/m axes in a m -vs- h/m plot, therefore, give the critical amplitudes m_0 and h_0/m_0 , respectively. Such m^2 -vs- h/m plots for $a\text{-Fe}_{90+x}\text{Zr}_{10-x}$ and $a\text{-Fe-Co-Zr}$ are depicted in Figs. 4.2 and 4.3. Fig. 4.4 shows the same data plotted for $a\text{-Fe}_{88}\text{Co}_2\text{Zr}_{10}$ as those in Fig. 4.3 on a sensitive scale with a view to bring out clearly the values of m_0^2 and h_0/m_0 as intercepts on the m and h/m axes clearly. The values of the critical exponents and the amplitudes and the Curie temperatures deduced from the range-of-fit SES analysis method described above are tabulated in Table 4.1. It is observed from Figs. 4.2 and 4.3 that the experimental data fall on the universal curves without any appreciable deviations even at low fields and this implies that the values of the critical exponents and T_C are reasonably accurate. Also listed in Table 4.1 is the ratio $\mu_0 h_0 / k_B T_C$ which, along with the exponent values, is compared with the theoretical values predicted for an isotropic 3D NN Heisenberg ferromagnet. It is observed that, while the experimental values of the

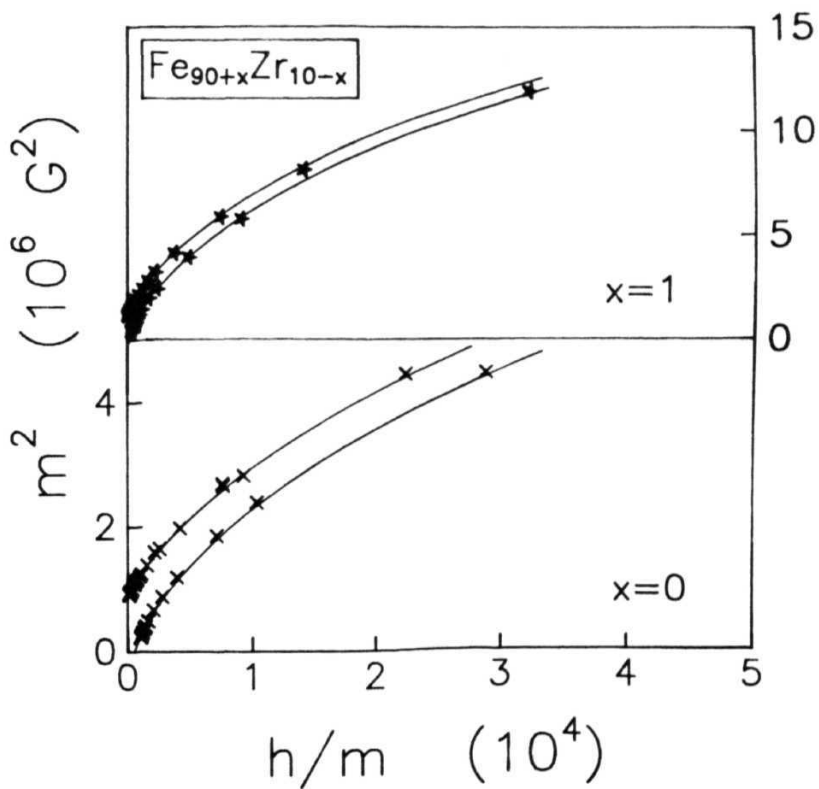


Fig. 4.2. m^2 -vs- h/m plot for $a\text{-Fe}_{90+x}\text{Zr}_{10-x}$ alloys constructed using the M data deduced from the FMR spectra recorded at different temperatures in the critical region.

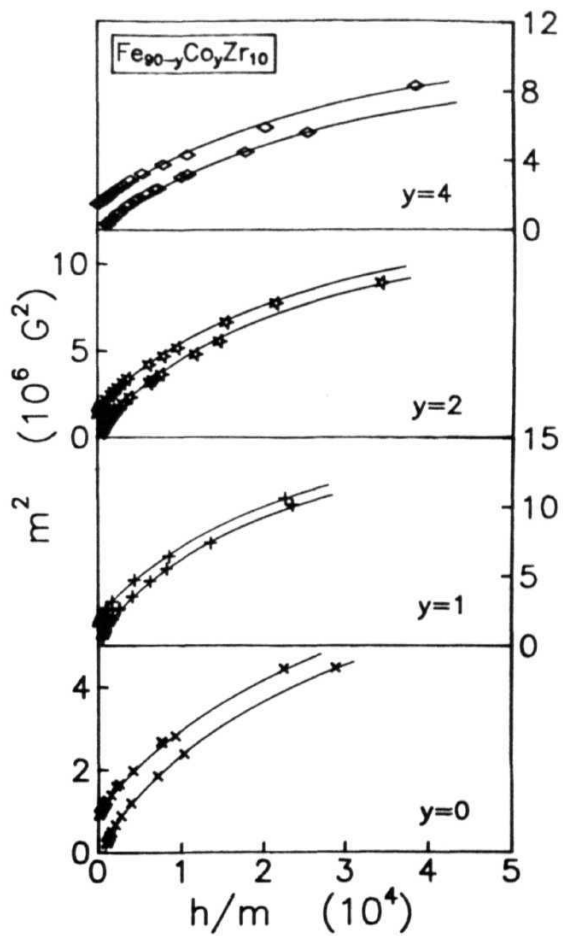


Fig. 4.3. m -vs- h/m plot for $\text{a-Fe}_{90}\text{Co}_y\text{Zr}_{10}$ alloys constructed using the M data deduced from the FMR spectra recorded at different temperatures in the critical region.

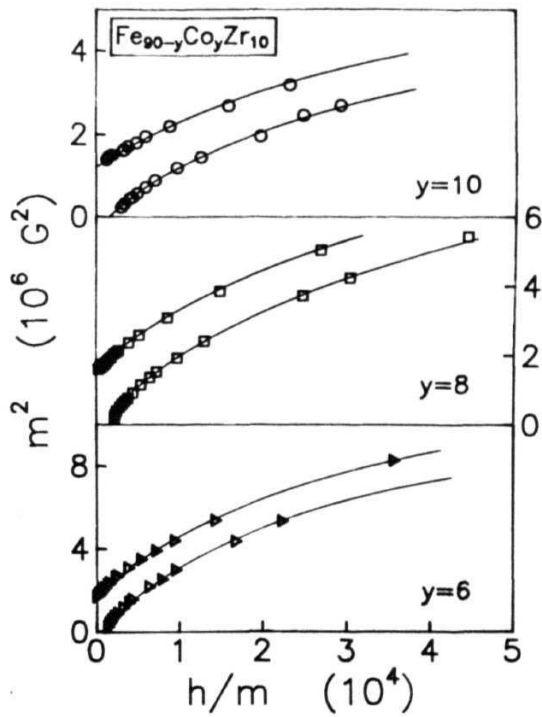


Fig. 4.3. Continued.

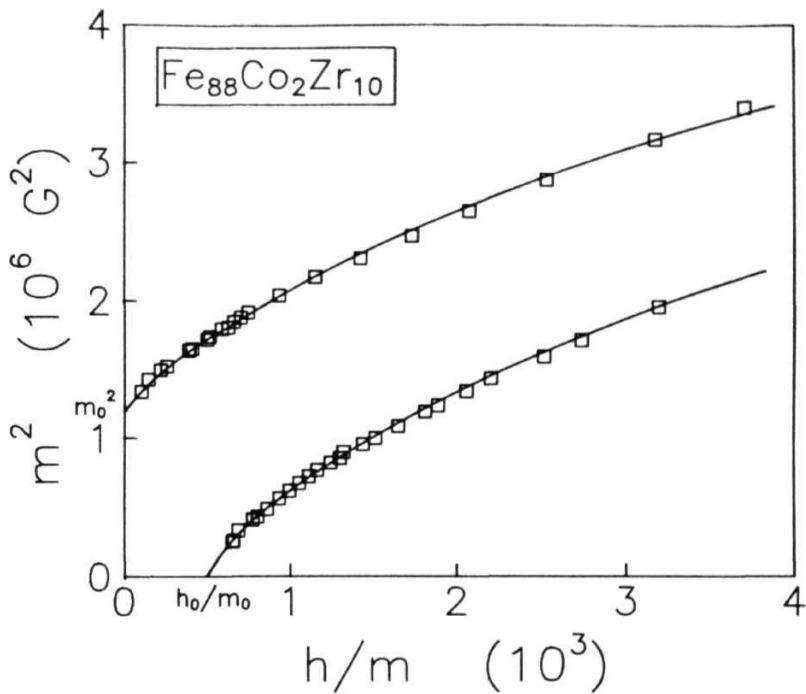


Fig. 4.4 Data near the origin for $\alpha\text{-Fe}_{88}\text{Co}_2\text{Zr}_{10}$ in Fig. 4.3 plotted on a sensitive scale with a view to bring out the values of the intercepts m_0^2 and h_0/m_0 on m and h/m axes clearly.

exponents are in close **agreement** with the theoretically predicted values, the observed value of the ratio $\mu_0 h_0 / k_B T_C$ is smaller than the theoretical value by an order of magnitude for all the alloy compositions. If h_0 is presumed to be an effective exchange interaction field and μ_{ff} is the average effective elementary moment involved in the FM-PM transition, then their product $\mu_{eff} h_0$, i.e., the effective exchange energy, is expected to equal the thermal energy at $T=T_C$, i.e., $k_B T_C$. From Table 4.1, it is obvious that unless μ_{eff} is taken to be much larger than μ_0 , this relation cannot be satisfied. Hence, in order that the ratio $\frac{\mu_0 h_0}{\mu_{eff} k_B T_C}$ equals the 3D Heisenberg value of 1.58, μ_{ff} assumes the values listed in Table 4.1. Also, the concentration of such effective moments is $c = \mu_0 / \mu_{ff}$. The values of c so computed and shown in Table 4.1, strongly indicate that only a small fraction of moments participates in the FM-PM phase transition. According to an earlier finding [2], the critical exponents assume smaller values with increasing Co content but they are still far greater than the 3D Heisenberg estimates. In contradiction with this result, the exponents β and r *do not depend* on the alloy composition and possess 3D **Heisenberg-like** values. This implies that the transition at T_C is well-defined and quenched disorder does not alter the critical behaviour of the pure spin system with specific heat critical exponent $\alpha < 0$, in accordance with the well-known Harris criterion. The Curie temperature, T_C , increases linearly with Co concentration as previously reported [8] for **a-Fe₉₀-Co Zr₀** alloys, presumably due to the fact that the partial replacement of Fe with Co brings into play the strongly ferromagnetic Fe-Co and Co-Co exchange interactions at the expense of *competing* Fe-Fe exchange

Table 4.1. Values for the parameters that characterize the critical behaviour near the FM-PM phase transition in a- $\text{Fe}_{90-y}\text{Co}_y\text{Zr}_{10}$ alloys and a comparison between the experimentally determined and theoretically predicted values for the critical exponents β and γ and for the universal critical amplitude ratio $\mu_0 h_0/k_B T_C$. The number in the parentheses denotes the least significant figure.

Alloy concentration (y)	T_C (K)	β	γ	m_0 (G)	h_0/m_0	h_0 (10^5 G)	μ_0 (μ_B)	$\frac{\mu_0 h_0}{k_B T_C}$	μ_{eff} (μ_B)	c (%)
0	238.50(15)	0.380(30)	1.38(5)	908(40)	519(50)	4.7(6)	1.311	0.174(15)	11.9(20)	11.0(10)
1	254.50(15)	0.380(30)	1.38(5)	1095(30)	419(50)	4.6(6)	1.368	0.166(20)	13.0(15)	10.5(15)
2	283.50(20)	0.380(20)	1.39(3)	1095(30)	450(50)	4.9(4)	1.385	0.161(30)	13.6(10)	10.2(15)
4	335.00(20)	0.390(20)	1.38(5)	1095(30)	700(50)	7.7(6)	1.365	0.209(20)	10.3(15)	13.2(12)
6	376.50(15)	0.380(30)	1.38(5)	1264(20)	950(50)	12.0(8)	1.423	0.303(20)	7.4(16)	19.2(15)
8	419.50(15)	0.375(25)	1.38(5)	1204(40)	1200(50)	14.4(8)	1.465	0.337(30)	6.9(18)	21.3(12)
10	462.50(20)	0.380(30)	1.39(5)	1100(40)	2000(50)	21.9(8)	1.532	0.485(25)	5.0(15)	30.7(18)
3D- Heisenberg		0.365(3)	1.386(4)						1.58	

interactions. The concentration dependence of the quantities μ_0 , c , T_C and the Gilbert damping parameter deduced in the critical region is depicted in Fig. 4.5.

From the foregoing text, it is evident that the **FMR** technique can be successfully employed to determine accurately the spontaneous magnetization and initial susceptibility critical exponents β and r , which characterize the **FM-PM** phase transition at T_C .

Secondary resonance

The secondary resonance has been an important and unique finding of the present study. This resonance mode, whose signature is first noticed at $T \approx T_C$ at a lower field value of 800-900 Oe, develops into a full-fledged resonance for $T > T_C + 10K$. In metallic glass ribbons, a finite probability exists for the occurrence of surface crystallization which grows with time due to the relaxation processes. If it happens, the observed resonances would not be representative of the bulk since the dynamic permeability attains its maximum value at the field corresponding to ferromagnetic resonance and the microwave radiation penetrates only a thin surface layer of typically 10 Å [9]. Hence, in order to rule out the possibility that the secondary resonance might just be a surface phenomenon, a series of polishing and etching experiments were performed on the samples for various lengths of time. The etchant used was **nital**, a solution of 10% concentrated anhydrous nitric acid and 90% ethyl alcohol. **FMR** measurements carried out on the alloy compositions before and after etching (polishing) treat-

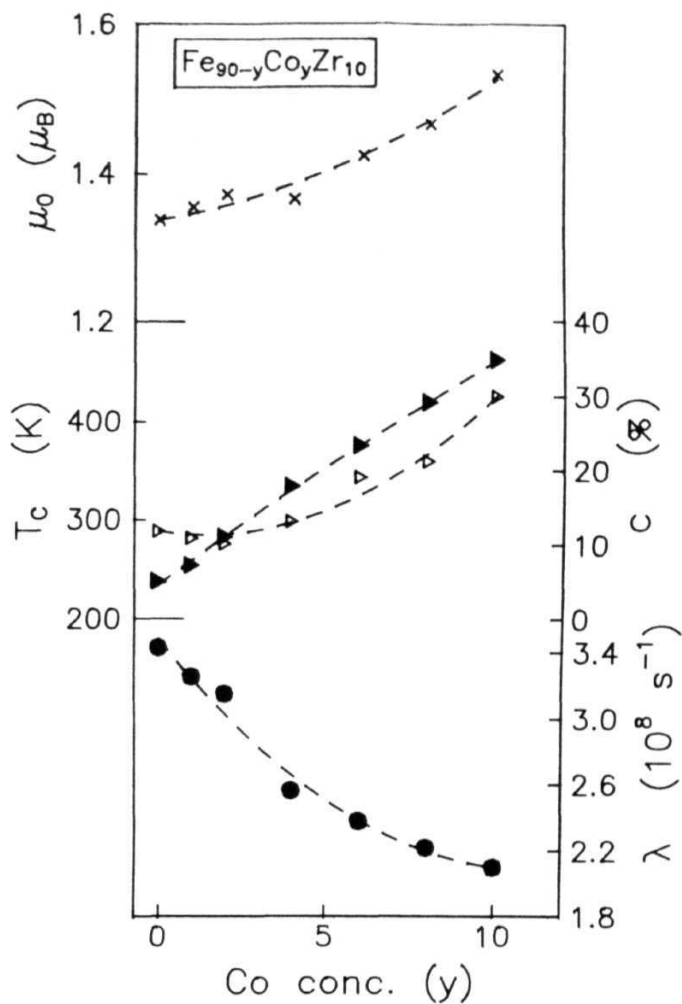


Fig. 4.5. Functional dependences of the magnetic moment per alloy atom at OK, μ_0 , the fraction of spins participating in the FM-PM phase transition, c , Curie temperature, T , and the Gilbert damping parameter, λ , on the Co concentration y for $a-Fe_{90-y}Co_yZr_{10}$ alloys. The dashed curves through the data points serve as a guide to the eye.

ment show that apart from a systematic downward shift in the resonance field versus temperature curve, with etching (or polishing), all the basic features present in the unetched sample are retained. This finding confirms that the secondary resonance originates from the bulk and not from the surface. The possibility of interpreting this resonance as arising from regions of sample that differ slightly in composition is also ruled out since this resonance is observed only for temperatures well above T_C and possesses properties quite different from those of the primary resonance that occurs below T_C . Any attempt to explain the origin of this resonance using the "Wandering-axis ferromagnet" model [10] is bound to prove futile since this model, by definition, precludes development of long-range ferromagnetic order at any temperature. This model can, at best, qualitatively explain some features of this resonance but certainly not the occurrence of this resonance only for temperatures above a certain temperature, T_C , and the existence of another (primary) resonance with properties characteristic of long-range ferromagnetic order. The antiferromagnetic (AFM) clusters plus ferromagnetic Fe-Zr matrix model [11] also fails to explain this resonance as there is no basis for the existence of any resonance above T_C in this model. A detailed appraisal of the results reveals that the infinite 3D ferromagnetic matrix plus finite spin clusters picture [12] provides the most plausible explanation for the origin and properties of the secondary resonance. This can be visualized as follows. The local anisotropy fields for temperatures well below T_C are expected to be very large [13-15] > 100 kOe, particularly in the vicinity of the interface between the spins of the 3D FM matrix and the finite

spin clusters. The spins within the zones that separate the finite spin clusters **from** the **FM** matrix are frustrated owing to large fluctuation in the exchange at the interface and large **magneto-**striction. If such is the **case**, external magnetic fields of less than 10 kOe, the field range covered in the present **experiments**, can hardly affect the orientation of the spin clusters and hence they do not participate in the resonance process. As T is increased beyond **T** where *local* anisotropy fields are negligible, these frustration zones start '**melting**' away because the increased randomness in the spins constituting the FM matrix, caused by thermal agitation, weakens the exchange interaction among them whereas the direct exchange interaction between the spins within the finite clusters is strong enough to polarize the spins originally belonging to the frustration zones as also some of the spins belonging to the FM matrix. In the process, two or more neighbouring clusters coalesce to form a bigger cluster and the clusters grow in size and their relaxation rate decreases. When such clusters **are** exposed to an external magnetic field, the cluster spins start precessing around H. In the presence of field, the relaxation rate is further reduced, which explains the sharpening of the resonance line as T is increased. But beyond a certain temperature, the clusters start shrinking in size as the thermal energy weakens the ferromagnetic coupling between the spins within the clusters and they disintegrate into smaller clusters and individual paramagnetic spins and hence, the resonance starts broadening. Further increase in temperature brings about nucleation which is an irreversible atomic ordering process (crystallization) and in case of **Fe₉₁Zr₉** this happens around **T=450K** and beyond this temperature

both linewidth, ΔH , and **resonance**, H_{res} , decrease with increasing temperature. However, electron micrographs taken at room temperature on samples which had undergone thermal cycling to 500K do not show any crystalline regions on the surface, even though relaxation effects were evident in spectra taken for $T > 450K$ in that the location and sharpness of the resonance depended on the duration of time for which the sample was at a particular temperature. Thus the secondary resonance is observed only for $T > T_c$ and since the 'easy' direction of magnetization for the spin clusters always lies along the external magnetic field direction owing to the fact that the field bodily orients the clusters along its own direction, $H \approx 0$ for the secondary resonance. This observation is supported by the results of the angular dependence study of the resonance field at $T = 1.2T_c$ (Section 3.3.3), where this resonance gets clearly resolved. It is found that H has a small positive value of $\approx 20 \pm 10$ Oe, which is independent of the Co concentration and does not scale with saturation magnetization M . The presence of clusters for $T > T_c$ is also vindicated by the results of previous bulk magnetization measurements [4,16], which indicate the presence of strongly interacting giant **"superparamagnetic-like"** clusters for temperatures well above T_c , and recent high-resolution small-angle neutron scattering studies [17] on $a\text{-Fe}_{90+x}\text{Zr}_{10-x}$ alloys, which reveal that two types of spin clusters (those which **are** typically 200-400Å in size, presumably static and persist to temperatures well beyond the bulk T_c , and those which disintegrate at T_c and are responsible for a steep increase in the spin-spin correlation length as T_c is approached on either side) coexist in these alloys.

Another **important** fact to be noted **is that at $T \approx T_C$** , most of **the** spins are present in the clusters and not in the FM matrix. This is borne out by the fact that the fraction, c , of spins that actually participates in the **FM-PM** phase transition is as small as **≈ 10 %** in the case of $\alpha\text{-Fe}_{90}\text{Zr}_{10}$. The partial substitution of Fe by Co leads to an overall decrease in the average size of the clusters and this leads to more number of spins being present in the FM matrix. This is clearly indicated by the increase in c with Co **concentration**.

4.1.2. *Temperatures in **the** low and intermediate ranges*

It is observed from Figs. 3.2 and 3.3, which depict the temperature variation of the primary resonance field, **H_{res}** , for **$\alpha\text{-Fe}_{90+x}\text{Zr}_{10-x}$** and **$\alpha\text{-Fe}_{90-y}\text{Co}_y\text{Zr}_{10}$** alloys in the intermediate temperature range, that H_{res} exhibits a slow increase up to **$T \approx 0.8T_C$** and then increases steeply as **$T \rightarrow T_C$** . This behaviour of H_{res} can be attributed to the temperature variation of saturation magnetization, M_s . It must be recalled here that the values of H_{res} are the '**true**' resonance centers as deduced from the lineshape analysis (Section 2.2). The values of M_s at different temperatures obtained using the lineshape analysis have been depicted in Fig. 3.14 for the $\alpha\text{-Fe-Zr}$ and $\alpha\text{-Fe-Co-Zr}$ alloys. In the recent past, the nature of low-lying excitations in the above-mentioned alloys has been a subject of much controversy. While Krishnan et al [18] found that the '**in-field**' magnetization varies with temperature as, $M(H,T) \propto T^{3/2}$ for $T > T^*$, a characteristic temperature, in **external** magnetic fields up to 140 kOe for **$\alpha\text{-Fe}_{90}\text{Zr}_{10}$** and that the spin-wave stiff-

ness coefficient D increases with increasing H , attaining a maximum value of 39.1 meV\AA , Beck and Krönmüller [19] observed that the thermal demagnetization in the temperature range $0 \leq T \leq 0.5T_C$ was governed by Stoner single-particle excitations for $H < 2.7\text{kOe}$ and spin-wave excitations for $H > 2.7\text{kOe}$ and that D decreases from 50 to 35 meV\AA as H is increased from 2.7 to 40kOe . The conclusion [20], based on inelastic neutron scattering studies on $\alpha\text{-Fe}_{91}\text{Zr}_9$, that no propagating excitations were evident at any temperature below T_C for the wave vector transfer range $0.05\text{\AA}^{-1} \leq q \leq 0.12\text{\AA}^{-1}$ complicated the issue further. Contrasted with the above findings, the recent high-precision bulk magnetization (BM) data of Kaul [12] revealed that both Stoner single-particle and spin-wave excitations contribute to the thermal demagnetization, besides the local spin density fluctuations, and D has a field-independent value of $32 \pm 1 \text{ meV\AA}^2$ for $\alpha\text{-Fe}_{90}\text{Zr}_{10}$.

Such divergent viewpoints prompted us to analyze the $M(H,T)$ data deduced from the FMR measurements so as to determine the different contributions to the thermal demagnetization and arrive at a reliable estimate of the spin-wave stiffness coefficient D . In this regard, it must be emphasized that the present $M(H,T)$ data deduced from the FMR spectra, even under most favourable conditions, cannot match the accuracy of BM data. Nevertheless, the precision in the deduced $M(H,T)$ data suffices to determine the dominant contributions to thermal demagnetization with reasonable accuracy.

The contributions due to the spin-wave and single-particle excitations to the thermal demagnetization of "in-field" magneti-

zation, i.e. $[M(H,0) - M(H,T)]/M(H,0) \cdot \Delta m$, are given by [21,22]

$$\Delta m = \Delta m_{sw} + \Delta m_{sp} \quad (4.6)$$

where

$$\begin{aligned} \Delta m_{sw} = \frac{g\mu_B}{M(H,0)} \left[Z\left(-\frac{3}{2}, t_H\right) \left(\frac{k_B T}{4\pi D(T)}\right)^{3/2} \right. \\ \left. + 15\pi\beta Z\left(-\frac{5}{2}, t_H\right) \left(\frac{k_B T}{4\pi D(T)}\right)^{5/2} \right] \end{aligned} \quad (4.7)$$

is the spin-wave contribution, and

$$\Delta m_{sp} = S(H) T^{3/2} \exp(-\Delta/k_B T) \quad (4.8a)$$

(for strong itinerant **ferromagnet**)

$$\Delta m_s = S(H) T^2 \quad (4.8b)$$

(for weak itinerant ferromagnet) is the single-particle contribution. In Eq. (4.7), the Bose-Einstein integral functions

$$Z(s, t_H) = \sum_{n=1}^{\infty} n^{-s} \exp(-nt_H) \quad (4.9)$$

with

$$t_H = T_g/T = g\mu_B H_{eff}/k_B T \quad (4.10)$$

allow for the extra energy **gap**, $g\mu_B H_{eff} (=k_B T)$, in the spin-wave spectrum arising from the effective field

$$H_{eff} = H - 4\pi N M + H_A \quad (4.11)$$

(where N , M and H_A are the demagnetizing factor, magnetization and anisotropy field, respectively) which the spins experience within

the sample. Alternatively, in the presence of the external magnetic field, H , the **magnon** dispersion relation takes the form

$$E_q(T) = \hbar\omega_q(T) = g\mu_B H_{\text{eff}} + D(T) q^2 (1 - \beta q^2) \quad (4.12)$$

where the coefficient β is related to the mean-square range of the exchange interactions, $\langle r \rangle = 20 \beta$ and the spin wave stiffness coefficient D **renormalizes** with temperature according to the relations [12]

$$D(T) = D(0) (1 - D_2 T^2) \quad (4.13)$$

and

$$D(T) = D(0) (1 - D_{5/2} T^{5/2}) \quad (4.14)$$

in case of itinerant- and localized-electron models, respectively. The demagnetization factor N in Eq. (4.11) has been determined from earlier low-field magnetization data and the splitting factor g ($=2.07 \pm 0.02$) and the anisotropy field, H_A , from **ferromagnetic** resonance measurements [23]. Theoretical least-squares fits to the A_m data based on Eqs. (4.6)-(4.11) with the temperature dependence of spin-wave stiffness coefficient in Eq. (4.7) described either by Eq. (4.13) or by Eq. (4.14), have been **attempted**. When the least-squares fit involving six parameters, i.e. $M(H,0)$, $D(0)$, D or $D_{5/2}$, β , S and A , yielded the result $\Delta/k_B = 0 \pm 1K$, Eqs. (4.6), (4.7) and (4.8b) involving the combinations $D(T) = D(0)$, $D(T) = D(0)(1-D_2 T^2)$ and $D(T) = D(0)(1-D T^{5/2})$ with either $\beta = S = 0$ or $\beta \neq 0$, $S=0$ or $\beta=0$, $S \neq 0$ were used for the subsequent **fits**. In order to ascertain the relative importance of the spin-wave and single-particle contributions to A_m within the temperature range covered in the present experiments, a '**range-of-fit**' analysis has been carried out in which the values of the free fitting parameters in

the above-mentioned theoretical fits are monitored as the temperature interval $t_i \leq t=T/T_C \leq t_{\max}$ is progressively broadened by keeping t_{\min} fixed at 0.4 (0.3) and varying t_{\max} from 0.5 (0.4) to 0.95 (0.95) in the case of $a\text{-Fe}_{90+x}\text{Zr}_{10-x}$ and $a\text{-Fe}_{90-y}\text{Co}_y\text{Zr}_{10}$ alloys with $y=1$ and 2 (alloys with $y \geq 4$). The reverse process, i.e., keeping t_{\max} fixed at some value and varying the range by varying t_i , was also carried out. The results of this exercise reveal that the observed variation of M with T over the entire temperature range is best described by the fit which is based on Eqs. (4.6)-(4.11) and sets $\beta=S=0$ with $D(T)$ given by Eq. (4.13), indicating that the thermal demagnetization is dominated by spin-wave excitations. It has also been observed that, regardless of the temperature range chosen for the fit, inclusion of the single-particle contribution (the T term) or the higher-order spin-wave term (the $T^{5/2}$ term) besides the $T^{3/2}$ term in Eqs. (4.6)-(4.7) leaves the values of the parameters of the $T^{3/2}$ fit (i.e., the fit that makes use of Eqs. (4.6) and (4.7) with $M = \beta = 0$) practically unaltered and does not bring forth any improvement in the quality of the fit and the value of the reduced sum of deviation squares, χ_r^2 , which is given by $\chi_r^2 = \chi^2/(N-N_{\text{para}})$ where N is the total number of data points and N_{para} is the number of free fitting parameters, does not show any systematic variation with the range of temperatures used for the fits. In certain temperature ranges, χ_r becomes comparable to that obtained for the case with spin-wave contribution only. This implies that the values of magnetization deduced from FMR measurements in the present case are not accurate enough to make an unambiguous separation of spin-wave and single-particle contributions to the thermal demagnetization

possible. The optimum values of the parameters that yielded the best theoretical fits to the M data for the alloys in question are displayed in Table 4.2. The best theoretical fits so obtained are represented by continuous curves in the M versus T plot shown in Figs. 4.6 (a) and 4.6(b) for $a\text{-Fe}_{90+x}\text{Zr}_{10-x}$ and $a\text{-Fe-Co-Zr}$ alloys, respectively. The variation of the spin-wave stiffness coefficient, $D(0)$, determined from such fits, with Co concentration is shown in Fig. 4.7. It is noticed that $D(0)$ has a non-linear dependence on the Co concentration. It must be stated here that the above-mentioned analysis carried out for the $a\text{-Co-Zr}$ alloy, which represents the end composition on the Co rich side of the $a\text{-Fe}_{90}\text{Co-Zr}_{10}$ alloy series, reveals that $D(0)$ has a value of -335 meV\AA^2 . Bearing in mind that the change in magnetization for this composition is less than 5% over the investigated temperature range, and hence, there is bound to be a large error in the M values so deduced, the value of $D(0)=335 \text{ meV\AA}$ compares well with the value of 385 meV\AA , obtained from an analysis of bulk magnetization data [12]. A plot of $D(0)$ against T , the Curie temperature (determined from the scaling analysis) is depicted in Fig. 4.8, which also includes the predictions of the three-dimensional Heisenberg model which either takes into account the exchange interactions between the nearest neighbours (NN) only (dashed straight line) or considers both the NN and the next-nearest neighbour (NNN) exchange interactions (solid straight line) [24]. This figure also includes $D(0)$ and T_c data available in the literature on other similar glassy alloy systems. In accordance with the theoretical predictions [24], the $D(0)$ values for amorphous ferromagnetic alloys, when plotted against T_c , fall on a

Table 4.2. Magnetic and spin-wave parameters for $\text{a-Fe}_{90-\text{Co}}\text{Zr}_0$ alloys. The numbers in parentheses denote estimated uncertainty in the least significant figure.

Alloy	Concentration	M(0)	D(0)	D ₂	D(0)/T _C
	(y)	(G)	(meVÅ ²)	(10 ⁻⁶ K ⁻²)	(meV Å ² K ⁻¹)
	0	950(10)	32(4)	1.819(15)	0.13(3)
	1	990(10)	43(4)	4.837(15)	0.17(3)
	2	1002(10)	51(4)	4.612(15)	0.18(3)
	4	987(10)	71(4)	4.290(15)	0.21(3)
	6	1027(10)	76(4)	2.830(15)	0.20(3)
	8	1060(10)	83(4)	1.940(15)	0.20(3)
	10	1103(10)	90(4)	2.270(15)	0.19(3)
	18	1231(10)	123(6)	1.240(15)	0.18(3)
	90	1027(10)	335(10)	0.280(15)	

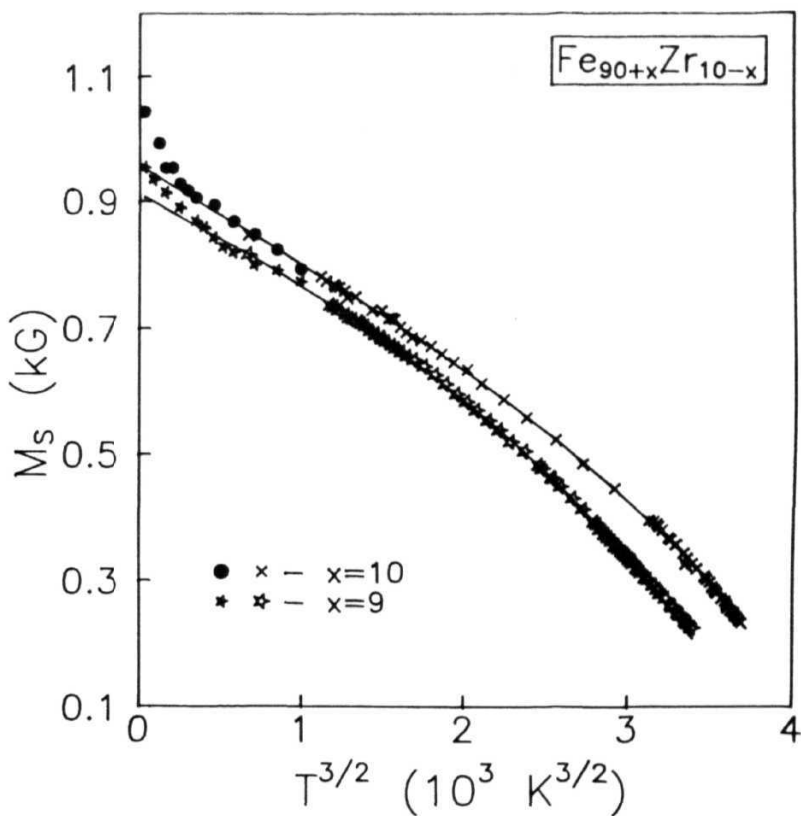


Fig. 4.6a. Variation of M_s with $T^{3/2}$ for $\text{Fe}_{90+x}\text{Zr}_{10-x}$ alloys.

The continuous curves through the data points are the best least-squares fits to the data taken in the intermediate temperature range $100\text{K} \leq T \leq 250\text{K}$ based on Eq.(4.7). Filled symbols indicate data taken in the low T region while the remaining symbols represent the data taken in intermediate T range.

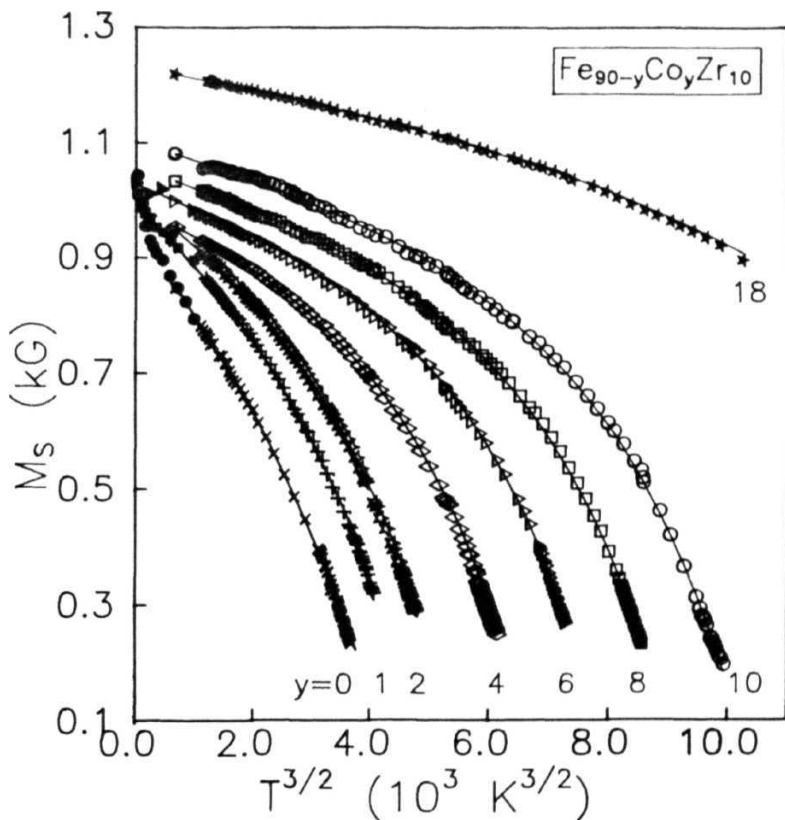


Fig. 4.6b. Variation of M_s with $T^{3/2}$ for α - $\text{Fe}_{90-y}\text{Co}_y\text{Zr}_{10}$ alloys. The continuous curves through the data points are the best least-squares fits to the data taken in the intermediate temperature range $100\text{K} \leq T \leq 250\text{K}$ based on Eq. (4.7). The symbols have the same meaning as in Fig. 4.6a.

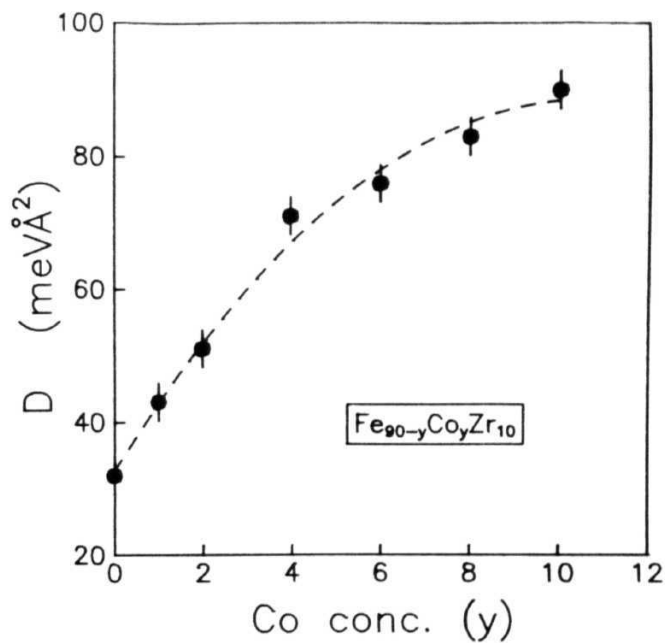


Fig. 4.7. Dependence of spin-wave stiffness coefficient, D , on Co concentration for $\alpha\text{-Fe}_{90-y}\text{Co}_y\text{Zr}_{10}$ alloys.

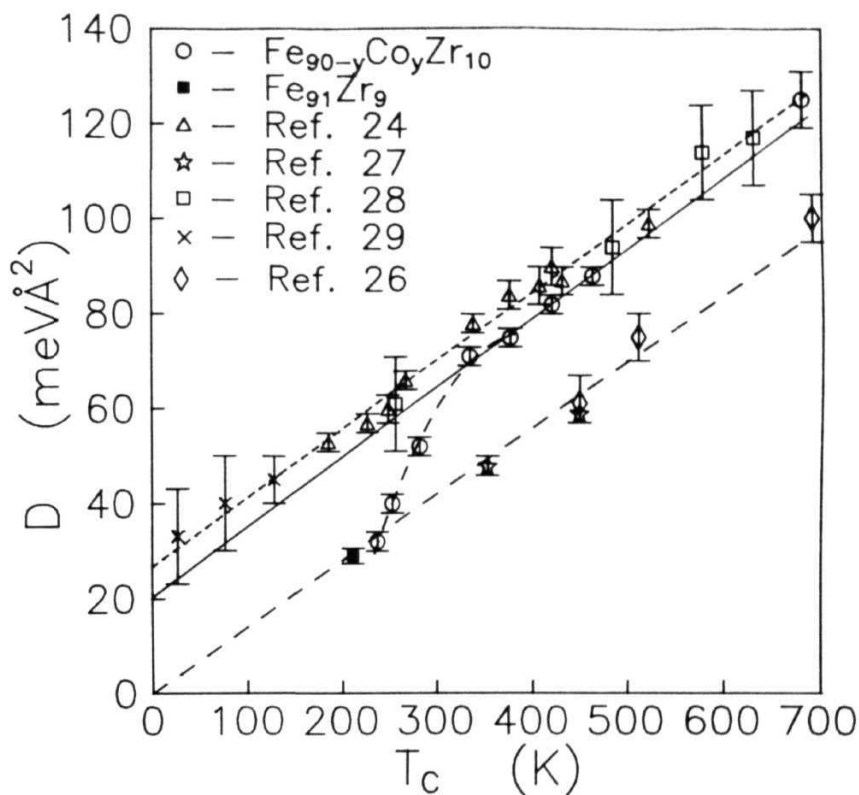


Fig. 4.8. Spin-wave stiffness coefficient, D , as a function of Curie temperature, T_C , for $\text{a-Fe}_{90-y}\text{Co}_y\text{Zr}_{10}$ alloys. $D(T_C)$ data available in the literature on other similar glassy alloy systems are also included in this figure for comparison.

straight line represented by the equation

$$D(0) = D_0 + m T_C \quad (4.15)$$

where $m = 0.144 \text{ meV}\text{\AA}^2 \text{ K}^{-1}$ and D_0 is either finite or zero, depending on whether the exchange interactions extend beyond the NN distance or not. It has been observed that while values of $D(0)$ for a-(Fe,M)-B alloys ($M = \text{Cr, Mn, W}$) [25-27] fall on a straight line with $m = 0.144 \text{ meV}\text{\AA}^2 \text{ K}$ passing through the origin, the $D(0)$ values for the a-(Fe,Ni)- M' alloys (where $M' = \text{P, B, Si, Al}$) [24,28,29] fall on another straight line which is parallel to the earlier one but with a finite intercept $D_0 \approx 24 \pm 3 \text{ meV}\text{\AA}^2$. Thus, the competing interactions in the former set of alloys confine the direct exchange interactions to nearest neighbours only whereas in the latter set, due to the absence or suppression of competing interactions, the direct exchange interactions involve not only the nearest neighbours but also the next-nearest neighbours. Now that the $D(0)$ values for the compositions with $x=0$ and 1 for a-Fe_{90+x}Zr_{10-x} alloy series and for compositions with $y=0$ and 1 for a-Fe_{90-y}Co_yZr alloy series fall on the straight line passing through the origin, it implies that the direct exchange interactions in these alloy compositions are being confined to nearest neighbours only by the competing interactions. With increasing amount of Fe being replaced by Co ($y = 6, 8, 10, 18$), the competing interactions are progressively suppressed, the alloys become more homogeneous and the direct exchange interactions now extend to next-nearest neighbours also. In the intermediate Co concentration range ($2 \leq y \leq 4$), a crossover from the short-ranged (NN distance) to the long-ranged (NNN distance) exchange takes place.

The angular dependence of the resonance fields, $H_{re}(\phi)$, for $T < T_C$, i.e., $T = 0.6T_C$, described in Section 3.3.3 throws some light on the nature of the anisotropy in these alloys. The analysis of the $H_{res}(\phi)$ data for $T < T_C$ shows that for the primary resonance in both in-plane and **out-of-plane** cases the uniaxial anisotropy field H_u is positive throughout the Co concentration range for **a-Fe_{90+x}Zr_{10-x}** alloys and increases with x from $H_k = 40$ Oe for $x=0$ to 160 Oe for $x=10$ (**Fig. 3.10(a)**). In addition, H_k scales with saturation magnetization, M (**Fig. 3.10(b)**). The uniaxial anisotropy in the investigated alloys, as in other ferromagnetic alloys in the amorphous state, presumably has its origin in the pseudodipolar atomic pair ordering mechanism [30].

At very low temperatures, resonance fields have been known to exhibit anomalous behaviour in many reentrant alloy systems [31] in that with decreasing temperature, H_{res} decreases faster than can be attributed to an increase in magnetization and the temperature dependence of H_{res} depends upon the thermal history [32], i.e., whether the sample has been **zero-field-cooled** (ZFC) or an external field has been applied during the cooling cycle. The low T drop in H_{res} is found to be isotropic, i.e., it does not depend on the orientation of the external field with respect to the sample, and is attributed to the increase in an anisotropy energy with an easy axis which is always in the direction of the external dc field in the reentrant state. In the present study, H_{res} exhibits the low-temperature anomaly and thermal history effects in **a-Fe_{90+x}Zr_{10-x}** alloys, as is evident from **Figs. 3.4(a)** and **3.4(b)**, but no such anomaly or thermomagnetic effects are discernible in the case of the Co containing alloys. As a **conse-**

quence, the saturation magnetization **values**, obtained from the lineshape analysis of the **FMR** spectra taken at low temperatures without allowing for the anisotropy field effects, included in **Figs. 4.6(a) and (b)** exhibit an upturn at a temperature (i.e., below this temperature the $M(H,T)$ data start deviating from the best fits to the M_s data obtained in the intermediate temperature range, see **Figs. 4.6(a) and (b)**), which coincides with T_{nr} , for the alloys with $x = 0$ and 1 and $y = 1$ but this upturn is completely suppressed for $y = 6$. This observation strongly indicates that the reentrant behaviour is completely suppressed for $y > 4$ in **a-Fe_{90-y}Co_yZr₁₀ alloys**.

4.2. Linewidths

The temperature dependence of FMR linewidth is divided into three temperature regimes and discussed separately as was the case while dealing with $H_c(T)$ in the preceding section. These regimes are : (i) the temperatures close to T_c , which highlight the critical behaviour of the primary resonance, and temperatures above T_c , that assume importance because of the appearance of the secondary resonance, (ii) the intermediate temperature regime and (iii) low temperatures which bring out certain important features of the the primary resonance.

4.2.2. *Critical behaviour and LLG damping*

Primary resonance

The variation of the peak-to-peak linewidth, ΔH , for the

primary resonance with temperature in the \parallel and \parallel^V configurations for $a\text{-Fe}_{90+x}\text{Zr}_{10-x}$ and $a\text{-Fe}_{90-y}\text{Co}_y\text{Zr}_{10}$ alloys has been depicted in Fig. 3.11 of Section 3.4. A part of this data taken in the critical region ($|c| < 0.06$, $c = (T - T_C)/T_C$) is shown in Fig. 4.9 for the \parallel sample configuration. It should be noted that in this temperature range, $AH(T)$ possess the same values for \parallel and \parallel^V configurations. Frequency-dependent studies of FMR in amorphous ferromagnets [33,34] have revealed that AH consists of a frequency-independent part, ΔH_0 , and a frequency-dependent part, ΔH_{LLG} . While ΔH_0 is most probably caused by the two- or multi-magnon scattering from spatially localized magnetization inhomogeneities [33], ΔH_{LLG} ($= 1.45 \lambda \omega / \gamma^2 M_s$) results from the LLG relaxation mechanism. Such contributions to the linewidth in the entire temperature region will be discussed in detail in the next section and at this stage it should suffice to emphasize that $AH(T)$ in the critical region can be very well described by the empirical relation

$$\Delta H_{pp}(T) = \Delta H_0 + [A/M_s(T)], \quad |c| < 0.05 \quad (4.16)$$

The second term on the right-hand-side of Eq. (4.16) can immediately be identified as $\Delta H_{T,C}$ and the damping parameter X can be calculated from the value of the coefficient A , determined from a least-squares-fit to the $AH(T)$ data for different compositions based on Eq. (4.16) (Fig. 4.10). The temperature-independent va-

8

8-1

lues of A so computed ranging between 2×10 and 3.5×10 sec are plotted against Co concentration in Fig. 4.5. These values of X do not differ significantly from those deduced from the least-squares fits to the $AH(T)$ data over the entire temperature range

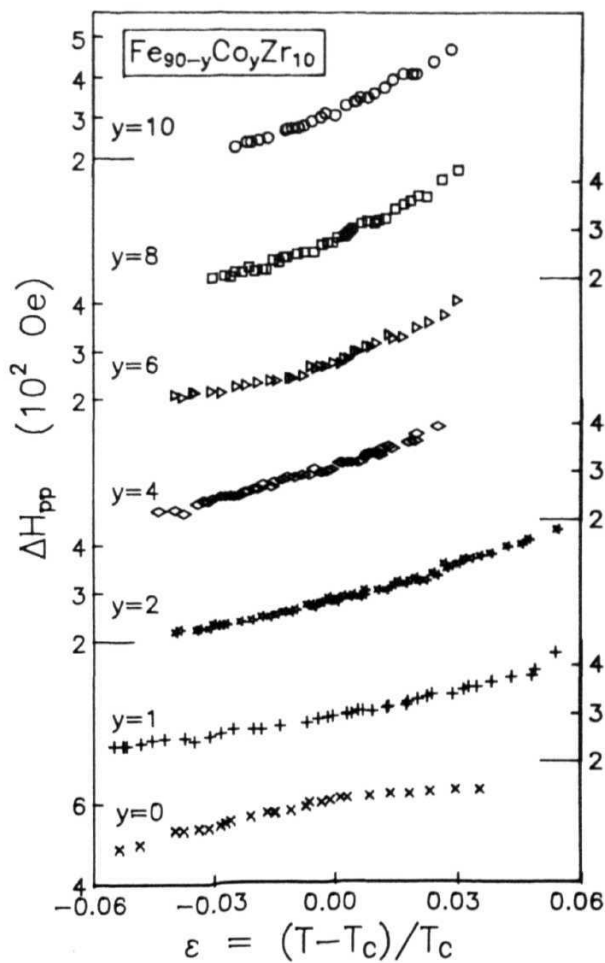


Fig. 4.9. Variation of the peak-to-peak linewidth, ΔH_{pp} , with temperature in the critical region for a-Fe_{90-y}Co_yZr₁₀ alloys.

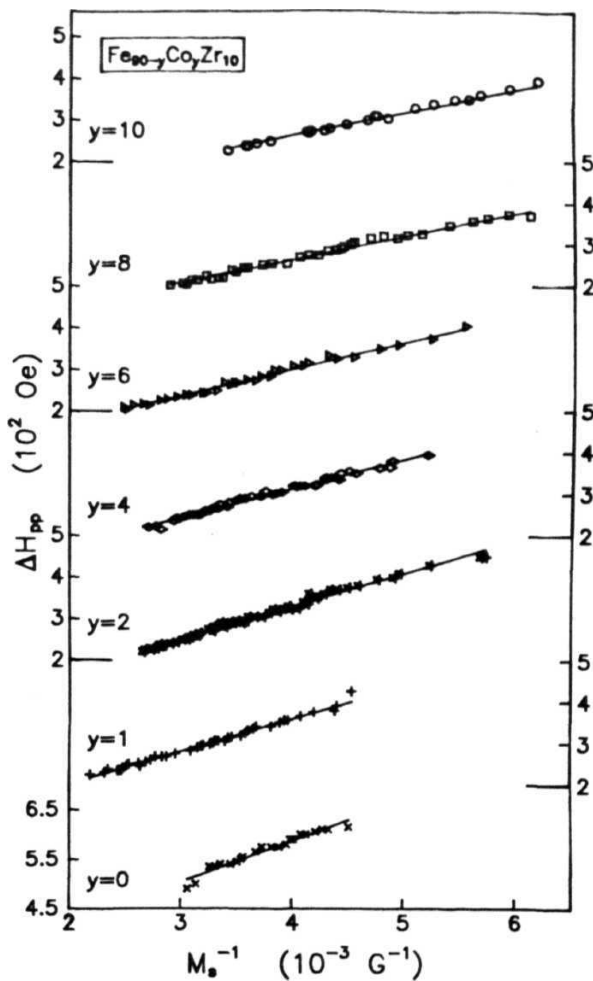


Fig. 4.10. ΔH_{hf} plotted against inverse saturation magnetization in the temperature interval $-0.05 \leq c \leq 0.05$ for $\alpha\text{-Fe}_{90-y}\text{Co}_y\text{Zr}_{10}$ alloys. The straight lines through the data points represent the least-squares fits to the data based on Eq. (4.16).

covered in the present experiments particularly for $y > 4$. Furthermore, in the critical **region**, the LLG term gives a dominant contribution to $AH(T)$ by virtue of its $1/M$ dependence. A **decreases** with increasing Co concentration so much so that it drops rapidly in the range $0 \leq y \leq 2$ from 3.4×10^{-8} sec to 3.1×10^{-8} sec for $y=2$ and finally reaches a value of 2.1×10^{-8} sec for $y=10$. The Lande splitting factor g deduced from the lineshape analysis shows a *temperature-* and **composit ion-independent** value of 2.07 ± 0.02 .

Secondary resonance

The variation of the peak-to-peak linewidth, AH , with temperature (Fig. 3.12(c), Section 3.4) for the secondary resonance, which becomes well-resolved at $T > T_C + 10K$, resembles that generally observed in cluster spin glasses but the resonance lineshape in the present case is much sharper and symmetrical with respect to the baseline than in cluster spin glasses.

4.2.2. Intermediate temperature regime

In this section, the variation of linewidth with temperature for $T < T_C$ is discussed. According to Figs. 3.11(a) and 3.11(b) of Section 3.4, the FMR linewidth exhibits a weak dependence on temperature in this region (increasing with decreasing temperature). As already mentioned in Section 4.2.1, the FMR linewidth, AH , in amorphous alloys comprises a frequency-dependent term and a term, ΔH_0 , which is independent of the frequency (also called the 'zero-frequency' term). The unambiguous determination of these two con-

tributions necessitates the measurement of ΔH at different microwave field frequencies. When the resultant data at a given temperature are plotted in the form of a ΔH vs. ν curve, the linear dependence of ΔH on the microwave field frequency becomes apparent and the intercept at zero frequency gives the value of ΔH_0 . Such an analysis was not possible in the present case because the ESR spectrometer available for measurements could operate only at a single frequency of 9.3 GHz in the **X-band**. Nevertheless, an attempt has been made to estimate the values of A and ΔH_0 through a least-squares fit analysis of the data. The temperature (T) and frequency (ν) dependence of the linewidth is described by

$$\Delta H_{pp}(\nu, T) = \Delta H_0(T) + \Delta H_{LLG}(\nu, T) \quad (4.17)$$

In Eq. (4.17), the second term on the r.h.s represents the LLG contribution which is proportional to $(\omega/\gamma)(\lambda/\gamma M_g)$. However, the origin of the first term, which manifests itself as a non-zero intercept at $\nu=0$, appears to be more complicated. Spano and Bhagat [34] attribute this additional contribution to inhomogeneities that are consequent upon a random placement of ferromagnetic atoms, which causes the exchange interaction to be a random function of position. These authors empirically model the **inhomogeneity** by a Gaussian distribution of local magnetizations and of internal dipolar fields and then calculate the linewidths that result from such a distribution. A different approach has been taken by Cochrane et al [35] based on ferromagnetic antiresonance (FMAR) measurements. According to this approach, ΔH_0 has its origin in the **two-magnon** scattering mechanism. The **magnon** scattering may be

caused by spatial inhomogeneities in the local magnetic anisotropy fields and/or inhomogeneities in the local exchange interaction [36]. These authors calculate the contribution to the linewidth due to two-magnon scattering processes using elliptically polarized **magnons** (since $4\pi\mathbf{M}$ is comparable to or much larger than the applied fields in iron-rich materials) and find that the two-magnon linewidth is proportional to \mathbf{M} in agreement with the observations. While performing the **least-squares-fit** analysis, the latter approach has been adopted in the present study by writing the constant term as,

$$\Delta H_0(T) = H_0 + a \mathbf{M}_s(T) + b \mathbf{M}_s^2(T) \quad (4.18)$$

where \mathbf{H} is a constant term independent of **temperature**, the second term arises due to two-magnon scattering processes and the third term presumably originates from higher-order **magnon** scattering processes. The least-squares (LS) fits to the ΔH (T) data are attempted based on Eqs. (4.17) and (4.18) by using a nonlinear LS fit computer program which treats the damping parameter A , \mathbf{H}_0 , a and b as free-fitting parameters and \mathbf{M} values used in this program are obtained from the lineshape analysis, mentioned earlier. Such LS fits have been attempted in the temperature range 77K to $(T_C + 15\text{K})$ for each of the alloy compositions. The solid lines through the ΔH vs. T data (Fig. 3.11(b)) represent the best LS fits based on the Eqs. (4.17) and (4.18). The main findings are :

- (i) the constant term \mathbf{H}_0 is either negligibly small or zero,
- (ii) contribution from the \mathbf{M}_s term is significant only in the case of **a-Fe_{90+x}Zr_{10-x}** and **a-Fe_{90-y}Co_yZr₁₀** alloys with low Co concentra-

tion ($\gamma \leq 2$); this term makes little or even no contribution to ΔH for $\gamma \leq 2$, (iii) the M^2 term gives a sizable contribution in the intermediate temperature range and (iv) the damping parameter A is independent of temperature (since its value does not depend on the temperature range chosen for the fit) in the entire temperature range which also includes the critical region. ΔH_0 does not exhibit any systematic trend with Co concentration. This could imply that ΔH_c is extremely sensitive to the thermal history of the material. The dominance of the M^2 term over the M^4 term in the Eq. (4.18) presumably implies that the higher-order magnon scattering processes are important. Fig. 4.11 shows the Gilbert damping parameter A plotted against Co concentration. The value of A ranges from $5.1 \times 10^{-8} \text{ sec}^{-1}$ for the parent alloy $\text{Fe}_{90}\text{Zr}_{10}$ to $1.5 \times 10^{-8} \text{ sec}^{-1}$ for the alloy with $\gamma=18$. The unusually large value of A for $\text{a-Fe}_{90}\text{Zr}_{10}$ and the variation of A with Co concentration can be understood in terms of the density of states at the Fermi level, $N(E_F)$, as follows. Heinrich et al [33] have shown that $A \propto N(E_F)$ for crystalline ferromagnets. Low-temperature specific-heat measurements on $\text{a-Fe}_{90+x}\text{Zr}_{10-x}$ alloys [37] yield a value of $N(E_F)$ for $\text{a-Fe}_{90}\text{Zr}_{10}$ as $N(E_F) = 3.4 \text{ states/eV atom}$. Such a large value of $N(E_F)$ for $\text{a-Fe}_{90}\text{Zr}_{10}$ has also been obtained from the uv photoelectron (UPS) technique [38], which is a more direct method. In view of the result that $N(E_F)$ falls rapidly with increasing Co concentration [39] in $\text{a-Fe}_{90-x}\text{Co}_x\text{Zr}_{10}$ alloys, it is, therefore, not surprising that A too decreases with increasing Co concentration.

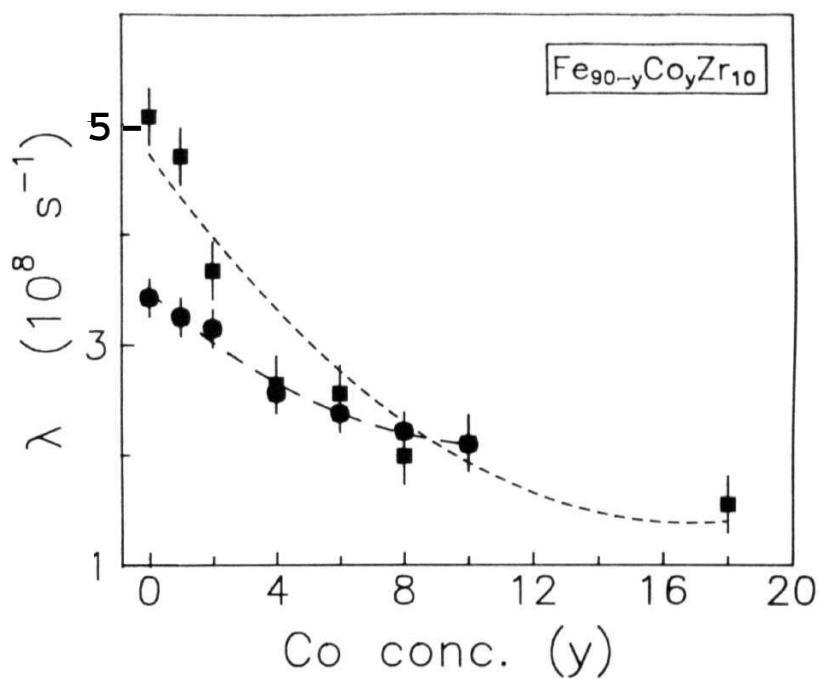


Fig. 4.11. Functional dependence of Gilbert damping parameter, λ , computed in the critical region (•) and over the entire investigated temperature range (▪), on Co concentration.

4.2.3. Low temperature behaviour

In a number of concentrated spin glasses and reentrant systems the linewidth increases rapidly [23,32,34,40,41] when the temperature is decreased below $\sim 2T_{SG}$ and $\sim 2T_c$, respectively. Bhagat *et al* [42] have shown that this rapid increase can be described by an empirical relation of the form (Section 3.4.1),

$$\Gamma(x, \nu, T) = \Gamma_0(x, \nu) + \Gamma_1(x) (T/T_0)^n \exp(-T/T_0) \quad (4.19)$$

where Γ_1 and T_0 are empirical parameters and Γ is the value of the linewidth in the intermediate temperature regions where it is either independent or weakly dependent on temperature. The value of the exponent n may be 1 or 0 depending on whether or not the linewidth goes through a maximum at very low temperatures. In the present study, FMR measurements down to 10K were performed on amorphous $Fe_{90}Zr_{10}$, $Fe_{91}Zr_9$, $Fe_{89}Co_1Zr_{10}$ and $Fe_{84}Co_6Zr_{10}$ alloys. The low temperature dependence of the linewidth for these alloys has already been depicted in Fig. 3.11(c) along with the best LS fits to the data. While fitting Eq. (4.19) to the low-temperature AH (T) data, the parameters Γ_1 and T_0 are treated as free-fitting parameters while n is set equal to unity and Γ_0 is assigned a value which ΔH has in the **intermediate** temperature range where the linewidth is nearly independent of temperature. From Fig. 3.11(c), it is observed that Eq. (4.19) provides a reasonably good fit to the data. The maxima at low temperatures in AH (T) are characteristic of many reentrant systems [34,40,43]. Though it has been suggested earlier that these maxima may be identified with the reentrant temperatures [43], the present results do not sup-

port such a conclusion. The T_{RE} values for Fe-Zr alloys and Fe-Co-Zr alloys with low Co concentrations deduced from low-field magnetization data [8] are much higher than the T values deduced from the linewidth data and any coincidence between these two could be fortuitous. Within the framework of the infinite FM matrix plus finite clusters model [44-46], the exponential increase in linewidths at low temperatures may be explained in terms of a theory proposed by Continentino [47]. Continentino proposed that the finite clusters may be described as a set of magnetic two-level systems (TLS) represented by an asymmetric double well potential with energy splitting E and analogous to tunneling centers in glasses and the relaxation processes that are associated with these clusters invoke transitions between the two levels. The low-energy spin-wave excitations in the infinite FM clusters relax through channels provided by the finite clusters and get coupled to them. The **Hamiltonian** which describes the spin waves in the infinite FM cluster interacting with the finite clusters is given by

$$\mathcal{H} = \sum_{\mathbf{k}} \epsilon_{\mathbf{k}} a_{\mathbf{k}}^{\dagger} a_{\mathbf{k}} + J \vec{\sigma} \cdot \vec{S} + D \cdot \vec{\sigma} \times \vec{S} \quad (4.20)$$

where $\epsilon_{\mathbf{k}} = A + D k$ is the energy of the spin waves with stiffness constant D_0 due to exchange interaction between spins within the infinite cluster, A is the spin-wave gap arising from anisotropic interactions between these spins, \mathbf{k} is the wave vector of magnons and $a_{\mathbf{k}}^{\dagger}$, $a_{\mathbf{k}}$ are **Holstein-Primakoff** creation and annihilation boson operators. The second and third **terms** in Eq. (4.20) refer to the TLS. The **"average"** coupling constants J and D describe the **effec-**

tive isotropic exchange and anisotropic Dzyaloshinskii-Moriya (DM) interactions between the spins S of the infinite cluster and the finite clusters represented by the **Pauli matrices** σ_i . The effect of coupling between the spin waves (**magnons**) and the TLS on the spin-wave propagation can be described by a shift in the energy and a damping of these excitations. This damping, which manifests itself as the **FMR** linewidth, consists of two contributions: the first one, called the resonant contribution, arises from the interaction between the clusters mediated by magnons excited in the infinite cluster by the microwave field and is characterized by a transverse or fast relaxation time of the clusters, whereas the second one, called the relaxation contribution, results from a distribution of energy splittings (states) E of the TLS and activation energies V (or barrier heights across which the transitions between the TLS are effected by thermal activation) due to the random nature of the atomic ordering. For the range of temperatures covered in the present experiments and the microwave frequency used (9.3 GHz), the resonant contribution to the linewidth is expected to be negligibly small compared to the relaxation contribution. The energy splittings E of the TLS are assumed to be a constant function with value n from zero to a cutoff value E_{\max} and zero otherwise and the probability distribution of the activation energies (energy barriers) becomes exponential for large V ,

$$P(V) = (1/V_0) \exp(-V/V_0) \quad (4.21)$$

With the longitudinal relaxation time given by $\tau_1 = \tau_0 \exp(V/kT) \operatorname{sech}(E/2kT)$ whenever the conditions $\omega\tau_0 \ll 1$ and $kT/V_0 < 1$ are

satisfied, Continentino [47] arrives at the following expression for linewidth

$$\Delta H_{\text{rel}} = \frac{2\pi S n_0}{\hbar \gamma N_0} \frac{D^2}{V_0} kT \exp(-T/T_0) \quad (4.22)$$

with the characteristic freezing temperature T_0 given by

$$T_0 = V_0 / |\ln(\omega \tau_0)| \quad (4.23)$$

In Eq. (4.23), ω is the frequency of the **magnons** in the infinite cluster that are excited by the rf field, **N** is the **number** of spins in the infinite cluster, τ is the inverse of an attempt frequency and the other symbols have their usual meaning. Combining Eqs. (4.22) and (4.23), one obtains Eq. (4.19) with $n=1$ and

$$\Gamma_1 = \frac{2\pi S n_0}{\hbar \gamma N_0} \frac{D^2 k}{|\ln(\omega \tau_0)|} \quad (4.24)$$

Eq. (4.22) also reproduces the maxima observed in the linewidth versus temperature curve at $T=T_0$. Though this theory can satisfactorily explain the increase in **FMR** linewidth at low temperatures, it has some obvious limitations. For instance, contrary to the observation that Eq. (4.19) is obeyed up to temperatures as high as $2T_{\text{DF}}$, this expression according to the theory due to Continentino is strictly valid only at very low temperatures, i.e., for $kT/V_0 \ll 1$. Moreover this theory predicts a large shift in the linecenter concomitant **with increased linewidths**, which has not been observed in many random spin systems. Systematic studies of frequency dependence in concentrated amorphous spin glass systems

[48] have revealed that Γ_1 exhibits a **"resonant anomaly"** as a function of frequency and for very low **frequencies**, Γ_1 increases roughly by a factor of five as contrasted with the theoretical prediction that Γ_1 is frequency-independent. This could **imply** that the distribution functions of two-level systems might be more complicated than assumed in the theory due to Continentino. Hence, a more detailed, microscopic theory of linewidths in these systems is required.

Another important aspect of the present data is the concentration dependence of the low-temperature linewidth. It is observed that for Co concentrations greater than 2 at.%, the exponential increase in linewidth at low temperatures is completely suppressed (Fig. 3.11(c)). This behaviour is indicative of the fact that reentrant behaviour has been suppressed for higher Co concentrations. The effect of partially replacing Fe with Co can be explained on similar lines as the discussion of spin-wave stiffness coefficient D in Section 4.1.2. It was shown earlier that in **a-Fe_{90+x}Zr_{10-x}** and **a-Fe_{90-y}Co_yZr₁₀** alloys, the range of direct exchange interactions in alloys $x, y = 0$ and 1 is confined to nearest neighbours only due to the presence of competing interactions whereas for alloys with y in the range $6 \leq y \leq 18$, the direct exchange extends to next-nearest neighbours also, indicating either a suppression or absence of competing interactions. Since the Fe-Co and Co-Co exchange interactions are ferromagnetic and stronger than Fe-Fe exchange coupling, the addition of Co suppresses the competing interactions in the frustration zones (Section 1.6) [12] surrounding the clusters and this leads to **breaking-up**

of these clusters into smaller clusters. Consequently, as the Co concentration **increases**, the number of spins constituting the FM matrix increases at the expense of those forming the clusters, the spin system becomes more and more homogeneous and the reentrant behaviour gets progressively suppressed [49]. One can also find an interpretation for this in terms of the theory due to Continentino. According to Continentino [47], the energy barrier V arises from interactions between the cluster and its surroundings taking place across the zones that separate the cluster proper from its environment. This energy barrier is a sum over the surface of contributions random in magnitude and sign, i.e., clusters of all sizes v . For large clusters, the probability distribution $P(V, v)$ is a Gaussian with a variance proportional to the number of spins on the surface of the cluster v^X [50], i.e.,

$$P(V, v) \propto \exp(-av^2/v^X) \quad (4.25)$$

According to the percolation theory for three-dimensional systems above the percolation threshold [51], the cluster size distribution, in case of large v , is

$$C(v) \ll \exp(-bv^Y) \quad (4.26)$$

where y takes a value of $2/3$. Then the probability distribution of the barrier heights is given by

$$P(V) = \int C(v) \cdot P(V, v) \, dv \quad (4.27)$$

which, when evaluated **asymptotically** for large V , results in an equation of the form of Eq. (4.21). Thus, it is clear that the

characteristic temperature T_* is related to the characteristic barrier height V through the cluster size v and any change in v is bound to affect V , and hence, T_* . Since the increase in C_0 concentration results in reducing the cluster **sizes**, V and T_* progressively decrease and hence, the reentrant behaviour is suppressed.

SECTION - B

MOSSBAUER EFFECT4.3. Hyperfine field distributions

The analysis of the Mossbauer spectra of various alloy compositions (Section 3.10) gives their hyperfine field distribution curves $P(H_{hf})$, depicted in Figs. 3.19 - 3.23 for $a\text{-Fe}_{90}\text{Zr}_{10}$, $a\text{-Fe}_{91}\text{Zr}_9$, $a\text{-Fe}_{89}\text{Co}_1\text{Zr}_{10}$, $a\text{-Fe}_{88}\text{Co}_2\text{Zr}_{10}$ and $a\text{-Fe}_{86}\text{Co}_4\text{Zr}_{14}$, respectively. Since all the above-mentioned alloy compositions with the exception of $a\text{-Fe Co Zr}$ exhibit similar hyperfine field distribution curves, the results for a representative composition, i.e., $a\text{-Fe}_{90}\text{Zr}_{10}$, only will be discussed in detail. The hyperfine field distribution curves, $P(H_{hf}^{TP})$, deduced from the two-pattern (TP) fit analysis, and $P(H_{hf}^W)$, deduced from the Window analysis, for $a\text{-Fe}_{90}\text{Zr}_{10}$ shown in Figs. 3.19(b) and 3.25, demonstrate the existence of a **bimodal** structure in $P(H_{hf})$ for all temperatures below T_C since the presence of a low-field component in them is clearly **noticed**. This low-field component, reported previously by a number of workers [8,10,11,52-55], however, does not manifest itself as a well-resolved peak as is normally the case with bimodal distributions, but appears more as a shoulder on the low-field side of the main peak. In a recent paper, Ryan and Ren [56] observe a low-field **shoulder** in $P(H_{hf})$ for $\text{Fe}_{92}\text{Zr}_8$ at all temperatures below T_C , but they dismiss its existence on the pretext that the statistical fluctuations in the central region of the **Mössbauer-effect** (ME) spectra give rise to this specious

effect. Statistical fluctuations in the measured spectra manifest themselves in $P(H_{hf})$ only when the number of terms N in the Fourier expansion used for the evaluation of $P(H_{hf})$ greatly exceeds the optimum value of N (Section 3.8). An unequivocal evidence for a **bimodal $P(H_{hf})$** in **a-Fe_{90+x}Zr_{10-x} alloys** is provided by the bimodal frequency distribution of the spin-echo amplitude [57] and also by the observation (Section 3.9) that neither a single-Gaussian nor a three-Gaussian **distributions**, but only a two-Gaussian distribution of the $P(H_{hf})$ form an adequate description of the observed ME spectra. This observation regarding the bimodal character of $P(H_{hf})$ has also been made in a study on **a-Fe₉₂Zr₈** alloy by Morrish et al [58]. It is appropriate at this stage to invoke the models described in Section 1.6 in order to describe the behaviour of the hyperfine field distributions. The transverse-spin freezing (TSF) model of Gabay and Toulouse [59] cannot account for a bimodal distribution of $P(H_{hf})$ as it basically insists on a microscopically homogeneous nature of magnetic ordering. Therefore, recourse has to be taken to the models (Section 1.6) that postulate a spatially segregated coexistence of **finite** spin clusters and an **infinite** ferromagnetic (FM) matrix [11,12,54] to explain the bimodal $P(H_{hf})$. Within the framework of such models, the low- and high-field peaks in $P(H_{hf})$ originate from the spin clusters and the FM matrix, respectively. In view of the finding that a sum of two-Gaussian distributions adequately describes both $P(H_{hf}^{TP})$ (Figs. 3.19 (b)-3.22 (b)) as well as $P(H_{hf}^W)$ (Fig. 3.25 in case of **a-Fe₉₀Zr₁₀** and the structure with very low probability observed at weak fields particularly at low temperatures may be discarded as it is an artifact of the **Window**

analysis), the areas under the low- and **high-field** Gaussian curves normalized to the total area under the $P(H_{hf})$ -vs- H_{hf} curve give the fraction of the spins belonging to the clusters [low-field spin (LFS) fraction] and to the **FM matrix** [high-field spin (HFS) fraction], respectively. Since the two-pattern (TP) fits reproduce the observed spectra with much higher accuracy than the Window fits (Section 3.9), the TP fits yield more reliable estimates for the LFS and HFS spin **fractions**. Fig. 4.12 shows the temperature dependence of the LFS and HFS fractions for **a-Fe₉₀Zr₁₀**. It is evident from the figure that the LFS fraction increases at the expense of the HFS fraction as the temperature is raised beyond $T \approx 150K$ and amounts to about 90 % of the total Fe spins at $T \approx T_C$. Since either of the models which postulate that the spin system consists of **antiferromagnetic (AFM)** spin clusters and FM matrix (AFM-FM) or FM spin clusters and FM matrix (**FM-FM**) (Section 1.6) is capable of explaining the **bimodality** in $P(H_{hf})$, it is imperative to find out which of these yields a variation of LFS and HFS with temperature that is consistent with **the one** borne out by the present experiments. In the AFM-FM **model**, the spin clusters are **Fe-rich** regions in which Fe spins are antiferromagnetically coupled as in **fcc** γ -Fe. Then the LFS fraction is expected to remain essentially constant for temperatures well below the cluster **Néel** temperature ($T_N \approx 70K$ for γ -Fe) and decrease at an increasingly faster rate when the temperature is raised well above T_N because the spins within the clusters would get completely disordered for $T > T_N$ ($T_N^C \ll T_N^{FM}$) and get easily polarized by the spins belonging to the **FM** matrix. The corresponding changes that should occur in $P(H_{hf})$ as the temperature is increased through T_N ,

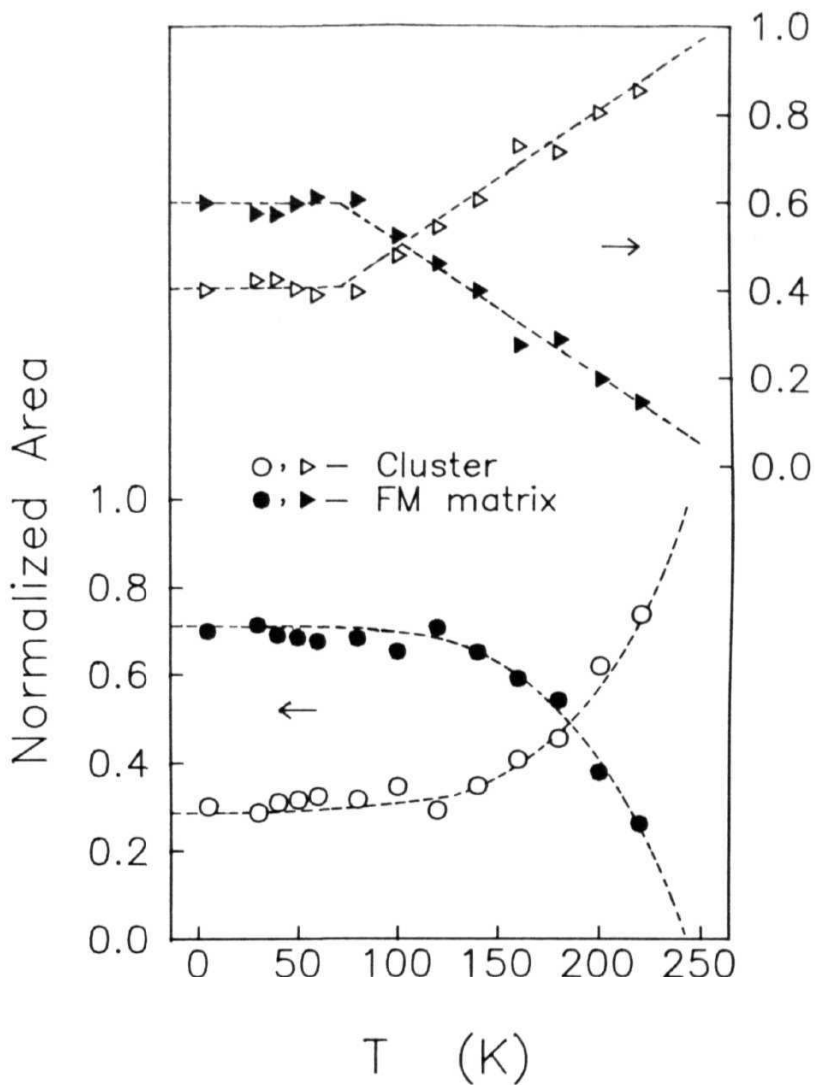


Fig. 4.12. Temperature dependence of normalized area under the low-field Gaussian curve, "low-field spin fraction" [Window (A); two-Gaussian (○)] and under the high-field Gaussian curve, "high-field spin fraction" [Window (•); two-Gaussian (•)].

are that the low-field Gaussian peak should narrow down and its peak position shift to lower fields as $T \rightarrow T_N$ such that the area under this peak, i.e., the LFS fraction, remains essentially unaltered in the initial stages of this process and then rapidly broadens out at temperatures well above T_N . As a consequence, the two peaks in $P(H_{hf})$ should become better resolved as $T \rightarrow T_N$ (considering the fact that the position of the high-field peak hardly changes in this temperature range) and the low-field peak should appear more as a shoulder to the main high-field peak for temperatures well above T_N . None of these trends is observed either in the $P(H_{hf})$ [Figs. 3.19(b) and 3.25] or in the LFS fraction-vs-T curve (Fig. 4.12). Read et al [11] calculate the LFS fraction from the **zero-Doppler** velocity Mossbauer absorption, $A(T)$, thermal scan data. At very low temperatures ($T \ll T \approx 70K$), the spins constituting the AFM clusters and those forming the FM matrix are expected to be in a magnetically ordered **state**, whereas for $T > T_N$ (e.g., $T = 80K$), the cluster spins get disordered and give rise to a paramagnetic absorption at such temperatures, while the FM spins continue to remain in the ordered state. At $T > T_N$, all Fe atoms are paramagnetic so that the ratio $[A(80K) - A_0(300K)] / A_N(300K)$ should correspond to the LFS fraction. The value of this ratio calculated from the zero-velocity absorption (ZVA) data, shown in Fig. 4.13, comes out to be ≈ 0.19 . A comparison of this value with the estimate 0.30 given by the TP analysis (Fig. 4.12) underlines the futility of the approach adopted by Read et al [11]. Also from the ZVA data shown in Fig. 4.13, it is clear that the value of the LFS fraction deduced from such data crucially depends on the value of T_N assumed (a coincidence between the Néel

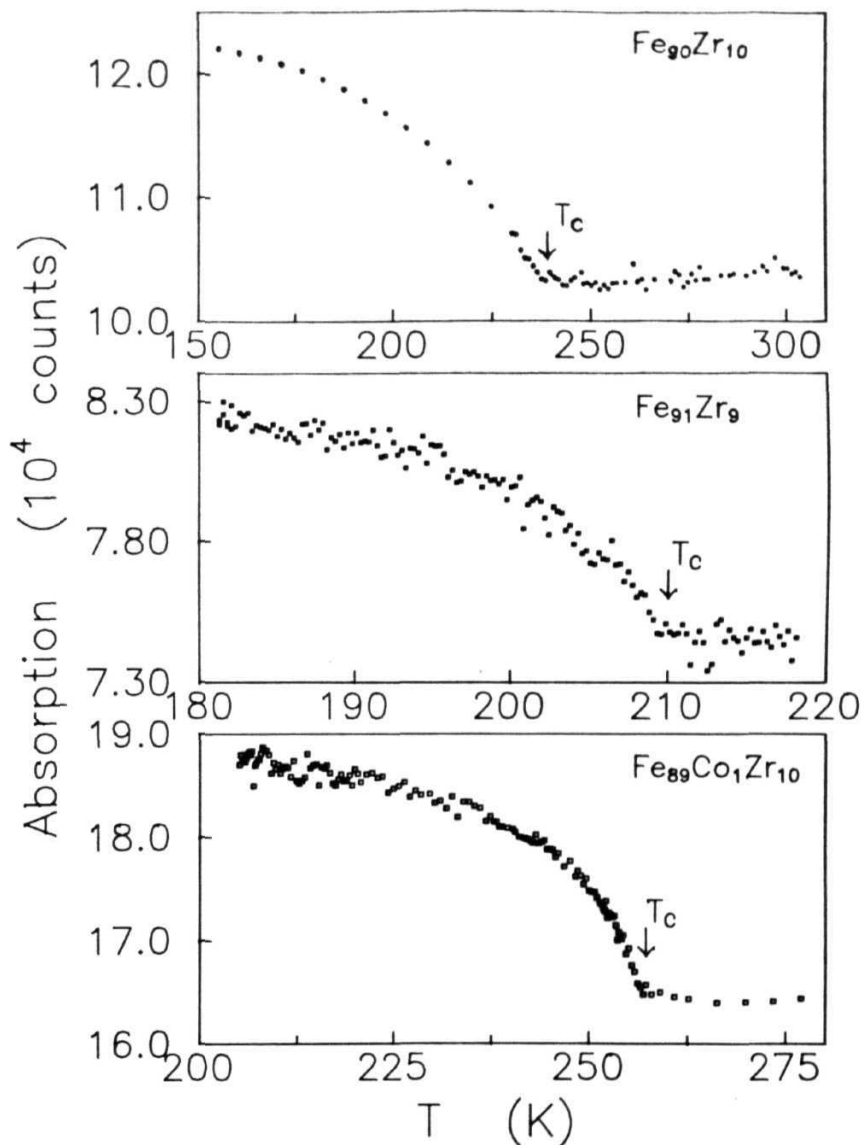


Fig. 4.13. Zero-velocity Mossbauer absorption data plotted against temperature for $\alpha\text{-Fe}_{90}\text{Zr}_{10}$, $\alpha\text{-Fe}_{91}\text{Zr}_9$ and $\alpha\text{-Fe}_{89}\text{Co}_1\text{Zr}_{10}$ alloys. The arrows indicate the values of T_c .

temperature for **AFM** clusters and γ -Fe could be fortuitous), particularly when $T_N > 150K$, and greater the value of T_N compared to this temperature, lower the LFS fraction and larger the discrepancy between the values of the LFS fraction obtained from ZVA data and TP analysis. Further, the AFM-FM model yields a variation of the LFS fraction with temperature that is in direct contradiction with the one depicted in Fig, 4.12 and cannot account for the fact that the positions of the low-field and high-field Gaussian peaks both decrease in direct proportion to the applied magnetic field [52,58,60]. By contrast, the **FM-FM** model correctly predicts the variation of the LFS and HFS fractions with temperature in that the exchange interaction between the spins in the FM matrix weakens as $T \cdot T_C$ while the **FM** coupling between the spins within the clusters is still quite strong due to the higher T for the clusters so that the cluster spins polarize an increased number of spins originally belonging to the FM matrix and grow in size at the expense of the FM matrix. The results of the **FMR** measurements on the same alloy series (Section 3.1 - 3.6) and earlier work [6,23,61,62] lend further support to this interpretation. From Fig. 4.12, it is observed that for temperatures in the immediate vicinity of T , only about 10% of the total Fe spins in a-Fe Zr_{10} constitute the FM matrix. This result is consistent with the observation, based on FMR measurements in the critical region (Section 4.1) [6], that only **~11%** of the total Fe spins actually participate in the FM-PM phase transition. Recognizing that the Curie temperature for the FM clusters greatly exceeds the bulk T_C and that the relaxation time of the clusters, τ_{cl} , is much larger than the ^{57}Fe Mossbauer

measurement time, $\tau \approx \hbar/\Gamma \approx 10$ s, where Γ is the resonance linewidth of the Mössbauer transition, at all temperatures ranging from 4.2K to $T > T_C$, the observation that the bimodal structure in $P(H, f)$ persists to temperatures as high as T is in consonance with SANS evidence [17] for huge (200-400Å) static clusters which do not disorder at T_C and also with the existence of giant "superparamagnetic-like" clusters for temperatures well above T_C , as inferred from earlier BM [4,53,63] and Mossbauer [60,64] results. Contrary to this behaviour, a paramagnetic contribution to Mossbauer spectra is expected for $T > T_C$, which lies well below T_C , in terms of the AFM-FM model.

More drastic effects are noticed in the $P(H, f)$ at low temperatures as a function of Co concentration in a-Fe_{1-y}Co_yZr_{1-y-2y} alloys. For the alloys with y in the range $0 \leq y \leq 2$, the $P(H_{hf}^{TP})$ at 80K is bimodal for $T < T_C$, comprising two Gaussian peaks, as described earlier. When the Co concentration is increased beyond $y=4$, the low-field component is completely suppressed (Fig. 4.14). This behaviour is in consonance with the FMR result (Section 4.2) that FMR linewidth increases exponentially at low temperatures for alloys with $y \leq 2$ and this exponential increase gets suppressed for alloys with $y \geq 4$. Hence, a strong evidence exists for the suppression of the reentrant behaviour for $y \geq 4$. The effect of partial replacement of Fe with Co in the parent alloy a-Fe₉Zr can be gauged by an inspection of the concentration dependence of the low-field Gaussian peak in Fig. 4.14. It is observed that the area under this peak progressively gets reduced with increase in Co concentration, implying that the number of spins in the FM clus-

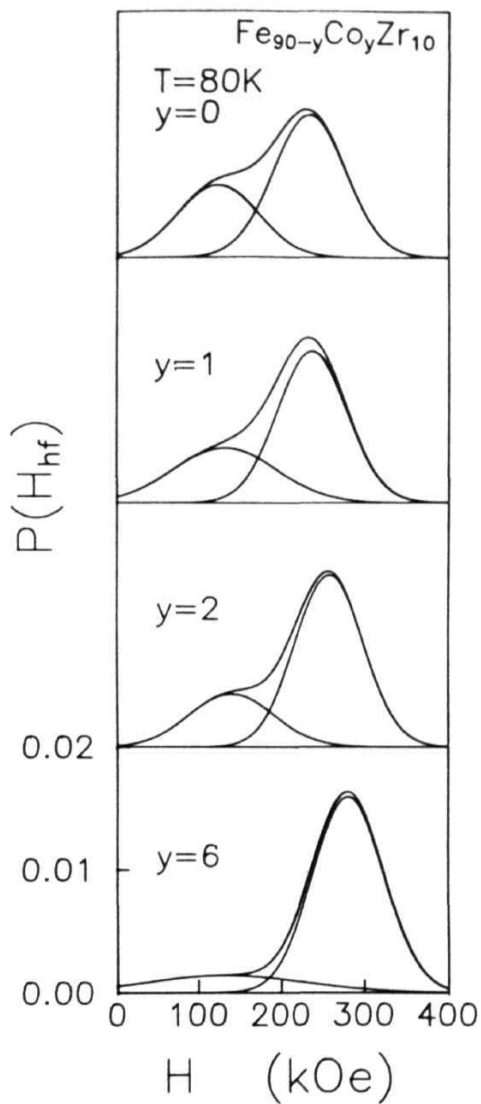


Fig. 4.14. Concentration dependence of $P(H_{hf})$ at 80K, showing the suppression of the low-field peak with increasing Co concentration.

ters is being **reduced**, or that the clusters are getting smaller and smaller in size. This can come about only when the addition of Co suppresses the competing interactions in the frustration zones surrounding the cluster, as suggested earlier, leading to a disintegration of these clusters into smaller ones.

4.4. Hyperfine fields

The average hyperfine field deduced from the TP analysis is denoted by \bar{H}_{hf}^{TP} and the peak positions of the two-Gaussian distributions corresponding to the peak values of the low-field and high-field components of $P(H_{hf}^{TP})$ are identified with the average hyperfine fields for the clusters and the FM matrix, respectively, and denoted by \bar{H}_{hf}^{CL} and \bar{H}_{hf}^{FM} . \bar{H}_{hf}^W is the average hyperfine field obtained from the Window analysis. The variation of the reduced average hyperfine fields \bar{H}_{hf}^W , \bar{H}_{hf}^{TP} , \bar{H}_{hf}^{FM} and \bar{H}_{hf}^{CL} with temperature has been analyzed in terms of the following expressions,

$$\begin{aligned} \bar{H}_{hf}(T)/\bar{H}_{hf}(0) &= [g\mu_B \xi(3/2)/M(0)] \\ &\times [k_B T / 4\pi D(0) (1 - D_2 T^2)]^{3/2} \end{aligned} \quad (4.28)$$

for spin-wave excitations, and

$$[\bar{H}_{hf}(T)/\bar{H}_{hf}(0)]^2 = A - BT^2 \quad (4.29)$$

for single-particle excitations.

Fig. 4.15 shows the quantities $[H_{hf}(T)/H_{hf}(0)]$ and $[\bar{H}_{hf}(T)/\bar{H}_{hf}(0)]^2$ plotted against $T^{3/2}$ and T^2 , respectively, for the various **above-mentioned** reduced average hyperfine fields for **a-Fe₉₀Zr₁₀**. For comparison, the spontaneous magnetization data

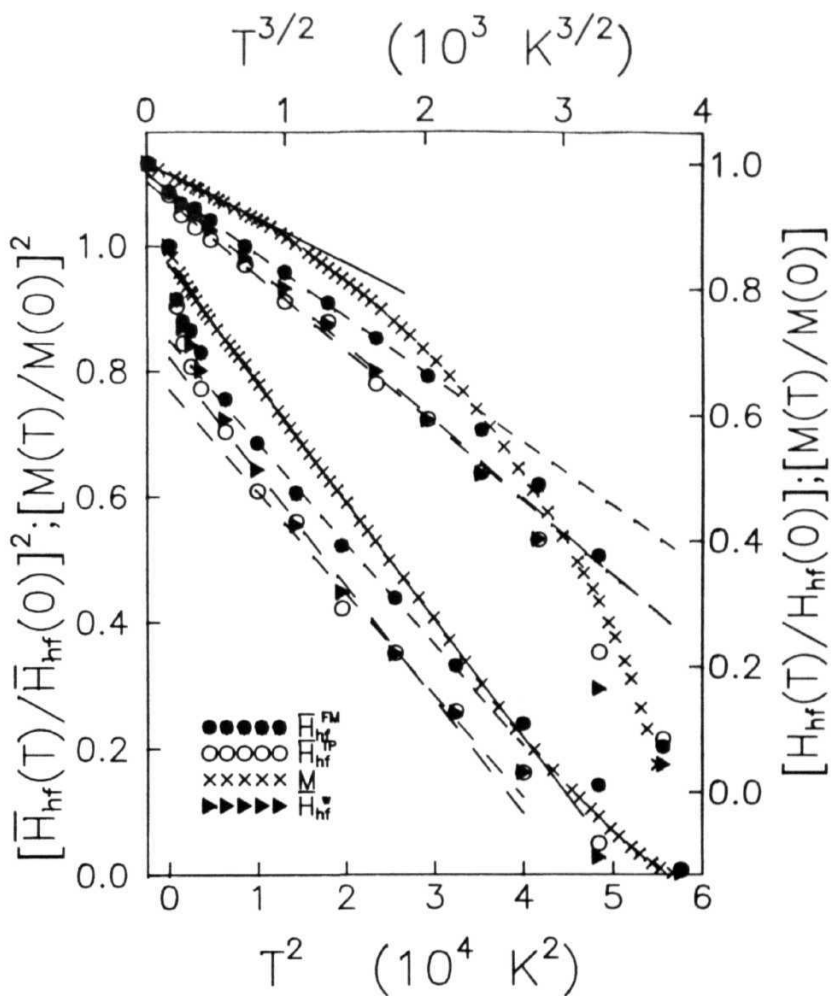


Fig. 4.15. Reduced average hyperfine fields, $h(T) \equiv H_{hf}(T)/H_{hf}(0)$, and reduced magnetization $m(T) \equiv M(T)/M(0)$ plotted against $T^{3/2}$, and the plots of $m^2(T)$ and $h^2(T)$ versus T . The curves drawn through the data points denote the best least-squares fits attempted in different temperature ranges based on Eqs. (4.28) and (4.29).

$M(0, T)$ obtained through an extrapolation of the $M^{1/\beta}$ vs. $(H/M)^{1/\gamma}$ isotherms [65] is plotted in the same format as the **hyper** fine fields. It is observed that the $\bar{H}_{hf}^W(T)/\bar{H}_{hf}^W(0)$ [$\bar{H}_{hf}^{TP}(T)/\bar{H}_{hf}^{TP}(0)$, $\bar{H}_{hf}^{FM}(T)/\bar{H}_{hf}^{FM}(0)$] data can be successfully fitted to Eq. (4.28) in two different temperature regions, i.e., in $0 < T < 0.21T_C$ with the choice of parameters $M(0) = 1000(1)$ [1001(4), 1000(3)] G, $D(0) = 24(2)$ [22(2), 25.5(20)] $\text{meV}\text{\AA}^2$, and $D_2 \approx 0$, and within $0.17T_C < T < 0.92T_C$ with $M(0) = 1000(3)$ [1000(3), 1000(3)] G, $D(0) = 29(2)$ [28(2), 31(2)] $\text{meV}\text{\AA}^2$, and $D_2 = [2.36(110)] \times 10^{-6}$ {[2.3(11)] $\times 10^{-6}$, [2.1(11)] $\times 10^{-6}$ } K^{-2} , respectively, in case of **a-Fe₉₀Zr₁₀**. Even though in the temperature range $0.33T_C < T < 0.75T_C$, Eq. (4.29) could also form a reasonable description of the various reduced average hyperfine fields, Eq. (4.28) provides a decidedly better fit to the data. It must be noted, however, that both the expressions mentioned above fail to describe the variation of \bar{H}_{hf}^{cl} with temperature.

The above analysis of the temperature dependence of the average hyperfine fields yields the following results : (i) spin-wave excitations are mainly responsible for $\bar{H}_{hf}^W(T)$, $\bar{H}_{hf}^{TP}(T)$ and $\bar{H}_{hf}^{FM}(T)$ in the range $T < 0.2T_C$ where these quantities as well as $M(0, T)$ deduced from BM data [12, 65] yield the same value, $D(0) \approx 24$ $\text{meV}\text{\AA}$, for the spin-wave stiffness coefficient; (ii) over a wide range of intermediate temperatures ($0.2T_C < T < 0.9T_C$) $D(0)$ possesses a higher value ($D(0) \approx 32$ $\text{meV}\text{\AA}$) and (iii) the hyperfine fields mentioned above do not follow the temperature dependence of spontaneous magnetization $M(0, T)$ obtained through an extrapolation of the $M^{1/\beta}$ vs. $(H/M)^{1/\gamma}$ isotherms, as is normally expected. To

elucidate the last point further, it is found that these fields mimic the temperature dependence of spontaneous **magnetization**, $M'(0,T)$, that is extracted from the '**in-field**' magnetization, as shown in Fig. 4.16. In this figure, $\bar{H}_{hf}^W(T)$, $\bar{H}_{hf}^{WF}(T)$ (peak value of the high-field Gaussian component of $P(H_{hf}^W)$), $\bar{H}_{hf}^{TP}(T)$, $\bar{H}_{hf}^{FM}(T)$ and $\bar{H}_{hf}^{CL}(T)$ are compared with $M(0,T)$ and $M'(0,T)$, where $M(0,T)$ is explained above and $M'(0,T)$ is the spontaneous magnetization data generated using the optimum parameter values [$M(0,0) = 1006G$, $D(0) = 32 \text{ meV}\text{\AA}^2$, $D = 1.5 \times 10^{-6} \text{ K}^{-2}$ and $S = 1.1 \times 10^{-6} \text{ K}^{-2}$] corresponding to the best **least-squares** fit to the "**in-field**" magnetization $M(H,T)$ data in the expression [65]

$$\begin{aligned} M'(0,T)/M(0,0) = [g\mu_B \xi(3/2)/M(0,0)] \times [k_B T / 4\pi D(0) (1 - D_2 T^2)]^{3/2} \\ + ST^2 \end{aligned} \quad (4.30)$$

It is well-known [12] that the thermoremanent and **thermomagnetic** effects as well as local-spin-density **fluctuations**, which arise from the corrections to the Stoner model, are completely suppressed by fields $H > 5kOe$ and hence, $M'(0,T)$ data, unlike the $M(0,T)$ data, do not make any allowance for the local-spin-density fluctuations as well as for the softening of the spin-wave modes for $T < 0.2T_N$. Thus the shaded region in Fig. 4.16 depicts the contribution to thermal demagnetization due to fluctuations in *local* magnetization. In view of this remark, the observation that the temperature dependence of \bar{H}_{hf}^W , \bar{H}_{hf}^{TP} , and \bar{H}_{hf}^{FM} coincides only with $M'(0,T)$ but not with $M(0,T)$, far from implying a wide disparity between the results of the local (**Mössbauer**) and bulk (magnetization) measurements, brings into focus the inadequacy of the Window and TP methods to describe the ME spectra for a spin system in

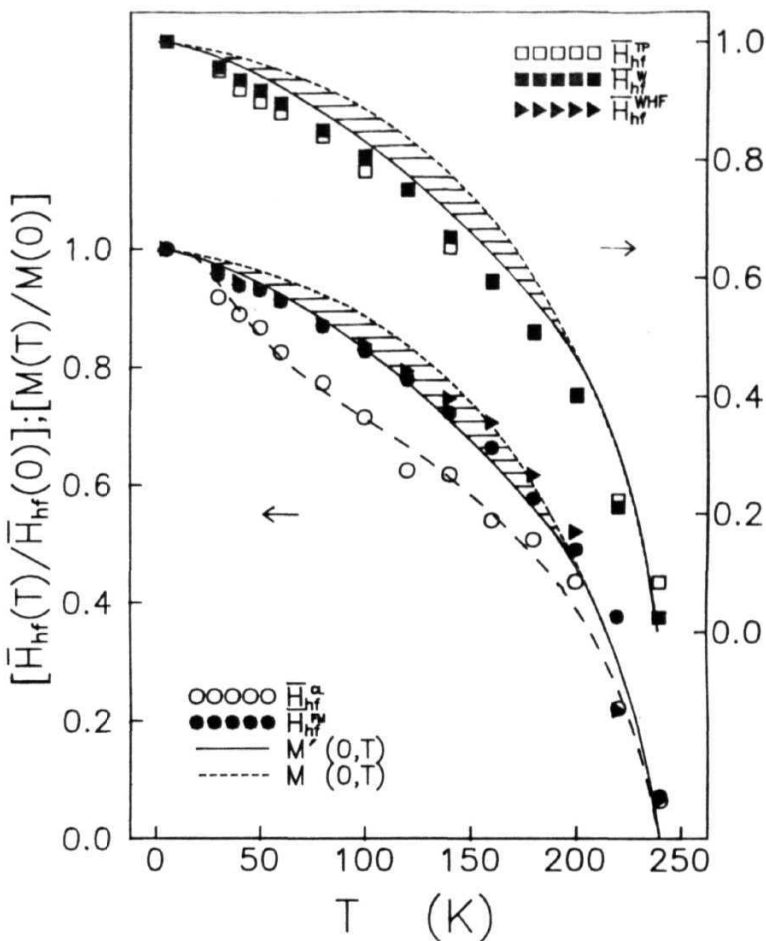


Fig. 4.16. Temperature dependence of the average hyperfine fields \bar{H}_{hf}^{TP} (\square), \bar{H}_{hf}^W (\blacksquare), the most probable hyperfine fields \bar{H}_{hf}^{CL} (\circ), \bar{H}_{hf}^{FM} (\bullet), \bar{H}_{hf}^{WHF} (\blacktriangleright) and of the spontaneous magnetization $M(0,T)$ (small dashed curve), $M'(0,T)$ (continuous curve). The dashed curve drawn through the open circled data points represents the least-squares fit to the $\bar{H}_{hf}^{CL}(T)$ data based on Eqs. (4.31) and (4.32) with the choice of parameters given in the text.

which the relaxation effects, arising from the JocaJ-spin-density (and hence local hyperfine field) **fluctuations**, are important. This limitation of the above methods stems from their underlying assumption that the spin correlation time $\chi \ll \tau$, the **Mössbauer** lifetime, or, in other words, in the time scales of the order τ , the hyperfine field and its distribution are assumed to be static. Therefore, a more rigorous analysis of the ME spectra recorded on the alloys in question, in which χ is expected to be comparable to τ , than that attempted hitherto should include the effects of lineshape originating not only from a distribution of hyperfine fields caused primarily by the structural fluctuations in these noncrystalline materials but also from the fluctuations in the hyperfine fields. Due to the lack of a proper underlying theoretical framework such an analysis has not been undertaken at present. In this connection, it should be mentioned that a stochastic model [66], which calculates the ME lineshape in the presence of a fixed axially symmetric **electric-field** gradient (EFG) and a magnetic hyperfine field which fluctuates randomly between the limits $+\hbar$ and $-\hbar$ and is directed either along or perpendicular to the axis of the EFG, has been successfully used by Rancourt et al [67] to describe the ME spectra in crystalline Fe-Ni Invar alloys. An attempt has been recently made by Ren and Ryan [68] to extend this model to amorphous systems and they too arrive at the above-mentioned contention that relaxation contributions to the ME spectra are important.

It has been reported earlier [60] that there is a break in slope in the temperature dependence of $H_{hf}(T)$ at a characteristic

temperature, T_f , which depends on the composition, in $a\text{-Fe}_{90+x}\text{Zr}_{10-x}$ alloys. This temperature was identified with the reentrant spin glass transition temperature below which an abrupt increase in $H_{hf}(T)$ occurs and the alloys enter into a reentrant spin glass-like state. Some workers [69], however, do not observe such an abrupt rise in $H_{hf}(T)$ at T_r and attribute this to the fact that T_r is too close to T_c for the composition $a\text{-Fe}_{90}\text{Zr}_{10}$. In the present study, the density of data points in the low temperature region ($5\text{K} < T < 80\text{K}$) is not adequate enough to unambiguously discern such an abrupt increase in $H_{hf}(T)$. Nevertheless, given the earlier observation that $\bar{H}_{hf}^{FM}(T)$ can be fitted over two temperature ranges, one ranging from 4.2K to $0.21T_c$ with $D(0)=24.0 \text{ meV}\text{\AA}^2$ and the other spanning temperatures from $0.17T_c$ to $0.92T_c$ with $D(0)=29.0 \text{ meV}\text{\AA}^2$, in a $\bar{H}_{hf}^{FM}(T)/\bar{H}_{hf}^{FM}(0) - \text{vs-} T^{3/2}$ plot, shows that there are deviations at low temperatures.

As mentioned earlier in the text, $\bar{H}_{hf}^{CL}(T)$ follows a unconventional behaviour. It is observed from Fig. 4.18 that \bar{H}_{hf}^{CL} differs markedly from $M'(0,T)$ and its temperature dependence resembles that of the hyperfine fields of Mn impurities in an Fe host [70]. Following a theoretical approach similar to that of Callen, Hone and Heeger [71] and of Wolfram and Hall [72], the weak coupling between the finite **FM** spin clusters and the infinite **FM** matrix may be approximated by a molecular (exchange) field acting on the spin clusters (impurities) due to the spins in the FM matrix (host) with the result that the reduced hyperfine field $\bar{H}_{hf}^{CL}(T)/\bar{H}_{hf}^{CL}(0)$ is given by

$$\bar{H}_{hf}^{CL}(T)/\bar{H}_{hf}^{CL}(0) = B_s(y) \quad (4.31)$$

with

$$\begin{aligned} y &= (g\mu_B H_{ex} S/k_B T) [M'(0, T)/M(0, 0)] \\ &= \lambda (T_C/T) [M'(0, T)/M(0, 0)] \end{aligned}$$

and

$$\lambda = g\mu_B H_{ex} S/k_B T_C$$

where B is the Brillouin function corresponding to the spin S of the clusters, $[M'(0, T)/M(0, 0)]$ is the reduced magnetization of the **FM** matrix, X is the **molecular-field** coupling parameter, and H_{6X} is the exchange (molecular) field experienced by the spin clusters on account of the FM matrix spins. An attempt to fit Eq. (4.31) to the $\bar{H}_{hf}^{cl}(T)/\bar{H}_{hf}^{cl}(0)$ data using a non-linear **least-squares-fit** computer program which treats X as a free-fitting parameter reveals that Eq. (4.31) (represented in Fig. 4.16 by the dashed curve) is obtained only when the temperature dependence of X takes the form

$$\lambda(T) = \alpha_0 - \exp[-(T/T_0)^\beta] \quad (4.32)$$

where the parameters α , β , and T_0 take on the values $\alpha = 1.32(3)$, $\beta_0 = 1.80(8)$ and $T_0 = 150(5)K$ for **a-Fe₉₀Zr₁₀**. The stretched exponential form of $A(T)$ is suggestive of the hierarchical nature of the exchange interaction between the spins contained within the clusters and those forming the FM matrix, and T_0 is a "characteristic" temperature beyond which **the** cluster-matrix exchange coupling picks up in strength at a more rapid rate. Such a situation may be visualized if there exist clusters within clusters such that with temperature increasing from 4.2K, first the spins belonging to the largest cluster and then those constituting the smaller **and smal-**

ler clusters are exposed to the exchange field of the FM matrix spins. In such a picture, T_0 marks a temperature above which an increasing number of smaller clusters "feel" the presence of the FM matrix and grow in size at the expense of the FM matrix. This interpretation is consistent with that given to the increase in the LFS fraction with temperature in Section 4.3.

In a measurement involving various compositions in an alloy series or for amorphous alloys of a similar kind, it is customary to compare the average value of the hyperfine field, H_{hf} , with the magnetic moment obtained from bulk magnetization measurements as a function of composition in order to find out whether or not there exists a quantitative relationship between H_{hf} and the magnetic moment, and if so, examine the implications about the relative importance of the different contributions to the H_{hf} . According to the phenomenological model commonly used to analyze the H_{hf} data in transition metals, there are two main contributions to H_{hf} , one of which is proportional to the local on-site moment and the other, to the surrounding moments [73]:

$$H_{hf} = A\mu_L + B\bar{\mu} \quad (4.33)$$

The local term $H_{hf}^{loc} (= A\mu_L)$ accounts for the polarization of the inner-shell (core) electrons by the localized 3-d electron spins, and the second term $H_{hf}^- (= B\bar{\mu})$ arises on account of the polarization of the conduction-electron spins by the moments on the surrounding atoms. Instead of following the customary approach mentioned above to estimate the coefficients A and B in Eq.

(4.33), these values are determined in the present case from the $H_{hf}(T)$ -vs- $\mu_{Fe}(T)$ plot (where $\mu_{Fe}(T)$ is calculated from the $M'(0, T)$ data) shown in Fig. 4.17. The dashed straight line passing through the origin in this figure corresponds to the coupling constant $B \approx 155 \text{ kOe}/\mu_B$ found in a-Fe. From this figure, it is noticed that the coefficient B has nearly the same value for the average hyperfine fields, $\bar{H}_{hf}^{FM}(\bar{\mu})$, $\bar{H}_{hf}^{TP}(\bar{\mu})$ and $\bar{H}_{hf}^W(\bar{\mu})$ in a-Fe₉₀Zr₁₀ as for $\bar{H}_{hf}(\bar{\mu})$ in a-Fe, but the former sets of data yield a finite intercept on the ordinate. In view of a finite value of H_{hf}^{OC} , the usual practice [10,69] of using the conversion factor $150 \text{ kOe}/\mu_B$ (valid for a-Fe) for calculating the iron moment from the observed H_{hf} for a-Fe₉₀+xZr_{10-x} alloys or sometimes for other Fe-based amorphous alloys can lead to erroneous results. This can be explained by taking the case of a-Fe at 4.2K for which $H_{hf}^{loc} = -200 \text{ kOe}$, $H_{hf}^{\Sigma} \approx -145 \text{ kOe}$ [73] and the moment at each site is the same so that $\mu = \mu = 2.212\mu_B$, the slope $B' (=A+B) \approx 156 \text{ kOe}/\mu_B$, and $H_{hf}(\bar{\mu}=0) = 0$. Contrasted with this behaviour, $H_{hf}^{loc} = 22(6) [-14(4)]$ and $H_{hf}^{\Sigma} = 156(5)\bar{\mu}_{Fe} [155(5)\bar{\mu}_{Fe}]$ in units of kOe for \bar{H}_{hf}^{FM} [\bar{H}_{hf}^{TP} or \bar{H}_{hf}^W] in a-Fe₉₀Zr₁₀ with $\bar{\mu}_{Fe}=1.53\mu_B$ at 4.2K, and the moment in this alloy differs from site to site due to topological disorder. From the above comparison, it is seen that H_{hf}^{loc} is one order of magnitude smaller while H_{hf} is about 1.6 times larger in a-Fe Zr₀ than in a-Fe. Therefore, the agreement in the values of the slope B for a-Fe₉₀Zr₁₀ and a-Fe is deceptive. Consequently, the moment values computed from H_{hf} using the above conversion factor [10,64,69] cannot be considered as reliable and the discrepancy between the moment values so calculated and those directly measured used as an argument [10,69] for the existence of noncollinear magnetic

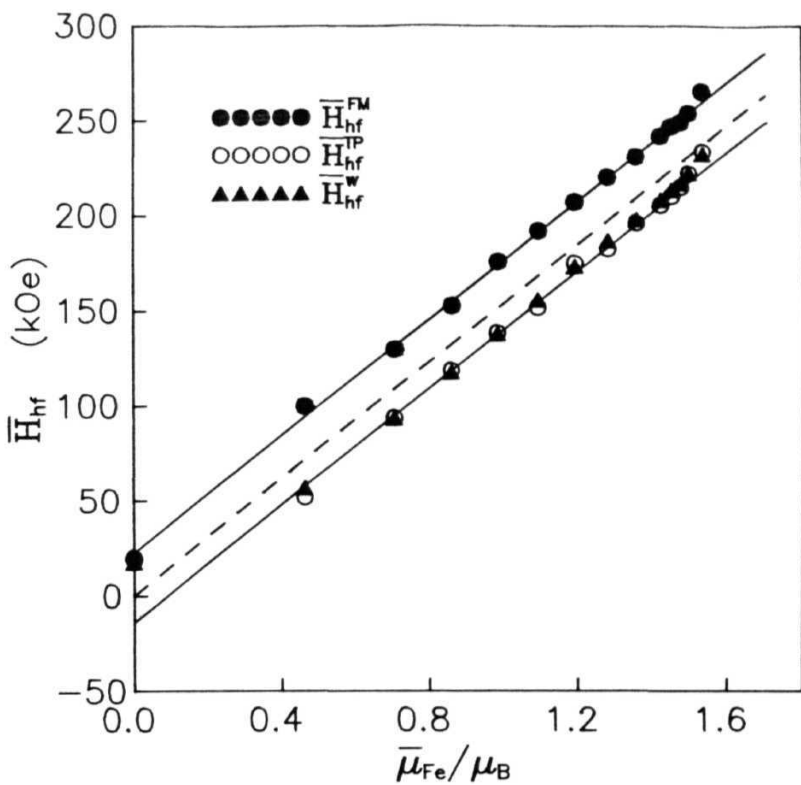


Fig. 4.17. Average hyperfine field, \overline{H}_{hf} , as a function of average magnetic moment on the Fe atom, $\overline{\mu}_{Fe}$.

structure in the ground **state** should be regarded with great caution. In this context, it is important to note that the estimate of $\approx 0.7\mu_B$ for the moment corresponding to the low-field peak in $P(H_{hf})$, calculated [8,10,57,64] from the value of \bar{H}_{hf}^{cl} at 4.2K following the above procedure and generally taken as evidence for the presence of **γ -Fe** regions in the amorphous FM matrix, does not make any sense in the light of the present finding that \bar{H}_{hf}^{cl} does not scale with $\bar{\mu}_F$. Moreover, the phenomenological model based on Eq. (4.33) is expected to find limited application so far as the systems in which local magnetization fluctuations govern the thermal demagnetization are concerned.

At this stage, it is relevant to point out that ME spectroscopy has also been used earlier to determine the critical exponent β for spontaneous magnetization [74-77]. This technique makes use of the existence of a linear relationship between the hyperfine field $H_{hf}(T)$ and $M_S(T)$ in the critical region. In analogy with Eq. (4.3) of Section A (FMR), the relation

$$H_{hf}(T)/H_{hf}(0) = r_{00}(-c)^*, \quad c < 0 \quad (4.34)$$

is used to deduce β from the measured $H_{hf}(T)$. However, the reliability of the values for β obtained by this method, particularly for amorphous **ferromagnets**, is in doubt since the accuracy in the hyperfine field measurements required for a precise determination of β can at best be obtained only for the spectra taken at reduced temperatures $|e| > 0.04$, i.e., for temperatures just outside the critical region. The problem that lies at the root of this observation is that ME spectra for

amorphous ferromagnets in the temperature range $|c| < 0.04$ are poorly resolved due to progressive smearing of the already broadened linewidths caused by the increasing width of the hyperfine field distribution as T/T_C . Therefore, reliable values of $H_f(T)$ cannot be obtained for $|c| < 0.04$, making the **asymptotic** critical region inaccessible to this technique. Hence, no attempt has been made in the present study to use the ME technique to study the critical behaviour.

The variation of the hyperfine fields with Co concentration y is shown in Fig. 4.18(a). Such a comparison between samples of different Co concentrations would be meaningful when it is made at the same T/T_C value. Hence the figure shows \bar{H}_{hf}^{TP} and \bar{H}_{hf}^{FM} as functions of y at $T \approx 0.6T_C$. It is observed that both \bar{H}_{hf}^{TP} and \bar{H}_{hf}^{FM} increase rapidly up to $y=2$ and then reach a plateau **for $y=6$** . This increase in hyperfine field can be mainly attributed to the increase in the polarization of the conduction-electron spins by the enhanced moment on the surrounding Fe atoms in the Co containing alloys. Assuming that the moment on the Co site does not change from the value of $1.53\mu_B$ for $Co_{90}Zr_{10}$, rapid increase in the average moment per alloy atom in **a-Fe₉₀ Co Zr** alloys for $y < 4$ (cf. Fig. 3.15)) reflects a strong increase in $\bar{\mu}$. The difference between \bar{H}_{hf}^{TP} and \bar{H}_{hf}^{FM} is initially large but narrows down with increasing Co concentration. This can be also explained on the basis of the discussion on the **bimodal** hyperfine field distribution and its suppression in the preceding section. It is obvious that the difference in \bar{H}_{hf}^{TP} and \bar{H}_{hf}^{FM} for $y < 2$ is caused by the presence of the low-field component in $P(H_{hf})$ **due to** large clusters. For $y > 2$,

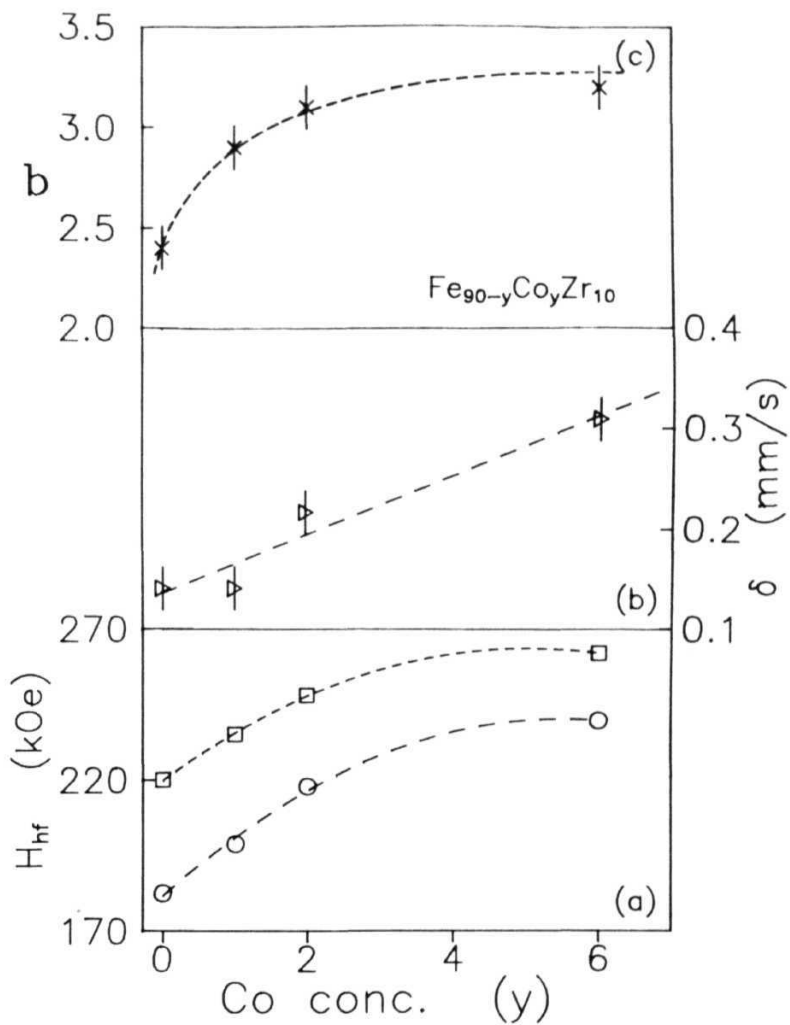


Fig. 4.18. Concentration dependence of the Mossbauer parameters, (a) average **hyperfine** fields, \bar{H}_{hf} (o) and \bar{H}_{hf}^{FM} (D), (b) **isomer** shift, and (c) **intensity** ratio, at $0.4T_c$.

the large clusters disintegrate into smaller clusters leading to the suppression of the low-field peak in $P(H_{hf})$ and hence the difference between δ_{hf}^{FM} and δ_{hf}^{FM} becomes less with increasing y .

4.5. Isomer shift

The temperature dependence of the average isomer shift δ for a-Fe Zr relative to a-Fe at 300K, shown in Figs. 3.26(b) and 3.27(b) deduced from the Window and TP analysis, respectively, reveals that while $\delta^M(T)$ and $\delta^{FM}(T)$ remain constant at $\approx -0.09(1)$ mm.s⁻¹ and $\approx -0.143(21)$ mm.s⁻¹ for $T < 150K$ and increase roughly linearly with temperature for higher temperatures, $\delta^{CL}(T)$ $-0.045(17)$ mm.s⁻¹ throughout the temperature range $5K \leq T \leq 240K$. As described in Section 2.8.1, the temperature-dependent contribution to the isomer shift is caused by the second-order Doppler (SOD) shift, whose slope is a linear function of temperature with a value given by $-3k_B/2Mc$. For ^{56}Fe , this slope has a value -7.2×10^{-4} mm.s⁻¹K⁻¹. For a-Fe₉₀Zr₁₀, the least-squares fits in the temperature range $140K < T < 240K$ ($140K < T < 220K$) yield the value $\partial\delta^{FM}(T)/\partial T = 7.4(3) \times 10^{-4}$ mm.s⁻¹K⁻¹ [$\partial\delta^M(T)/\partial T = 7.4(3) \times 10^{-4}$ mm.s⁻¹K⁻¹]. The slope turns out to be positive since the absorber is at a lower temperature relative to the source for temperatures up to 240K. A close agreement between the experimental and theoretical values of $\partial\delta(T)/\partial T$ indicates that the linear increase of $\delta(T)$ for $T > 150K$ is due to the SOD shift.

In Fig. 4.18(b), $\delta^{FM}(0.6T_C)$ is plotted against Co concentration. δ^{FM} is found to increase linearly with Co concentration

implying thereby that with increasing Co concentration the screening of **s-electrons** due to **d-electrons** increases so that the probability density of s-electrons at the Fe nucleus is progressively reduced.

4.6. Linewidth

Mössbauer linewidths $\Gamma^W(T)$, $\Gamma^{FM}(T)$ and $\Gamma^{CL}(T)$ for **a-Fe₉₀Zr₁₀**, displayed in Figs. 3.26(c) and 3.27(c), demonstrate that Γ^W has a **temperature-independent** value of $0.365(45) \text{ mm.s}^{-1}$ within the temperature region $5\text{K} < T < 240\text{K}$ as contrasted with Γ^{FM} and Γ^{CL} which remain constant at $\Gamma^{FM} = 0.378(12) \text{ mm.s}^{-1}$ and $\Gamma^{CL} = 0.45(5) \text{ mm.s}^{-1}$ for $T > 200\text{K}$, exhibit a steep fall above this temperature, and approach the intrinsic linewidth of the Fe source as **T•T_C**. The discrepancy between the results of the Window and TP fitting methods for $T > 200\text{K}$ is not genuine since it is known that the Window method does not yield reliable results for temperatures close to **T_C**. A rapid decline in the value of Γ as **T•T_C** is generally attributed to the narrowing down of the distribution of magnetic moments [78] (and hence of hyperfine fields) with increasing temperature due to long-range correlations between individual magnetic moments. This interpretation is, however, strictly valid only when the distribution of hyperfine fields is the sole cause of broadening and in that case $\Gamma(T) \propto H_{hf}(T)$. A perusal of Figs. **3.26(a)** and 3.26(c) and Figs. **3.27(a)** and 3.27(c) shows that such a direct correlation between $\Gamma(T)$ and $H_{hf}(T)$ does not exist particularly for $T < 200\text{K}$ where $\Gamma(T)$ is roughly constant while $H_{hf}(T)$ continues to increase as the temperature is lowered below 200K. It has already been mentioned in Section 4.4 that the

local-spin-density fluctuations **significantly** contribute to thermal demagnetization over a wide range of temperatures including those in the close proximity to T_C and hence, the above comparison between $\Gamma(T)$ and $H_{hf}(T)$ points to the inherent limitation of the TP and **Window** methods in that none of them incorporates the relaxation contribution to Γ and $H_{hf}(T)$. Practically no change in Γ with Co concentration in **a-Fe_{90-v}Co_vZr₁₀ alloys** could be discerned within the uncertainty limits.

4.7. Intensity ratio and magnetic moment alignment

The intensity ratio b , by virtue of its definition (Section 2.8.5)

$$b = 4\sin^2\vartheta / (1 + \cos^2\vartheta) \quad (4.34)$$

in terms of the angle ϑ between the γ -ray and *local* magnetic hyperfine field (or *local* magnetic moment) directions, provides useful information about the local-spin arrangement. According to Eq. (4.34), $b = 2$ for a perfectly random alignment of the local moments (spin glass order) whereas b assumes the limiting values 0 and 4 when all the moments are aligned *parallel* ($\vartheta=0^\circ$) and *perpendicular* ($\vartheta=90^\circ$) to the γ -ray direction, respectively. The average intensity ratio b therefore reflects the *average* orientation of the moments, which, in turn, can be represented by an alternative form of Eq. (4.34), i.e.,

$$\langle \cos^2\vartheta \rangle = (4-b)/(4+b) \text{ or } \langle \sin^2\vartheta \rangle = 2b/(4+b) \quad (4.35)$$

where $\langle \rangle$ denotes the average over the distribution of angle ϑ . The **temperature** dependence of the average intensity ratios b^v , b^m and

b^{cl} for $a\text{-Fe}_{90}\text{Zr}_{10}$, shown in Figs. 3.26(d) and 3.27(d), demonstrates that $b^u(T)$ conforms very well with $b^{FM}(T)$ in that both of them exhibit a sharp fall for $T < 1.5T_{RE}$, a very weak or no variation (within error limits) with temperature in the intermediate range $50K < T < 200K$ and a steep rise for $T > 200K$, as contrasted with a roughly constant value of $b^{cl} = 1.55(10)$ for $T < 150K$, and a rapid increase in $b^{cl}(T)$ for $T > 150K$. When $\langle \vartheta \rangle$ is calculated from Eqs. (4.34) and (4.35) for different intensity ratios, it turns out that the mean angle $\langle \vartheta^{FM} \rangle$ corresponding to b^{FM} (or b^u) increases from 59° to 61° as b^{FM} decreases from 2.5 to 2.3 in the temperature range $50K < T < 200K$. The calculated values of $\langle \vartheta^{FM} \rangle$ indicate that, on average, the moments point 30 out of the sample plane presumably due to the competition between the magnetic anisotropy and the shape anisotropy; the former anisotropy field tends to orient the moments away from the sample plane while the latter one tries to constrain them within the sample plane. A rapid decline in the value of b^{FM} or b^u for $T < 1.5T_{RE}$ is, therefore, a manifestation of a steep increase in the strength of the local random anisotropy (LRA) fields [12] which develop at the interface between the frozen FM clusters and the FM matrix, as the temperature is lowered below T_{RE} and the freezing process progressively curtails the freedom of the spin clusters around their random mean orientations. These LRA fields may, in turn, be responsible for the slight canting of spins within the FM matrix and thereby result in the softening of spin-wave modes. The fact that $b^{FM} \rightarrow 2$ at $T = 5K$ should not be interpreted as a transition to a pure (cluster) spin-glass state or alternatively, termed as a complete destruction of the long-range ferromagnetic order due to the imposition

of a large LRA field on the FM matrix by the clusters frozen in random orientations. This is so because, (i) the spontaneous moment does not go to zero as $T \rightarrow 5K$ [12,65], (ii) value of b^{CL} is quite different from 2.0, and (iii) for temperatures as low as 4.2K, b has values close to 2.0 for Fe-rich amorphous $Fe_{100-x}B_x$ alloys, which do not exhibit reentrant behaviour at any temperature. The existence of a mixed state for $T < T_{D.F.}$ is also corroborated by the persistence of a well-defined domain structure down to 4.2K [79] for $a-Fe_{90+x}Zr_{10-x}$ alloys. The value of b^{CL} , which stays constant at 1.55(10) from $T \approx 150K$ down to the lowest temperature (in sharp contrast to the variation of b^{FM}), when substituted in Eq. (4.35) yields the result $\langle \theta^{CL} \rangle = 48(2)^\circ$. While $\langle \theta^{CL} \rangle \approx 45^\circ$ implies that the "out-of-plane" magnetic anisotropy energy and the demagnetizing energy are nearly of the same magnitude for the spin clusters, the temperature-independent nature of b^{CL} for $T < 150K$ suggests that the freezing of the spin clusters in random orientations starts at a temperature well above T but $< 150K$. A sudden increase in $b^{CL}(T)$ for $T > 150K$ as well as in $b^{FM}(T)$ for $T > 200K$ towards $b=4.0$ reflects the dominance of the shape anisotropy as a result of a drastic reduction in the magnetic anisotropy for temperatures close to T .

ted by the persistence of a well-defined domain structure down to 4.2K [79] for $a-Fe_{90+x}Zr_{10-x}$ alloys. The value of b^{CL} , which stays constant at 1.55(10) from $T \approx 150K$ down to the lowest temperature (in sharp contrast to the variation of b^{FM}), when substituted in Eq. (4.35) yields the result $\langle \theta^{CL} \rangle = 48(2)^\circ$. While $\langle \theta^{CL} \rangle \approx 45^\circ$ implies that the "out-of-plane" magnetic anisotropy energy and the demagnetizing energy are nearly of the same magnitude for the spin clusters, the temperature-independent nature of b^{CL} for $T < 150K$ suggests that the freezing of the spin clusters in random orientations starts at a temperature well above T but $< 150K$. A sudden increase in $b^{CL}(T)$ for $T > 150K$ as well as in $b^{FM}(T)$ for $T > 200K$ towards $b=4.0$ reflects the dominance of the shape anisotropy as a result of a drastic reduction in the magnetic anisotropy for temperatures close to T .

The intensity ratio is found to increase with Co concentration as shown in Fig. 4.18(c). The figure shows the variation of $b^{FM}(0.6T_C)$ with y and it is observed that after an initial steep increase from 2.4 for $y=0$ to 2.9 for $y=1$, it settles down at a value of 3.2 for $y=6$. This indicates that the shape anisotropy dominates as other anisotropy contributions weaken with increasing Co concentration.

REFERENCES

- [1] H. Yamauchi, H. Onodera and H. **Yamamoto**, J. Phys. **Soc. Jpn.** **53**, 747 (1984).
- [2] K. **Winschuh** and M. Rosenberg, J. **Appl.** Phys. **61**, 4401 (1987).
- [3] **L.C.** Le Guillou and J. **Zinn-Justin**, **Phys.** Rev. B21, 3976 (1980).
- [4] S.N. **Kaul**, J. Phys. F: Met. Phys. 18, 2089 (1988).
- [5] H. Hiroyoshi, **K. Fukamichi**, A. Hoshi and Y. **Nakagawa**, in *High Field Magnetism*, edited by M. Date (North-Holland, Amsterdam, 1983), **p.113**.
- [6] **S.N.** Kaul and **P.D.** Babu, **Phys.** Rev. **B45**, 295 (1992).
- [7] D.S. Rodbell, Phys. Rev. Lett. 13, 471 (1964); **S.** Haraldson and L. Petterson, J. Phys. **Chem. Solids** **42**, 681 (1981).
- [8] P. Deppe, **K. Fukamichi**, F.S. Li, M. Rosenberg and M. Sostarich, IEEE Trans. Magn. **MAG-20**, 1367 (1984).
- [9] B. Heinrich, J.M. Rudd, K. Urquhart, K. Myrtle and J.F. Cochran, J. **Appl.** Phys. 55, 1814 (1984).
- [10] D.H. Ryan, J.M.D. Coey, E. Batalla, Z. Altounian and **J.O. Ström-Olsen**, Phys. Rev. B35, 8630 (1987).
- [11] D.A. Read, **G.C. Hallam** and M. Chirwa, J. Magn. Magn. Mater. 82, 83 (1989).
- [12] S.N. Kaul, J. Phys. :Condens. Matter 3, 4027 (1991); S.N. Kaul and P.D. Babu, J. Phys. :**Condens.** Matter 4, 6429 (1992).
- [13] C. **Elsässer**, M. **Fähnle**, E.H. Brandt and **M.C.** Böhm, J. Phys. F: Met. Phys., 18, 2463 (1988).
- [14] **M.C.** Böhm, C. **Elsässer**, M. **Fähnle** and **E.H.** Brandt, Chem. Phys. **130**, 65 (1989).

- [15] H. **Kronmüller**, Phys. Status Solidi (b) **127**, 531 (1985).
- [16] R. Reisser, M. **Fähnle** and H. **Kronmüller**, J. **Magn. Magn. Mater.** 75, 45 (1988).
- [17] J.J. Rhyne, **R.W.** Erwin, J.A. Fernandez-Baca and G.E. Fish, J. **Appl. Phys.** 63, 4080 (1988)
- [18] R. Krishnan, K.V. Rao and H.H. Liebermann, J. Appl. Phys. 55, 1823 (1984).
- [19] **W.** Beck and H. **Kronmüller**, Phys. Stat. Sol. (b) 132, 449 (1985)
- [20] **G.E.Fish** and J.J.Rhyne, J. Appl. Phys. 61, 454 (1987).
- [21] F.Keffer, in *Encyclopaedia of Physics*, edited by H.P.J. **Wijn** (Springer, Berlin, 1966) **Vol.XVIII**, Pt. 2, p. 1
- [22] J.Mathon and **E.P.Wohlfarth**, **Proc. R. Soc. London**, Ser. A 302, 409 (1968).
- [23] S.N.Kaul and V.Siruguri, J. Phys. :Condens. Matter 4, 505 (1992) .
- [24] S.N.Kaul, Phys. Rev. B27, 5761 (1983).
- [25] S. Dey, U. Gorres, H.J.V. Nielsen, M. Rosenberg and M. Sostarich, J. Physique 41, C8-678 (1980).
- [26] T. **Soumura**, K. Takeda, T. Wakano, K. Terasawa and T. Maeda, J. Magn. Magn. **Mater.** 58, 202 (1986).
- [27] S.N. **Kaul** and T.V.S.M. Mohan Babu, J. Phys. :Condens. Matter 1, 8509 (1989).
- [28] R.J. **Birgeneau**, J.A. Tarvin, G. Shirane, E.M. Gyorgy, **R.C.** Sherwood, H.S. Chen and C.L. Chien, Phys. Rev. **B18**, 2192 (1978).
- [29] G. Hilscher, R. Haferl, H, **Kirchmayr**, M. **Müller** and H.J. **Güntherodt**, J. Phys. **F11**, 2429 (1981).
- [30] H. Fujimori, in *Amorphous Metallic Alloys*, edited by F.E.

Luborsky (Butterworths, London, 1983), p. 300.

- [31] D.J. Webb, S.M. Bhagat, K. **Moorjani**, T.O. Poehler and F.G. Satkiewicz, Solid State Commun. 43, 239 (1982).
- [32] D.J. Webb and S.M. Bhagat, J. Magn. Magn. Mater. 42, 109 (1984).
- [33] B. Heinrich, K. Myrtle, J.M. **Rudd**, J.F. Cochran and R. Hasegawa, J. Magn. Magn. Mater. 31-34, 1597 (1983); B. Heinrich, D. Fraitova and V. **Kambersky**, Phys. Status Solidi 23, 501 (1967).
- [34] M.L. Spano and S.M. Bhagat, J. Magn. Magn. Mater. 24, 143 (1981).
- [35] J.F. Cochran, K. Myrtle and B. Heinrich, J. Appl. Phys. 53, 2261 (1982).
- [36] J.F. Cochran, B. Heinrich and R. Hasegawa, J. Appl. Phys. 57, 3690 (1985).
- [37] U. Mizutani, M. Matsuura and K. **Fukamichi**, J. Phys. F: Met. Phys. 14, 731 (1984).
- [38] **H.Neddermeyer** and **Th.Paul**, Phys. Rev. **B36**, 4148 (1987).
- [39] M. Rosenberg, U. Hardebusch, A. **Schöne-Warnefeld**, R. Wernhardt and K. Fukamichi, J. Phys. F : Met. Phys. 18, 259 (1988).
- [40] **B.R.** Coles, B.V.B. Sarkissian and R.H. Taylor, Phil. Mag. B37, 789 (1978).
- [41] **M.J.** Park, S.M. Bhagat, M.A. **Manheimer** and K. Moorjani, J. Magn. Magn. Mater. 59, 287 (1986).
- [42] S.M. Bhagat, M.L. Spano and J.N. Lloyd, Solid State Commun. **38**, 261 (1981).
- [43] **T.F. Rosenbaum**, **L.W. Rupp,Jr.**, **G.A. Thomas**, **W.M. Walsh,Jr.**,

- H.S. Chen, J.R. Banavar and P.B. Littlewood, *Solid State Commun.* **42**, 725 (1982).
- [44] S.N. **Kaul**, *Solid State Commun.* **36**, 279 (1980); *Phys. Rev.* **B22**, 278 (1980).
- [45] S. N. Kaul, *IEEE Trans. Magn.* **MAG-20**, 1290 (1984).
- [46] S. N. Kaul, *J. Magn. Magn. Mater* **53**, 5 (1985).
- [47] M.A. Continentino, *J. Phys. C* **16**, L71 (1983) ; *Phys. Rev.* **B27**, 4351 (1983) .
- [48] S.B. Liao, S.M. Bhagat, M.A. **Manheimer** and M.J. Park, *Solid State Commun.* **63**, 119 (1987).
- [49] V. Siruguri, S.N. Kaul, A.K. **Nigam**, G. Chandra, **R.M. Kadam** and M.D. Sastry, in *Proc. Int. Workshop on Ordering Disorder*, (**AIP**, New York, 1993) to be published.
- [50] M.H. Cohen and M.A. Continentino, *Solid State Commun.* **55**, 609 (1985).
- [51] D. Stauffer, *Phys. Rep.* **54**, 1 (1979).
- [52] M. Ghafari, U. Gonser, H.-G. Wagner and M. **Naka**, *Nucl. Instrum. Methods* **199**, 197 (1982).
- [53] H. **Yamamoto**, H. Onodera, K. **Hosoyama**, T. **Masumoto** and H. **Yamauchi**, *J. Magn. Magn. Mater.* **31-34**, 1579 (1983).
- [54] S. N. Kaul, **C. Bansal**, T. **Kumaran** and M. Havalgi, *Phys. Rev.* **B38**, 9248 (1988).
- [55] V. Siruguri, S. N. Kaul, G. **Rajaram** and G. Chandra, *Proc. Solid State Physics Symp. (India)* **31C**, 233 (1988); *Anales de Fisica* **B86**, 181 (1990).
- [56] **D. H. Ryan** and H. Ren, *J. Appl. Phys.* **69**, 5057 (1991).
- [57] H. Lerchner and M. Rosenberg, *Hyper. Inter.* **39**, 51 (1988).
- [58] A. H. Morrish, R. J. Pollard, Z. S. Wronski and A. **Calka**,

Phys. Rev. B32, 7528 (1985).

- [59] **M. Gabay** and **G. Toulouse**, Phys. Rev. Lett. 47, 201 (1981).
- [60] **M. Ghafari**, **N. Chmielek**, **W. Keune** and **C. P. Foley**, Physica B161, 222 (1989).
- [61] **S. N. Kaul** and **V. Siruguri**, Anales de Fisica B86, 70 (1990).
- [62] **S. N. Kaul** and **Ch. V. Mohan**, J. Phys. :Condens. Matter 3, 2703 (1991).
- [63] **S.N.Kaul**, Phys. Rev. **B27**, 6923 (1983).
- [64] **M. Ghafari**, **W. Keune**, **R. A. Brand**, **R. K. Day** and **J. B. Dunlop**, Mat. Sci. Engg. 99, 65 (1988).
- [65] **S.N. Kaul**, **V. Siruguri** and **G. Chandra**, Phys. Rev. B45, 12343 (1992).
- [66] **M. Blume** and **J. A. Tjon**, Phys. Rev. 165, 446 (1968).
- [67] **D. G. Rancourt**, **S. R. Julian** and **J. M. Daniels**, J. Magn. Magn. Mater. 51, 83 (1985); **D. G. Rancourt**, **H. H. A. Smit** and **R. C. Thiel**, J. Magn. Magn. Mater. 66, 121 (1987).
- [68] **H. Ren** and **D.H. Ryan**, J. Appl. Phys. 70, 5837 (1990).
- [69] **D. H. Ryan**, **J. O. Ström-Olsen**, **R. Provencher** and **M. Townsend**, **J. Appl. Phys.** 64, 5787 (1988).
- [70] **V. Jaccarino**, **L. R. Walker** and **G. K. Wertheim**, Phys. Rev. Lett. 13, 752 (1964).
- [71] **H. Callen**, **D. Hone** and **A. Heeger**, Phys. Lett. 17, 233 (1965).
- [72] **T. Wolfram** and **W. Hall**, Phys. Rev. 143, 284 (1966).
- [73] **P. Panissod**, **J. Durand** and **J. I. Budnick**, **Nucl. Instr. Methods** 199, 99 (1982).
- [74] **C.L.Chien** and **R.Hasegawa**, Phys. Rev. **B16**, 3024 (1977).
- [75] **H.Keller**, **K.V.Rao**, **P.G.Debrunner** and **H.S.Chen**, J. Appl. Phys. **52**, 1753 (1981).

- [76] **A.K.Bhatnagar** and N.Ravi, Solid State **Commun.** **44**, 905 (1982).
- [77] **A.K.Bhatnagar**, **B.Bhanu Prasad** and **R.Jagannathan**, Phys. Rev. B29. 4896 (1984).
- [78] **J. Balogh** and **I. Vincze**, Solid State Commun. 25, 695 (1978).
- [79] **S. Senoussi**, **S. Hadjoudj** and **R. Foumeaux**, Phys. Rev. Lett. 61, 1013 (1988).

SUMMARY AND CONCLUSIONS

SUMMARY AND CONCLUSIONS

Detailed **ferromagnetic** resonance (FMR) and **"zero-field"** Mössbauer effect (ME) measurements have been performed on amorphous (a-) $\text{a-Fe}_{90+x}\text{Zr}_{10-x}$ ($0 \leq x \leq 1$) and $\text{Fe}_{90-y}\text{Co}_y\text{Zr}_{10}$ ($0 \leq y \leq 18$ and $y=90$) alloys over a wide ranges of temperatures from 5K to 500K.

The FMR results have shown that, for alloys in question, there exist two distinct resonances, which manifest themselves in specific temperature regimes. For temperatures $T < T_C$, the spectra consist of a single primary resonance which shifts to higher fields and broadens out as temperature is **raised**. At $T \approx T_C$, a secondary resonance appears at a lower field value which gets well-resolved for temperatures $T > T_C + 10\text{K}$.

The critical exponents β and γ have been determined to a reasonably high accuracy using the FMR technique, and, contrary to earlier findings, they are found to be *independent* of the alloy composition and possess 3D **Heisenberg-like** values, thus implying that the transition at T_C is well-defined and quenched disorder does not alter the critical behaviour of the pure spin system with specific heat critical exponent $\alpha < 0$, in accordance with the well-known Harris criterion. The fraction, c , of spins actually participating in the ferromagnetic (FM) to paramagnetic (PM) phase transition is very small ($c \approx 11\%$) in $\text{a-Fe}_{90+x}\text{Zr}_{10-x}$ and increases with Co concentration to $\approx 30\%$ for $y=10$ in $\text{a-Fe}_{90}\text{Co}_y\text{Zr}_{10}$ alloys.

While the dominant contribution to thermal demagnetization is from spin-wave excitations, additional contribution from single-particle excitations may not be ruled out. Spin wave stiffness coefficient **renormalizes** with temperature in accordance with the predictions of the itinerant-electron model. Competing interactions in **a-Fe_{90+x}Zr_{10-x}** and **a-Fe_{90-y}Co_yZr₁₀** ($0 \leq y \leq 2$) alloys confine the range of direct exchange interactions to nearest neighbours only, and the replacement of Fe with Co results in the suppression of competing interactions and the range of direct exchange interactions now extends to next-nearest neighbours also.

The temperature dependence of **FMR** linewidths can be described by the relation, $\Delta H_{pp}(T) = \Delta H_0(T) + \Delta H_{LLG}(T)$ over the intermediate temperatures and the critical region. While ΔH_{LLG} is the Gilbert relaxation term, ΔH_0 has its origin in the two- or **multi-magnon** scattering mechanism and has the form $\Delta H_0(T) = H_0 + aM_s(T) + bM(T)$. ΔH_0 approaches a constant value $\propto H_0$ in the critical region where the terms involving M_s are negligibly small. The **Landau-Lifshitz-Gilbert** damping parameter A is *temperature-independent*, and decreases with increasing Co concentration in the case of **a-Fe_{90-y}Co_yZr₁₀** alloys. The Lande splitting factor g is also temperature-independent but has a **concentration-independent** value of 2.07 ± 0.02 . At low temperatures ($10K \leq T \leq 80K$) the FMR linewidth for **a-Fe_{90+x}Zr_{10-x}** and **a-Fe_{90-y}Co_yZr₁₀** alloys with $y \leq 2$ increases exponentially according to the empirical relation, $\Gamma(T) = r + \Gamma_0 (T/T_0)^n \exp(-T/T_0)$, and for Co concentrations exceeding $y=4$ only a slight increase in linewidth occurs with lowering of temperature indicating progressive suppression of the reentrant

behaviour.

Temperature and angular (at $T \approx 0.6T_C$) dependences of the FMR resonance fields for the primary resonance have shown that the uniaxial anisotropy field, H_u , scales with M and increases with Co concentration. The origin of H_k presumably lies in the pseudo-dipolar atomic pair ordering mechanism, as in other ferromagnetic amorphous alloys. By contrast, $H_k \approx 0$ for the secondary resonance.

A detailed analysis of ME measurements on $a\text{-Fe}_{90}\text{Co}_{10}\text{Zr}_{10}$ and $a\text{-Fe}_{90}\text{Co}_{10}\text{Zr}_{10}$ alloys with $y \leq 2$ shows that the hyperfine field distribution in these alloys at all temperatures $< T_C$ is **bimodal**, comprising low- and high-field components. This finding contradicts the claims made earlier that this **bimodality** is an artifact of the fitting procedures used. The temperature dependence of these components, which have their origin in the *infinite* FM matrix-plus- finite spin clusters picture, show that the bulk of the spins (90% for $a\text{-Fe}_{90}\text{Zr}_{10}$) are in the clusters at $T \approx T_C$, thus leaving only a small fraction ($\approx 10\%$ for $a\text{-Fe}_{90}\text{Zr}_{10}$) of them in the FM matrix to participate in the FM-PM transition, in consonance with the FMR results. A bimodal hyperfine field is a characteristic aspect of the reentrant behaviour. The low-field component (Gaussian) of the hyperfine field distribution is completely suppressed for Co concentrations greater than 4. Consistent with the FMR results, this observation indicates a total suppression of the reentrant behaviour for $y > 4$ in $a\text{-Fe}_{90}\text{Co}_{10}\text{Zr}_{10}$ alloys.

The spin freezing process does not begin at any specific

temperature T_L but this process proceeds gradually over a wide range of temperatures starting from $\approx 3T_{RE}$ down to the lowest temperature. The spontaneous magnetization does not go to zero at any temperature below T_{RE} and there exists a "mixed" phase (ferromagnetic order plus cluster spin-glass order) for $T < T_{RE}$. For temperatures below $\approx 1.5T_{RE}$, the softening of spin waves takes place.

The usual practice of comparing the moment values computed from H_{hf} using the conversion factor of $150 \text{ kOe}/\mu_B$ (valid for $\alpha\text{-Fe}$) with those directly measured must be taken with great caution. The argument used by some authors to attribute the low-field peak in the hyperfine field distribution to the presence of $\gamma\text{-Fe}$ regions in the FM matrix is incorrect.

The temperature dependence of the average hyperfine fields $H_f(T)$ exposes the limitation of the existing methods of Mössbauer data analysis in that they do not take into account the relaxation contributions arising from the local-spin-density fluctuations (and hence from hyperfine field fluctuations), which are dominant over a wide range of intermediate temperatures in Fe-rich $a\text{-Fe}_{90-y}\text{Co}_y\text{Zr}_{10}$ alloys.

Of all the existing theories the finite FM clusters and infinite FM matrix model offers the most plausible explanation for all the diverse aspects of the FMR and ME results.

Scope for further work

There is a lot of scope for further research work in $\text{a-Fe}_{90+x}\text{Zr}_{10-x}$ and $\text{a-Fe}_{90}\text{CoZr}_{10}$ alloys. FMR measurements in the present investigation have been limited to fields of $\sim 10\text{kOe}$. Availability of higher magnetic fields would help to study the spin wave resonances and the surface magnons. Frequency-dependent FMR studies, especially at lower frequencies, would throw more light on the origin of ΔH_0 , the frequency-independent part of the line-width.

In-field Mossbauer is also a very useful tool. The disappearance of the 2 and 5 lines of the Mossbauer spectrum in such a measurement when the external magnetic field of sufficient strength so as to saturate longitudinal ferromagnetic order applied above a characteristic temperature T_{xy} and their subsequent appearance on cooling through T_{xy} been used as an argument for the validity of the transverse-spin freezing (TSF) model. If this model were correct then the temperature T_{xy} at which the 2 and 5 ME lines appear should not change when the sample is cooled through T_{xy} at different but fixed values of applied fields that exceed the field H^* required to saturate the sample for $T > T_{xy}$ and should not depend on whether the field is applied during the heating or cooling cycle. It would be most interesting to verify this aspect since according to the finite spin clusters and infinite FM matrix model, this temperature would depend on the value of the applied field for $H > H^*$ and also on the thermomagnetic of the sample.

The **methods** presently used to analyze the ME spectra in **amorphous** alloys do not take into account the relaxation effects arising from *local* spin-density fluctuations and hence hyperfine field **fluctuations**. A theoretical framework which incorporates such relaxation effects into the analysis **is** called for.

LIST OF PUBLICATIONS

Papers published in refereed journals

1. "FMR study of amorphous weak itinerant **ferromagnet**"
V.Siruguri and S.N.Kaul
Key Engg. Mater. 13-15. 679 (1987).
2. "Origin of magnetism in amorphous $\text{Ni}_{81.6}\text{B}_{18.4}$ alloy"
S.N.Kaul and V.Siruguri
J. Phys. F: Met. Phys. 17, **L255** (1987).
3. "FMR studies on amorphous $\text{Fe}_{90+x}\text{Zr}_{10-x}$ alloys"
S.N.Kaul and V.Siruguri
Anales de Fisica **B86**, 70 (1990).
4. "Evidence for reentrant spin glass behaviour in amorphous Fe_9Zr alloy from Mossbauer measurements"
V.Siruguri, S.N.Kaul, **G.Rajaram** and G.Chandra
Anales de Fisica **B86**, 181 (1990).
5. "Ferromagnetic resonance evidence for long-range ferromagnetic ordering in amorphous Fe-rich $\text{Fe}_{100-x}\text{Zr}_x$ alloys"
S.N.Kaul and V.Siruguri
J. Phys.: Condens. Matter **4**, 505 (1992).
6. "Magnetization and Mossbauer study of the reentrant amorphous $\text{Fe}_{90}\text{Zr}_{10}$ alloy"
S.N.Kaul, V.Siruguri and G.Chandra
Phys. Rev. **B45**, 12343 (1992).

Papers presented at Conferences and published in their Proceedings

1. "Nature of magnetism in Fe-rich amorphous $\text{Fe}_{100-x}\text{Zr}_x$ alloys",
V.Siruguri and S.N.Kaul
Proc. of Solid State Phys. Symp. (India :DAE) **31C**, 234 (1988).
2. "**Mössbauer** studies on an amorphous reentrant alloy: $\text{Fe}_{90}\text{Zr}_{10}$ "
V.Siruguri, S.N.Kaul, G.Rajaram and G.Chandra
Proc. of Solid State Phys. Symp. (India :DAE) **31C**, 233 (1988).

3. "FMR investigation of amorphous Fe-Co-Zr alloys"
V.Siruguri and S.N.Kaul
Proc. of Solid State Phys. Symp. (India :DAE) **33C**, 274 (1991).
4. "FMR study of spin wave excitations in amorphous $\text{Fe}_{90-x}\text{Co}_x\text{Zr}_{10}$ alloys"
V.Siruguri and S.N.Kaul
Proc. of Solid State Phys. Symp. (India :DAE) **34C**, 121 (1991).
5. "Origin of secondary resonance in amorphous Fe-Zr alloys"
V.Siruguri, Ch.V.Mohan and S.N.Kaul
Proc. of Solid State Phys. Symp. (India :DAE) **34C**, 373 (1991).
6. "Magnetic properties of amorphous Fe-rich Fe-Zr and $\text{Fe}_{90-y}\text{Co}_y\text{Zr}_{10}$ alloys"
V.Siruguri
Proc. of Solid State Phys. Symp. (India :DAE) **35C**, 19 (1992).
7. Scaling behaviour of magnetization in the critical region of $\text{a-Fe}_{90-x}\text{Co}_x\text{Zr}_{10}$ alloys"
V.Siruguri, P.D.Babu and S.N.Kaul
Proc. of Indo-US Workshop on Ordering Disorder (India :Univ. of Hyderabad, 1993) to be published in AIP Conf. Proceedings.
8. Angular dependence of ferromagnetic resonance field in $\text{a-Fe}_{90-x}\text{Co}_x\text{Zr}_{10}$ alloys: Uniaxial anisotropy"
V.Siruguri and S.N.Kaul
Proc. of Indo-US Workshop on Ordering Disorder (India :Univ. of Hyderabad, 1993) to be published in AIP Conf. Proceedings.
9. Evidence for suppression of reentrant behaviour with Co- substitution in $\text{a-Fe}_{90-x}\text{Co}_x\text{Zr}_{10}$ alloys"
V.Siruguri, S.N.Kaul, A.K.Nigam, G.Chandra, R.M.Kadam and M.D.Sastry
Proc. of Indo-US Workshop on Ordering Disorder (India :Univ. of Hyderabad, 1993) to be published in AIP Conf. Proceedings.